A Granular Flow Model of an Annular Shear Cell

University of Cape Town

Sherry Bremner

Supervised by Dr Indresan Govender

A thesis submitted to the University of Cape Town for the degree of PhD in Physics

September 2015

The copyright of this thesis vests in the author. No quotation from it or information derived from it is to be published without full acknowledgement of the source. The thesis is to be used for private study or non-commercial research purposes only.

Published by the University of Cape Town (UCT) in terms of the non-exclusive license granted to UCT by the author.

University of Cape Town

Abstract

Machinery such as an IsaMill^{TM} used in communition to produce fine particle sizes that allow minerals to be extracted are best modelled using granular flows. A single rheological description that captures all the features of granular flows has not yet been realised, although considerable progress towards a complete theory has been made. Existing models of such horizontally stirred mills are empirical, tend to be extremely dependent on boundary conditions and do not allow for confident extrapolation beyond their window of design.

As a first step to understanding the dynamics inside the IsaMill^{TM}, a constitutive stress model of a horizontal annular shear cell is developed. This shear stress model was used in an athermal energy balance to develop a description of the power dissipation, which drives the communition purpose of the IsaMill^{TM}.

The key ingredients (velocity, shear rate and volume fraction distributions) to the granular flow model are extracted from experiments using Positron Emission Particle Tracking (PEPT), as well as Discrete Element Method (DEM) simulations. 5 mm glass beads were used to fill an annulus 51 mm wide. In the PEPT experiments, two different surfaces of the driving wall (the inner cylinder of the shear cell) were used, over two shearing velocities. The effect of two friction coefficients over a range of shearing wall velocities were examined in the DEM simulations.

The data were examined over 3 selected radial lines and utilised to calculate the shear stress distribution and the power dissipation from the developed models. It was found that even the usually simple relations describing the dynamics within a vertical shear cell are greatly modified by changing the orientation of the rotation axis.

Declaration

I, Sherry Bremner, hereby declare that the work on which this thesis is based is my original work (except where acknowledgements indicate otherwise) and was done in collaboration with my supervisor, Dr I Govender (Department of Physics, University of Cape Town). Neither the whole work nor any part of it has been, is being, or is to be submitted for another degree in this or any other university. I authorise the University to reproduce for the purpose of research either the whole or any portion of the contents in any manner whatsoever.

Sherry Bremner

Signed by candidate

Signature Removed

2 September 2015

Acknowledgements

I would like to thank my supervisor Dr I Govender, without whom this thesis would not be possible. Dr Govender's expert guidance, as well as his wisdom and patience have ensured that this thesis is a success. Beyond this, I would like to acknowledge the contribution of Mr D Giovannoni whose input to data analysis techniques, LaTex templates and considerable availability for reality checks is greatly appreciated. The PEPT experimental work was completed with the aid of the PEPT Cape Town team, Mr M van Heerden and Mr C Liu. Mr A Morrison was also instrumental in the initial stages of the PEPT data analysis. The financial support of the National Institute for Theoretical Physics and the Centre for Minerals Research was instrumental in the completion of the thesis. I would also like to thank my parents, sisters and friends whose belief in my abilities has never wavered.

Contents

List of figures

Chapter 1.

Introduction

Granular matter, such as sand, cereal, snow or rocks, is defined as a system of discrete, rigid, usually cohesionless, macroscopic particles, whose size is typically larger than 100 µm [Rao and Nott, 2008, Andreotti et al., 2013, Nedderman, 1992]. Flow systems consisting of granular media exhibit peculiar features and flow phases that have not yet successfully been captured in an encompassing theory.

Research into the behaviour of granular flows has many applications in industrial processes as well as the modelling of natural hazards such as landslides and avalanches. Understanding the flow of granular material is particularly important in the minerals processing industry, where transport and beneficiation of minerals rely heavily on the flow of granular media. In communition (the reduction of solid materials from one average particle size to a smaller average particle size) grinding, crushing and milling of granular materials occurs. The resultant average particle size is dependant on the method of communition. For fine particle sizes, specialist mills such as the IsaMill$^{\text{TM}}$ are used. This is a horizontally run mill, where the slurry feeds through a chamber with rotating disks.

These communition systems rely heavily on the flow of granular material to achieve size reduction and extraction of the useful mineral. The processes used to accomplish this are known to be inefficient in energy usage Mishra [2003]. There exist many empirical models which describe the properties of the materials flowing in and out of various crushers and mills. These models are based on material concentration, flow rate, rate of rotation of the mill and the type of grinding media used. They are dependant on the boundary conditions of the system they were designed for and extrapolating beyond these is ill-advised in light of evolving ore bodies. Very little is known about the actual flow dynamics within these systems, as exploring the internal dynamics can be impractical as sensors would be destroyed by the harsh environment. Thus it is necessary to explore the

internal dynamics using computer simulations and non-invasive experimental techniques, in order to gain an understanding of the mechanisms governing breakage and transport of these granular flows.

In processes such as the fine grinding required in mineral beneficiation high shear and compression forces are believed to dominate the particle breakage. Thus optimisation of such fine grinding systems requires an understanding of the shear energy distribution within the system. These systems and processes are best modelled using granular media.

Steady progress has been made towards a coherent description of granular flows. They are usually separated into three regimes: quasi-static, dense and inertial or turbulent [Jaeger et al., 1996]. The dense, quasi-static regime, is characterised by slow shear rates and particles interacting by frictional contacts, making plasticity theory an ideal model for this regime [Nedderman, 1992, Tardos, 1997, Rajchenbach, 2001, Geng et al., 2003].

In the turbulent regime, the granular media flows rapidly and the density is low. Particles interact mainly by inelastic binary collisions and a granular kinetic theory has been developed [Ding and Gidaspow, 1990, Gidaspow, 2012, Ogawa et al., 1980, Wildman et al., 2008, Jenkins and Savage, 1983, Lun et al., 1984, Jenkins and Zhang, 2002, Savage and Jeffrey, 1981, Savage, 2007, Goldhirsch, 2003]. Energy must be continuously supplied to maintain this state due to the dissipative collisions [Jaeger et al., 1996, Goldhirsch, 2003].

The dense regime behaves similar to a fluid. Particles in this flow regime interact by friction and collisions which are characterised by enduring contacts [GDR MiDi, 2004, Pouliquen and Chevoir, 2002]. The assumption of binary collisions that is made in the kinetic theory approach no longer applies. Most granular flows encountered in nature and industry fall within this regime. It has been extensively studied in many configurations, either in confined flows [Tardos et al., 1998, Miller et al., 1996, Bocquet et al., 2001, Baxter et al., 1989, Baran et al., 2006, Howell et al., 1999, Veje et al., 1999, Losert et al., 2000, da Cruz et al., 2005] or free surface flows [Pouliquen, 1999, Lemieux and Durian, 2000, Khakhar et al., 2001, 1997, Rajchenbach, 1990, Taberlet et al., 2003].

Jop et al. [2006] has made important advances in modelling the dense regime with a model based on local rheology and the dimensionless considerations of [GDR MiDi, 2004]. This work was further explored in [Pouliquen et al., 2006, Pouliquen and Forterre, 2002, Jop et al., 2006, Pouliquen et al., 2005, Forterre and Pouliquen, 2008].

The goal of this thesis is to develop a theoretical framework which fully captures the flow regimes within a horizontally oriented annular shear cell. The shear cell consists of

two concentric cylinders, the annulus between them filled with a granular media. The inner cylinder rotates at a prescribed rate, providing shear in the system. This model extends the visco-plastic rheology of Jop et al. [2006] to include kinetic and turbulent stresses.

An athermal energy balance in conjunction with the model-derived shear stress allows an investigation into the relationship between shear rate, shear stress, volume fraction and ultimately the power dissipation distribution within this simple couette geometry. Measurements from Positron Emission Particle Tracking (PEPT) experiments are used to derive key inputs to the model (velocity and shear rate). Slow and dense flow on the outer edge of the PEPT experiment prevented a full exploration of the flow dynamics using this technique. Thus, the system was explored further using Discrete Element Method (DEM) simulations, allowing for the volume fraction distribution and power dissipation along selected radial lines to be calculated.

There exists a large amount of literature on experiments and simulations conducted in a couette geometry similar to what is presented here. This includes the work by Bocquet et al. [2001], Mueth [2003], Tardos et al. [1998], Veje et al. [1999], Mueth et al. [2000], Howell et al. [1999], Miller et al. [1996], Losert et al. [2000], Hsiau and Jang [1998], Khakhar et al. [1997]. Changing the orientation of the rotation axis adds considerable complexity to the problem, as even the simple relations obtained for vertical cells change considerably. This exploration of the horizontal shear cell will provide the ground work for the understanding required to develop a model of fine grinding machinery, such as the IsaMill$^{\text{TM}}$.

The structure of the rest of this thesis is as follows:

1. Part I focuses on the development of the generalised combinatorial stress model that captures the flow regimes measured in a shear cell. Along with an athermal energy balance, this is utilised in the development of a model of the power dissipation distribution within the shear cell.

2. Part II describes the experiments in the horizontal shear cell conducted using Positron Emission Particle Tracking (PEPT), presenting the calculations of the volume fraction and velocity distributions.

3. Part III shows the procedure of Discrete Element Method (DEM) simulations, the results of which were also used in the calculation of the power dissipation calculations. Both of these techniques are used to test the assumptions made in the formulation of the model.

4. Part IV compares the kinematics of the DEM and PEPT results with literature results and takes a look at possible scaling laws for this system.

5. Part V presents the conclusions.

Part I.

Theoretical Model

Chapter 2.

Rheology of Granular Flows

The development of a generalised model of granular flows which captures the flow regimes measured in an annular shear cell (via PEPT and DEM), requires an understanding of the rheology of granular flows. Although there is a lack of a complete theory of granular flows, steady progress has been made towards a coherent description, including the development of constitutive relations which describe the local rheology in many granular systems [GDR MiDi, 2004]. This local rheology was extended to apply throughout the system by Jop et al. [2005], with further developments made by Forterre and Pouliquen [2008] and Lee and Huang [2012].

A frictional visco-plastic rheology is developed in this model by decomposing the shear stress into contributions which describe the behaviour of granular flows in the three flow regimes: quasi-static, dense and inertial/turbulent regimes. The model is based heavily on work from Bagnold [1954a], Ding and Gidaspow [1990], Jop et al. [2005], Forterre and Pouliquen [2008], Lee and Huang [2012] and GDR MiDi [2004]. Visco-plasticity in continuum mechanics characterises material deformation that is rate and load dependent. A visco-plastic fluid behaves like a rigid body when the applied stress is not sufficient to overcome a material-dependent yield stress. Above this yield stress, the material behaves like a viscous fluid with the effective viscosity dependent on both the shear rate and local pressure. Computational modelling (Discrete Element Method) of macroscopic granular flows utilises a visco-plastic model to model the contacts between particles in the form of a linear spring and dashpot model.

For rigid, cohesionless spheres in which boundary conditions are negligible, the relevant parameters are pressure, P, shear rate, $\dot{\gamma}$, particle size, d, and bulk density, $\rho = \rho_m \phi$, where ϕ is the solids concentration, or volume fraction, and ρ_m is the material density.

2.1. Frictional visco-plastic constitutive law

In the development of constitutive relations, GDR MiDi [2004] introduced a dimensionless number, later called the inertial number, I, by da Cruz et al. [2005], which quantifies the inertial effects on the material flow. The inertial number is the ratio of timescales governing the grain motion. The confinement time (or time of rearrangement), $T_P = d\sqrt{\frac{\rho_m}{P}}$, and the deformation time, $T_\gamma = \frac{1}{\dot{\gamma}}$. Thus,

$$I = \frac{\dot{\gamma} d}{\sqrt{\frac{P}{\rho_m}}}, \tag{2.1}$$

if we consider two layers of grains, one sliding on top of the other. T_γ is the shear time, the time for one grain to move a distance d with respect to a grain beneath it. The confinement time, T_P, can be interpreted as the time taken for the grain to fall or be pushed back into the hole between grains in the lower layer. These timescales are illustrated in Figure 2.1 and may differ to a large extent. In the quasi-static regime, the motion of the particle would consist of a slow sliding of the layers, with a rapid collapse into the hole between grains.

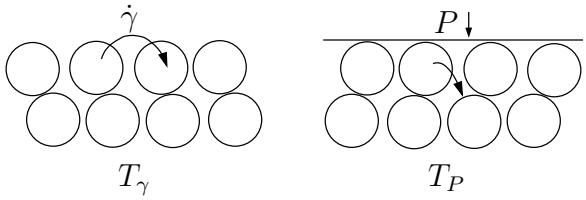

Figure 2.1.: Timescales governing grain motion. Reproduced from GDR MiDi [2004]

The inertial number is the square root of the Savage number, introduced by Savage and Hutter [1989]. This dimensionless number, which characterises the extent of fluidisation and the importance of collisional stresses, was derived by taking the ratio of the collisional stress to the total normal stress. Both I and the Savage number can be used to characterise the flow regime of the granular flow. da Cruz et al. [2005] set the limits between the regimes as follows. The quasi-static regime is characterised by very small I ($I \leqslant 10^{-2}$), the dense flow regime has $10^{-2} \leqslant I \leqslant 0.2$ and the collisional regime having values $I > 0.2$.

A second dimensionless number, the effective friction coefficient, was introduced by da Cruz et al. [2005] and confirmed in a number of different geometries by GDR MiDi

[2004].

$$\mu\left(I\right) = \left|\frac{\tau}{P}\right|, \tag{2.2}$$

can be thought of as the rescaled shear stress and is a function of I.

Jop et al. [2005] developed a basal friction law valid at the base of the flowing layer in a heap geometry, describing the behaviour of the effective friction with I.

$$\mu\left(I\right) = \mu_{min} + \frac{\mu_{max} - \mu_{min}}{I_0/I + 1}, \tag{2.3}$$

agrees with experimental findings at the base of the flowing layer, although there was no direct confirmation that it agreed elsewhere in the flowing layer. This local rheology was assumed to apply throughout the system. The shape of $\mu(I)$ starts off at a minimum value when $I = 0$ and increases until it asymptotically approaches the maximum value, as illustrated in Figure 2.2.

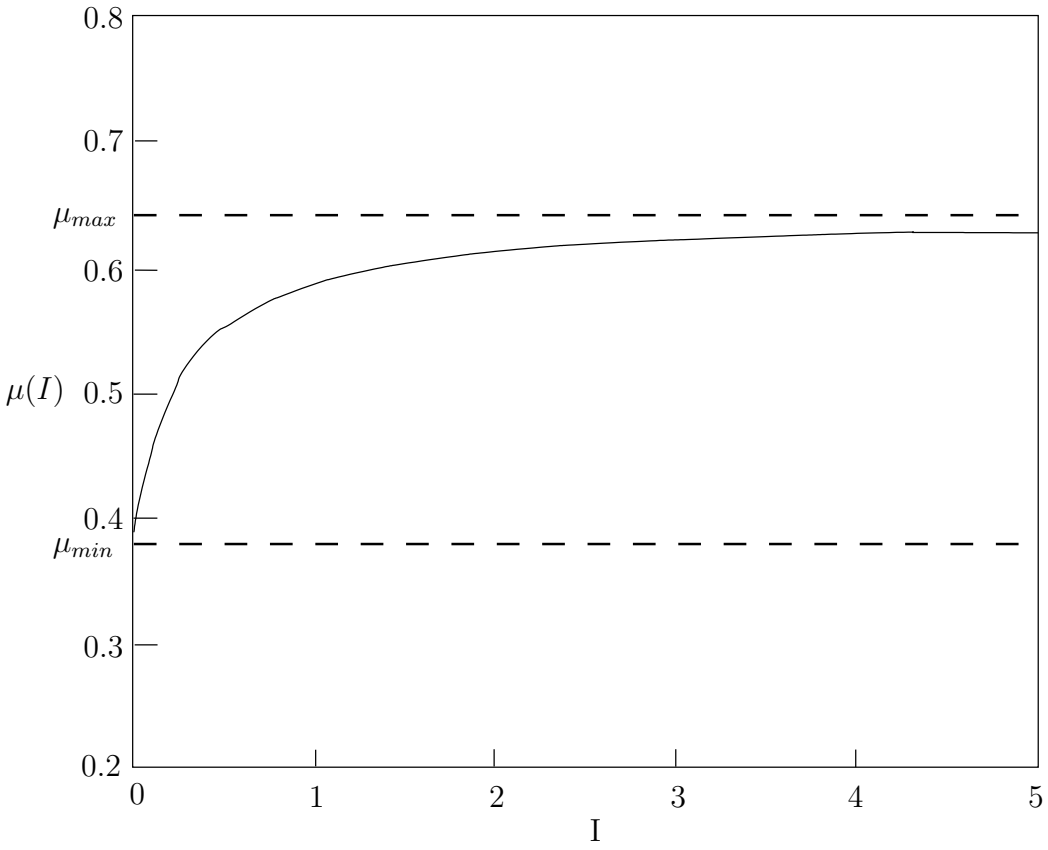

Figure 2.2.: The effective friction coefficient developed by Jop et al. [2005].

There is considerable evidence from both experiments and simulations to suggest that the constitutive relations of granular flow are given by the effective friction coefficient $\mu(I)$ and a suitable model for the volume fraction distribution with I, $\phi(I)$. The volume fraction is the ratio of volume occupied by the grains to the total volume of the system and as it is governed by the time during which the grains actually move, dependency on the inertial number is logical.

Although predictions from models formulated using such relations describe observations from various flow configurations quite accurately, there are some characteristics that are not captured [Forterre and Pouliquen, 2008]. The transitions between the three flow regimes are not described, as well as the hysteresis seen in the quasi-static regime in rotating drums and heap flows. The thickness of the localised shear band seen in confined flows is also not predicted by the model. For this reason, a composite granular flow rheology has been proposed and is discussed in detail below.

2.2. Composite Granular Flow Rheology

Lee and Huang [2012] developed a kinetic-theory-based model, where the shear stress was divided into rate-independent and rate-dependent components. The rate-independent stress captured the static contribution created by enduring contacts between grains, while the rate-dependent component accounted for the collisions between grains using granular kinetic theory. This model captured the hysteretic flow threshold, as well as the flow regime threshold. Takahashi [2009] also modelled debris flow with a shear stress tensor that was broken down into components describing different flow regimes.

Utilising this idea, a new model for the shear stress is developed. The shear stress tensor, τ, is decomposed into three parts:

- τ_s: The quasi-static shear stress applies in the dense regime. This regime is characterised by enduring contacts between grains and low inertial number (thus low shear rates, or high pressure).
- τ_c: The kinetic-collisional shear stress, capturing behaviour in the dense flow (intermediate) regime is based on Bagnold [1954a]. This regime is characterised by intermediate inertial numbers.

- τ_t: The turbulent shear stress captures the gaseous-like behaviour of low density, high shear rate flows and has very high inertial numbers. This regime is not expected to play a crucial role in the annular shear cell model proposed.

The total shear stress is then

$$\tau = \tau_s + \tau_c + \tau_t. \tag{2.4}$$

Similarly, the pressure (or normal stress) is described as a sum of components from turbulence, quasi-static and collisional terms,

$$P = P_s + P_c + P_t. \tag{2.5}$$

The contributions towards the shear and normal stress from each source are discussed below.

2.2.1. Total pressure and volume fraction

The total pressure, P, at some location within the system with inertial number I can be described by inverting Equation 2.1,

$$P = \left(\frac{\dot{\gamma} d}{I}\right)^2 \rho_m, \tag{2.6}$$

where the relationship between the material density, ρ_m, in Equation 2.6, the volume fraction distribution ϕ and the bulk density ρ is $\rho = \phi\rho_m$. Equation 2.6 highlights that as I increases towards the inertial regime, the total pressure, P necessarily decreases. However, in the inertial regime there is an increase in inter-particle collisions, resulting in an increase in the collision pressure component, P_c. In order for Equation 2.5 to remain valid in this case, mathematical consistency requires that $P_s + P_t$ is negative. As a negative pressure is not physical, the quasi-static pressure P_s should become 0 as I increases to a point where kinetic-collisional interactions are relevant. In this regime $P = P_c + P_t$.

Equation 2.6 also suggests that P will increase unbounded as $I \to 0$. This is both inconsistent with measurements [Josserand et al., 2006, Johnson et al., 1990] and against the intuition that some level of pressure saturation should be achieved, as predicted by the *Janssen Effect* [Andreotti et al., 2013]. As noted earlier, low inertial numbers are

consistent with the quasi-static regime, which is dominated by the quasi-static pressure component. Thus $P = P_s$ when $I \to 0$.

These conditions are necessary to maintain mathematical and physical consistency, but they also highlight a deficiency in the inertial number to fully describe the total pressure. In the quasi-static regime, where high loading is expected, the quasi-static pressure P_s is reported to obey the scaling law: $P_s = P_0 (\phi_0 - \phi_{min})$ [Lee and Huang, 2012, Johnson et al., 1990, Josserand et al., 2006], which vanishes in the inertial regime, when $\phi < \phi_{min}$. The volume fraction as $I \to 0$, ϕ_0, and P_0 are dependent on the particle properties in a non-trivial manner, which makes them difficult to determine.

The solution to these problems is to carefully choose a volume fraction distribution as a function of the inertial number, such that the balance between mathematical and physical consistency is achieved.

In this regard, Pouliquen et al. [2006] developed a dilatancy law by considering the simple picture of a single grain moving over a layer of grains just below. They assumed that the volume fraction was at it's maximum when the bead was in a hole formed between the two grains below. As a shear stress is being applied to the material, the particle moves out from the hole and the volume fraction decreases to a minimum. Using the typical time of rearrangement (used in the derivation of I), the linear relation,

$$\phi (I) = \phi_{max} - (\phi_{max} - \phi_{min}) I, \tag{2.7}$$

for the dilatancy law was developed.

Typical values were found to be $\phi_{max} = 0.6$ and $\phi_{min} = 0.4$. Although the constitutive laws developed by Pouliquen et al. [2006] described the flow well, especially in plane shear flows, there were parts that broke down when gravity was present, or the shear occurred in a cylindrical geometry.

A similar linear dilatancy law was given by da Cruz et al. [2005], which was also used by Koval et al. [2009], Daniel et al. [2008] and Rognon et al. [2008], who extended the model to cohesive particles. This linear law,

$$\phi (I) = \phi_{max} - aI, \tag{2.8}$$

was found to break down at high values of I.

Another dilatancy law was developed by Hatano [2007], that described the relationship as a power law. This power law was developed from three dimensional discrete element

simulations of isobaric plane shear.

$$\phi_{max} - \phi = aI^{\delta}, \tag{2.9}$$

where, ϕ_{max} in this case is the limit of the volume fraction as the shear rate tends to 0. The constants were found to be $a = 0.11$ and $\delta = 0.56$, and were also independent of the model details. The above equation was derived for small inertial numbers. This form of the dilatancy law was also used by Lee and Huang [2012].

These models are shown together in Figure 2.3. They have $0.3 \leq \phi \leq 0.6$ for the inertial range $10^{-4} \leq I \leq 1$, using the parameters from Lee and Huang [2012] for the models. The inertial range for the dense regime in rotating drums, as derived from 3D measurements by Orpe and Khakhar [2007], is $0 < I < 0.4$. The upper limit in this range corresponds to the free surface, where $I_{upper} = 0.4$ is imposed. This range in inertial number corresponds to $0.48 \leq \phi \leq 0.6$, which is too narrow a range when comparing to the experimentally derived volume fraction of $0.2 < \phi \leq 0.6$ in Pathmathas [2015]. The range of volume fraction and inertial number within a horizontally rotated annular shear cell is explored experimentally in later chapters of this thesis, although intuition suggests that both the quasi-static and dense flow regimes are present in this configuration, thus a range of volume fraction similar to that of the rotating drum is expected.

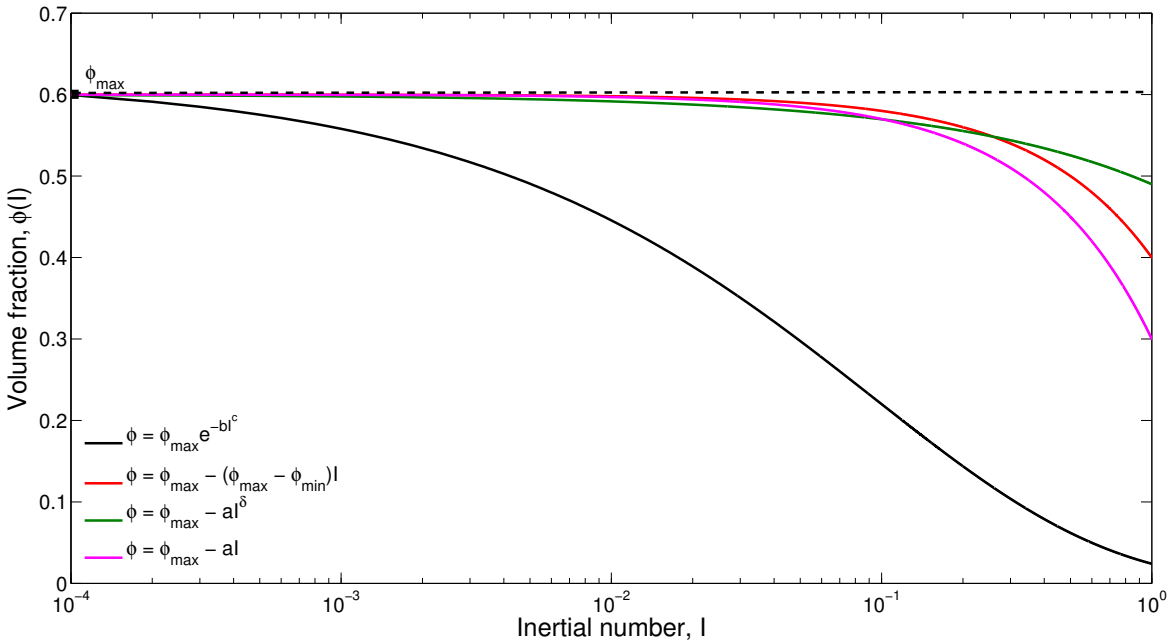

Figure 2.3.: The volume fraction as a function of I, as discussed in the models of da Cruz et al. [2005] (purple line), Hatano [2007] (green line), Pouliquen et al. [2006] (red line), using the parameters in Lee and Huang [2012] and the model discussed here (black line).

To more adequately describe the volume fraction for the range of inertial number values expected, an empirical dilatancy model,

$$\phi = \phi_{max} e^{-bI^c}, \tag{2.10}$$

was developed. This dilatancy model was applied to rotating drums in Govender et al. [2014], with the values $b = 1.848$, $c = 0.6014$, $\phi_{max} = 0.6$. These values were chosen such that the average inertial number at the free surface was $\langle I_{FS} \rangle = 0.4$, consistent with experiments and the average volume concentration at the free surface $\langle \phi_{FS} \rangle = 0.2$. It appears alongside the other dilatancy models discussed in Figure 2.3. As the volume fraction distribution in the horizontal shear cell is slightly different to that of the rotating drum, these values were only used as a starting point for a function fit to the volume fraction in the shear cell, with final parameters being $b = 3.2480$, $c = 0.4963$ and $\phi_{max} = 0.704$.

The total pressure can then be determined by substituting Equation 2.10 in to Equation 2.6, which yields

$$P = (\dot{\gamma} d)^2 \rho_m \left[\frac{1}{b} \ln \left(\frac{\phi_{max}}{\phi} \right) \right]^{-\frac{1}{c}}. \tag{2.11}$$

In most shear cell literature, the total pressure is usually taken as a simple gravitational pressure, $P = \rho g h$. The orientation of the horizontal shear cell and the existence of collisional stresses makes the use of this purely hydrostatic model inaccurate. Thus, Equation 2.11 is favoured, as the shear rate and volume fraction can be determined from DEM and PEPT experiments, which means the inertial number and pressure can be predicted from the model discussed here.

2.2.2. Kinetic-Collisional Component

The kinetic-collisional shear stress captures the behaviour of the material in the dense flow regime. This component is based on Bagnold [1954a], who used ideas from the kinetic theory of gases to model the collisions between pairs of grains and develop a radial distribution function that was based on the solids concentration. The component used here is

$$\tau_c = \frac{\rho_m}{c^n} (Gd)^2 \dot{\gamma}^2, \tag{2.12}$$

where the sphericity of the grains is c^n, with n being a fitting parameter, ρ_m is the grain material density, G describes the radial distribution function, d the particle diameter and $\dot{\gamma} = \frac{\partial v_\theta}{\partial r}$ is the shear rate. The form of G used here is according to Savage [1998],

$$G = \phi g(\phi) = \frac{\phi(16 - 7\phi)}{16\left(1 - \frac{\phi}{\phi_{max}}\right)^2}, \tag{2.13}$$

where ϕ_{max} is the maximum possible packing fraction.This form of the radial distribution function, makes the stresses diverge as the solids concentration approaches the maximum value. The form is similar to that used by Lun [1991], Ding and Gidaspow [1990], Savage [1988] and was implicit in Bagnold [1954a] and Ogawa et al. [1980]. For finite granular flow systems, the value of ϕ_{max} can be as low as 0.55 depending on the geometry of the shearing space [Lun, 1991]. For the closest random packing of spheres ϕ_{max} is approximately 0.64 and the closest regular packing ϕ_{max} is 0.7404 [Lun, 1991, Savage, 1988, Bagnold, 1954a].

The pressure in the kinetic-collisional regime is described in Roufail et al. [2012] and Bagnold [1954a] as proportional to the shear-stress energy tensor,

$$P_c = N\tau_c. \tag{2.14}$$

Kinetic theory of gases gives $N = 3$, the applicability in granular flows will be investigated using experimental data.

2.2.3. Turbulent Component

The formulation of the turbulent shear stress component comes from Takahashi [2009], where

$$\tau_t = \rho l^2 \dot{\gamma}^2, \tag{2.15}$$

and is applicable in the gaseous regime. This is equivalent to the pressure term derived by Hotta [2012], which is based on Prandtl's mixing length theory. Thus, in this work the turbulent pressure is taken to be equal to the turbulent shear stress component,

$$P_t \approx \tau_t. \tag{2.16}$$

Hotta [2012] proposed the use of the mixing length defined by Ashida et al. [1985],

$$l = \sqrt{\kappa_t} \left(\frac{1-\phi}{\phi} \right)^{\frac{1}{3}} d, \tag{2.17}$$

where κ_t is the parameter from Suzuki et al. [2003]. This captures the disorder scale of the particle gap. In the model for the mixing length, $k_t = 5.24$ is chosen, which corresponds to a mixing length of $2d$.

Using Equation 2.17 and recalling that $\rho = \rho_m \phi$, the turbulent component of the shear stress is then described by

$$\tau_t = \kappa_t \rho_m d^2 \phi^{\frac{1}{3}} (1-\phi)^{\frac{2}{3}} \dot{\gamma}^2. \tag{2.18}$$

2.2.4. Quasi-static Component

The quasi-static shear stress applies in the dense regime, where there are enduring contacts between grains. This regime has a low inertial number, thus implying low shear rates or high pressure. The quasi-static shear stress is decomposed into τ_w, the shear stress at the side walls, and τ_i, the internal shear stresses within the bed so that

$$\tau_s = \tau_i + \tau_w. \tag{2.19}$$

Taberlet et al. [2003] developed a friction law for an inclined channel which accounted for the constant internal friction between particles and the friction due to the sidewalls. This effective friction was then applied to a rotating drum configuration in Taberlet et al. [2006], which yielded

$$\tan\theta_s = \mu_i + \mu_w \frac{h}{W}. \tag{2.20}$$

Here μ_i is the internal friction coefficient, μ_w is the sidewall friction coefficient (an effective friction coefficient that accounts for both the rolling and sliding of grains along the sidewalls), W is the width of the channel and h is the height of the flowing layer. Applying the coulomb criterion, the term for the quasi-static shear stress follows [Jop et al., 2005, Lee and Huang, 2012, Bagnold, 1954a] and is given by

$$\tau_s = P_s \tan\theta_s. \tag{2.21}$$

The static internal friction angle is given by θ_s. This was found to be the angle of inclination of the free surface (in rotating drums), as the incline got large enough for flow to start. The quasi-static component of the shear stress is thus dependent on the expression for the effective friction coefficient. The problem then remains to determine proper descriptions of μ_i and μ_w.

μ_w is considered to be a constant based on the granular material and the material used in the confining system. The basal friction law given in Equation 2.3, developed by Jop et al. [2005], has been applied in many systems with decent success. As mentioned previously, various problems exist with this formulation. In terms of the annular shear cell considered here, this friction law has less applicability. The constants μ_{min}, μ_{max} and I_0 are all dependent on the angle of inclination of the free surface and the phase transition between quasi-static and dense flow is not captured [Forterre and Pouliquen, 2008].

Thus the form of Equation 2.21 was modified to apply to a confined flow (not dependent on the free surface inclination) and to more fully describe the phase transition. The hysteresis observed in many granular flows in the quasi-static regime is also described with this formulation. The shear stress used to describe this regime is

$$\tau_s = \mu_i e^{-\phi I} P_s + \mu_w \left(\frac{r}{R}\right) P_s, \tag{2.22}$$

where the τ_w term has been converted to cylindrical coordinates for ease of use in the annular shear cell model. The μ_i used here is now a material dependent constant, and the variation of $\mu(I)$ with inertial number and volume fraction is described by $e^{-\phi I}$. As I increases from 0, $\mu(I)$ initially decreases from its initial value until a minimum is reached (the transition from a solid to flowing regime) and then it increases with increasing inertial number (as the flow becomes a dense inertial flow).

The pressure due to the quasi-static contribution can then be determined using the total pressure in the system (Equation 2.11) and the contributions from the other terms,

$$P_s = P - P_c - P_t. \tag{2.23}$$

2.2.5. Effective friction coefficient

The components described above allow for the effective friction coefficient from Equation 2.2 to be calculated. The ratio of the total shear stress and the total pressure

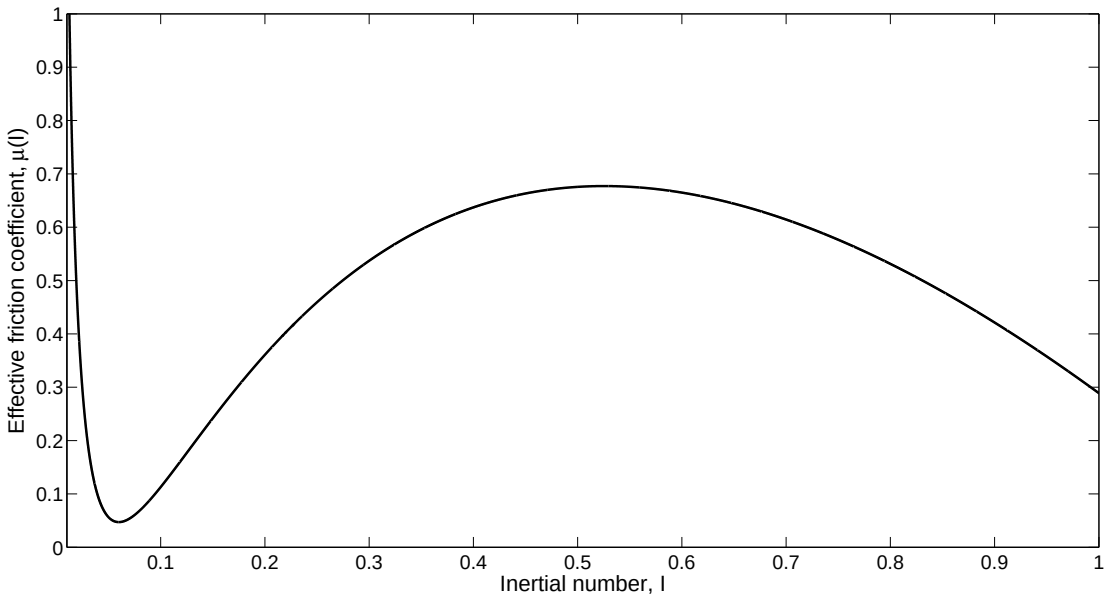

Figure 2.4.: The effective friction coefficient derived from the model discussed here, at a point 2 particle diameters from the shearing wall. The parameters used were those discussed in the previous sections and are shown in Table 2.1.

yields

$$\mu(I) = \left(\frac{G^2}{c^n} + \kappa_t \phi^{\frac{1}{3}} (1-\phi)^{\frac{2}{3}}\right) I^2 + \left(\mu_i e^{-\phi I} + \mu_w \left(\frac{r}{R}\right)\right) \left(1 - \frac{NG^2}{c^n \left[\frac{1}{b} \ln\left(\frac{\phi_{max}}{\phi}\right)\right]^{-\frac{1}{c}}} - \frac{\kappa_t \phi^{\frac{1}{3}} (1-\phi)^{\frac{2}{3}}}{\left[\frac{1}{b} \ln\left(\frac{\phi_{max}}{\phi}\right)\right]^{-\frac{1}{c}}}\right). \quad (2.24)$$

The effective friction coefficient is plotted in Figure 2.4, using the model values discussed above and shown in Table 2.1, where the radial distance, r, is taken at a point of 2 particle diameters from the shearing wall.

In the quasi-static regime, at very small inertial numbers, the effective friction coefficient is large. As the regime changes to the dense regime, a minimum is reached in the effective friction coefficient. A maximum value of the effective friction is reached at around $I \approx 0.5$, after which it decreases. This is the transition to the turbulent (or collisional) regime, although this occurs at higher I than specified by da Cruz et al. [2005].

Table 2.1.: Parameters used in Equation 2.24 to produce Figure 2.4.

Parameter	Value
N	3
c^n	1
κ_t	5.24
b	3.24
c	0.49
R	50 mm
r	10 mm
μ_i	0.5
μ_w	0.8
ϕ_{max}	0.6

The above rheology is applied to an annular shear cell configuration in order to determine the power dissipation distribution within the system. This forms the first step towards a comprehensive model of fine particle grinding in machinery such as an IsaMill$^{\text{TM}}$.

Chapter 3.

Power Dissipation Distribution

The problem of modelling the behaviour of granular systems often utilises continuum mechanics. In these models, the granular medium is assumed to be continuous, thus quantities such as velocity and density are modelled as smooth functions of position and time. Considering that these systems are discrete, often to the naked eye, the applicability of continuum mechanics needs to be explored. The motivation for assuming a continuum lies in the shear complexity of the mathematics required to model a discrete system of a large amount of particles. This is rather eloquently summarised by [Truesdell and Muncaster, 1980, pg. xvi-xvii]

> However discrete may be nature itself, the mathematics of a very numerous discrete system remains even today beyond anyones capacity. To analyse the large, we replace it by the infinite, because the properties of the infinite are simpler and easier to manage. The mathematics of large systems is the infinitesimal calculus, the analysis of functions which are defined on infinite sets, and whose values range over infinite sets. We need to differentiate and integrate functions. Otherwise, we are hamstrung if we wish to deal effectively, precisely with more than a few dozen objects able to interact with each other. Thus somehow, we must introduce the continuum.

The problem then lies in defining the conditions under which a continuum model can be applied. Batchelor [1967] considered a fluid as a continuum when the fluid property being measured was constant over a volume element which was small in relation to the scale of macroscopic properties of the fluid such as pressure and temperature, but large on the microscopic scale. Thus the volume element should be large enough to contain numerous molecules, and large enough for fluctuations due to the particle nature of the material to have no effect on the observed fluid property. This volume element should

also be small enough so that the observed fluid property does not change if the element is reduced in size. This same idea was supported by Fung [1969]. A more rigorous condition is formulated using the Knudsen number, the ratio of the mean free path to the characteristic length of the physical boundaries of interest. If the Knudsen number is greater than one, the mean free path of the particle is comparable to the length scale of interest, thus the continuum approximation is not valid [Chung, 2007].

While discussing the concept of the density of a gas, Chapman and Cowling [1953] noted that the time scale of the movement of particles also played a role in the validity of a continuum model. The macroscopic quantity (density in this case) being measured was averaged over a small time, t. This was long, when compared to the average time for a molecule to cross the volume element under consideration, yet short compared to the time variations of the macroscopic properties.

Rao and Nott [2008] considered this in the context of granular flows, in which the first condition is often violated. It is possible for a small volume element ΔV to effectively contain a large number of particles (or grains), if the second condition holds. In the shear cell considered here, the particles had a diameter of 5 mm and ΔV was a rectangular bin with sides 5 x 5 x 90 mm. At any given time, the maximum number of particles contained in ΔV was 5. If particles travel on average at 0.5 ms^{-1}, there is a flux of 100 particles through ΔV in 0.2 s. Then ΔV effectively contains a large number of particles, provided timescales greater than roughly 0.2 s are considered. This estimate gets smaller with increasing speed of the particles.

Thus the momentum and energy balances of continuum mechanics are used here to describe the power dissipation distribution within the shear cell.

3.1. Shear Cell Model

The annular shear cell model is set up using cylindrical coordinates, with the z-axis pointing along the axis of rotation and the gravitational force in the negative y direction. This is an atypical orientation of a standard shear cell, as the model is the first step to understanding breakage and power dissipation in the fine griding mills used in minerals processing. The coordinate system is shown in Figure 3.1.

Although mechanical energy is not conserved in a flow system, it is still possible to write an equation of change for mechanical energy within the system. A momentum balance over a small volume element through which the material is flowing is considered.

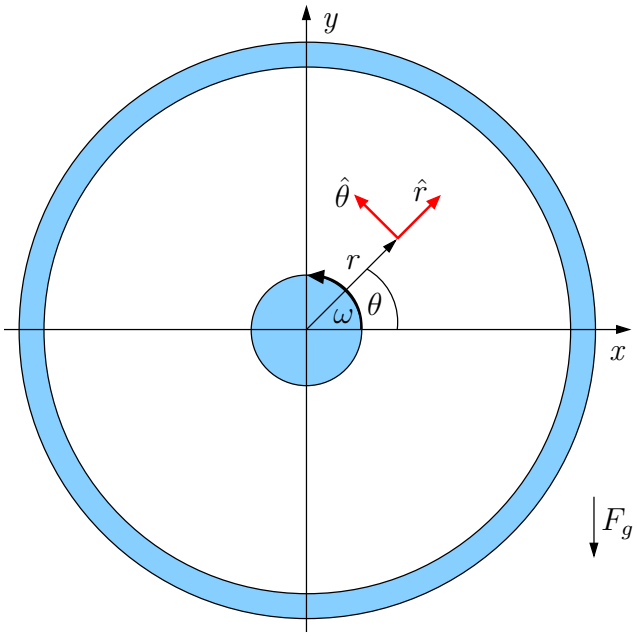

Figure 3.1.: The coordinate system for the annular shear cell model.

This volume element is then reduced to an infinitesimal size, thus treating the material as a continuum. The equation of motion,

$$\frac{\partial}{\partial t}\rho\mathbf{v} = -\left[\boldsymbol{\nabla}\cdot\rho\mathbf{v}\mathbf{v}\right] - \boldsymbol{\nabla}P - \left[\boldsymbol{\nabla}\cdot\boldsymbol{\tau}\right] + \mathbf{F}, \tag{3.1}$$

for flow in an isothermal system of a pure fluid is generated [Bird et al., 2002, pg. 80], following the notation used therein. The velocity, $\mathbf{v}$, material density, ρ, pressure, P and stress energy tensor, $\boldsymbol{\tau}$, are used to describe the rate of increase of momentum per unit volume. This is represented by the sum of momentum contributions from the rate of addition of momentum (per unit volume) by: convection (the divergence of the dyadic product $\rho\mathbf{v}\mathbf{v}$); molecular transport (the gradient of the pressure, $\boldsymbol{\nabla}P$ and the divergence of the stress energy tensor, $\boldsymbol{\nabla}\cdot\boldsymbol{\tau}$); and any external forces ($\mathbf{F}$).

Taking the dot product of $\mathbf{v}$ with (3.1), the equation of change for kinetic energy is derived [Bird et al., 2002, pg. 81], with the result

$$\begin{aligned}\frac{\partial}{\partial t}\left(\frac{1}{2}\rho v^2\right) = &-\left(\boldsymbol{\nabla}\cdot\frac{1}{2}\rho v^2\mathbf{v}\right) - \left(\boldsymbol{\nabla}\cdot P\mathbf{v}\right) - P\left(-\boldsymbol{\nabla}\cdot\mathbf{v}\right)\\ &- \left(\boldsymbol{\nabla}\cdot\left[\boldsymbol{\tau}\cdot\mathbf{v}\right]\right) - \left(-\boldsymbol{\tau}:\boldsymbol{\nabla}\mathbf{v}\right) + \left(\mathbf{v}\cdot\mathbf{F}\right).\end{aligned} \tag{3.2}$$

Equation 3.2 describes the rate of increase of kinetic energy per unit volume as the sum of contributions from convection, pressure, an increase in internal energy, viscous

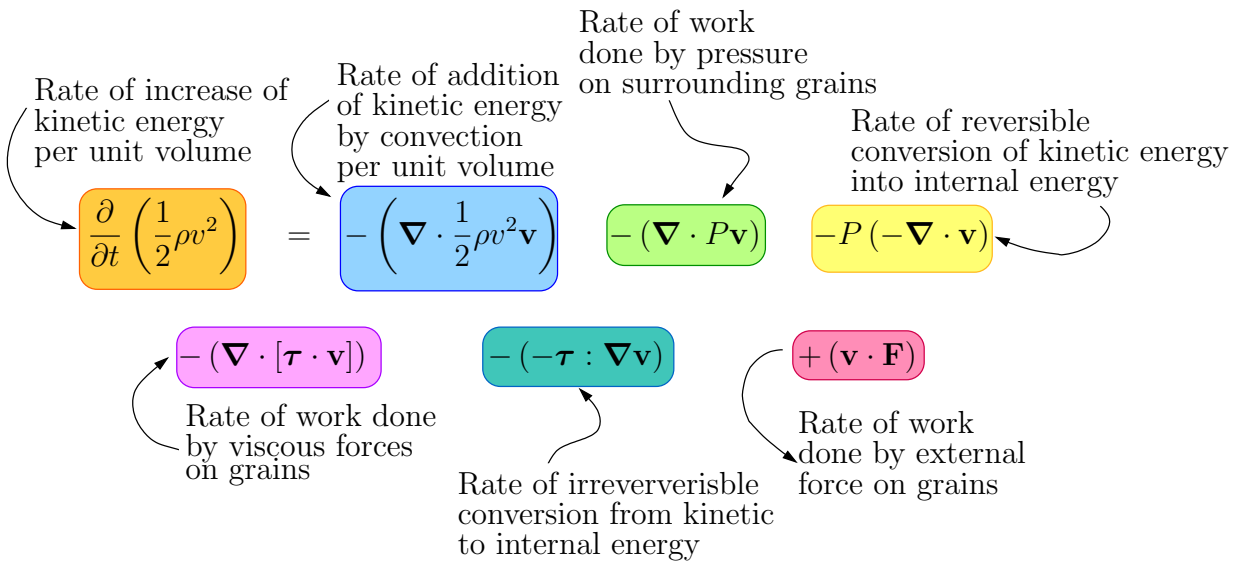

Figure 3.2.: Diagram explaining terms of equation 3.2.

forces and external forces. Figure 3.2 shows the physical meaning of each term in (3.2). This equation contains only mechanical terms and is often referred to as the equation of change of mechanical energy. The term describing the irreversible conversion from kinetic to internal energy, or the degradation of mechanical energy into thermal energy, $-(\boldsymbol{\tau}:\nabla\mathbf{v})$, is sometimes called viscous dissipation heating. The pressure term can be either positive or negative, depending on if the fluid is expanding or contracting.

The above equations are fluid equations derived for an isothermal system. These are systems in which there are no externally imposed temperature gradients and no appreciable temperature change resulting from expansion, contraction or viscous dissipation.

3.2. Model hypotheses

In the annular shear cell, the granular media forms an athermal system. Thus, the increase of internal energy of the particles does not influence the macroscopic dynamics of the system. The form of Equation 3.2 can be further simplified by making the following assumptions.

1. The flow is in a steady-state, thus

$$\rho\frac{\partial}{\partial t}\left[\frac{1}{2}v^2\right]=0. \tag{3.3}$$

This is valid over short distances, of the order of the natural length scale (the particle diameter, d) of the system.

2. The stress-energy tensor is symmetric, resulting in

$$\tau_{ij} = \tau_{ji}. \tag{3.4}$$

This arises from the condition that there are no localised torques on the grains, which requires the stress-energy tensor to be symmetric in order to satisfy the angular momentum balance.

3. The velocity components are assumed to be only radially dependent, with the tangential component dominating the flow. Thus,

$$v_z \backsimeq 0, \tag{3.5}$$
$$v_\theta = v_\theta(r), \tag{3.6}$$
$$v_r = v_r(r), \tag{3.7}$$
$$v_\theta \gg v_r, v_z. \tag{3.8}$$

4. Over short distances, motive and dissipative stresses are balanced (the velocity divergence is negligible) such that

$$\frac{\partial v_\theta}{\partial \theta} = \frac{\partial v_r}{\partial r} = \frac{\partial v_z}{\partial z} = 0. \tag{3.9}$$
$$\tag{3.10}$$

5. The external force under consideration is

$$\mathbf{F} = \rho \mathbf{g}. \tag{3.11}$$

6. A consequence of the athermal formulation is that fluctuations of a thermal origin are irrelevant. The fluctuations seen in PEPT data and DEM simulations are caused by grains sliding over adjacent corrugated layers. Fluctuating volume fraction is due to particle layering as well. Therefore the rate of irreversible conversion from kinetic to internal energy is irrelevant and

$$\boldsymbol{\tau} : \boldsymbol{\nabla} \mathbf{v} \approx 0. \tag{3.12}$$

Using the tensor identity for a symmetric tensor,

$$\begin{aligned} \boldsymbol{\tau} : \boldsymbol{\nabla}\mathbf{v} &= \boldsymbol{\nabla} \cdot [\boldsymbol{\tau} \cdot \mathbf{v}] - \mathbf{v} \cdot [\boldsymbol{\nabla} \cdot \boldsymbol{\tau}] && (3.13) \\ 0 &\approx \boldsymbol{\nabla} \cdot [\boldsymbol{\tau} \cdot \mathbf{v}] - \mathbf{v} \cdot [\boldsymbol{\nabla} \cdot \boldsymbol{\tau}] && (3.14) \\ \mathbf{v} \cdot [\boldsymbol{\nabla} \cdot \boldsymbol{\tau}] &\cong \boldsymbol{\nabla} \cdot [\boldsymbol{\tau} \cdot \mathbf{v}] \,. && (3.15) \end{aligned}$$

7. The pressure within the shear cell is predominantly radial, $P = P(r)$. Thus,

$$\mathbf{v} \cdot (\boldsymbol{\nabla} p) \cong \frac{\partial P}{\partial r} v_r, \tag{3.16}$$

which implies that the only non-zero components of $\boldsymbol{\tau}$ are $\tau_{r\theta} = \tau_{\theta r}$.

3.2.1. Reducing terms in Equation 3.2

To simplify $\mathbf{v} \cdot [\boldsymbol{\nabla} \cdot \boldsymbol{\tau}]$:

$$[\boldsymbol{\nabla} \cdot \boldsymbol{\tau}] = \sum_k \boldsymbol{\delta_k} \left(\sum_i \frac{\partial}{\partial x_i} \tau_{ik} \right), \tag{3.17}$$

where the k-th component is $[\boldsymbol{\nabla} \cdot \boldsymbol{\tau}]_k = \sum_i \nabla_i \tau_{ik}$. The components are

$$\begin{aligned} [\boldsymbol{\nabla} \cdot \boldsymbol{\tau}]_r &= \sum_i \nabla_i \tau_{ri} = \nabla_r \tau_{rr} + \nabla_\theta \tau_{r\theta} + \nabla_z \tau_{rz}, && (3.18) \\ [\boldsymbol{\nabla} \cdot \boldsymbol{\tau}]_\theta &= \sum_i \nabla_i \tau_{\theta i} = \nabla_r \tau_{\theta r} + \nabla_\theta \tau_{\theta\theta} + \nabla_z \tau_{\theta z}, && (3.19) \\ [\boldsymbol{\nabla} \cdot \boldsymbol{\tau}]_r &= \sum_i \nabla_i \tau_{zi} = \nabla_r \tau_{zr} + \nabla_\theta \tau_{z\theta} + \nabla_z \tau_{zz}. && (3.20) \end{aligned}$$

Based on the hypotheses the only non-zero components of $\boldsymbol{\tau}$ are $\tau_{r\theta} = \tau_{\theta r}$. Therefore,

$$[\boldsymbol{\nabla} \cdot \boldsymbol{\tau}] = [\boldsymbol{\nabla} \cdot \boldsymbol{\tau}]_r + [\boldsymbol{\nabla} \cdot \boldsymbol{\tau}]_\theta + 0 \tag{3.21}$$

and

$$\mathbf{v} \cdot [\boldsymbol{\nabla} \cdot \boldsymbol{\tau}] = v_r \left[\nabla_\theta \tau_{r\theta} \right] + v_\theta \left[\nabla_r \tau_{r\theta} \right]. \tag{3.22}$$

In cylindrical coordinates, the gradient is

$$\boldsymbol{\nabla} = \boldsymbol{\delta_r}\frac{\partial}{\partial r} + \boldsymbol{\delta_\theta}\frac{1}{r}\frac{\partial}{\partial \theta} + \boldsymbol{\delta_z}\frac{\partial}{\partial z}. \tag{3.23}$$

Therefore (3.22) becomes

$$\mathbf{v}\cdot[\boldsymbol{\nabla}\cdot\boldsymbol{\tau}] = v_r\left(\frac{1}{r}\frac{\partial}{\partial\theta}\tau_{r\theta}\right) + v_\theta\left(\frac{\partial}{\partial r}\tau_{r\theta}\right). \tag{3.24}$$

If the stress-energy tensor is radially dependant, $\tau_{r\theta} = \tau_{r\theta}(r)$, then the final identity is

$$\mathbf{v}\cdot[\boldsymbol{\nabla}\cdot\boldsymbol{\tau}] = v_\theta\left(\frac{\partial}{\partial r}\tau_{r\theta}\right). \tag{3.25}$$

Note that (3.25) will involve the gradient of the shear rate and that acceleration type terms tend to be unreliable with PEPT data. Thus $\boldsymbol{\nabla}\cdot[\boldsymbol{\tau}\cdot\mathbf{v}]$ is examined to see if a term more useful for data analysis can be determined.

From the definition $\boldsymbol{\tau}\cdot\mathbf{v} = \sum_i \boldsymbol{\delta_i}\left(\sum_j \tau_{ij}v_j\right)$, the components are

$$[\boldsymbol{\tau}\cdot\mathbf{v}]_r = \tau_{rr}v_r + \tau_{r\theta}v_\theta + \tau_{rz}v_z, \tag{3.26}$$

$$[\boldsymbol{\tau}\cdot\mathbf{v}]_\theta = \tau_{\theta r}v_r + \tau_{\theta\theta}v_\theta + \tau_{\theta z}v_z, \tag{3.27}$$

$$[\boldsymbol{\tau}\cdot\mathbf{v}]_z = \tau_{zr}v_r + \tau_{z\theta}v_\theta + \tau_{zz}v_z. \tag{3.28}$$

In this system

$$[\boldsymbol{\tau}\cdot\mathbf{v}] = [\boldsymbol{\tau}\cdot\mathbf{v}]_r + [\boldsymbol{\tau}\cdot\mathbf{v}]_\theta \tag{3.29}$$

$$= \tau_{r\theta}v_\theta\hat{\mathbf{r}} + \tau_{\theta r}v_r\hat{\theta}. \tag{3.30}$$

Finally,

$$\boldsymbol{\nabla}\cdot[\boldsymbol{\tau}\cdot\mathbf{v}] = \nabla_r\left(\tau_{r\theta}v_\theta\right) + \nabla_\theta\left(\tau_{r\theta}v_r\right) \tag{3.31}$$

$$= \frac{\partial}{\partial r}\left(\tau_{r\theta}v_\theta\right) + \frac{1}{r}\frac{\partial}{\partial\theta}\left(\tau_{r\theta}v_r\right) \tag{3.32}$$

$$= \frac{\partial v_\theta}{\partial r}\tau_{r\theta} + v_\theta\frac{\partial}{\partial r}\tau_{r\theta} + \frac{1}{r}\frac{\partial v_r}{\partial\theta}\tau_{r\theta} + \frac{v_r}{r}\frac{\partial}{\partial\theta}\tau_{r\theta}. \tag{3.33}$$

Recalling that both the stress and velocity vary radially only,

$$\boldsymbol{\nabla}\cdot[\boldsymbol{\tau}\cdot\mathbf{v}] = \frac{\partial v_\theta}{\partial r}\tau_{r\theta} + v_\theta\frac{\partial}{\partial r}\tau_{r\theta}. \tag{3.34}$$

With (3.15), the above equation can be used to substitute $\boldsymbol{\nabla} \cdot [\boldsymbol{\tau} \cdot \mathbf{v}]$ in (3.2). This has at least one well behaved term, $\left(\frac{\partial v_\theta}{\partial r}\right) \tau_{r\theta}$, which will hopefully dominate the contribution to the power density.

Using the above hypotheses, Equation 3.2 reduces to

$$\rho \frac{\partial}{\partial t}\left(\frac{1}{2}v^2\right) = -\mathbf{v} \cdot \boldsymbol{\nabla} P - \mathbf{v} \cdot [\boldsymbol{\nabla} \cdot \boldsymbol{\tau}] + \mathbf{v} \cdot \mathbf{F}, \tag{3.35}$$

$$0 = -\frac{\partial P}{\partial r} v_r - \frac{\partial v_\theta}{\partial r} \tau_{r\theta} - v_\theta \frac{\partial}{\partial r} \tau_{r\theta} + \rho g \left(sin\theta - \mu cos\theta\right) v_\theta, \tag{3.36}$$

$$\rho g \left(sin\theta - \mu cos\theta\right) v_\theta = \left[\frac{\partial v_\theta}{\partial r} \tau_{r\theta} + v_\theta \frac{\partial}{\partial r} \tau_{r\theta}\right] + \frac{\partial P}{\partial r} v_r. \tag{3.37}$$

This states that the rate of work done by external forces (gravity and friction) is equal to the sum of the rate of work done by viscous forces and the rate of work done by pressure of surrounding grains, as illustrated in Figure 3.3. This is the same as writing the differential power density as a sum of a compressive term and a shear term.

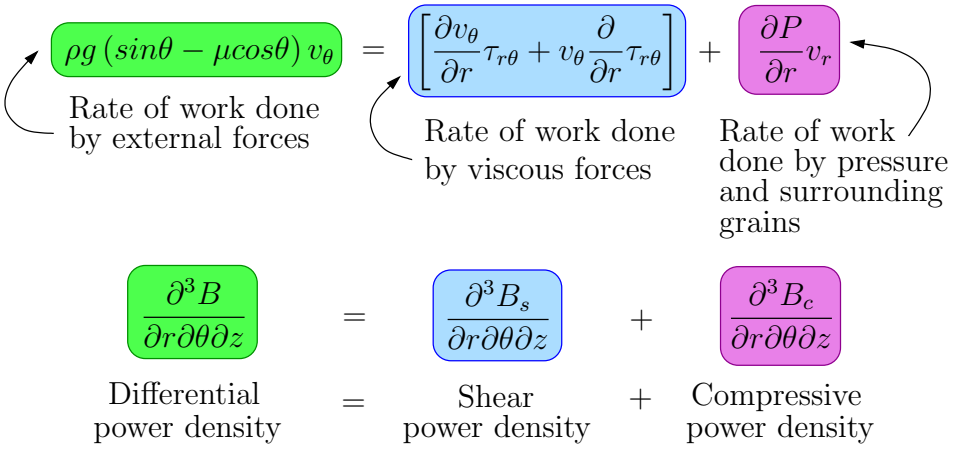

Figure 3.3.: Illustration of power dissipation equation.

3.3. Power dissipation distribution

The form of the stress-energy tensor discussed in Chapter 2 is substituted into Equation 3.37, to determine the power dissipation distribution:

$$\frac{\partial^3 B_s}{\partial r \partial \theta \partial z} = \frac{\partial v_\theta}{\partial r} \tau_{r\theta} + v_\theta \frac{\partial}{\partial r} \tau_{r\theta}, \tag{3.38}$$

$$\frac{\partial^3 B_c}{\partial r \partial \theta \partial z} = \frac{\partial P}{\partial r} v_r. \tag{3.39}$$

Recalling that

$$\tau = \tau_{\mathbf{i}} + \tau_{\mathbf{w}} + \tau_{\mathbf{c}} + \tau_{\mathbf{t}}, \tag{3.40}$$

$$P = P_s + P_c + P_t, \tag{3.41}$$

where

$$\tau_{\mathbf{i}} = \mu_i e^{-\phi I} P_s, \tag{3.42}$$

$$\tau_{\mathbf{w}} = \mu_w \left(\frac{r}{R}\right) P_s, \tag{3.43}$$

$$\tau_{\mathbf{c}} = \frac{\rho_m}{c^n} (Gd)^2 \dot{\gamma}^2, \tag{3.44}$$

$$\tau_{\mathbf{t}} = \kappa_t \rho_m d^2 \phi^{\frac{1}{3}} (1-\phi)^{\frac{2}{3}} \dot{\gamma}^2, \tag{3.45}$$

and

$$P_c = N\tau_{\mathbf{c}}, \tag{3.46}$$

$$P_t = \tau_{\mathbf{t}}, \tag{3.47}$$

$$P_s = P - P_t - P_c, \tag{3.48}$$

$$P = (\dot{\gamma} d)^2 \rho_m \left[\frac{1}{b} ln \left(\frac{\phi_{max}}{\phi}\right)\right]^{-\frac{1}{c}}. \tag{3.49}$$

Substituting the above into 3.37 results in equations for the shear and compressive differential power density,

$$\begin{aligned}\frac{\partial^3 B_s}{\partial r \partial \theta \partial z} =& \dot{\gamma} \left(\mu_i e^{-\phi I} P_s + \mu_w \left(\frac{r}{R}\right) P_s + \frac{\rho_m}{c^n} (Gd)^2 \dot{\gamma}^2 + \kappa_t \rho_m d^2 \phi^{\frac{1}{3}} (1-\phi)^{\frac{2}{3}} \dot{\gamma}^2\right) \\ &+ v_\theta \frac{\partial}{\partial r} \left(\mu_i e^{-\phi I} P_s + \mu_w \left(\frac{r}{R}\right) P_s + \frac{\rho_m}{c^n} (Gd)^2 \dot{\gamma}^2 + \kappa_t \rho_m d^2 \phi^{\frac{1}{3}} (1-\phi)^{\frac{2}{3}} \dot{\gamma}^2\right),\end{aligned} \tag{3.50}$$

$$\frac{\partial^3 B_c}{\partial r \partial \theta \partial z} = v_r \frac{\partial}{\partial r} \left((\dot{\gamma} d)^2 \rho_m \left[\frac{1}{b} ln \left(\frac{\phi_{max}}{\phi}\right)\right]^{-\frac{1}{c}}\right). \tag{3.51}$$

As these equations are not solvable analytically, the distributions were determined from experiments performed using Positron Emission Particle Tracking (PEPT) and Discrete Element Method (DEM) modelling, allowing the determination of the solids

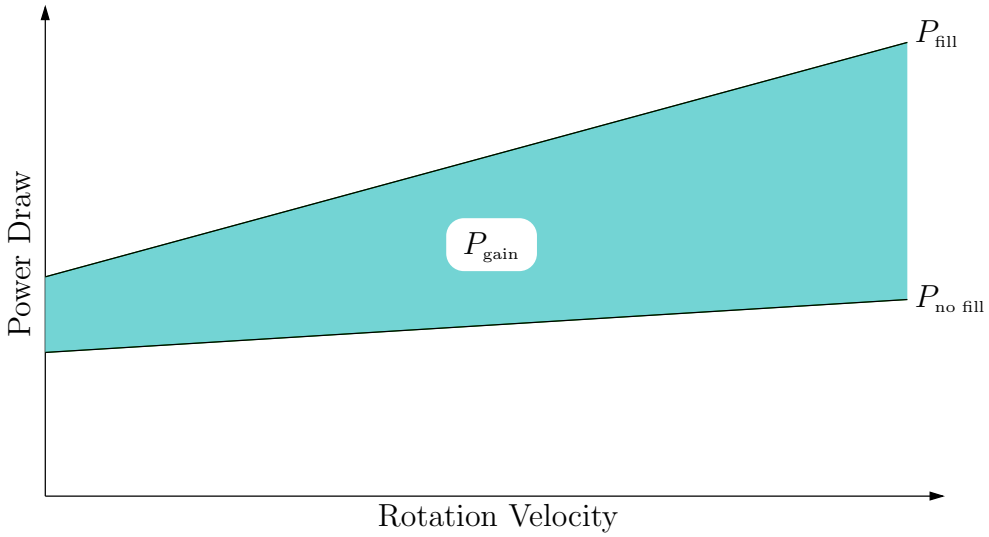

Figure 3.4.: Illustration of power dissipation measurements.

concentration distribution and velocity profile. It is also possible to experimentally determine the energy dissipated by the granular media.

Power going into the shear cell is broken up into mechanical power and lost power. Power can be lost or dissipated through heat, sound and particle breakage. The assumption is made that power lost through breakage is much greater than that lost through heat and sound ($P_b \gg P_h, P_s$). Thus the power dissipation distribution shows the distribution of particle breakage within the system. The power going into the fill, P_{gain}, can be determined by measuring the power drawn by the shear cell when there is a fill and when there is no fill. The difference between these measurements is the power going into the fill, which is broken up as mentioned above. The diagram in Figure 3.4 shows this.

Part II.

Positron Emission Particle Tracking

Chapter 4.

Positron Emission Particle Tracking

4.1. Introduction to Positron Emission Particle Tracking

Positron Emission Particle Tracking (PEPT) is a tracking method that relies on the detection of 511 keV γ-rays that are produced when a positron annihilates with an electron. A tracer particle is labelled with a radionuclide that decays by emitting a positron, which then annihilates close to the tracer particle, producing a pair of γ-rays that travel on almost the same path but in opposite directions. Thus the source of the positron lies somewhere along the line defined by this path. Coincident detection of these γ-rays allows a line of response (LOR) to be determined. The location of the source can be determined if more than one coincident event is detected. Successive detections of these γ-rays allows the location of the tracer particle to be triangulated, and velocity can be derived from the change in position over time [Parker et al., 1997b].

PEPT is performed using a positron emission tomography (PET) scanner. PEPT Cape Town is a facility for PEPT based at iThemba Laboratory for Accelerator Based Science (LABS), where experiments were performed. This ring geometry camera is the EXACT3D model of CTI/Siemens 966 PET scanner. It consists of 48 rings of standard bismuth germinate detector elements, each with dimensions 4.39 mm transaxial x 4.05 mm axial x 30 mm deep. The camera has a ring diameter of 82 cm and an axial field of view of 23.4 cm. The I/O and computing hardware can maintain a sustained acquisition rate of approximately 4 million coincidence events/second. The mean spatial resolution is 4.8 $\pm$ 0.2 mm FWHM (transaxial, 1 cm off axis) and 5.6 $\pm$ 0.5 mm (axial, on axis) Buffler et al. [2009]. A schematic showing the general principle of the triangulation is shown in Figure 4.1.

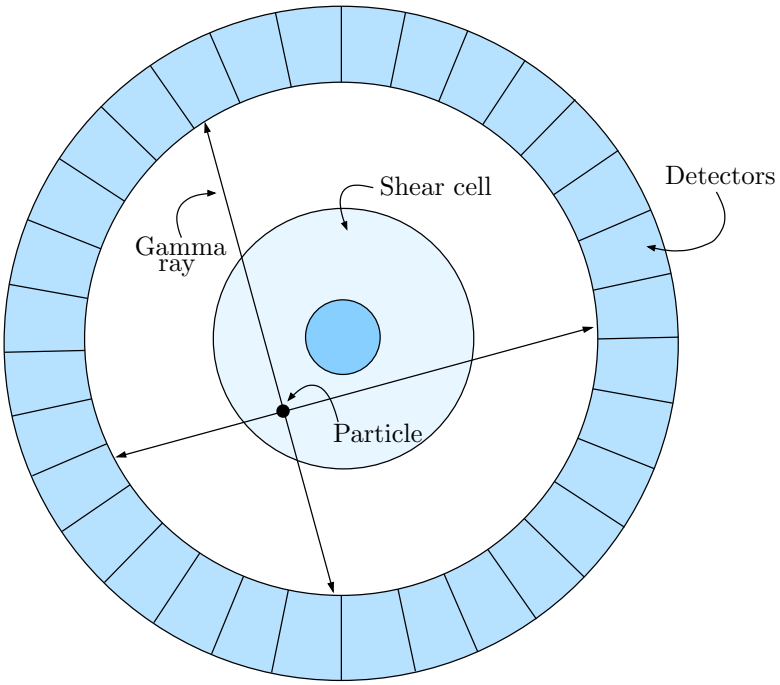

Figure 4.1.: The basic principle behind Positron Emission Particle Tracking.

The triangulation of the tracer particle in theory only requires two LORs to produce a location (as is seen in Figure 4.1). However, various effects such as Compton scattering or attenuation of the γ-rays as they move through the bulk material, can result in a situation where two coincident γ-rays are detected but are not associated with the same annihilation event. Thus, a larger number of LORs are required to get a more certain fix on the tracer location. The position of the tracer is located by dividing the coincidence events into groups of an equal number. The centroid of the LORs in each slice is located by iteratively rejecting the outlying LORs until a desired fraction of the original number remain. The uncertainty in the location of the tracer is inversely proportional to the square root of the number of events used to define the centroid [Buffler et al., 2009]. A simplified example of a slice of coincidence events is shown in Figure 4.2a, with the spurious events removed in Figure 4.2b. As the detection of events occurs at many thousands per second, tracking a fast moving tracer particle is possible. This technique was developed at the University of Birmingham in the 1990s by Hawkesworth et al. [1991], Parker et al. [1993, 1994].

The effect of tracer activity on the particle tracking has been studied by Volkwyn et al. [2011]. The activity on the tracer needs to be approximately 300 to 1000 µCi. The more material there is, the higher the activity on the tracer needs to be in order to locate the tracer with low uncertainty. The half life of the isotope used to label the tracer needs to be reasonably short, as it is not always feasible to locate the tracer in the bulk

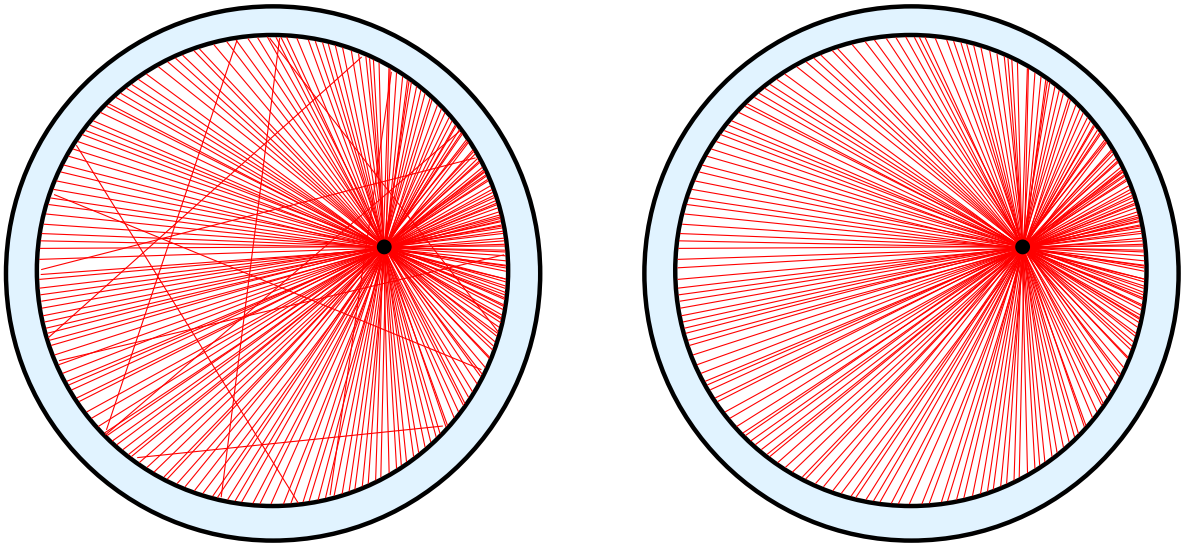

(a) Coincidence events detected in one slice of data.

(b) Removal of the spurious events allows the location of the tracer to be found.

Figure 4.2.: PEPT algorithm locates the position of the tracer by finding the centroid of the LORs, removing spurious events in the process.

material once the study is complete. The half life of the isotope therefore needs to be long enough to be useful for the duration of the study, but short enough so that the tracer can be safely discarded with the bulk material after the study. Various isotopes are used, including ^{68}Ga which has a half life of 68 min and ^{18}F with a half life of 109 min. Longer surviving isotopes are also used like ^{66}Ga, with a half life of 9.45 h and ^{64}Cu, half life 12.7 h.

Tracer particles are created through direct irradiation of a particle, ion-exchange in a radioactive solution, tracer surface modification or placing a radioactive resin inside a hole in the particle [Parker et al., 1997b, Buffler et al., 2009]. The challenge remains to get a larger activity onto a smaller tracer.

The precision of this tracking method decreases as the speed of the particle increases, thus requiring more activity on the tracer to produce the necessary number of detection events required for a low uncertainty location.

PEPT has been used to study a number of industrial systems including fluidised beds [Wildman and Parker, 2002], stirred mills [Conway-Baker et al., 2002, Barley et al., 2004], pipe flow [Fairhurst et al., 2001], tumbling mills [Lim et al., 2003, Volkwyn et al., 2011, Bbosa et al., 2011, Govender et al., 2013, Tupper et al., 2013, Govender et al., 2011] and IsaMills [van der Westhuizen et al., 2011]. A modular design of a PET camera has allowed for larger scale systems to be studied [Ingram et al., 2007].

Wildman et al. [2008] conducted PEPT experiments on an upright shear cell, driven by the bottom boundary. The top boundary was free to move vertically, meaning that this configuration was pressure-controlled. They measured the mean velocity and volume fraction profiles within the rapidly sheared dry granular media within the shear cell.

4.2. Experiment description

The side view of the experimental rig used in these experiments is shown in Figure 4.3. The dimensions of the rig are the same as those used in the DEM simulations, apart from the end parts, where there is a gap between the end wall and the rotor to allow for bearings. This section of data was removed before the analysis was performed. The cylinders were made of high density polyethylene (HDPE), with the end walls consisting of a thick, transparent perspex. The annulus formed between the cylindrical surfaces was filled with glass beads with a 5 mm diameter. The shear cell was filled while standing upright, the end wall put in place and then turned on it's side. The shifting around allowed the beads to settle into a closer packing, meaning that the rig was only approximately 90% full.

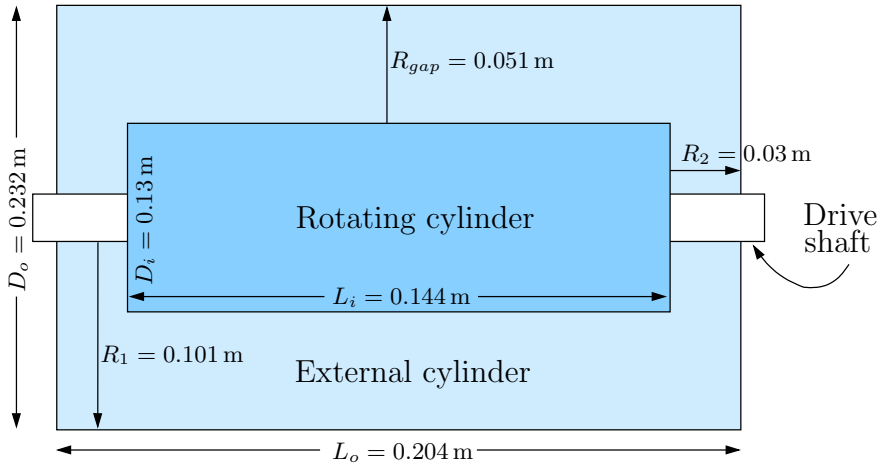

Figure 4.3.: Side view of experimental system, showing the dimensions of the shear cell.

Two friction surfaces for the inner rotating cylinder of the shear cell were utilised in these experiments. These consisted of a slightly grooved surface and a surface with the same glass beads used in the experiment glued on to it, shown in Figure 4.4.

Initial investigations at high rotational velocities resulted in high temperatures and a steep temperature gradient within the bulk material. Thus, to limit the heating effect, runs were performed in 5 min segments at 300 rpm and 400 rpm, where 300 rpm was the

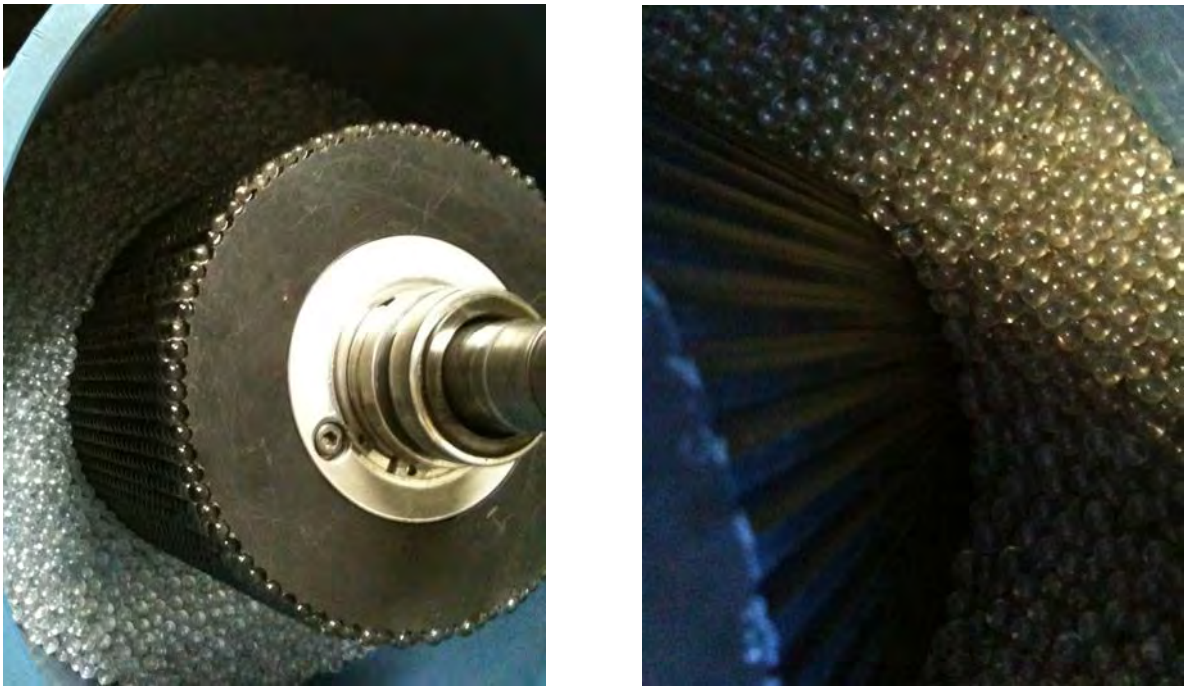

(a) Beaded surface of rotating cylinder. **(b)** Grooved surface of rotating cylinder.

Figure 4.4.: Different friction surfaces of the rotating cylinder used in PEPT experiments. Pictures taken during the filling of the rig.

lowest possible speed of the motor. The material was allowed to cool between runs. Each time the experimental rig was moved, a location marker run was performed. This consisted of readings taken from a stationary source placed around the edge of each side of the shear cell. These markers were then used to centre the data from each run, so they could be compared, and removed the need to have the rig placed in exactly in the same position each time a new tracer was used or the bulk material was replaced. An example of the location markers is shown in Figure 4.5. The triangle points form a partial outline of the experimental rig, allowing the data to be corrected to a standard set of coordinates. The circular points shown in Figure 4.5 are stationary tracers within the rig, used to test the ability to locate a particle with the given radioactivity within the stationary mass.

The density of the glass beads used was $2500\,\mathrm{kg\,m^{-3}}$ and the total mass of all the beads used in the experiment was $M_T \approx 10.5\,\mathrm{kg}$. Thus the total number of glass beads in the experiment was $N \approx 8000$. The portion in the annulus would be slightly less than this, as there were still beads against the side walls by the bearings.

Particles were labelled using a drill and fill method. A hole was drilled into one of the 5 mm glass beads and a resin containing ^{68}Ga was placed inside. The hole was then glued closed and the tracer placed in the centre of the annulus. The activity on the tracer

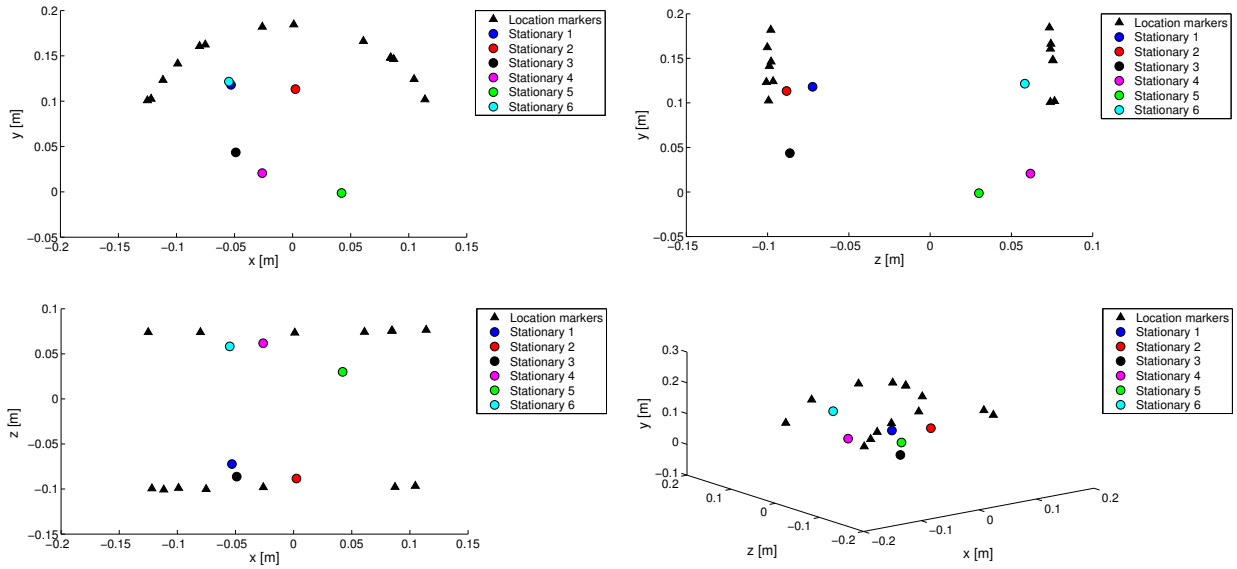

Figure 4.5.: Example of location markers used to fit the dimensions of the rig to the data. The triangular points indicated the edges of the rig, while the circular points are stationary tracers within the rig.

ranged from 1196 µCi to 1589 µCi. The isotope ^{68}Ga was used in these experiments as it is currently possible to achieve the highest radioactivity on the smallest resin bead with this particular isotope, using the set up at iThemba LABS.

4.3. Data Analysis

A total of 36 experimental runs were performed, initially at 5 min per experiment and then 15 min, after it was determined that the tracer particle was not being destroyed in the shearing. Some of these experiments were rejected, as the tracer got stuck close to the side wall, which was out of the zone that was considered useful (avoiding end wall effects). Examples of the particle track are shown in Figures 4.6. The tracer particle spent the majority of the time in the rapidly sheared region (Figure 4.6a), only occasionally making it out to the slower moving material of the shear cell (Figure 4.6b). When this did happen, it often took almost the entire experimental run to complete a circuit of the rig and once again move into the rapid zone. Figure 4.6c shows the tracer particle stuck on the side wall. A zone of chaotic behaviour can be seen at the top of the rig, where the beads had space to move freely without being trapped by the bulk material.

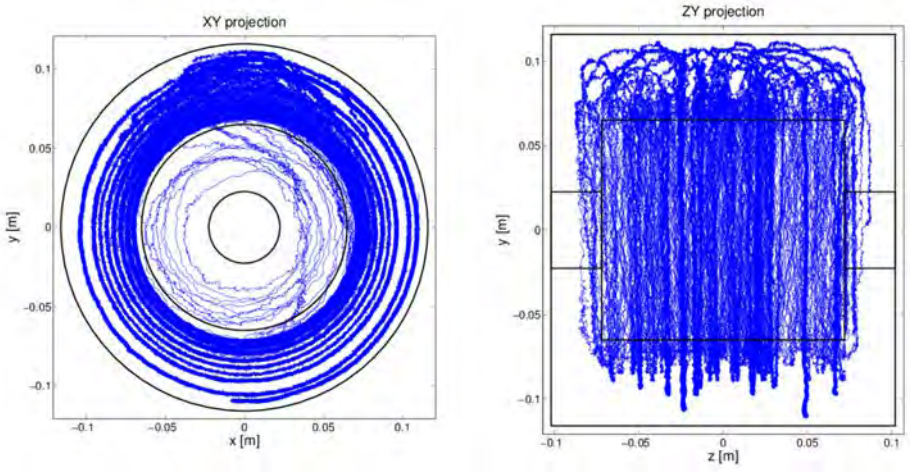

(a) Particle track showing good system coverage.

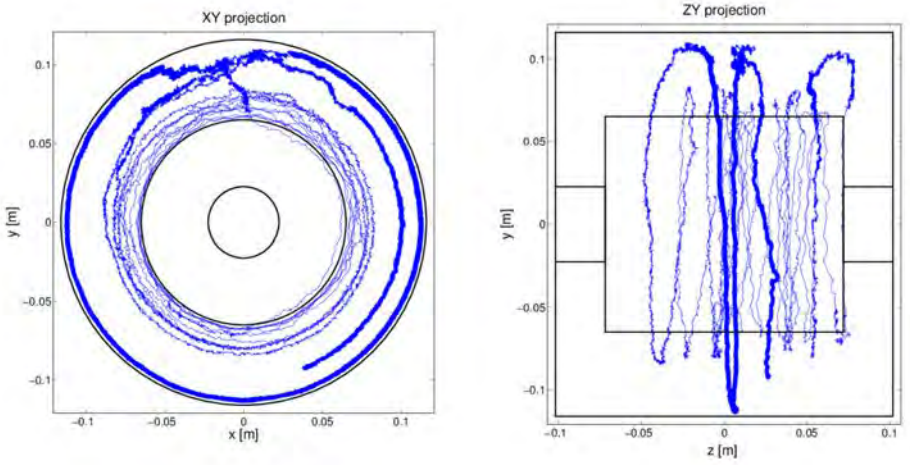

(b) Particle track showing that the particle got stuck on the outer edge, moving slowly.

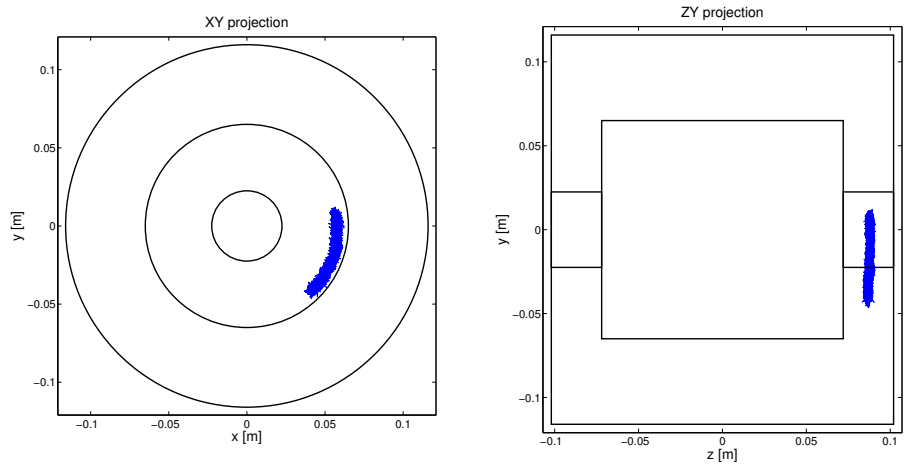

(c) Particle track showing that the particle got stuck on the side wall, moving slowly, outside of the zone of interest.

Figure 4.6.: Examples of a few PEPT particle tracks.

The file of coincident events for each experiment was reduced to a list of time stamped tracer coordinates using the procedure described above. Data for each experiment was integrated over the entire duration of the run, thus the fraction of time that the tracer particle spent at each location was studied. This same procedure was performed in Parker et al. [1997a]. Thus it is assumed that the system under study is an ergodic system, where the time averaged behaviour of a single particle is equivalent to the ensemble average of the bulk material.

Successive visits to each volume element are treated as if they are simultaneous which allows the time averaged velocity and acceleration distributions to be determined, as well as the location probability density distribution.

The particle track was then binned into a spatial grid of 5 x 5 mm in the transaxial plane and over the entire length of the rotating cylinder. The details of this binning procedure are discussed in Morrison [2012]. This procedure uses successive locations of the tracer particle to determine a second order Lagrange polynomial over three locations. The intercepts of this polynomial with the predetermined spatial grid are calculated and thus used to determine the presence of the tracer in a bin. The times at which these polynomials cross the grid lines are used to calculate the velocity of the tracer particle in each bin it crosses. Thus producing distributions of time spent in a bin (occupancy or residence time) and the average velocity of the tracer in each bin.

The volume fraction is determined in each spatial grid using

$$\phi_i = \frac{F_i N \pi d^3}{6 V_i}, \tag{4.1}$$

where F_i is the fraction of time spent by the tracer in volume element V_i, d is the particle diameter, N is the total number of particles in the system [Wildman and Parker, 2002].

After the average behaviour of the tracer particle in each run was determined, the data for each experimental configuration was averaged, producing four sets of results. Table 4.1 shows how many runs were used in each configuration and the total time that these runs resulted in.

Table 4.1.: Total time for all experimental configurations.

Speed	Beaded	Runs	Grooved	Runs
300 rpm	2700 s	5	6000 s	8
400 rpm	3900 s	5	4500 s	5

4.4. Results

4.4.1. Volume Fraction

The results presented below are the averages over all suitable runs for each experiment configuration. As can be seen in Figure 4.7, showing the average volume fraction in each grid space for each configuration, the entire space was not covered by the total runs. The white space shows the absence of data, while blue (a volume fraction of almost 0) shows that very little information was garnered about this area. Thus, only the inner area of the shear cell (the rapidly shearing zone) was well covered by the experiments.

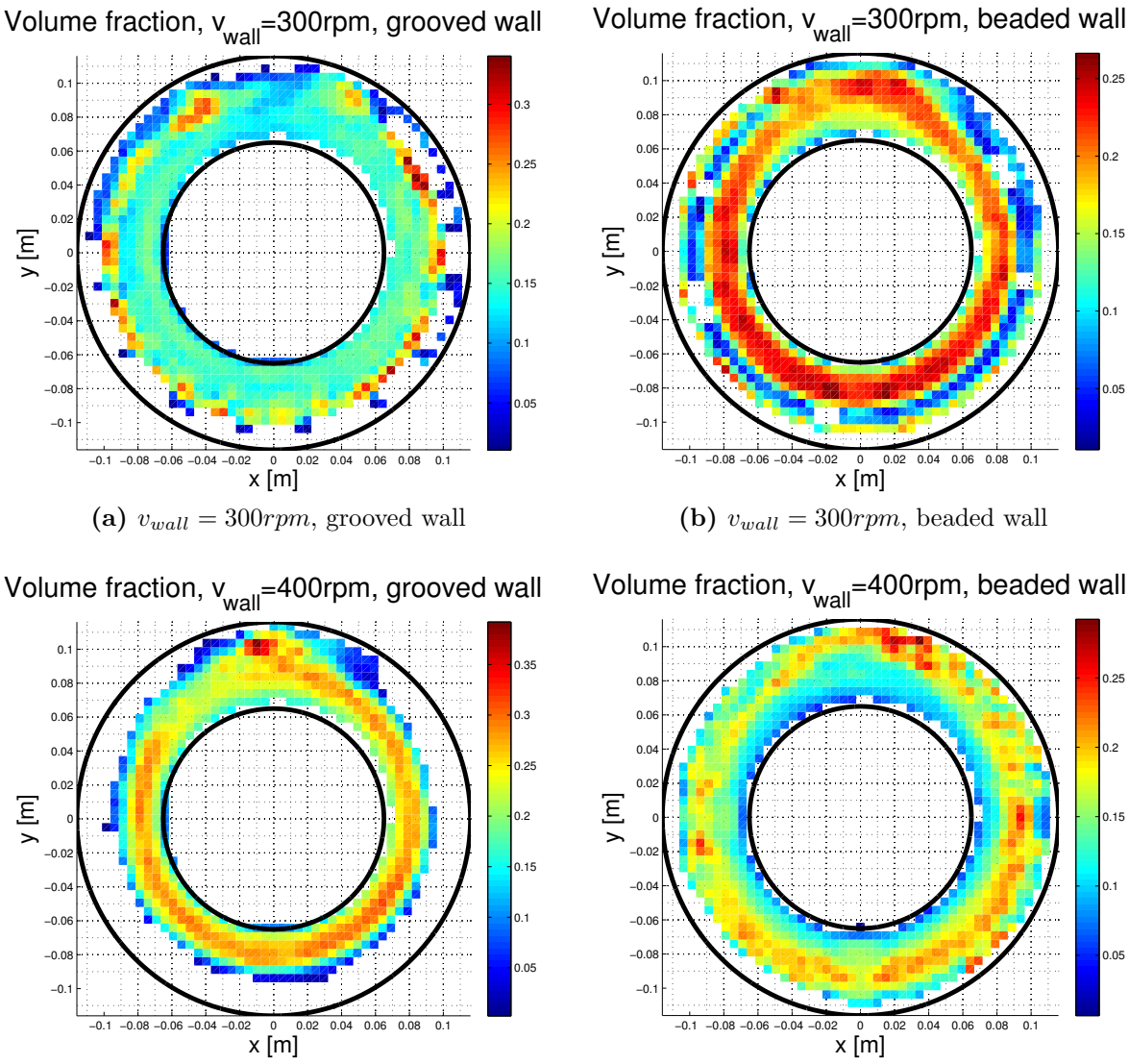

(a) $v_{wall} = 300rpm$, grooved wall

(b) $v_{wall} = 300rpm$, beaded wall

(c) $v_{wall} = 400rpm$, grooved wall

(d) $v_{wall} = 400rpm$, beaded wall

Figure 4.7.: Average volume fraction distributions for all experimental configurations.

For all four configurations shown in Figure 4.7 the volume fraction is low in the centre of the shear cell, close to the moving wall, while it increases to a maximum value with increasing radial distance from the shearing wall. There is a higher volume fraction in the lower half of the system, most noticeable in the 400 rpm, grooved wall (Figure 4.7c) and the 300 rpm, beaded wall (Figure 4.7b) configurations. An averaging filter was applied to smooth out the gaps in the data. This filter performed a sliding average on a 4x4 grid space.

The volume fraction along three lines in the experimental space (180°, 270° and 360°, where 0° is oriented along the positive x-axis) was selected in order to examine the volume fraction profile. Due to the incomplete coverage of the system during the experimental runs and the small portion of time that was spent by the tracer particle in the outer edge of the system, the volume fraction distributions are not good representations of the behaviour of the volume fraction, beyond the rapidly sheared zone close to the shearing wall.

The radial selections in Figure 4.8, show the volume fraction selected from the distributions in Figure 4.7. The angular selections in each configuration behave similarly, with the distributions at 180° and 270° with the grooved wall starting closer to the wall than that at 360°. The decrease of the volume fraction after a maximum has been reached is not a physical phenomenon, resulting purely from the incomplete coverage of the experiment. Experiments and simulations of annular shear cells in Jasti and Higgs [2008, 2009] show that the volume fraction should be greater on the stationary wall of the sheared system.

All configurations show that the volume fraction increases from the rapidly sheared zone at the inner wall. The range of volume concentration covered by these distributions is $0 < \phi < 0.375$, which indicates that the area covered by the PEPT experiments has an inertial number, $I > 0.03$, as determined from the model for dilatancy discussed in Chapter 2. Thus, the section of the shear cell examined with these data covers the dense flow regime and kinetic-collisional regime, as defined by da Cruz et al. [2005].

The extraction of a functional form that described the volume fraction distributions in Figure 4.8 was not possible, thus accurate calculations of the inertial number along the selected radial lines could not be performed, and hence the shear stress and power dissipation could not be calculated.

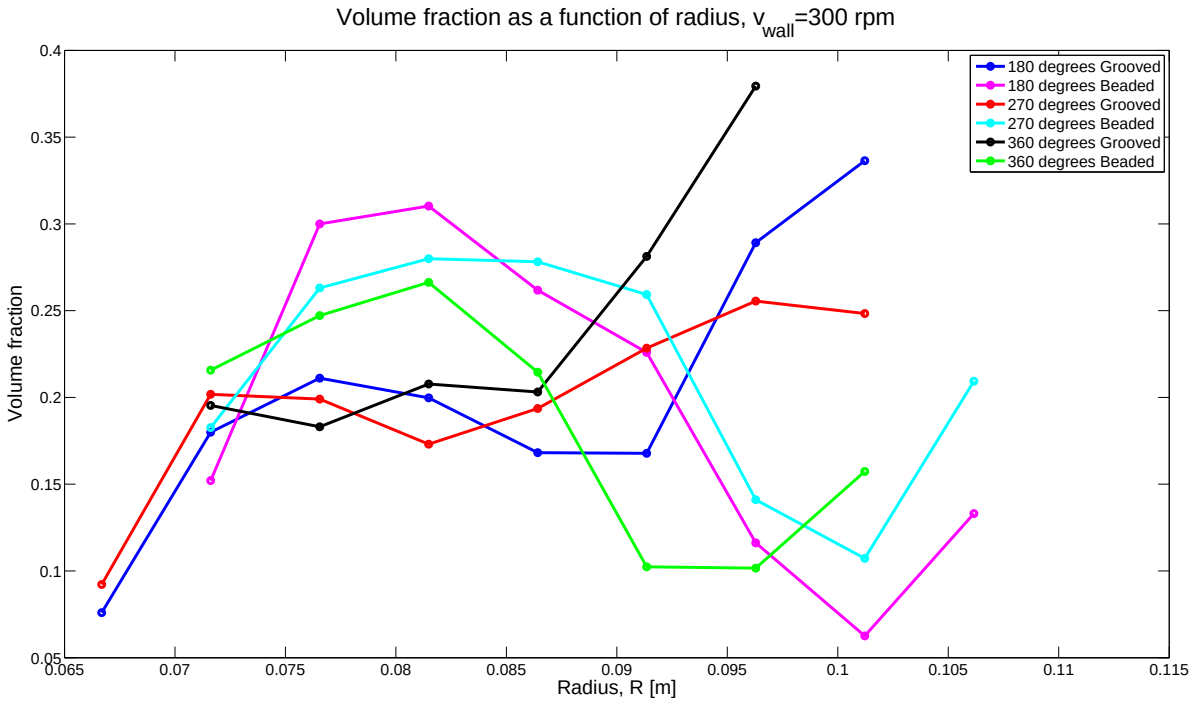

(a) $v_{wall} = 300\,\mathrm{rpm}$.

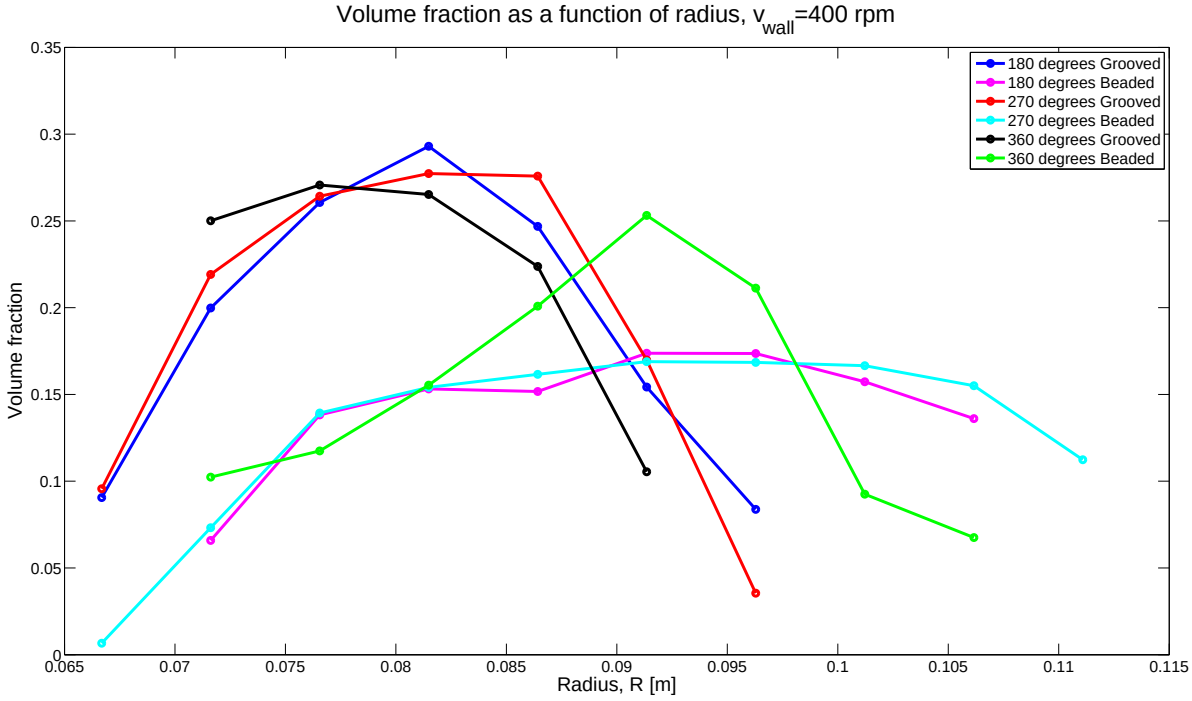

(b) $v_{wall} = 400\,\mathrm{rpm}$

Figure 4.8.: Average volume fraction as a function of radius at $180°, 270°, 360°$, $v_{wall} = 300\,\mathrm{rpm}$ and $v_{wall} = 400\,\mathrm{rpm}$.

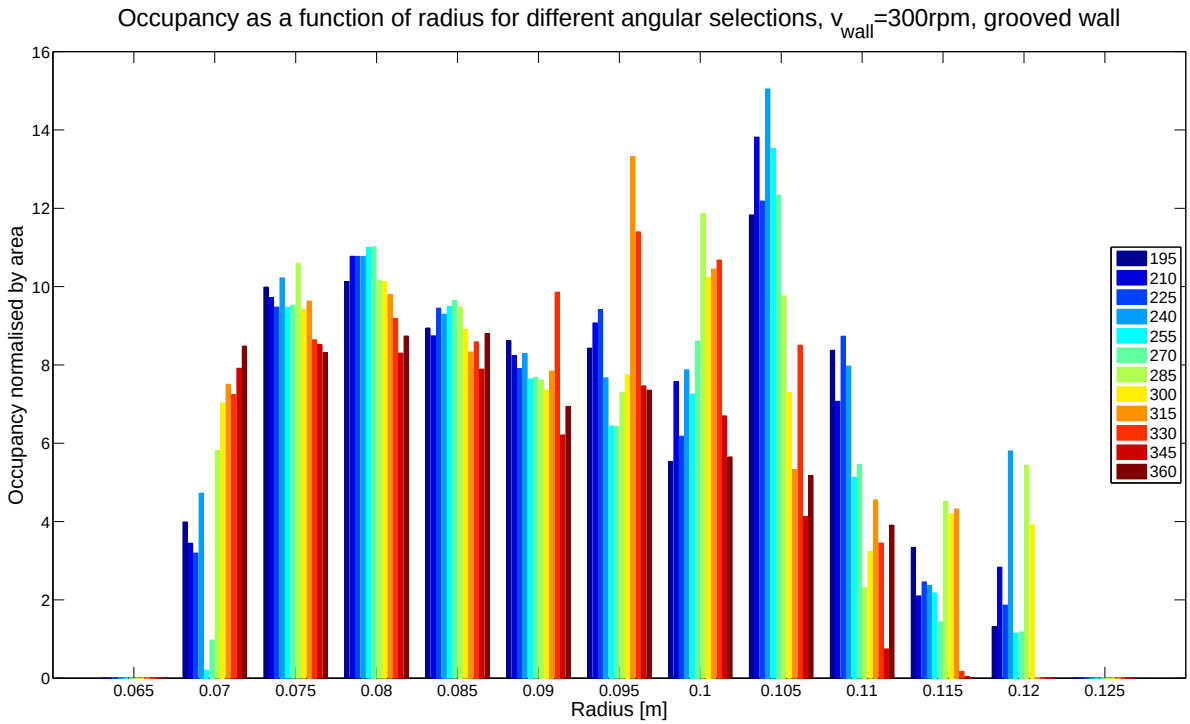

(a) Binned occupancy, grooved cylinder.

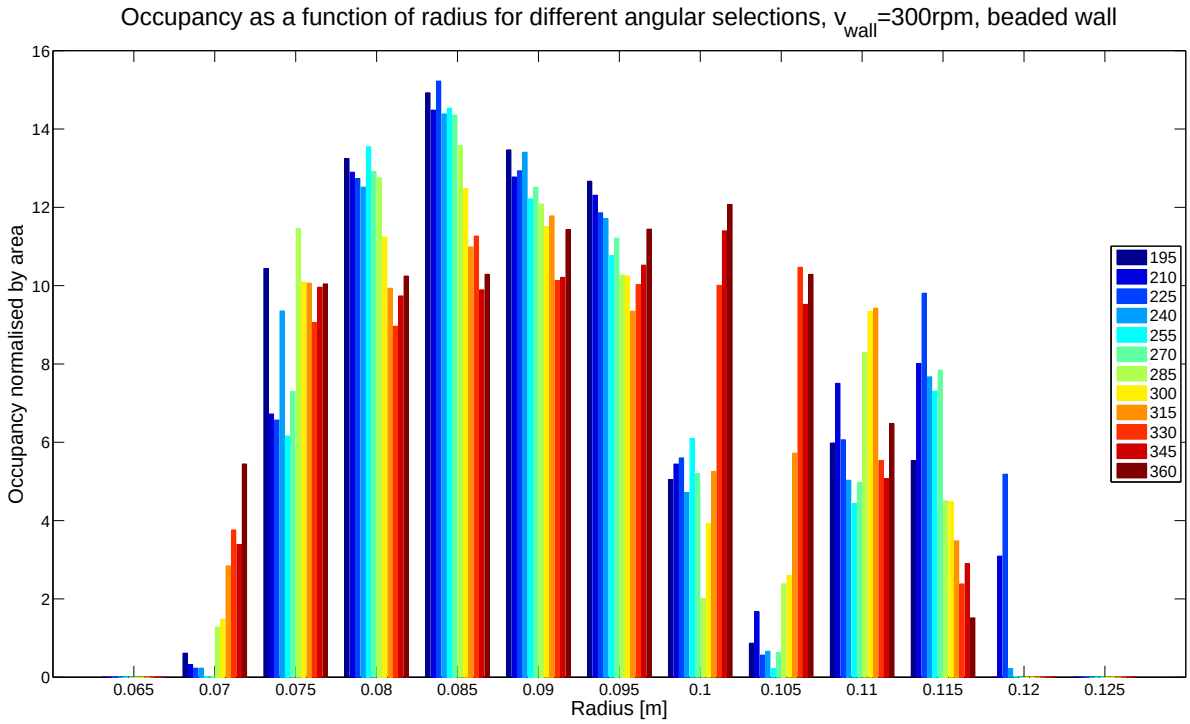

(b) Binned occupancy, beaded cylinder.

Figure 4.9.: Occupancy binned into 15° angular bins.

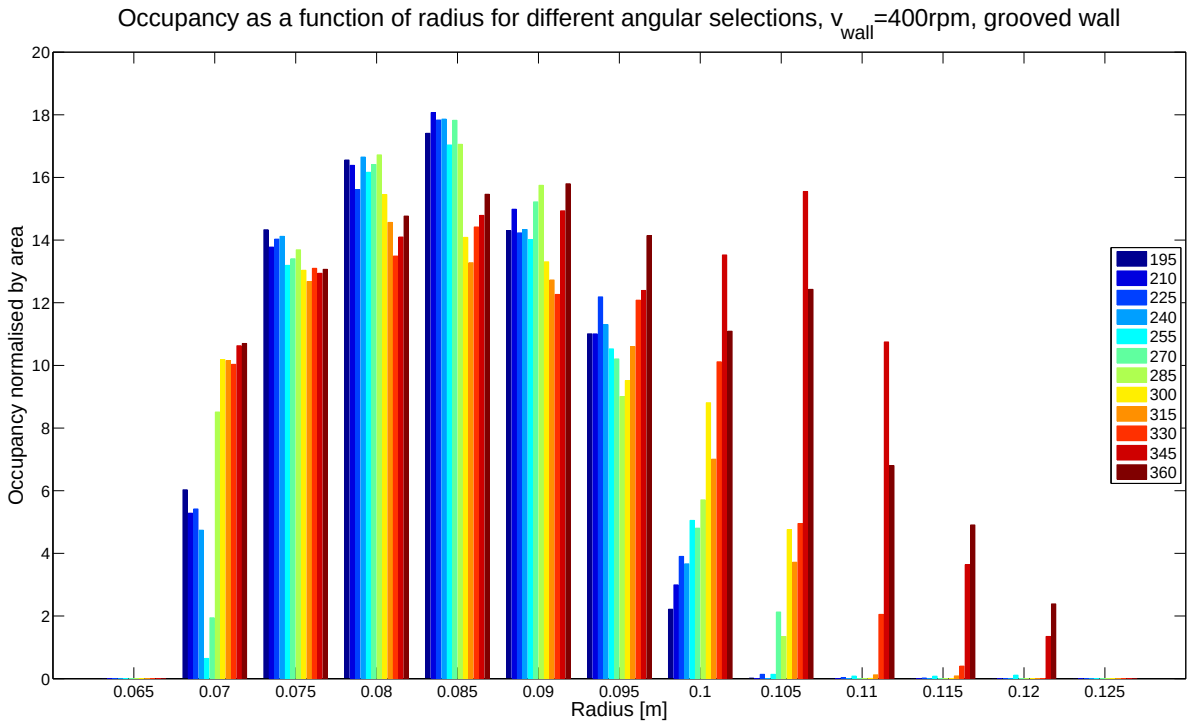

(a) Binned occupancy, grooved cylinder.

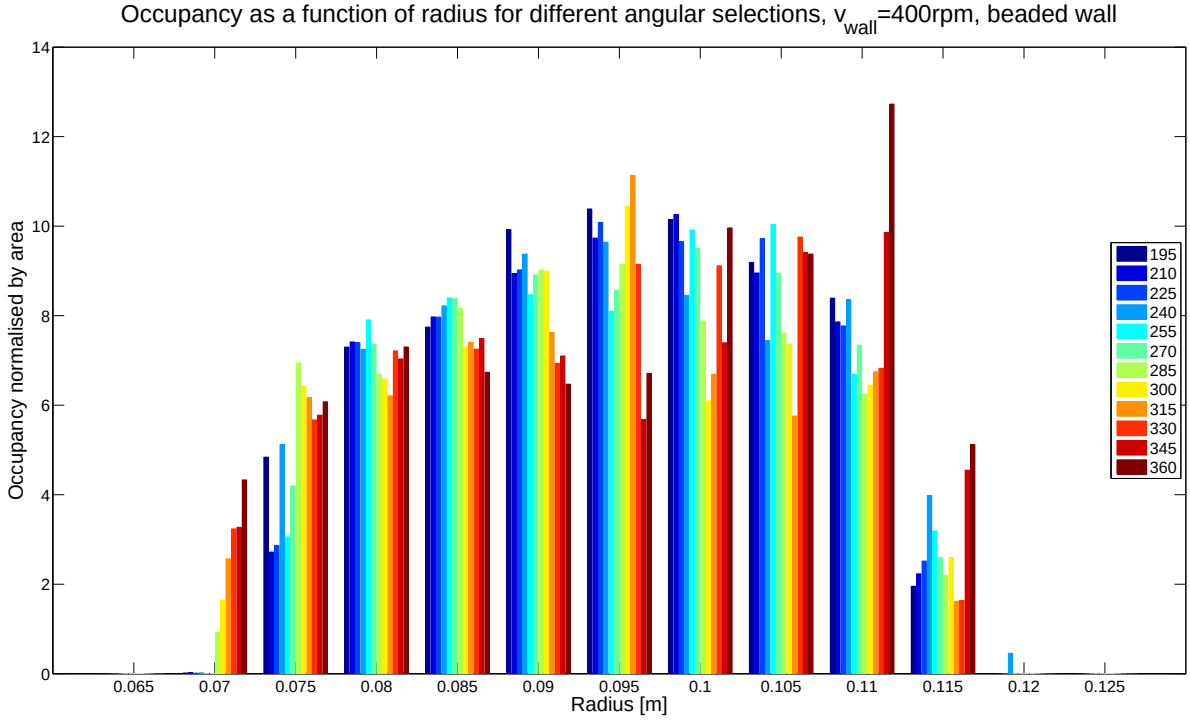

(b) Binned occupancy, beaded cylinder.

Figure 4.10.: Occupancy binned into 15° angular bins.

The occupancy distributions used to calculate the volume fraction were binned into 15° angular bins, the results shown in Figure 4.9 and 4.10. Each grouping of bars represents one radial bin, with the colours indicating the angular position. This was done in order to examine the angular dependence seen in the distributions in Figure 4.7. The occupancy is the total time spent by the particle in each bin, normalised by the number of times that it is in that bin. The volume fraction is a scaled occupancy, so the shape and behaviour of these bar graphs is comparable to what would be seen in the volume fraction bar graphs.

In the region that was well covered by the movements of the tracer particle the asymmetry in the angular bins was not that great, with the gravity-assisted side (180°) having slightly higher occupancy than the other side (360°). The occupancy starts out low close to the inner rotating wall and increases to a maximum value within a few particle diameters distance from the shearing wall. As distance from the inner wall increases towards the centre of the annulus, the angular dependence of the occupancy becomes more notable. Beyond the centre, the binning of the occupancy is strongly influenced by the lack of data.

4.4.2. Velocity

The velocity magnitudes (normalised by the maximum velocity magnitude in each configuration) for each configuration is shown in Figure 4.11. These distributions do not show the gaps in the data on the outer edge of the experiment system that are seen in the volume fraction distributions. This is due to the fact that the velocity distribution is expected to decrease to 0 with increasing radial distance from the centre. Therefore, the areas of the shear cell not explored in the PEPT experiments are expected to have a velocity that is close to $0\,\mathrm{m\,s^{-1}}$.

From Figure 4.11 it is apparent that the velocity is highest closest to the shearing wall, reducing to a minimum with increasing radius. The 400 rpm configuration with the beaded shearing wall has the shallowest velocity gradient. A very slight angular dependence can be detected in the distributions with the beaded shearing wall, with the band of moving material extending further radially on the 360° side than on the 180° side.

Figure 4.12 shows the total velocity vector distributions for all configurations. Here it can be seen that the main velocity component is in the tangential direction. The beaded configurations have a higher maximum velocity than the grooved configurations, and the

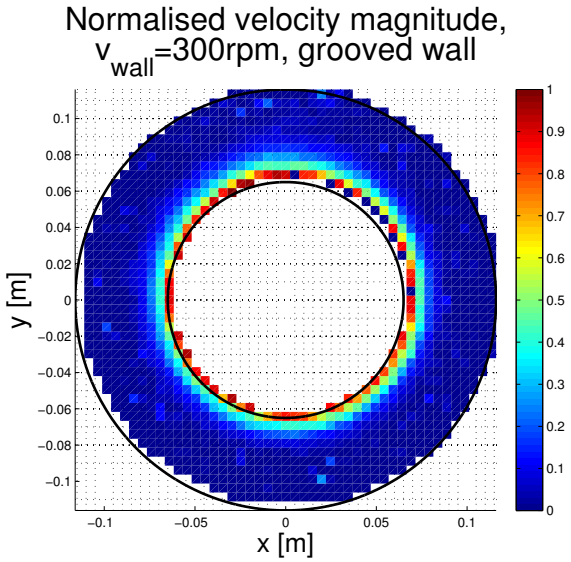

(a) $v_{wall} = 300rpm$, grooved wall

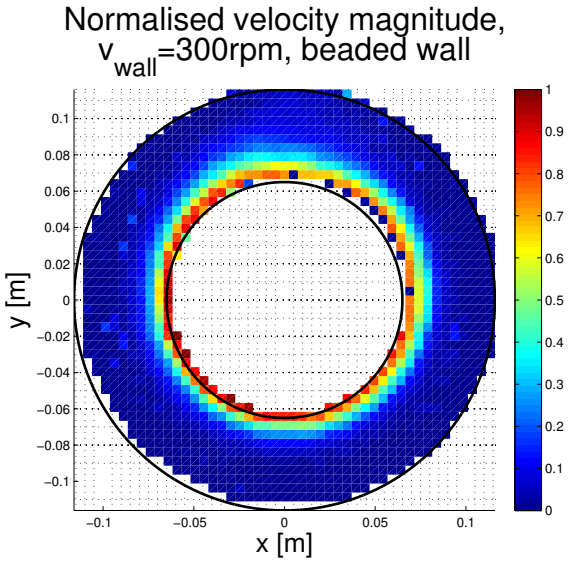

(b) $v_{wall} = 300rpm$, beaded wall

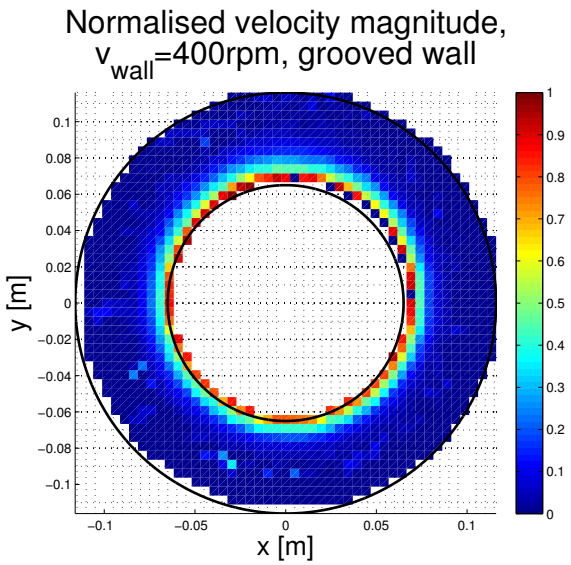

(c) $v_{wall} = 400rpm$, grooved wall

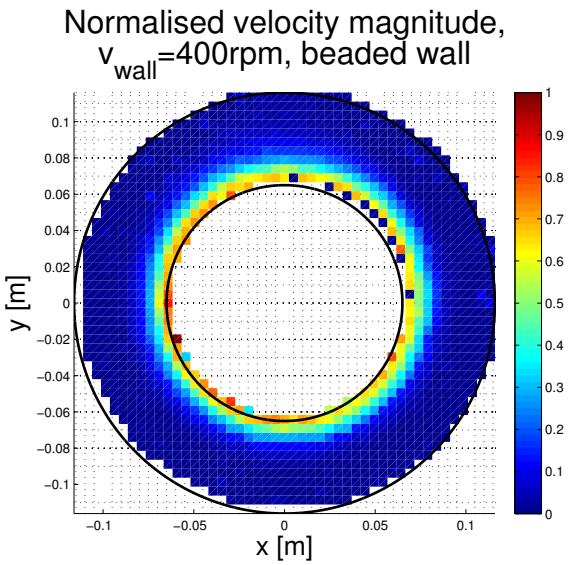

(d) $v_{wall} = 400rpm$, beaded wall

Figure 4.11.: Normalised velocity magnitude for all experimental configurations.

shear zone is also thicker in the radial direction. The grooved configurations have a much sharper velocity gradient.

Radial distributions of the tangential and radial components of the velocity are shown in Figure 4.13 and 4.14 at 3 angles selected for radial analysis (180°, 270°, 360°, where 0° is along the positive x-axis). For the configurations with the grooved shearing wall (Figure 4.13), the velocity in the 400 rpm set up is always higher, with both configurations approaching zero at a similar radial point. The radial velocity is mostly inconsequential

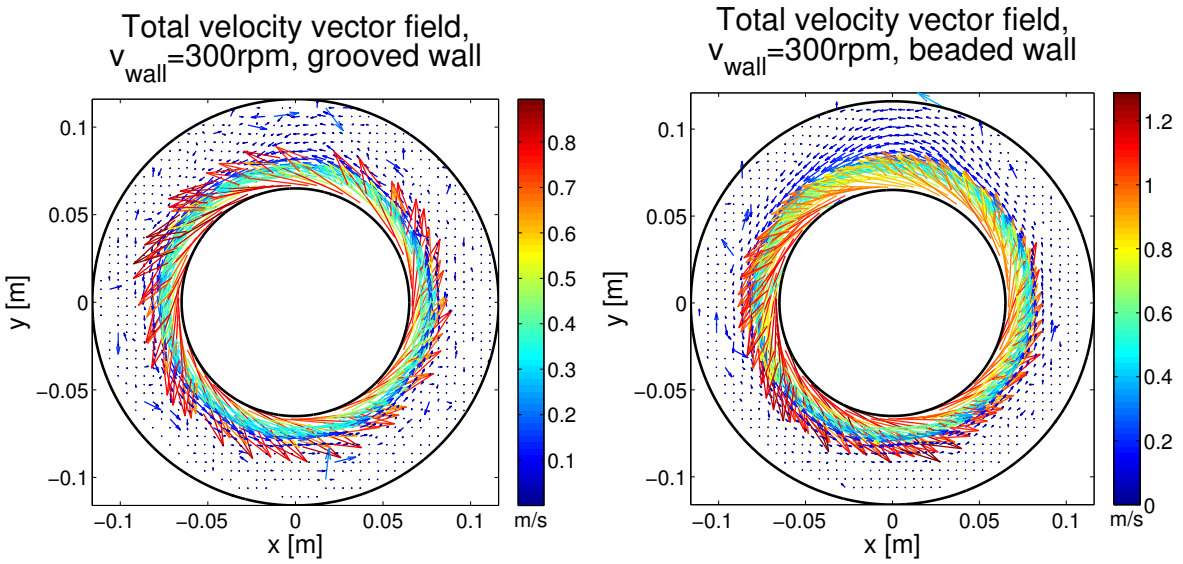

(a) $v_{wall} = 300rpm$, grooved wall

(b) $v_{wall} = 300rpm$, beaded wall

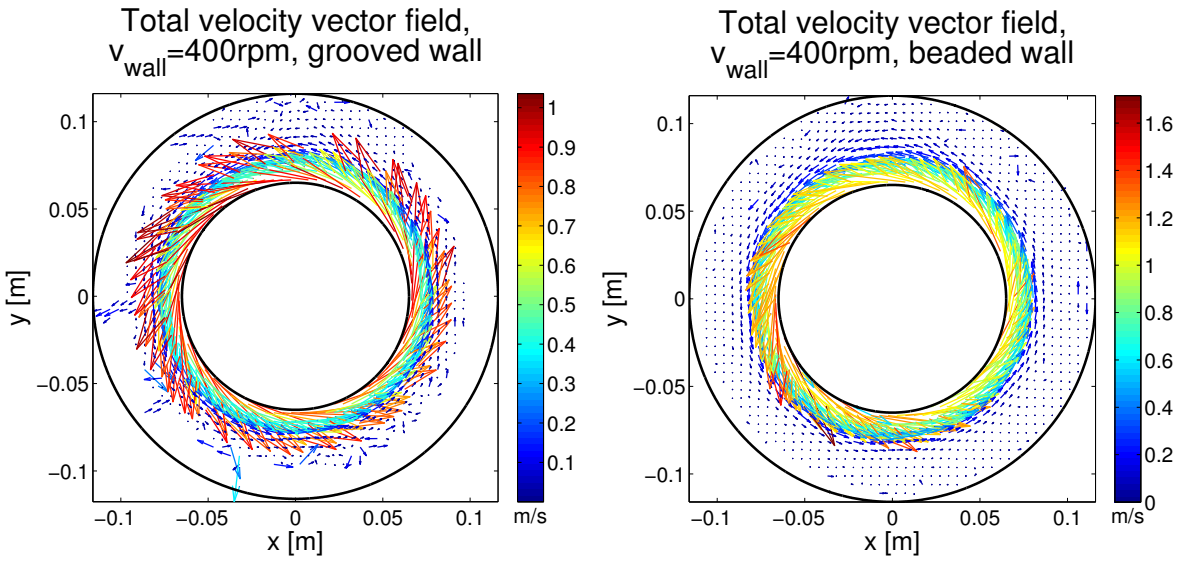

(c) $v_{wall} = 400rpm$, grooved wall

(d) $v_{wall} = 400rpm$, beaded wall

Figure 4.12.: Velocity vector field for all experimental configurations.

when compared to the tangential velocity, except for a portion of the 400 rpm radial velocity. The tangential velocity components are shown with an exponential function fit to the data. From these radial distributions, it would appear that the thickness of the band of material that is sheared decreases with the angle sampled, thus at 360°, where the material is moving against gravity, the shear band is narrower than at 180°, where the material is moving with gravity. The highest velocity is reached at 360° for both wall velocities.

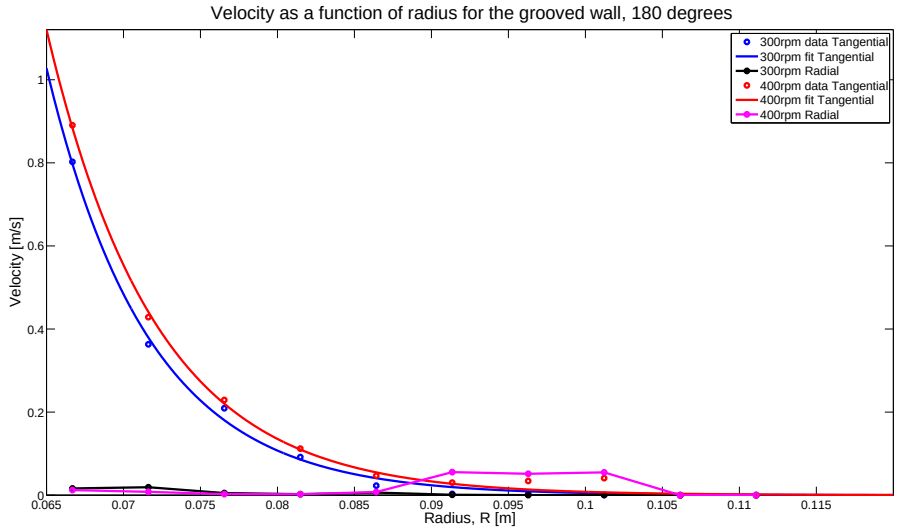

(a) Grooved wall, 180°

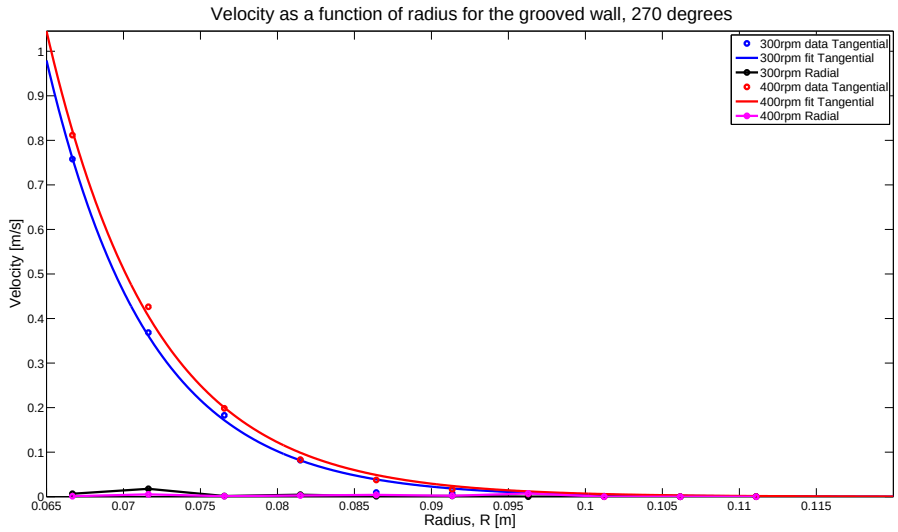

(b) Grooved wall, 270°

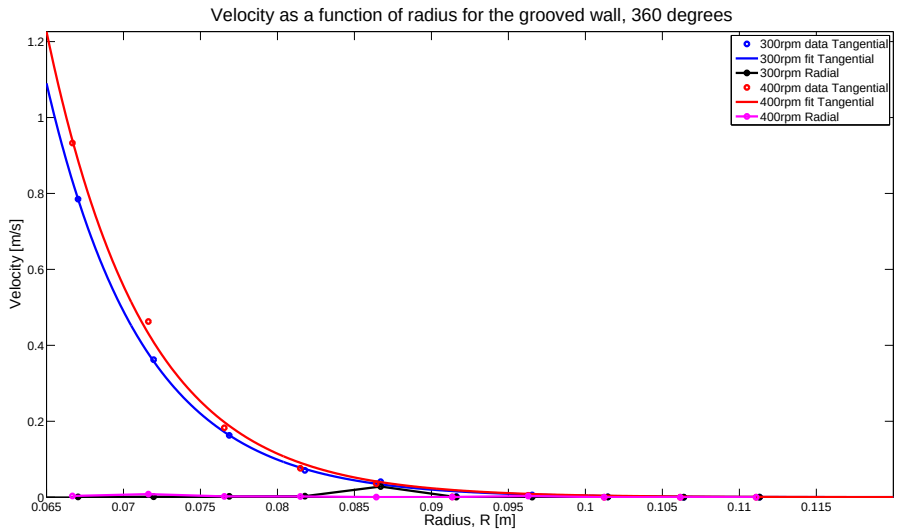

(c) Grooved wall, 360°

Figure 4.13.: Velocity as a function of radius at $180°, 270°, 360°$, $v_{wall} = 300\,\text{rpm}$ and $v_{wall} = 400\,\text{rpm}$, grooved wall.

The same radial distributions are shown for the beaded shearing wall in Figure 4.14. Here the tangential velocity (once again plotted with an exponential function fitted to the data) is also always higher in the 400 rpm configuration, with the radial components in both configurations being negligible. In this configuration the maximum values are reached in the 180° direction. Unlike the grooved wall case, the shear band is thickest at 360°.

Figure 4.15 shows the tangential velocity function fits for each shearing wall velocity, allowing for the comparison of the effect of the two different surfaces on the velocity to be examined. Both shearing wall velocities show a similar behaviour, with the beaded wall producing a higher velocity. The beaded wall angular components also have a greater variation, with the 180° starting out with the highest magnitude, decreasing as the angle moves to the other side of the experimental rig. The grooved wall components are much closer together, with the smallest maximum velocity coming from the 270° component. The shear band thickness for each configuration seems to be similar.

To further examine the shear band thickness dependence on angle and configuration, Figure 4.16 shows the average velocity in each configuration, calculated over the width of the shear band. Here the shear band is at the radial point where the shear rate drops below $1\,s^{-1}$. From this figure it can be seen that the 400 rpm, beaded has the largest shear band, which in this configuration gradually increases with angle, as the average velocity decreases. The 300 rpm beaded configuration also shows the average velocity decreasing with angle, however the relation between shear band width and angle does not hold. The grooved cylinder configurations have a different apparent relationship. The 360° components have the highest average velocity and smallest shear band, while the shear band is widest at 180°. The 270° components consistently have the lowest average velocity and median shear band.

As this definition of the shear band width is rather arbitrary and only indicative of the general behaviour, a more solid exploration is performed in Chapter 6, along side results from DEM simulations.

The angular effect was examined by binning each velocity distribution in 15° angular bins between 180° and 360°. These bar plots are shown in Figures 4.17 and 4.18. Each grouping of bars represents one radial bin, with the colours indicating the angular position. The position labelled on the axis is the end point of the bin, thus the first bin ranges from 0.065 m to 0.07 m. The velocity has been normalised by the area of it's respective bin. This was necessary because the cylindrical binning means that bins on the outer edge of the experimental space are larger than those close to the shearing wall.

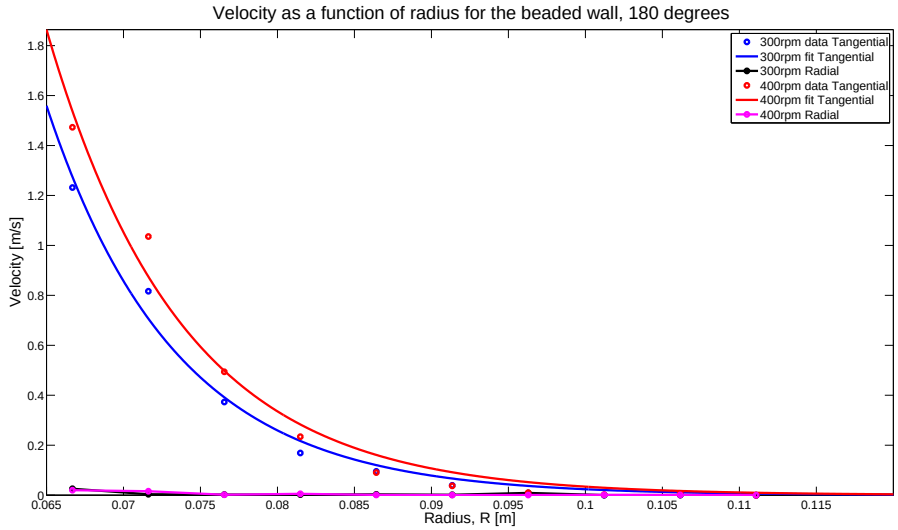

(a) Beaded wall, 180°

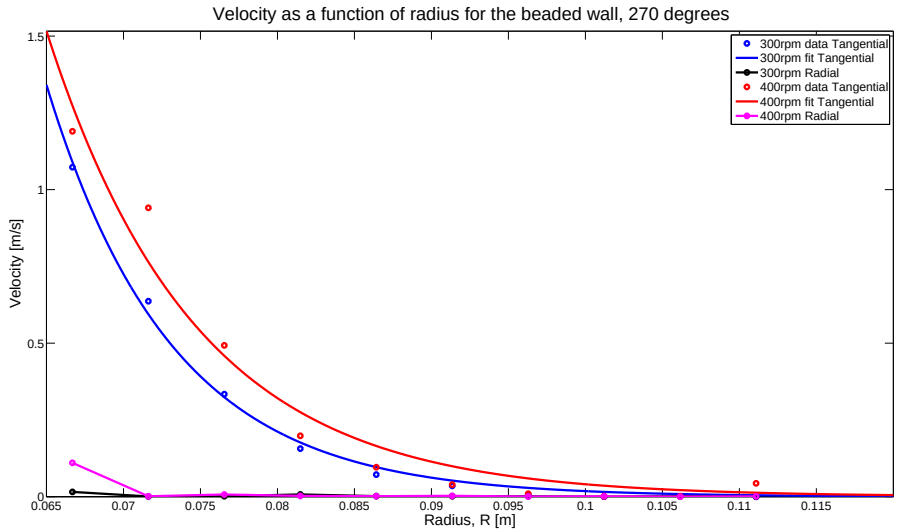

(b) Beaded wall, 270°

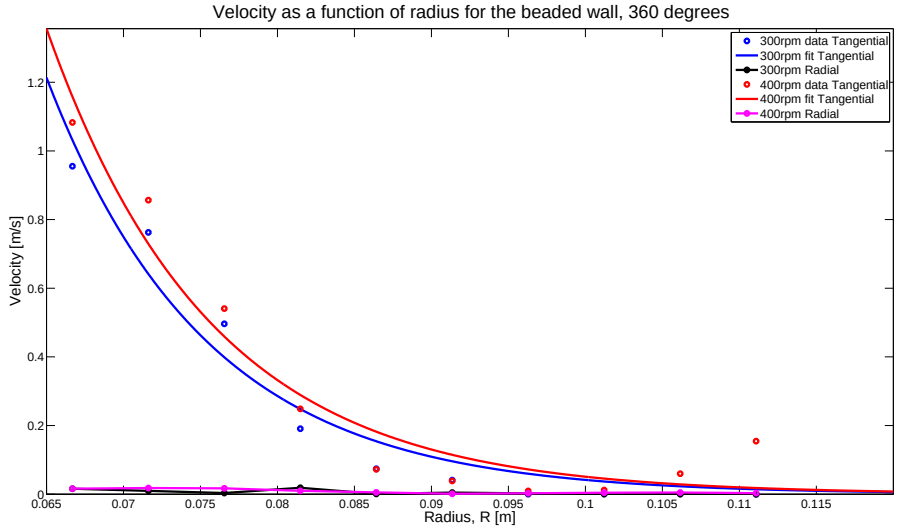

(c) Beaded wall, 360°

Figure 4.14.: Velocity as a function of radius at $180°, 270°, 360°$, $v_{wall} = 300\,\text{rpm}$ and $v_{wall} = 400\,\text{rpm}$, beaded wall.

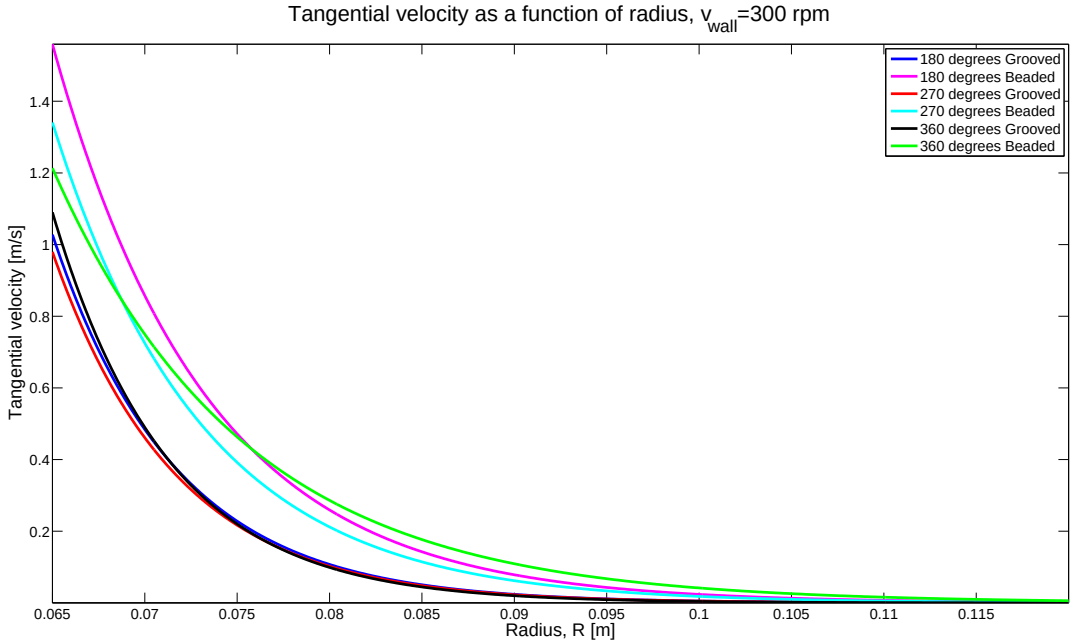

(a) $v_{wall} = 300\,\mathrm{rpm}$.

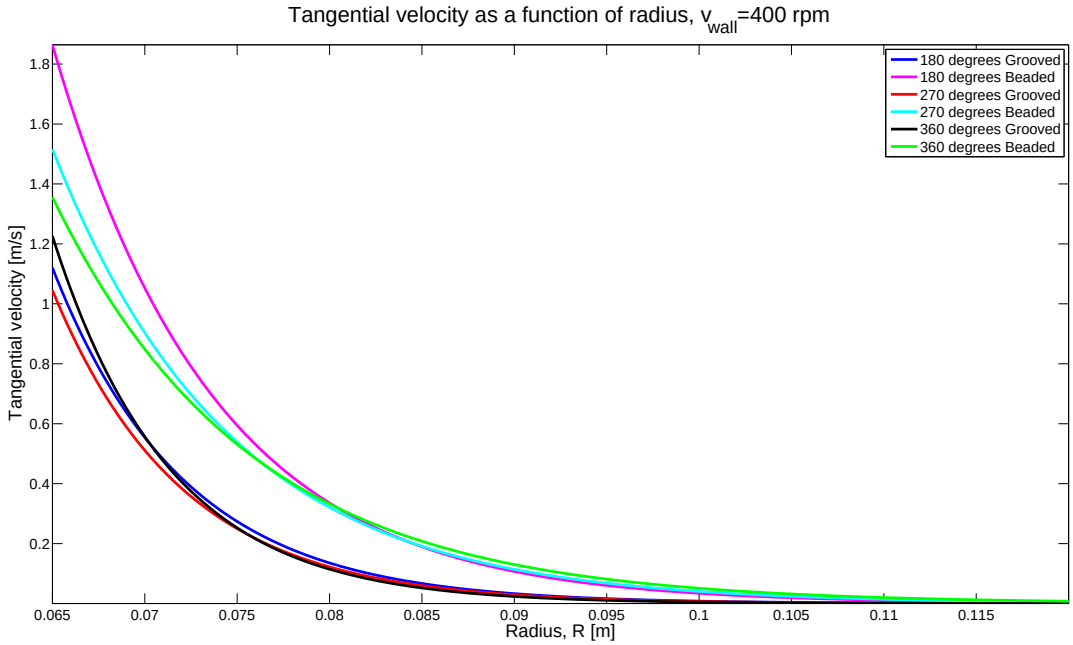

(b) $v_{wall} = 400\,\mathrm{rpm}$.

Figure 4.15.: Velocity as a function of radius at $180°, 270°, 360°$, $v_{wall} = 300\,\mathrm{rpm}$ and $v_{wall} = 400\,\mathrm{rpm}$.

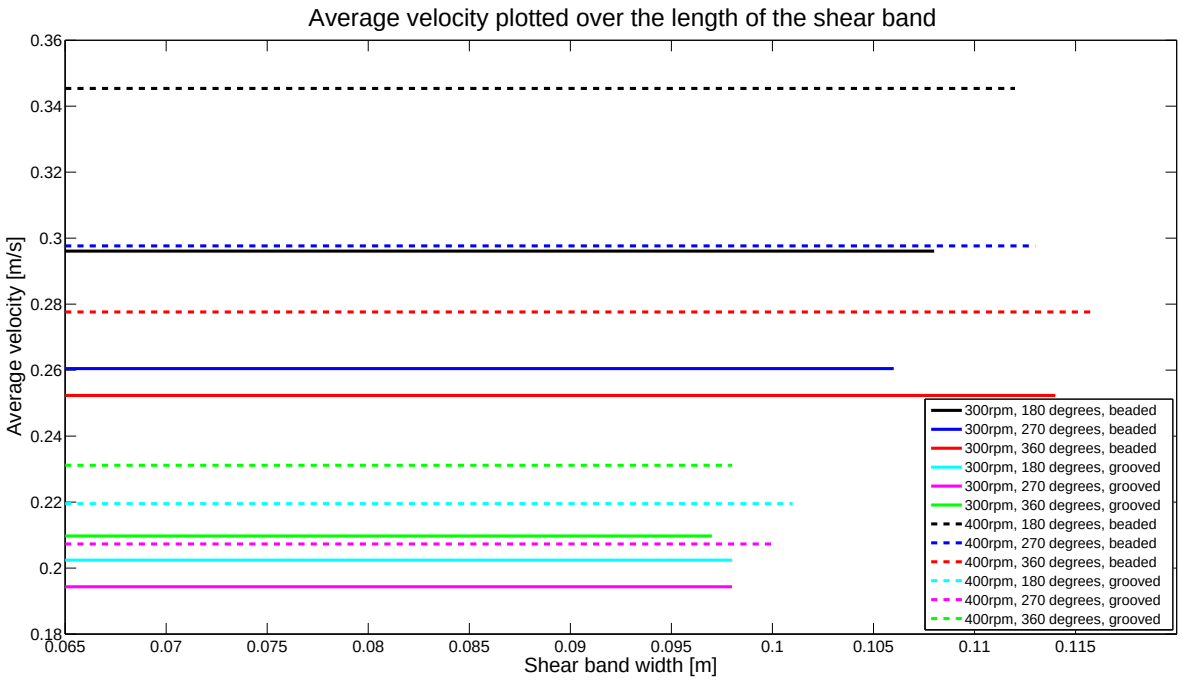

Figure 4.16.: The average velocity over the width of the shear band.

In Figure 4.17a, the radial bins show an asymmetry in the angular binning. Generally, the maximum velocity occurs close to 180° and the minimum at 360°. There are some fluctuations around this trend, but the material on the side of the rig that is moving in the same direction as the gravitational acceleration has a greater tangential velocity than the material moving in the opposite direction. This effect is seen much more clearly with the beaded wall configurations, show in Figure 4.17b.

The same trends are seen in Figure 4.18 for the configurations driven at 400 rpm. The side of the experiment aided by gravitational acceleration moves fast than the opposite side. The first radial bin in the case with the beaded wall shows only the basic trend, with a lot of oscillations as the angle increases.

The general angular trends seen in the histogram plots are different to the trends seen in the analysis along a line for the configurations with the grooved inner wall. This is due to the fact that the binning results in less sensitivity to fluctuations in velocity that may occur close to the inner wall.

Exponential fits performed on the tangential velocity profiles were used to calculate the shear rates within each configuration and angle. These are shown in Figure 4.19. The shear rates for the beaded wall show a greater variation between wall speed and angle than the grooved wall experiments.

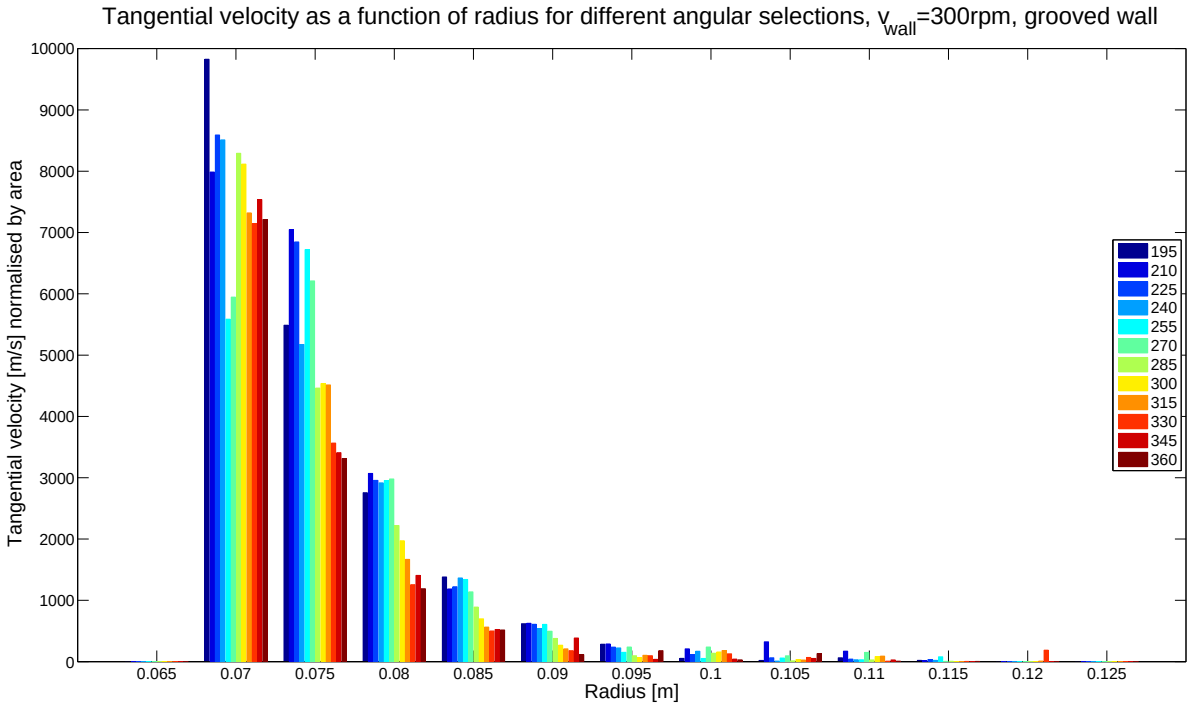

(a) Binned tangential velocity, grooved cylinder.

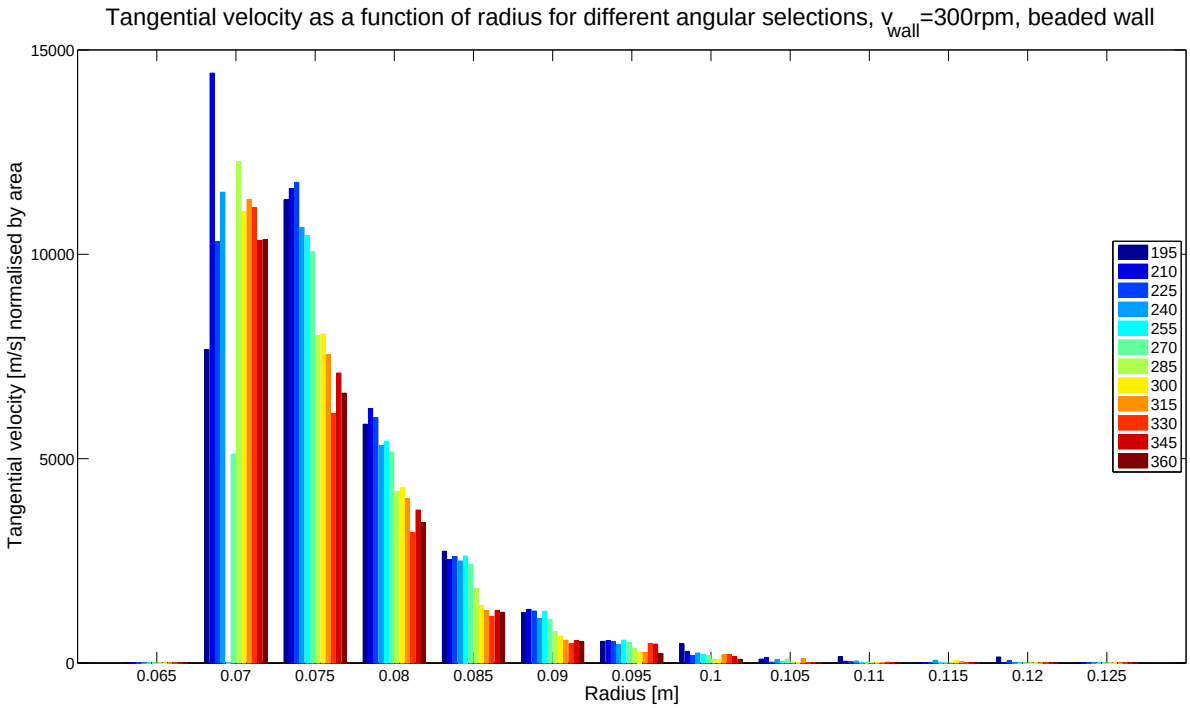

(b) Binned tangential velocity, beaded cylinder.

Figure 4.17.: Tangential velocity binned into 15° angular bins, $v_{wall} = 300\,\text{rpm}$.

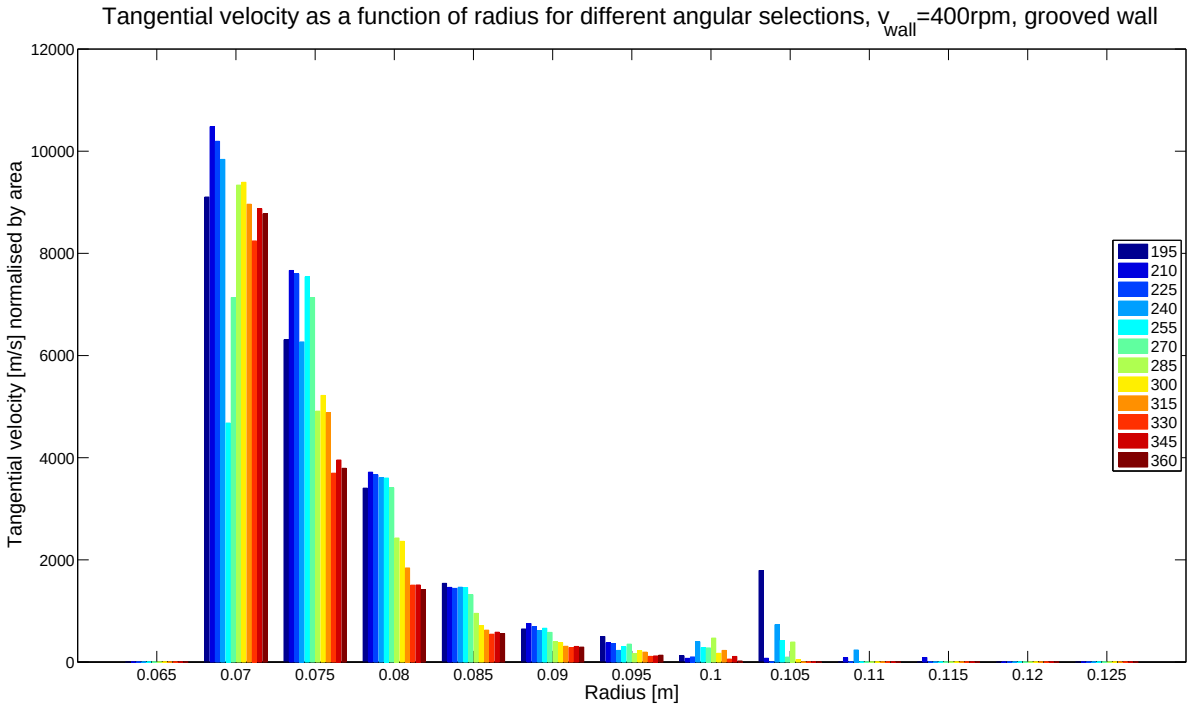

(a) Binned tangential velocity, grooved cylinder.

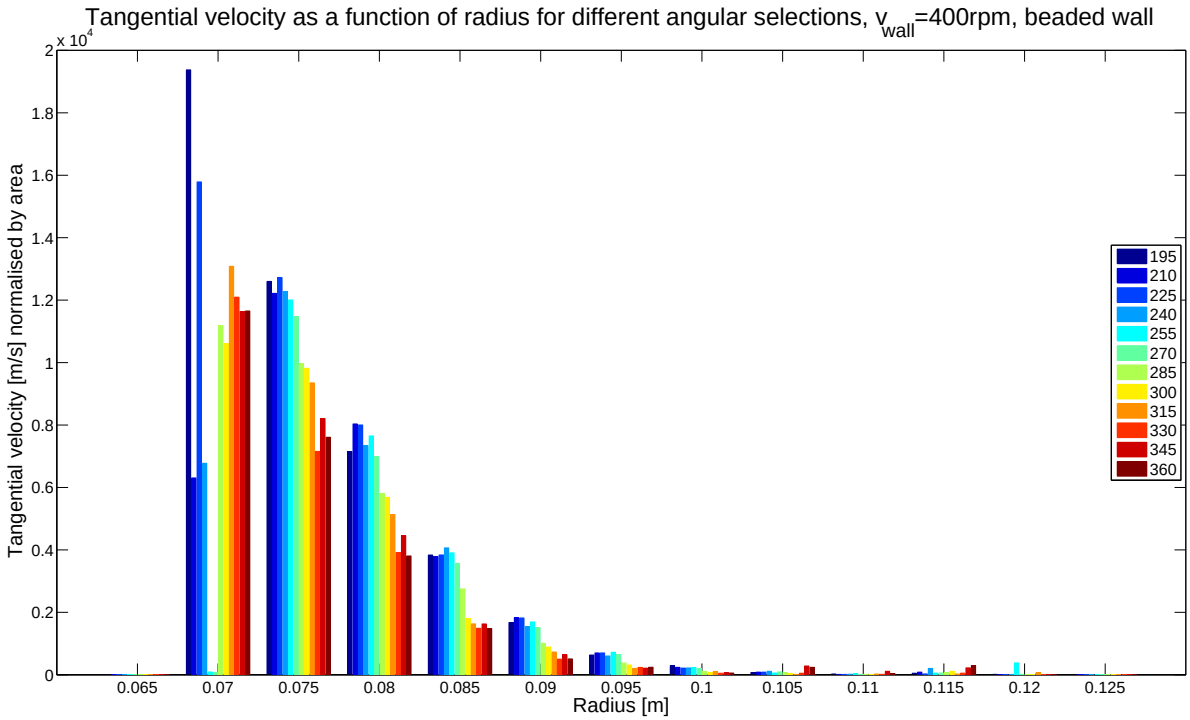

(b) Binned tangential velocity, beaded cylinder.

Figure 4.18.: Tangential velocity binned into 15° angular bins, $v_{wall} = 400\,\mathrm{rpm}$.

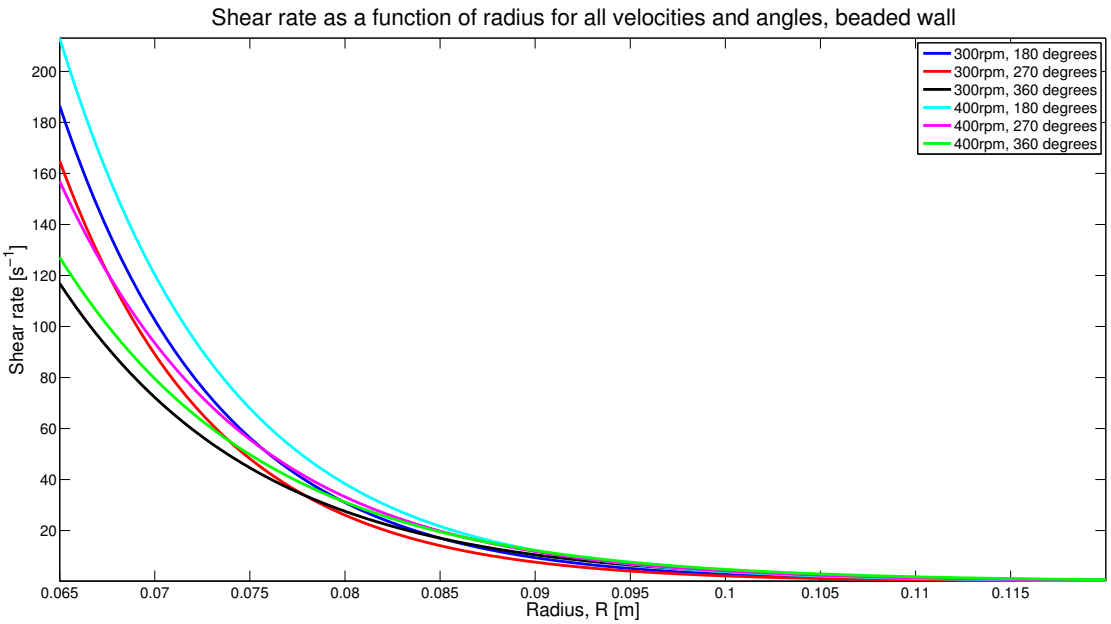

(a) Beaded wall.

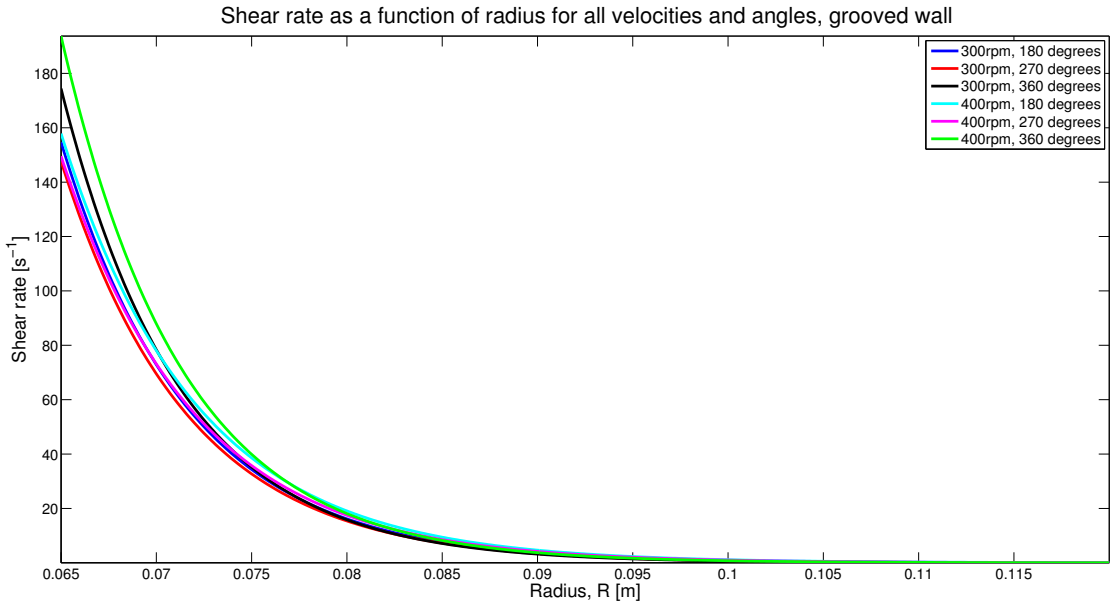

(b) Grooved wall.

Figure 4.19.: Shear as a function of radius at $180°, 270°, 360°$, $v_{wall} = 300\,\text{rpm}$ and $v_{wall} = 400\,\text{rpm}$.

4.5. Summary

The experiments performed here allow for the dynamics of an otherwise impenetrable system to be examined. The volume fraction distributions showed that $0 < \phi < 0.375$ in the area covered by the experiments, which leads to the conclusion that $I > 0.03$. Therefore the PEPT experiments cover the dense and kinetic-collisional regimes within the shear cell.

The velocity profiles along the selected radial lines were successfully extracted, showing an exponential decrease with distance from the shearing wall. There were noted differences in the behaviour of the velocity with angle between the grooved and beaded configurations. The grooved configurations showed that the maximum velocity was marginally greater at 360° than at 180°, while the beaded configurations showed a decrease with increasing angle. To further explore this discrepancy, histograms of tangential velocity binned in 15° arcs were considered and found that the angular trends matched those of the beaded configuration selections. The binning is less sensitive to fluctuations that may occur in the velocity profile close to the shearing wall.

The tangential velocity was found to be much greater than the radial velocity in all configurations, confirming one of the hypotheses made in the formulation of the power dissipation model. The apparent angular dependence of the tangential velocity refutes the assumption that the velocity had only radial dependence. The power dissipation model would have to be adapted to account for this variation.

The existence of the radial velocity suggests that there is a small amount of movement of material towards the stationary wall. As the experimental system was approximately 90% full, this movement radially outward is limited by lack of space for particles to move. The area at the top of the shear cell, where it was noted that the volume fraction was very low, can be considered as a chaotic mixing zone, which helps to replenish the material close to the shearing wall. The mixing occurring in this zone will need to be examined more fully with further simulation and experimental work.

There was no functional form of the volume fraction extracted from the data, due to lack of coverage of the complete system. Therefore the inertial number, shear stress and power dissipation could not be calculated along the selected radial lines. To gain further coverage of the system, longer experiment runs were considered. However, due to heating of the granular media in the rig, this action was rejected because of the worry of destroying the tracer particle. Experiments with the tracer placed on the outer wall were conducted, however the results were not useful, as the tracer stayed on the outer wall

and moved only a small amount during the course of the experiment. For this reason, Discrete Element Method (DEM) simulations were performed. As all the particles in the system are tracked in a DEM simulation, the problem of exploring the quasi-static region of flow on the outer edge of the shear cell was avoided.

A closer examination of how these experimental results compares with DEM simulations and other works appears in Chapter 6.

Part III.

Discrete Element Method Simulations

Chapter 5.

Discrete Element Method

5.1. Discrete Element Method Simulations

The Discrete Element Method (DEM) was initially developed by Cundall and Strack [1979]. The dynamics of a system of particles is simulated by tracing the movements of each individual particle. Disturbances propagate through the discrete medium from the boundaries through contacts between particles, which result in the movement of the particles. The speed of the disturbance propagation depends on the physical properties of the medium. Integration time steps are taken that are sufficiently small so that the accelerations and velocities of the particles can be assumed to remain constant and that the disturbances cannot propagate further than the immediate neighbours of a particle. Therefore the contacts of any particle at any time exclusively determine the resultant forces on that particle.

Once the resultant force on a particle has been determined from the vector sum of all a particle's contacts, Newton's second law is utilised to determine the resultant velocity and displacement. The contacts are once again determined, the force on each particle calculated and the velocity and position updated. This method can be utilised to follow the non-linear behaviour of a large number of interacting particles.

The contact search for N interacting particles, requires on the order of $N(N-1)/2$-pair searches, making it extremely computationally expensive [Mishra, 2003]. There are various methods to reduce the number searches conducted for each particle, most of them involving maintaining a list of nearest neighbours. In a method called boxing, the search area for one particular particle is limited to a box (or cube) with dimensions equal to the particle diameter, around the particle. Another particle is only considered as a nearest neighbour if it's circumscribing box intersects with the box of the particle in question.

The contact search is then only conducted on the nearest neighbours. After each update of the position, the nearest neighbours list is updated.

A soft contact method is used, where particles in contact are allowed to overlap by a small distance. The amount and rate of the overlap give rise to the contact force. The effect of the contact force model on the granular flow was investigated by Ji and Shen [2006]. The nonlinear contact force model produces qualitatively similar results to the linear contact model. Further investigations were conducted by [Ji et al., 2009], who suggested that a nonlinear contact force model, combined with the investigated effects of rolling friction would further improve the agreement between experimental and simulated systems. A comprehensive review and comparison of a number of contact-force models was performed by Di Renzo and Di Maio [2004], who found that a simple linear model performed as well as the more complex models based on Hertz theory and Mindlin and Deresiewicz [1953]. The simplest contact force model is a linear one in which the spring stiffness is constant. This, however, does not include force deformation and thus dissipation of the force in the contact area. Hertz theory and the use of a spring and dashpot system to model the contact allows this damping to be included.

The model used in the simulations performed here is a no-slip Hertz-Mindlin model, described in EDEM Technical Overview [DEM Solutions, 2012].

DEM simulations have been used extensively to explore granular flows in couette or annular shear cell geometry [Campbell and Brennen, 1985, Ji et al., 2009, Koval et al., 2009, Schwarz et al., 1998, Lätzel et al., 2000, Cheng et al., 2006] and granular flows in a more general geometry [Rycroft et al., 2009, Campbell, 2002]. Other computer simulation techniques have been used to study annular shear cells in Schollmann [1999] and Jasti and Higgs [2009].

The DEM simulation results, in the form of a list of particle positions and velocities as they change over time, were used to derive the components of the combinatorial stress model and the power dissipation model derived in Part 1. The velocity and volume fraction distributions were extracted directly from the results. These were then used to calculate the rest of the model components, including the shear rate and inertial number distributions. The functional forms of these components derived from the results were used to calculate the pressure and shear stress components, the effective friction coefficient distributions and the power dissipation distributions. A summary of the equations used appears in Table 5.1 and all constants used are summarised in Table 2.1.

Table 5.1.: List of equations used to calculate the components of the model.

Component	Equation
Shear rate, $\dot{\gamma}$	$\frac{\partial v_\theta}{\partial r}$
Inertial number, I	2.10
Total pressure, P	2.11
Pressure components, P_c, P_t, P_s	2.14, 2.16, 2.23
Shear stress components, τ_c, τ_t, τ_s	2.12, 2.18, 2.22
Total shear stress, τ	2.4
Effective friction coefficient, μ	2.24
Shear power dissipation	3.50
Compressive power dissipation	3.51

5.2. Experiment description

The Discrete Element Method simulations were performed using commercial software, EDEM. Firstly, a simple geometry was set up, matching the dimensions of the experimental rig used in the PEPT experiments. The dimensions of the system are shown in Figure 5.1, with the length of the mill being $L = 0.285\,\mathrm{m}$.

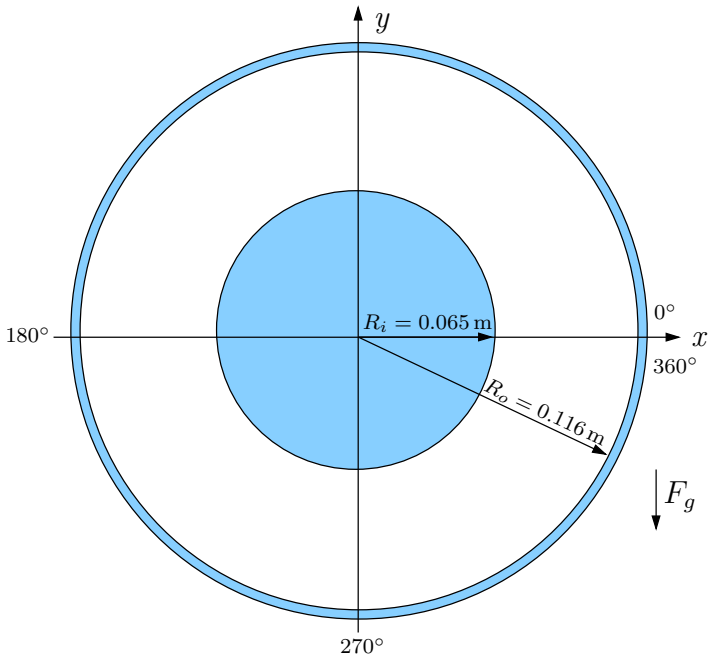

Figure 5.1.: Dimensions of experimental system.

The experimental set up is shown in Figure 5.2, as well as the progression of the particle population throughout the simulation. The geometry was created in AutoDesk Inventor and then imported into EDEM. The simulation was then filled with simulated glass beads of 5 mm diameter, making the space between the shearing walls approximately 10 particle diameters wide. The first second of simulated time was devoted purely to particle population, where the particles were placed randomly within the simulation space (see Figure 5.2b, where approximately half the particles have been placed in the simulation space.) It was found by Ji et al. [2009] and Campbell [2002] that the initial packing of particles had little influence on the final stresses produced within the system.

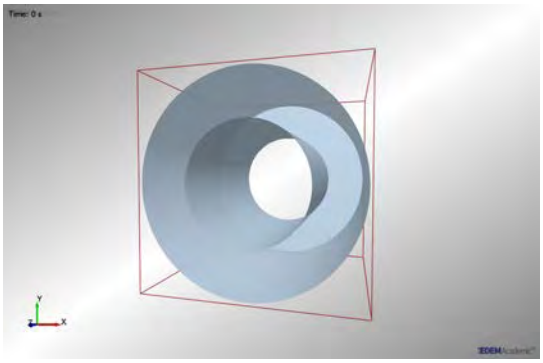

(a) Simulation geometry.

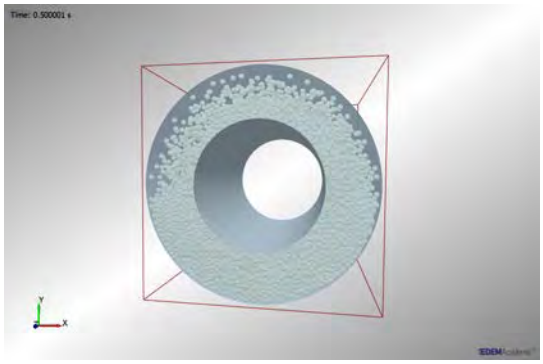

(b) Simulation at 0.5 s, approximately half the particles have been placed.

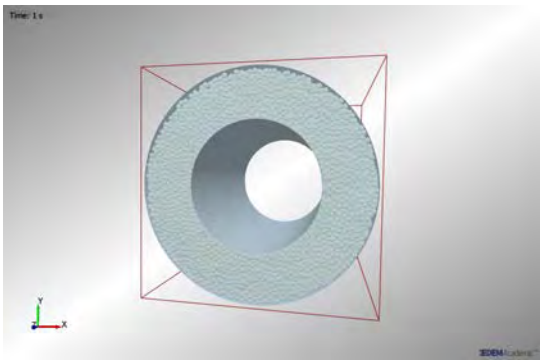

(c) Simulation at 1 s, all particles have been placed.

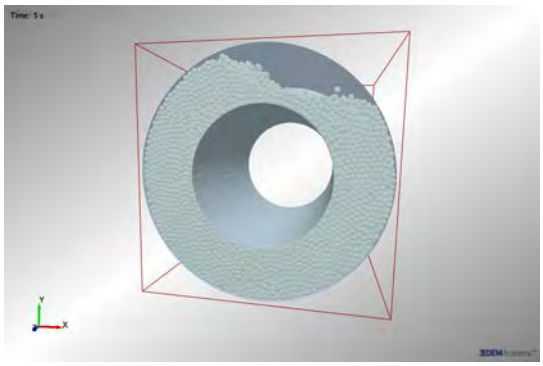

(d) Final state of the simulation at 5 s.

Figure 5.2.: Simulation setup and particle population.

After the particle population was completed, the inner cylinder was then rotated at a prescribed rate in an anti-clockwise direction. The total amount of time simulated was 5 s. As the PEPT experiments on the shear cell were run with the rotational axis horizontal, the force due to gravity was imposed in the direction perpendicular to the rotation axis.

Various simulations were run with the rotor (inner cylinder) rotating at speeds ranging from 150 rpm to 3500 rpm, the details are shown in Table 5.2. The simulations were also run with two instances of friction coefficients. The first was static friction coefficient of $\mu_s = 0.8$ and rolling friction coefficient $\mu_r = 0.3$, the second had $\mu_s = 0.5$ and $\mu_r = 0.1$. These values were chosen based on Campbell [2002], who investigated the effects of three different friction coefficients ($\mu = 0.1, 0.5, 1.0$) on the stresses in the simulated system considered there. It was observed that the larger the friction coefficient, the greater the energy dissipation (far from the solid boundaries). Therefore the middle and higher values of friction coefficients were chosen to further investigate this energy dissipation dependence. The total number of particles in each simulation remained constant.

Table 5.2.: List of rotor speeds simulated with $\mu_s = 0.8$, $\mu_r = 0.3$ and $\mu_s = 0.5$, $\mu_r = 0.1$.

$\mu_s = 0.5$, $\mu_r = 0.1$	$\mu_s = 0.8$, $\mu_r = 0.3$
200	150
300	200
400	250
800	300
1000	350
1500	400
2000	450
3000	2000
3500	2500
	3000
	3500

The other constants set in the DEM simulation are summarised in Table 5.3, where the Poisson ratio and shear modulus for the geometry refers to the interaction between the geometry and particles, while the particle values refer to the interaction between particles. The coefficient of restitution for the particles was set to $e = 0.7$ for all the simulations and interactions within. Campbell [2002] used $e = 0.1, 0.7$ and 1.0 in his simulations, finding that the restitution coefficient only had a noticeable effect on the stresses produced in cases where the shear rate was high, and thus there were large impact velocities. As the quasi-static regime was assumed to be more dominant than the turbulent regime in these shear cell simulations, the middle value was chosen.

Table 5.3.: Constants used in simulations.

	Geometry	Particle
Material	HDP	Glass
Density	$940\,\mathrm{kg\,m^{-3}}$	$2500\,\mathrm{kg\,m^{-3}}$
Poisson ratio	0.42	0.2
Shear modulus	$7 \times 10^8\,\mathrm{Pa}$	$6.4 \times 10^{10}\,\mathrm{Pa}$

5.3. Simulation Analysis and Results

A section of the data (as the simulation results consist of a list of particle positions and velocities, these results were considered as data points) corresponding to the particles in a 9 cm deep slice in the centre of the simulation domain, far from the edges of the system to avoid end wall effects, for each simulation were extracted. The data for each simulation with a given wall velocity and friction were exported into csv file format. This data consisted of a list of Particle ID, (x, y, z) coordinate and velocity components of each particle at each time step. The data was exported every 0.01 s of simulation time, only from the time where particle population had been completed. Thus for the simulated time of 4 s, there were in total 400 time steps. The selection contained, on average, 22000 particles for each time step.

The data were used to created a picture of the average behaviour of the particles in the shear cell.

5.3.1. Volume Fraction

For each time step, the list of positions were binned into a grid of 47 x 47 bins, covering an x and y length of 23 cm each, making the bins 5 mm across. The entire z-direction selection was binned, thus the total volume of each bin was 5 x 5 x 90 mm.

As the model of the power dissipation considers the system to be in a steady state, only the portion of the simulation where the particles had settled into a steady state was used. To determine this, a visual estimate was made on when steady-state occurred, by plotting the particle count as a function of radius and time as seen in Figure 5.3. The first second of exported data was considered to not be in steady state, so only the last 3 s of the simulation were used.

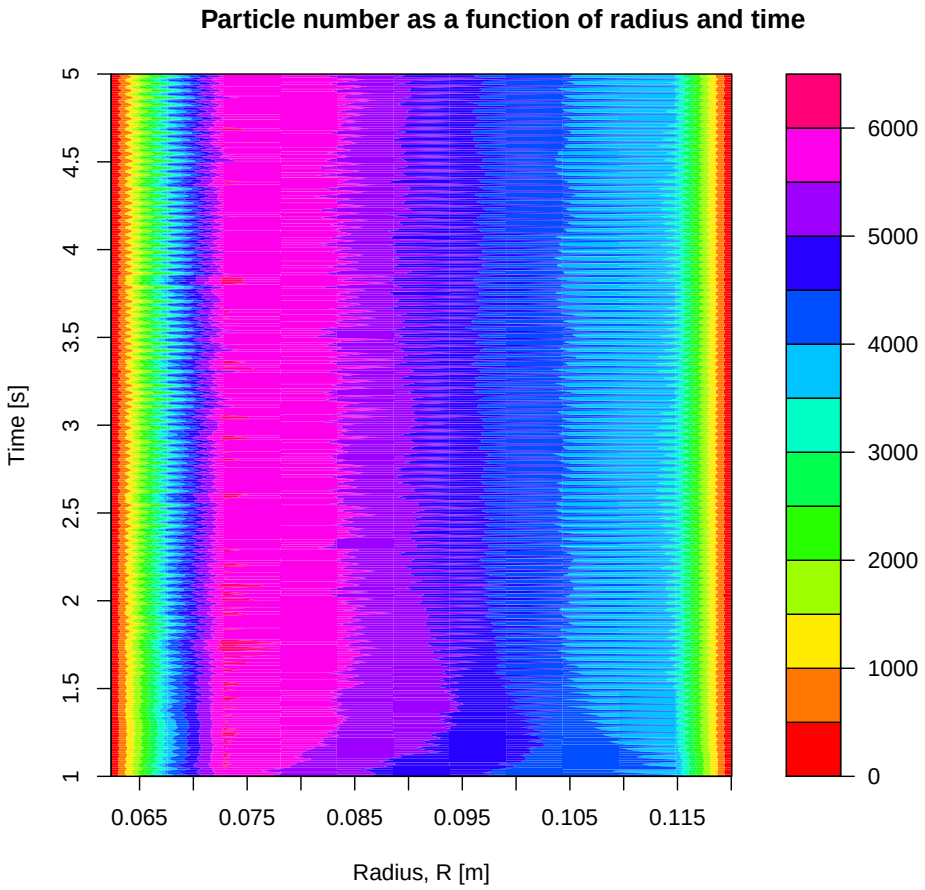

Figure 5.3.: Particle number as a function of radius and time to estimate steady state.

From Figure 5.3, it is also apparent that there is an oscillation in particle count over time. This is seen more clearly in Figure 5.4 where the total number of particles in the selected data for one simulation is plotted for each time step. The oscillation in particle number indicates that there is movement of the particles along the direction of the rotational axis. This movement of particles along the rotational axis could contribute to the development of bands of particles of different sizes seen in Conway et al. [2004]. The average number of particles in the selection was used in the volume fraction calculation.

The list of particle positions was binned by projecting the position onto the 5 x 5 mm grid, creating an index for the x and y position of each particle at each time step. This projection was determined by taking the position, subtracting the boundary position and dividing that by the length of the side of the bin. Thus, for example, the x index was

$$x_{ind} = \frac{x - x_{min}}{L_{bin}}. \tag{5.1}$$

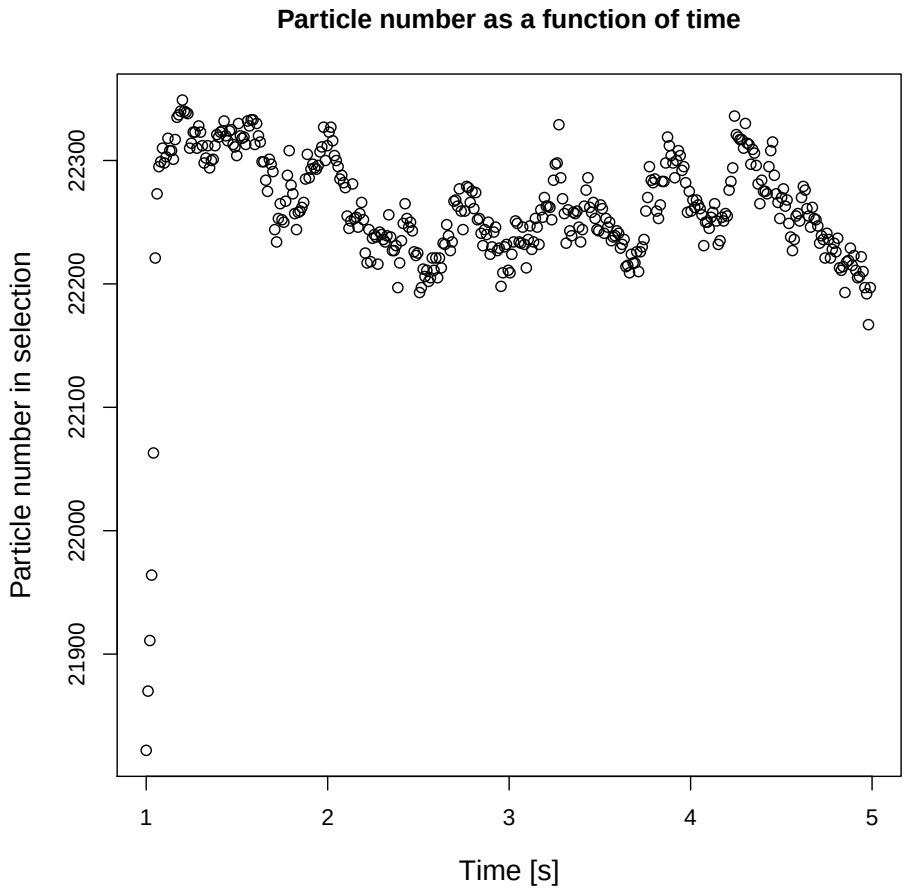

Figure 5.4.: Particle number in data selection as a function of time.

The number of particles occurring in any specific bin is then the number of occurrences of (x_{ind}, y_{ind}) pairs with that bin index.

An average over the time in which the system was in steady state was then conducted to calculate the average volume fraction distribution. The standard deviation of this averaged data was also calculated. The volume fraction in each bin was calculated by

$$\phi_{bin} = C_{bin} \frac{V_{particle}}{V_{bin}}. \tag{5.2}$$

Here the average count for each bin, C_{bin} is used.

An averaging filter was applied to the volume fraction to smooth anomalies caused by binning a cylindrical system into a square grid (the highest volume fraction was often seen where the outer shell connected with the boundary of the grid). The inertial number, I, was then calculated directly from this data using Equation 2.10. Data were

selected along three directions in the system to analyse. The directions chosen were $180°, 270°, 360°$. These directions are taken so that the positive x-axis is at $0°/360°$, as shown in Figure 5.1 and were the same angles investigated in the PEPT experiments. The analysis focused on the bottom half of the system, avoiding the free surface, which is a result of system not being completely filled.

Results

The volume fraction distributions represented in Figure 5.5, show that there is not a great difference between the distributions for different friction conditions, at the same driving velocity.

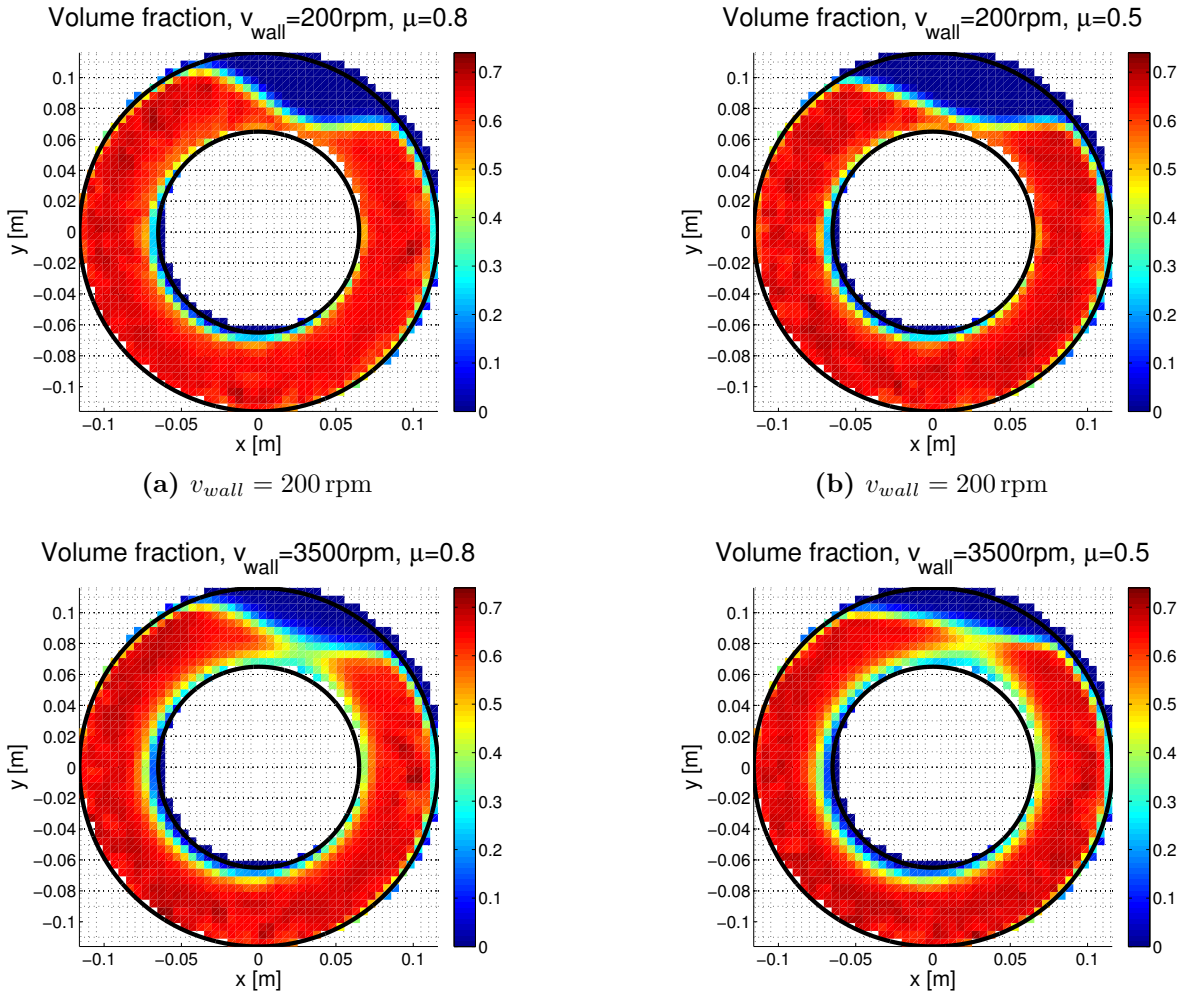

(a) $v_{wall} = 200\,\text{rpm}$ **(b)** $v_{wall} = 200\,\text{rpm}$

(c) $v_{wall} = 3500\,\text{rpm}$ **(d)** $v_{wall} = 3500\,\text{rpm}$

Figure 5.5.: The effect of friction values ($\mu_s = 0.5$ and $\mu_s = 0.8$) on volume fraction shown for a low and a high driving wall velocity.

There is a slight increase in volume fraction towards the outer wall in the distributions with a lower static friction set in the simulations, in comparison to the higher friction. In general the volume fraction increases slightly towards the outer wall, while there are lower values close to the rotating wall, accentuated on the side where the material is being driven downwards by the direction of the rotation.

The free surface is clearly seen in the distributions, with it being more curved for the distributions with a higher static friction coefficient. As the driving wall velocity increases, the free surface becomes more dilute close to the driving wall.

The volume fraction distributions at higher rotational velocities, shown in Figures 5.5c and 5.5d, show the change in the free surface more clearly. For the lower friction coefficient, the free surface is flatter and more dilute where it is closest to the driving wall. The dilute region close to the inner wall is also more visible and is extended further around the wall. The volume fraction is still higher closer to the outer wall.

The volume fraction was selected along three lines, resulting in the distributions shown in Figures 5.6-5.11. These figures show the volume fraction distribution for each angle and friction condition, as well as for each wall velocity.

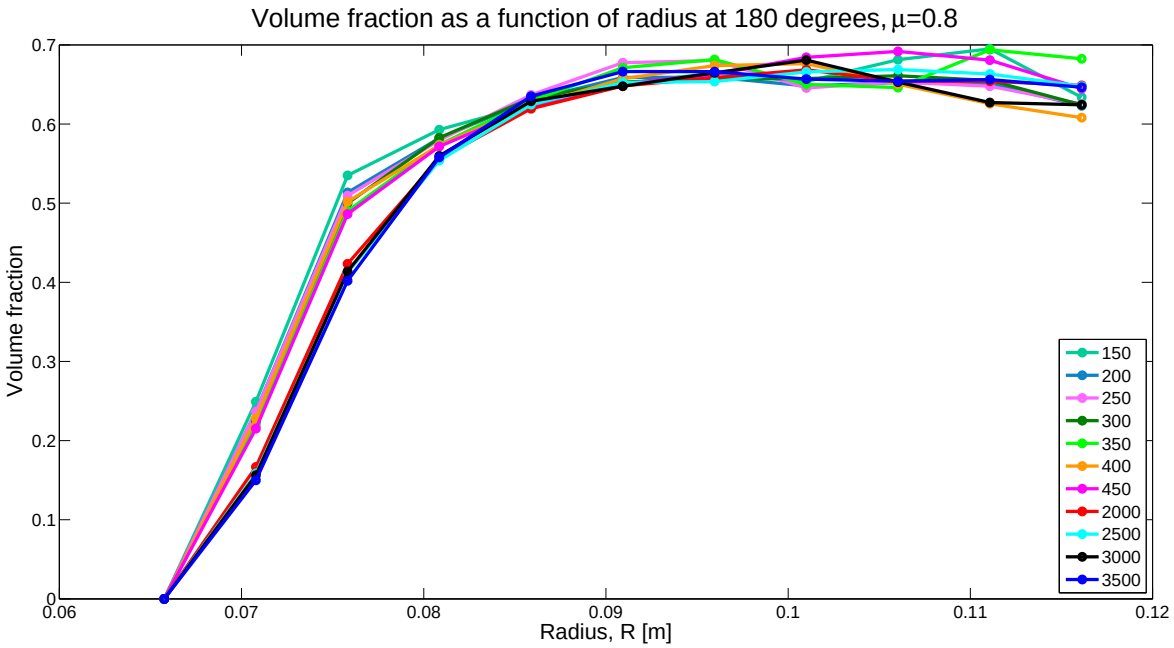

Figure 5.6.: Volume fraction as a function of radius for all wall velocities at 180°, $\mu = 0.8$.

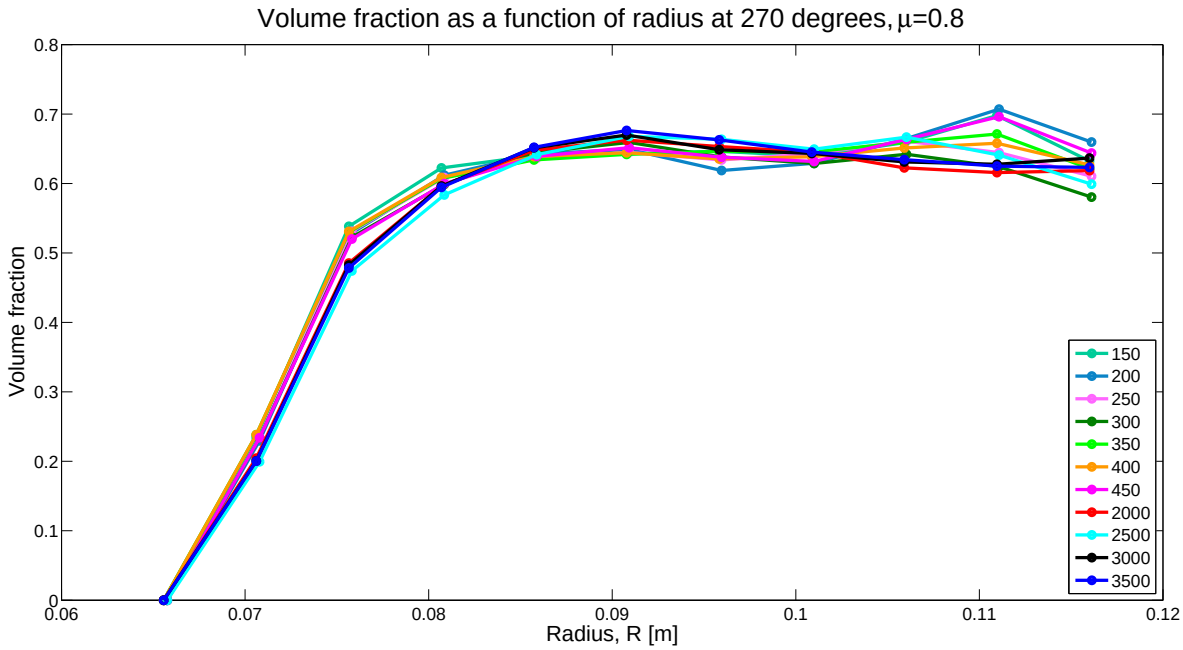

Figure 5.7.: Volume fraction as a function of radius for all wall velocities at $270°, \mu = 0.8$.

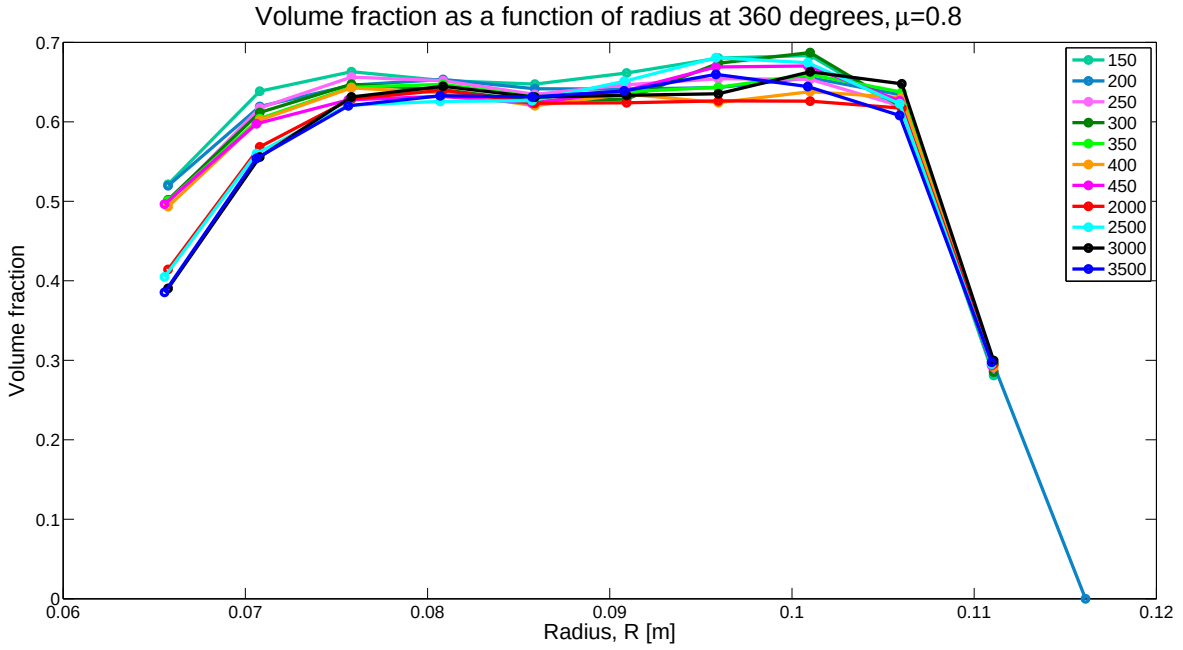

Figure 5.8.: Volume fraction as a function of radius for all wall velocities at $360°, \mu = 0.8$.

The volume fraction starts low close to the rotating wall and asymptotes to a maximum value. Most distributions show a slight oscillation, the width of which is equal to one particle diameter. None of the selected data show a great variation of volume fraction with driving wall velocity, although the lower velocities tend to have a slightly higher volume fraction than the higher velocities. The volume fraction starts at 0 for the angles

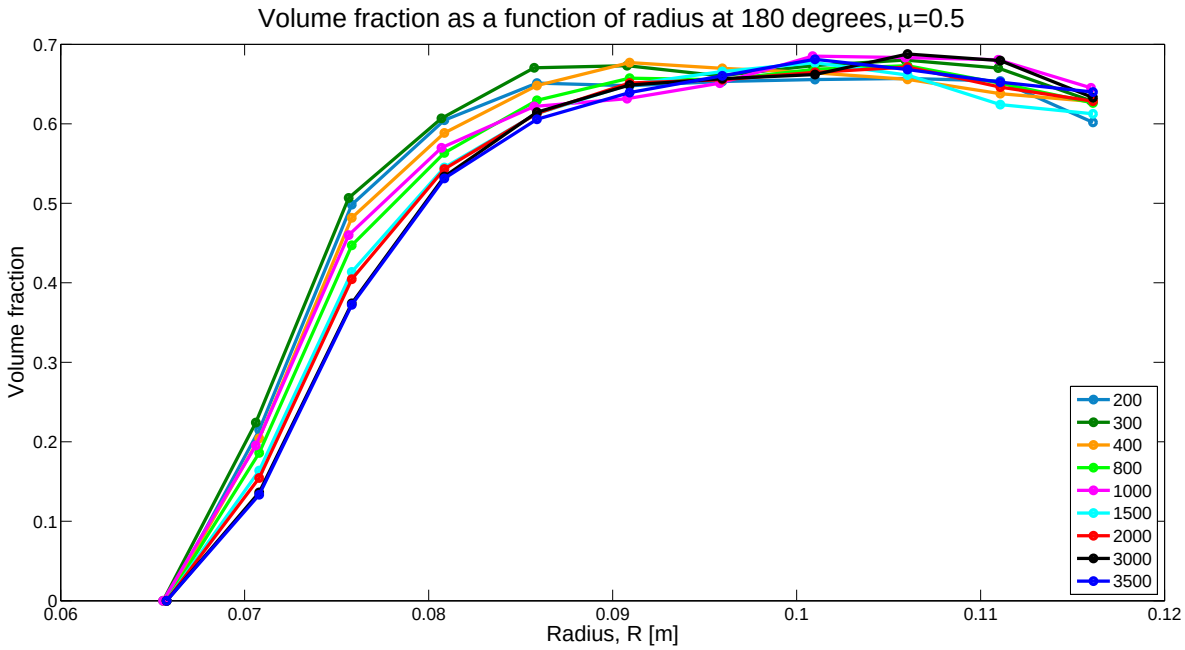

Figure 5.9.: Volume fraction as a function of radius for all wall velocities at 180°, $\mu = 0.5$.

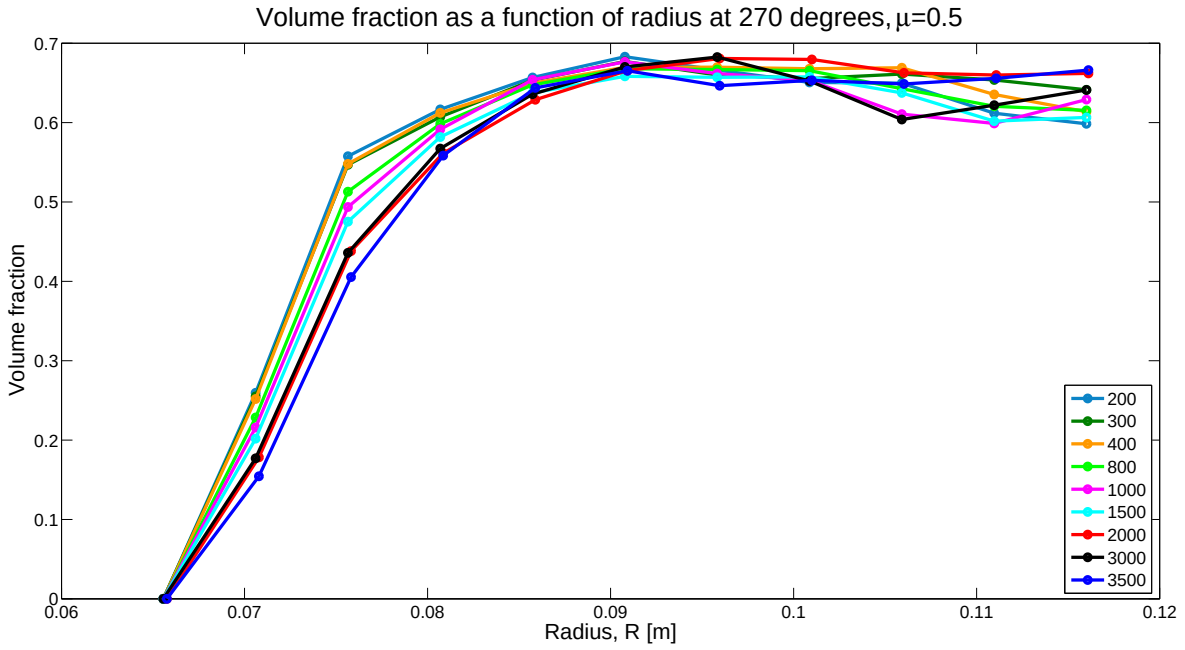

Figure 5.10.: Volume fraction as a function of radius for all wall velocities at 270°, $\mu = 0.5$.

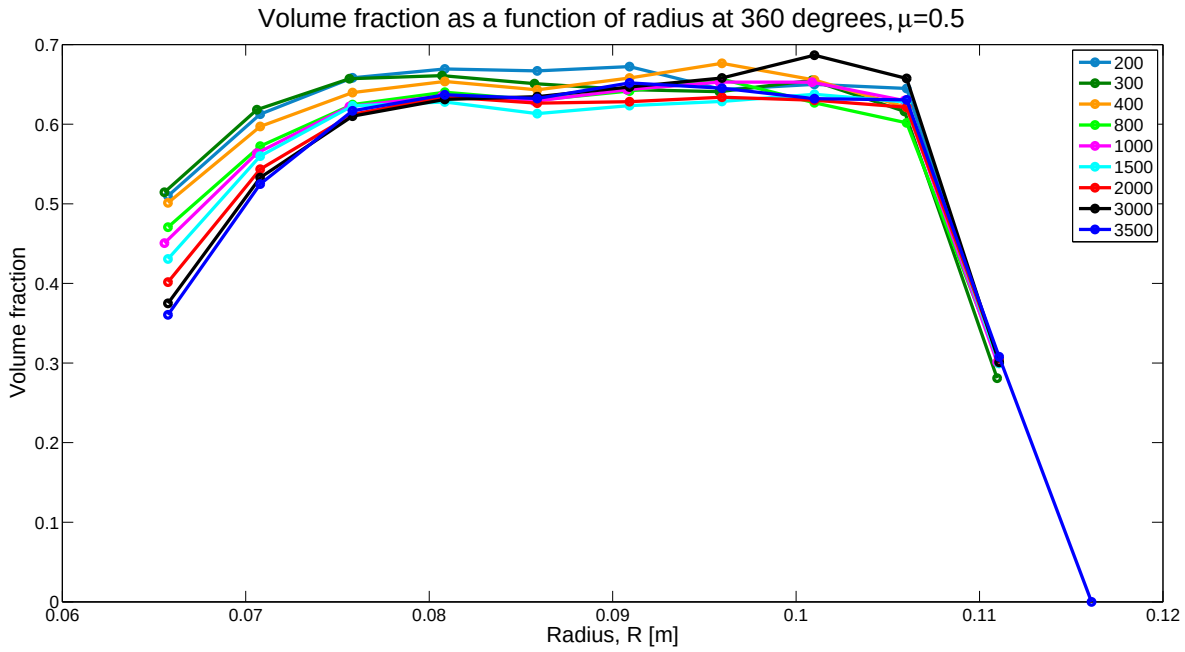

Figure 5.11.: Volume fraction as a function of radius for all wall velocities at 360°, $\mu = 0.5$.

180° and 270°, which is an effect due to the fact that everything binned up to there is 0 (there are no volume fraction values inside the rotation wall). Thus the distributions are only relevant from 1 particle diameter from the wall, $R = 0.07\,\mathrm{m}$.

In the 360° case (Figures 5.8 and 5.11), the distributions decrease sharply towards the outer wall. This is due to the binning of a circular system into a square grid, so the right hand side of the binned data contains empty space in the simulated system.

The volume fraction was fitted with a critically damped second order differential equation, with a shift, Φ_0, as the distribution does not start at 0. The solution of this differential equation,

$$\phi(r;r_0) = \Phi_0 + \Phi\left[1 + \frac{1}{2\sqrt{\zeta^2-1}}\left(\frac{1}{\sqrt{\zeta^2-1}+\zeta}e^{-k\left(\zeta+\sqrt{\zeta^2-1}\right)(r-r_0)} + \frac{1}{\sqrt{\zeta^2-1}-\zeta}e^{-k\left(\zeta-\sqrt{\zeta^2-1}\right)(r-r_0)}\right)\right], \tag{5.3}$$

depends on the damping coefficient, ζ, an amplitude scaling factor, Φ and a fitting parameter, k. Here, r_0 refers to the radius of the inner cylinder. As the continuum model and scale currently investigated here do not have the sensitivity to capture the oscillations seen in the distributions, it is preferred to introduce an apriori smoothing into the volume fraction functions provided that the first order effects are not smoothed

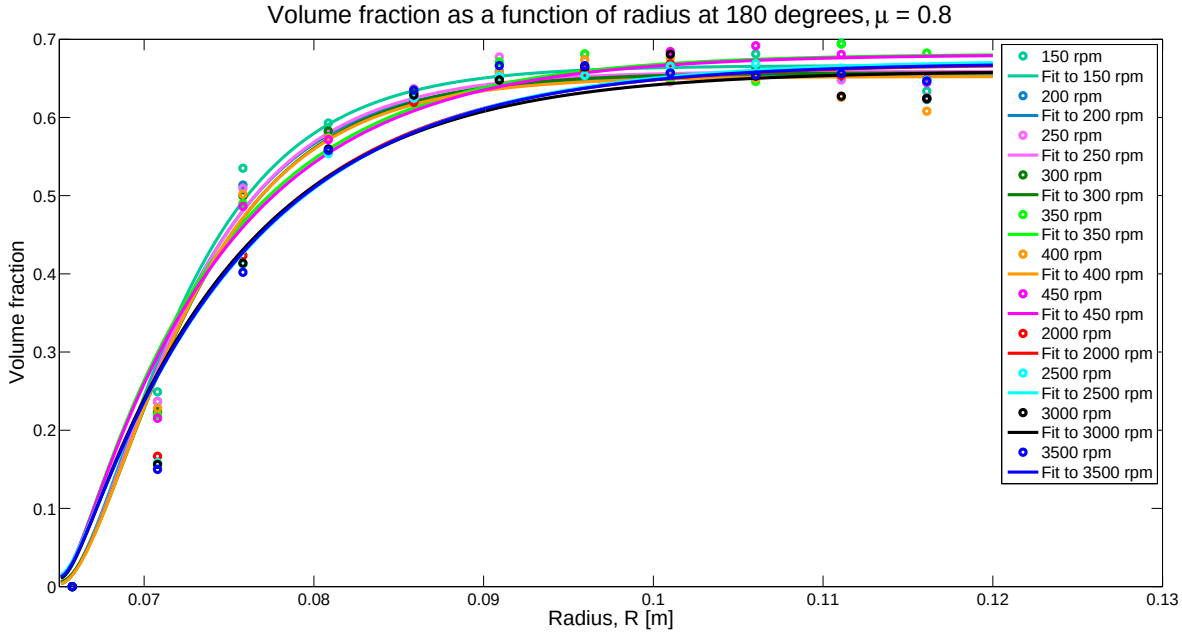

(a) Static friction $\mu = 0.8$

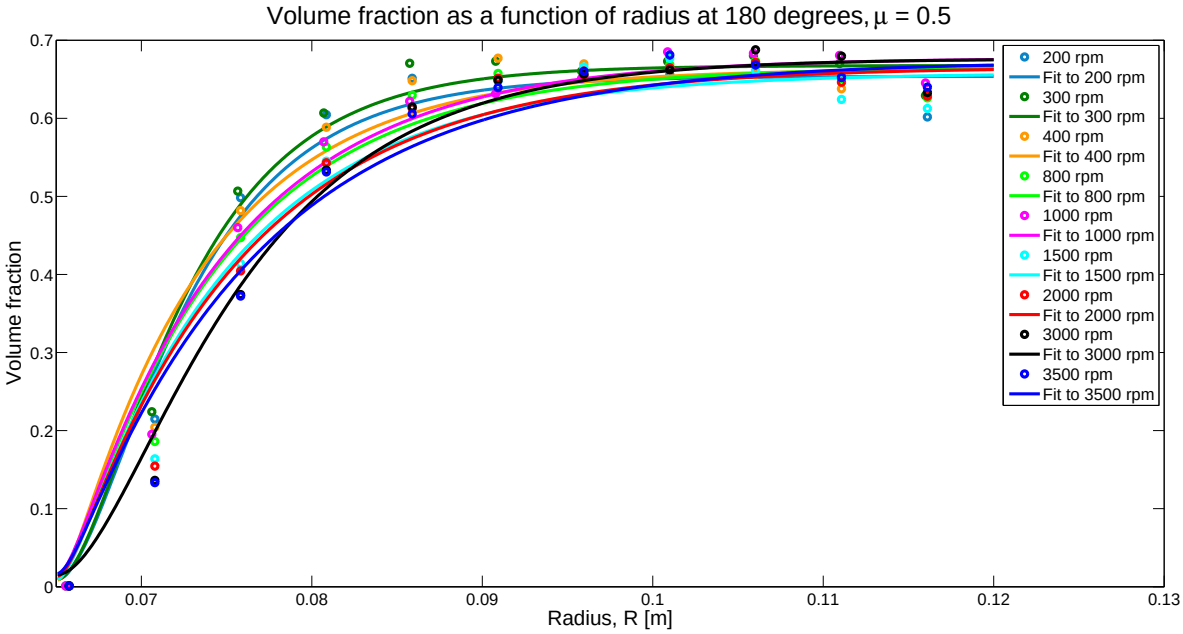

(b) Static friction $\mu = 0.5$

Figure 5.12.: Volume fraction as a function of radius for all wall velocities at 180°, with function fit.

out. The overall behaviour is well represented as seen in Figures 5.12-5.14. There is a minor decrease in volume fraction at larger radial values, suggested by the oscillations due to the particle packing. As this change is much smaller than the overall change, it is considered unimportant, but may require further investigation.

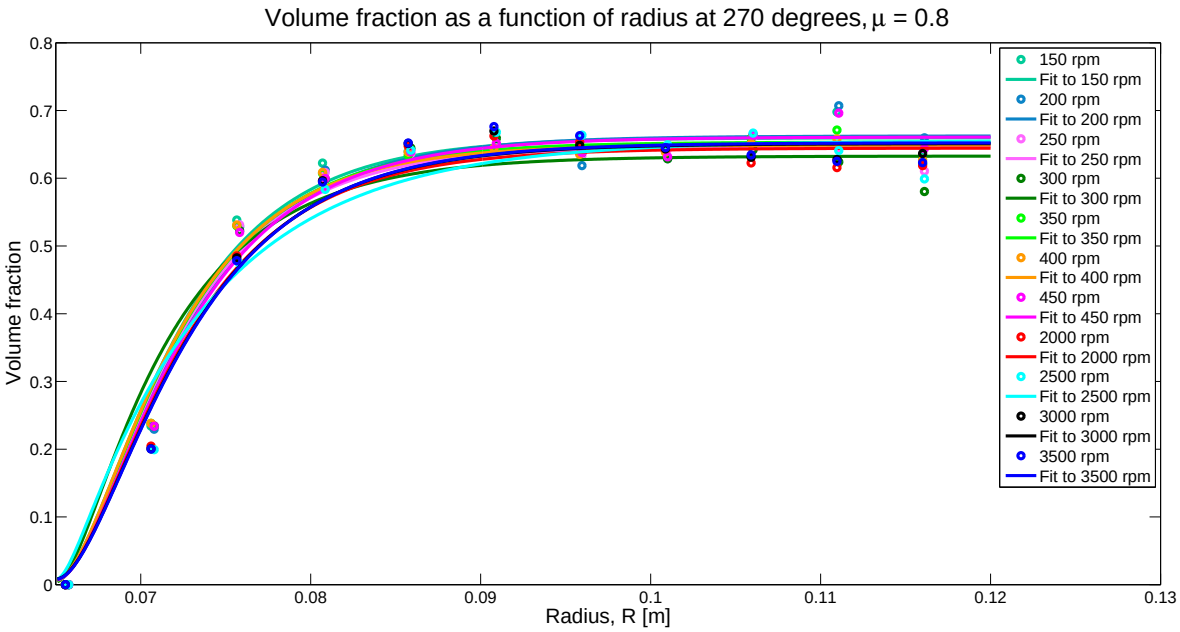

(a) Static friction $\mu = 0.8$

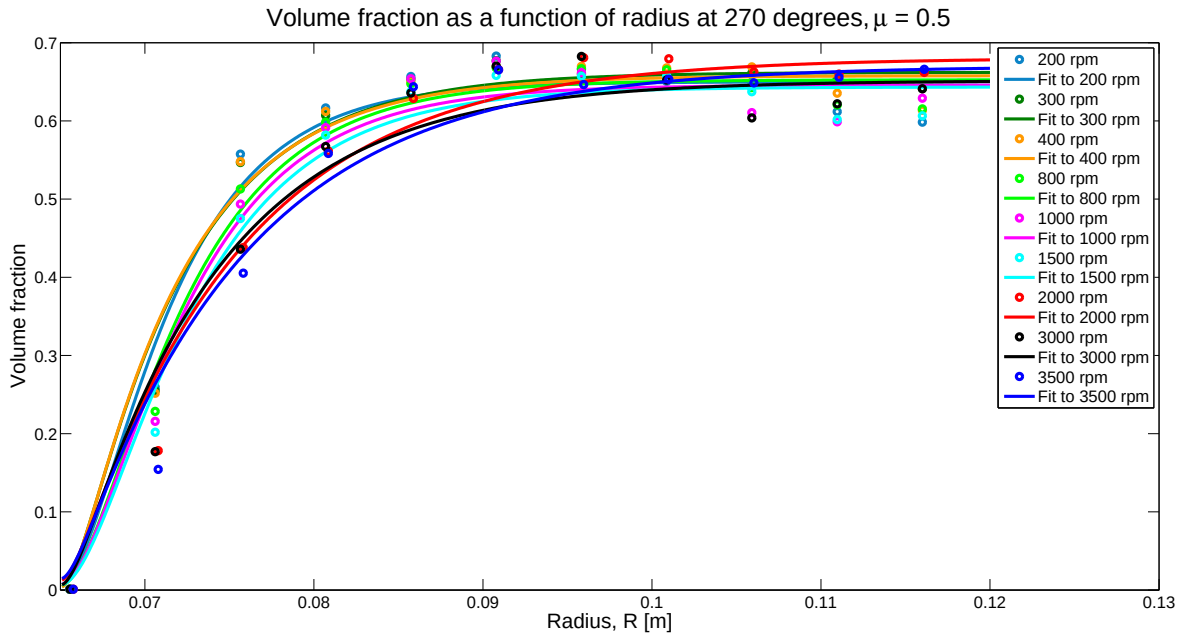

(b) Static friction $\mu = 0.5$

Figure 5.13.: Volume fraction as a function of radius for all wall velocities at 270°, with function fit.

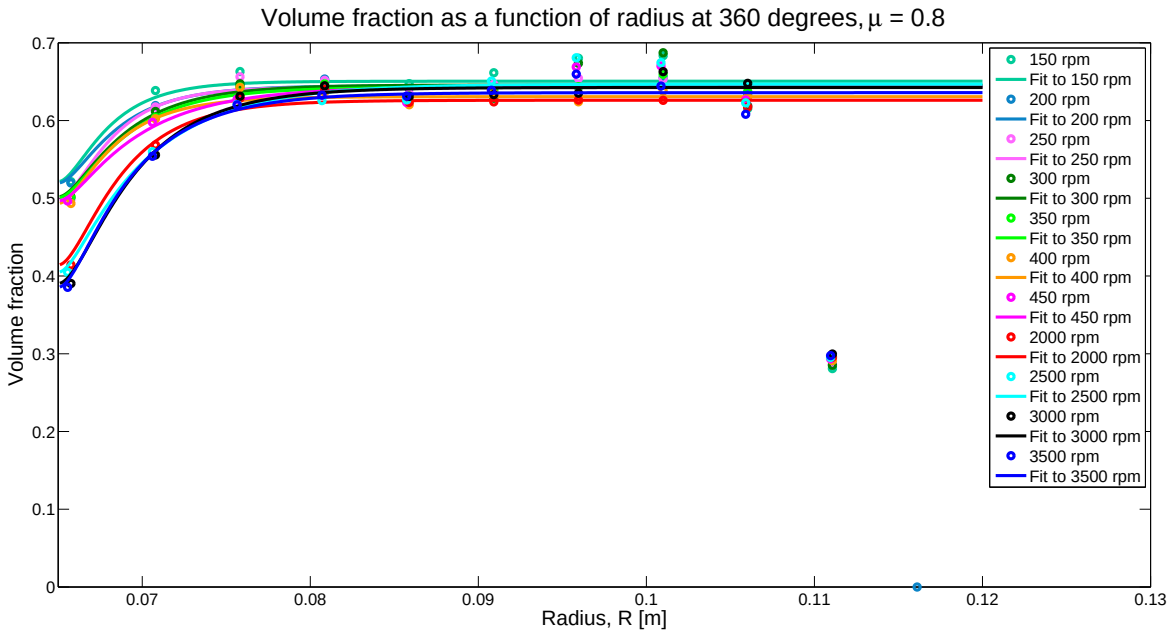

(a) Static friction $\mu = 0.8$

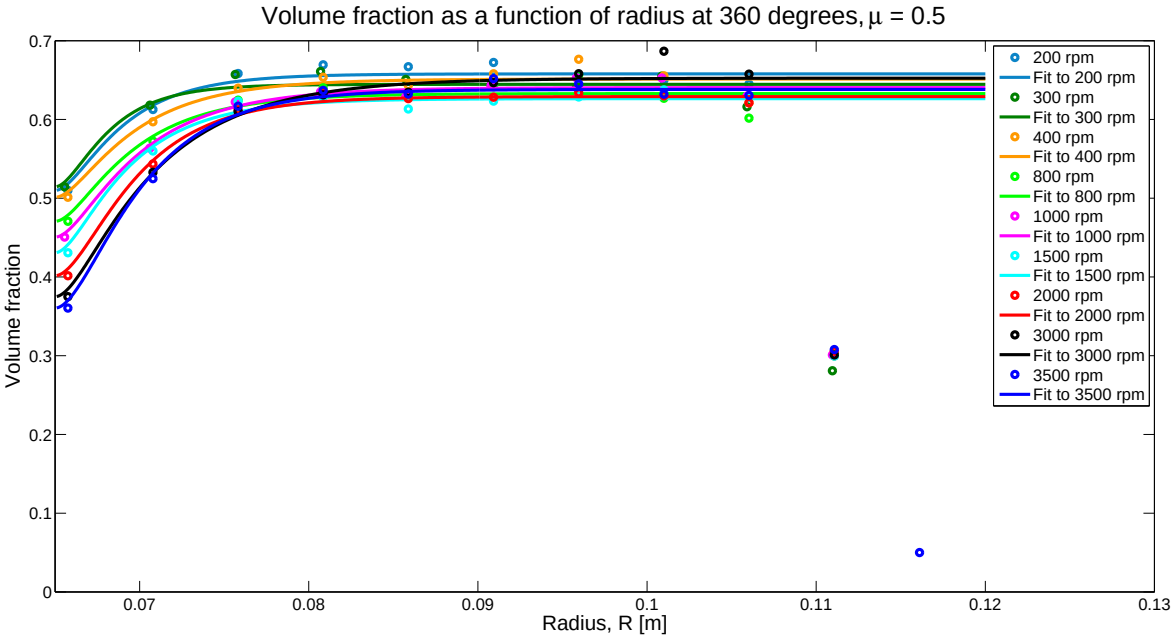

(b) Static friction $\mu = 0.5$

Figure 5.14.: Volume fraction as a function of radius for all wall velocities at 360°, with function fit.

A comparison of the volume fraction for different angles at 300 rpm and 3000 rpm can be seen in Figure 5.15. Here it is apparent that the volume fraction tends towards a similar maximum value for all three angles. The value close to the rotating wall is higher for the 360° case than it is for the other two angles, with the function fit starting close to 0. The behaviour is similar for the rest of the configurations.

In all the simulations, the volume fraction distribution showed that $0.1 < \phi < 0.7$. This indicates that all three granular flow regimes occur within this horizontal shear cell. The value of ϕ_{max} used in Equation 2.10 is also higher than shown in Figure 2.3.

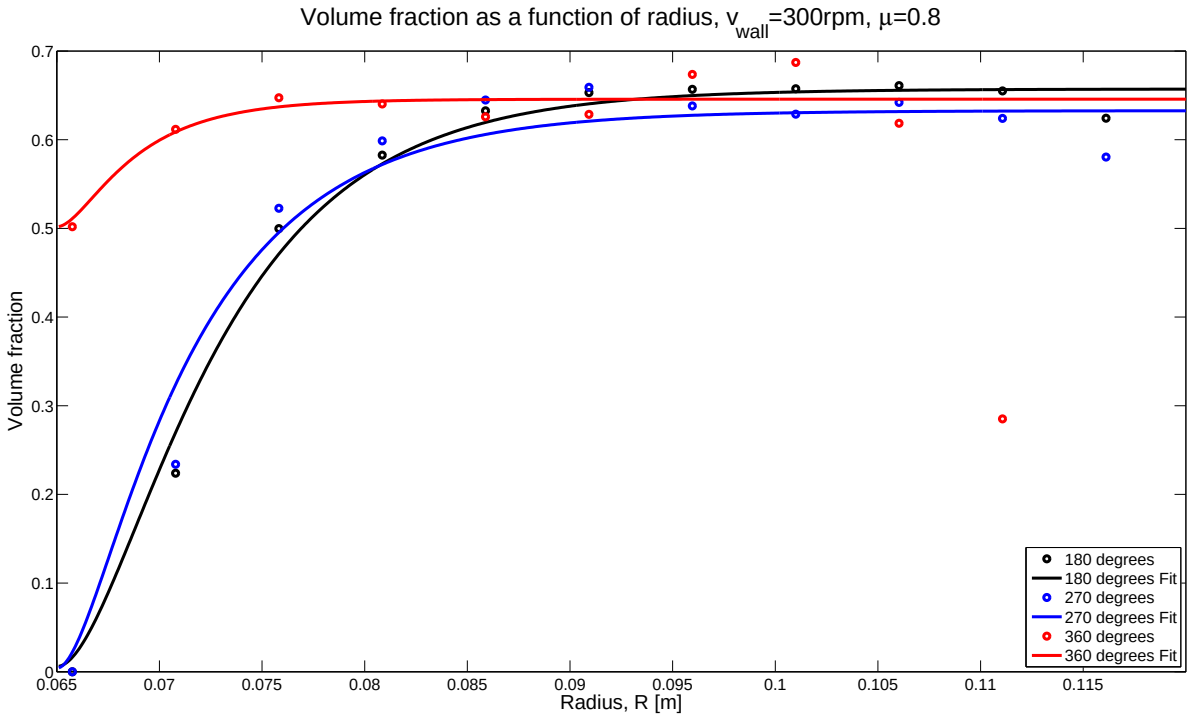

(a) Volume fraction in $v_{wall} = 300\,\mathrm{rpm}, \mu = 0.8$ configuration.

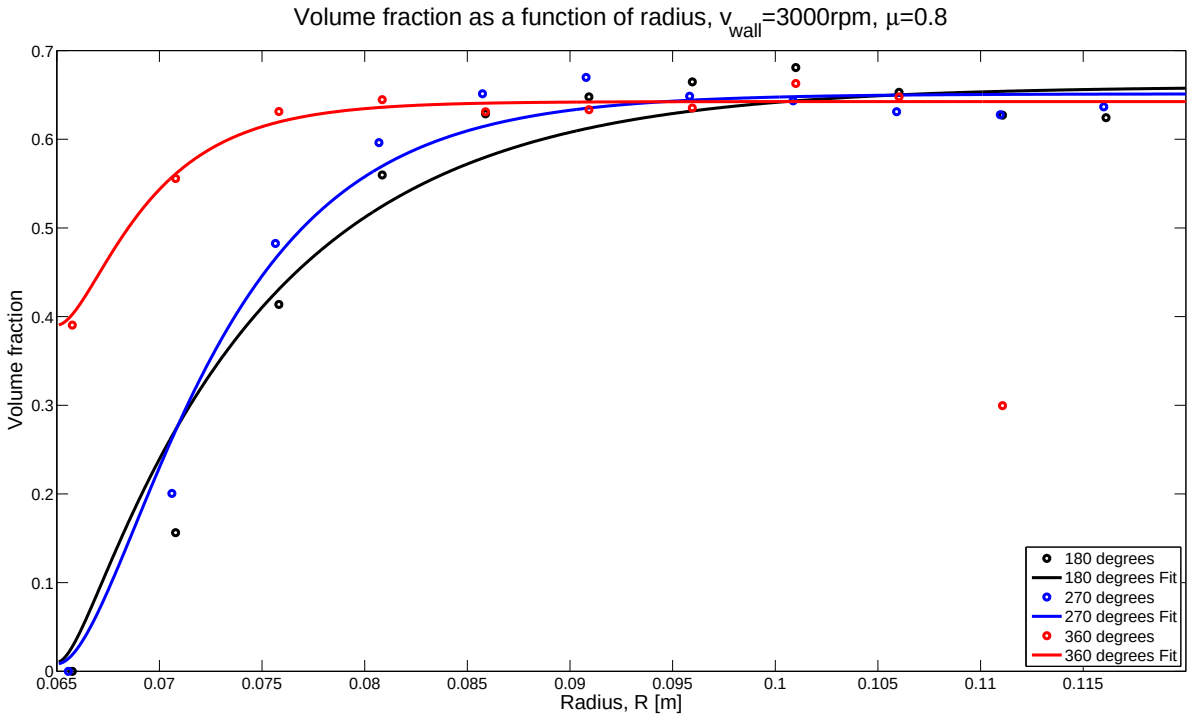

(b) Volume fraction in $v_{wall} = 3000\,\mathrm{rpm}, \mu = 0.8$ configuration.

Figure 5.15.: Volume fraction as a function of radius shown for a low and a high driving velocity, with function fit.

5.3.2. Velocity Analysis

The velocity components were binned using the same method as the position data, and then were averaged over the steady-state time. Thus two grids were created of average velocity in the $x-$ and $y-$directions. These velocity components were then converted to cylindrical coordinates, allowing analysis of the tangential and radial components. The velocity magnitudes for the lowest and highest driving wall velocity configurations are plotted in Figure 5.16. These values have been normalised by the maximum velocity in each configuration to allow comparison between the different simulations. The velocity magnitude distributions show that there is an anisotropy in the distribution. The velocity on the downward moving side is higher close to the rotating wall and drops off rapidly. The fall off on the upward moving side is much slower. This effect is more visible for the higher static friction coefficient and at lower driving wall velocities.

The total velocity vector plots shown in Figures 5.17 and 5.18 indicate that the velocity is mainly in the tangential direction. The asymmetry seen in the magnitude distribution plots is more obvious here. In the case of the lower driving wall velocities, there is more of a low velocity region on the side where material is moving against gravity (through the 360° line), while the downward side has a higher maximum velocity close to the driving wall, and a larger portion of the material is almost stationary. Figures 5.17a and 5.17b show the extreme case of this situation, while the effect is visible but not noteworthy in Figures 5.18a and 5.18b.

As the driving wall velocity is increased, the maximum velocity increases and the band of higher velocities spreads further out around the inner cylinder (as opposed to being localised on the downward moving side.) Figures 5.18c and 5.18d show the progression of this. The configuration at 3500 rpm and $\mu = 0.8$ (Figure 5.17d) has a much lower maximum material velocity than the same driving wall velocity and $\mu = 0.5$. It also has a larger asymmetry in maximum material velocity than in Figure 5.18d.

The tangential and radial velocities were selected in a line along 180°, 270° and 360°. The tangential velocity, normalised by the driving wall velocity, for each driving wall velocity and each angle is shown in Figure 5.19 as a function of number of particle diameters from the driving wall. The tangential velocities follow an exponential distribution at all three angles. The normalised distributions with higher driving wall velocity start at a lower velocity than the lower driving wall velocity distributions. This is opposite to the non-normalised distributions (shown in Figure 5.22 and 5.23), where the maximum velocity increases with driving wall velocity. This indicates that the higher

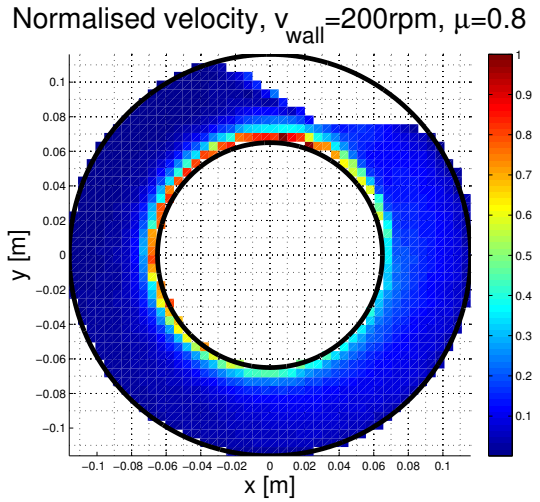

(a) $v_{wall} = 200\,\mathrm{rpm}$

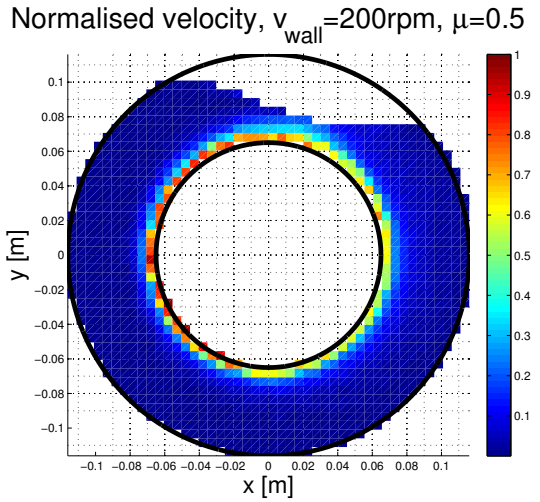

(b) $v_{wall} = 200\,\mathrm{rpm}$

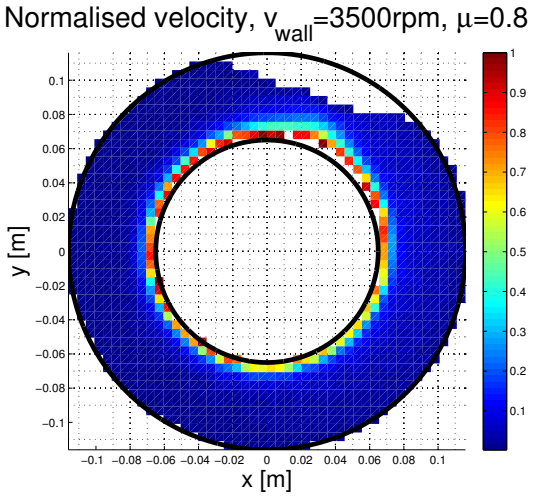

(c) $v_{wall} = 3500\,\mathrm{rpm}$

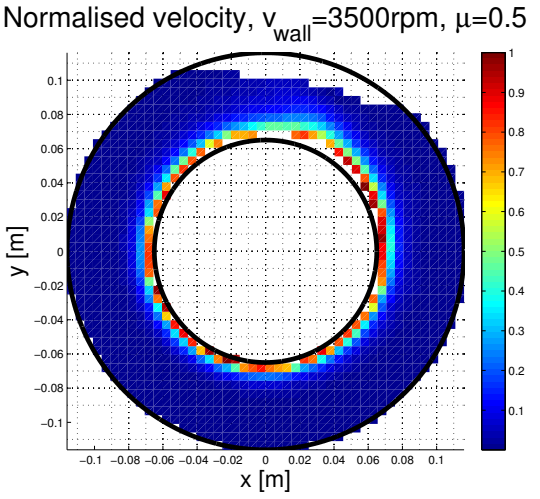

(d) $v_{wall} = 3500\,\mathrm{rpm}$

Figure 5.16.: Normalised velocity magnitude for the lowest and highest driving wall velocity, comparison for different surface friction of the particles.

driving wall velocity configurations experience a greater slip at the driving wall than the lower driving wall velocity configurations. As was noted in the vector plots, the velocities at a lower friction (dashed lines) are higher than those at the higher friction coefficient (solid lines). The tangential velocities all tend toward $0\,\mathrm{m\,s^{-1}}$ in the same radial region, around $R = 0.09\,\mathrm{m}$, which corresponds to 5 particle diameters from the rotating wall at 180°. The lower driving wall velocities for the $\mu = 0.8$ configurations at 270° and 360° remain non-zero throughout the shear space. The other configurations at those angles do tend toward zero, with the low velocity lower friction configurations taking longer to reach there than the rest.

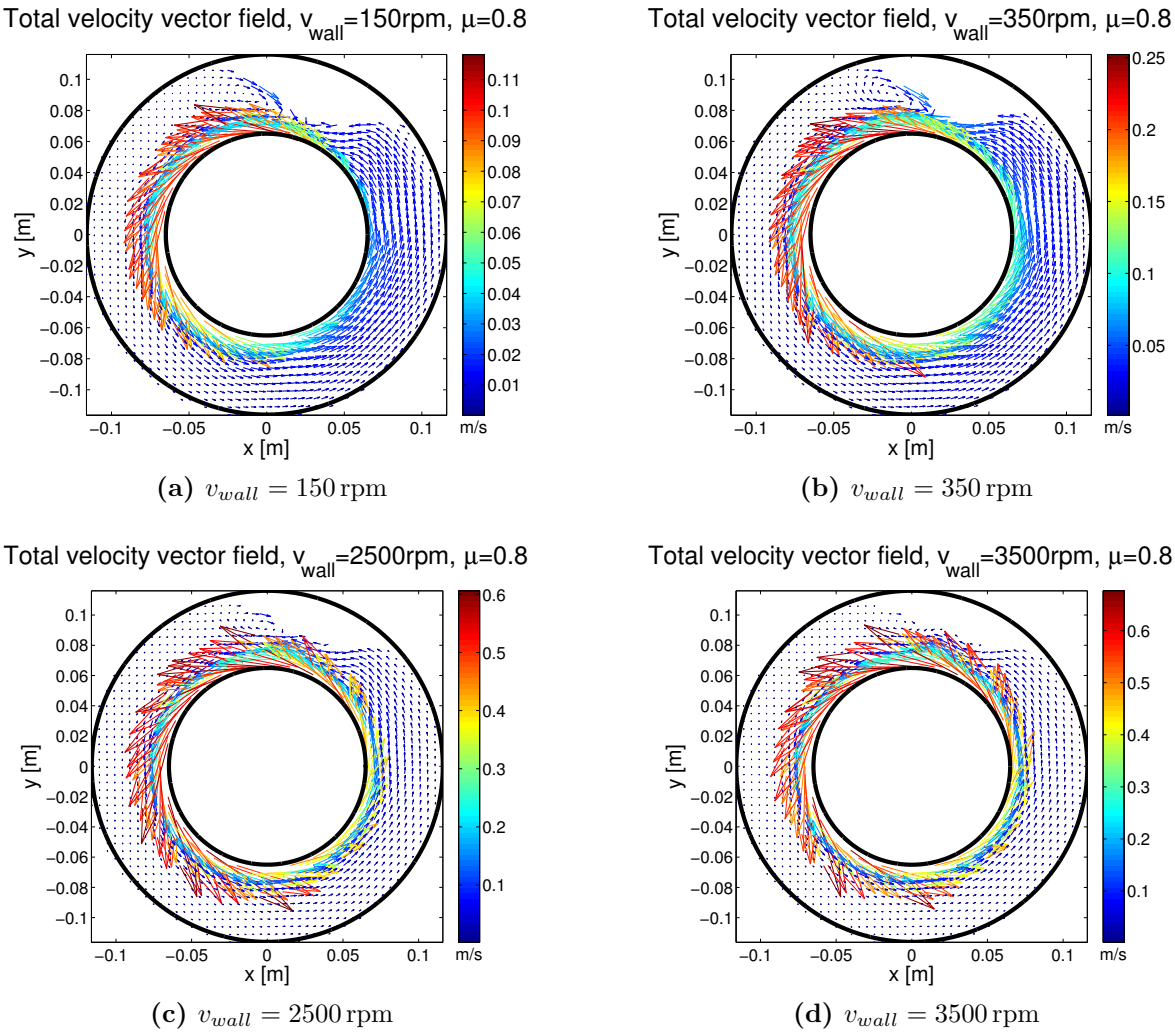

(a) $v_{wall} = 150\,\text{rpm}$ **(b)** $v_{wall} = 350\,\text{rpm}$

(c) $v_{wall} = 2500\,\text{rpm}$ **(d)** $v_{wall} = 3500\,\text{rpm}$

Figure 5.17.: Velocity vector field (higher friction condition).

The normalised radial velocities, shown in Figure 5.20, are negligible in comparison to the tangential velocities. The distribution is also a lot more haphazard, although they show a general decrease in magnitude with increase in distance from the shearing wall. The configurations with higher friction have a lower maximum radial velocity.

To explore the asymmetry of the velocity distributions, Figure 5.21 was plotted. These figures show both the radial and tangential components of the velocity at 3500 rpm and 200 rpm for all three angles, and both friction coefficients. The tangential velocity in all cases is very much larger than the radial velocity. The velocity at 180° is generally higher than that at 360° for the inner part of the system, while the velocity distributions at 270° and 360° have more of a non-zero tail. This effect is much more visible in the cases that have a higher friction coefficient and lower driving wall velocity (solid lines in Figure 5.21b). There is a bigger difference between the velocities at 180° and 270°

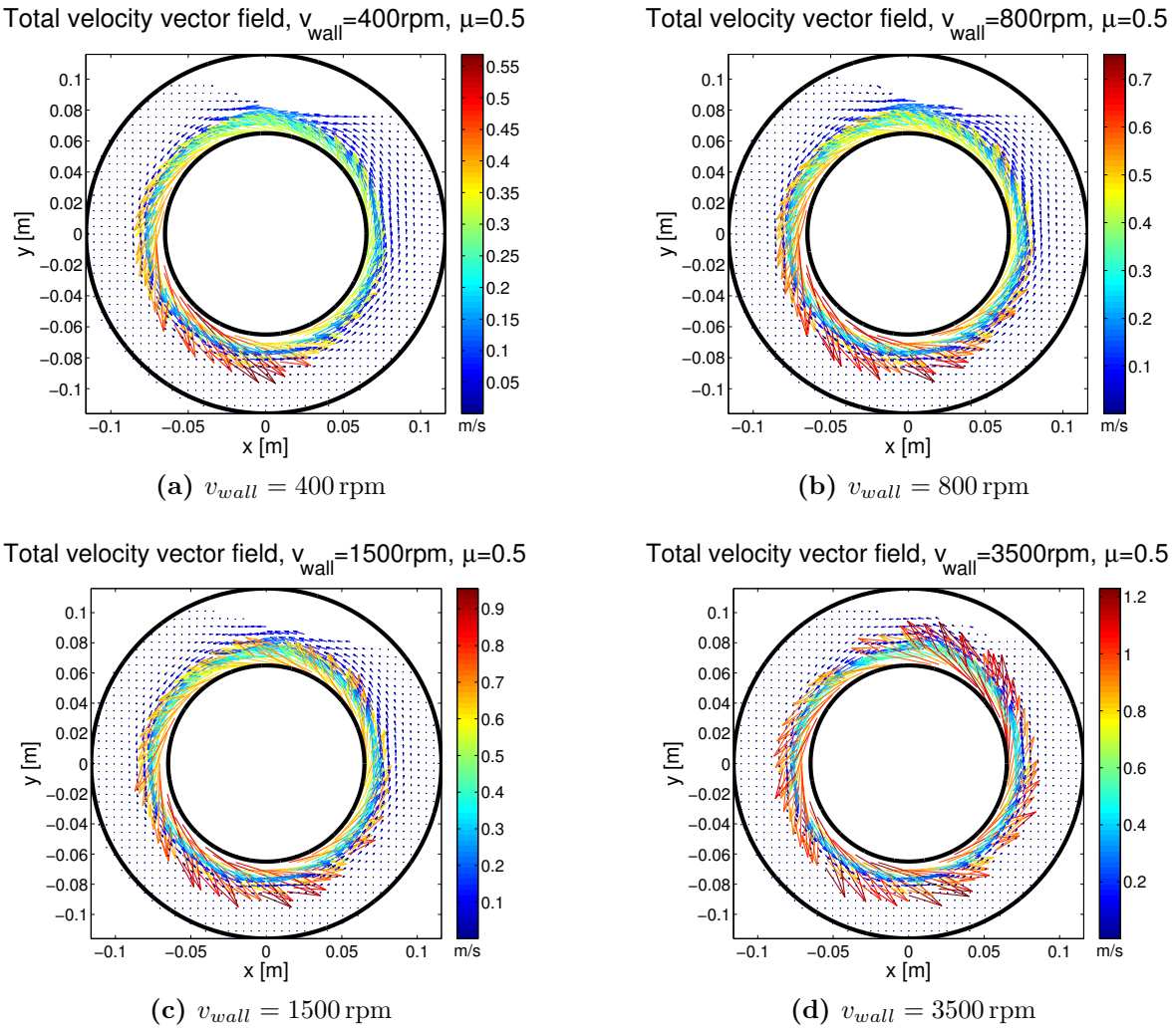

(a) $v_{wall} = 400\,\mathrm{rpm}$ **(b)** $v_{wall} = 800\,\mathrm{rpm}$

(c) $v_{wall} = 1500\,\mathrm{rpm}$ **(d)** $v_{wall} = 3500\,\mathrm{rpm}$

Figure 5.18.: Velocity vector field (lower friction condition).

in the 3500 rpm, $\mu = 0.8$ configurations than the $\mu = 0.5$ configurations. In all cases shown here, the 360° velocity selection starts at the driving wall, with the others only having data starting 1 particle diameter away from the wall. This is due to the binning algorithm, which shifts the centres of particles to the left edge of the bin.

To calculate the shear rate, an exponential function, with the form $v_\theta = Ae^{Br}$, was fit to the tangential velocity, as it is not possible to take the derivative of discrete data. These function fits are shown in Figures 5.22 and 5.23.

These fits were weighted using a weighting factor of $1/\sigma^2$, thus the data points with the greatest standard deviations had the lowest weighting. As the variation of velocity with time was greatest closest in to the driving wall, these data points often had the lowest weightings and were thus considered less important in the fit. The range of data

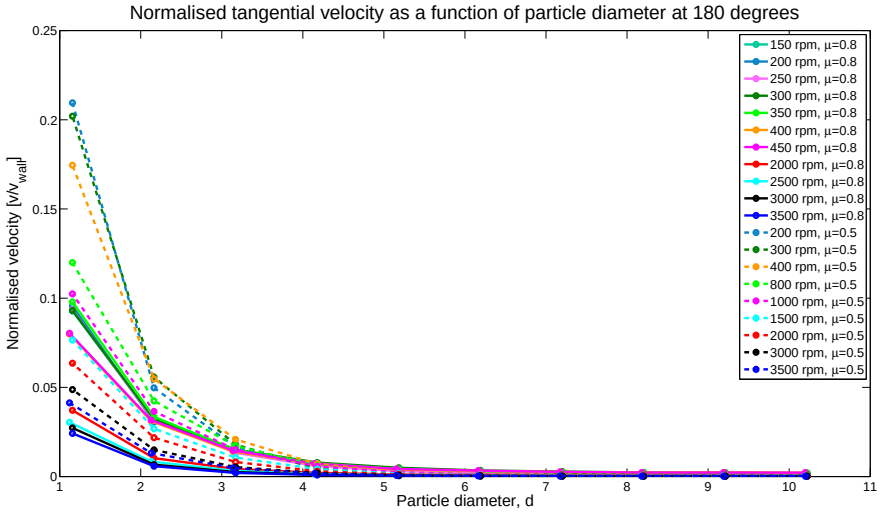

(a) Normalised tangential velocity at 180°.

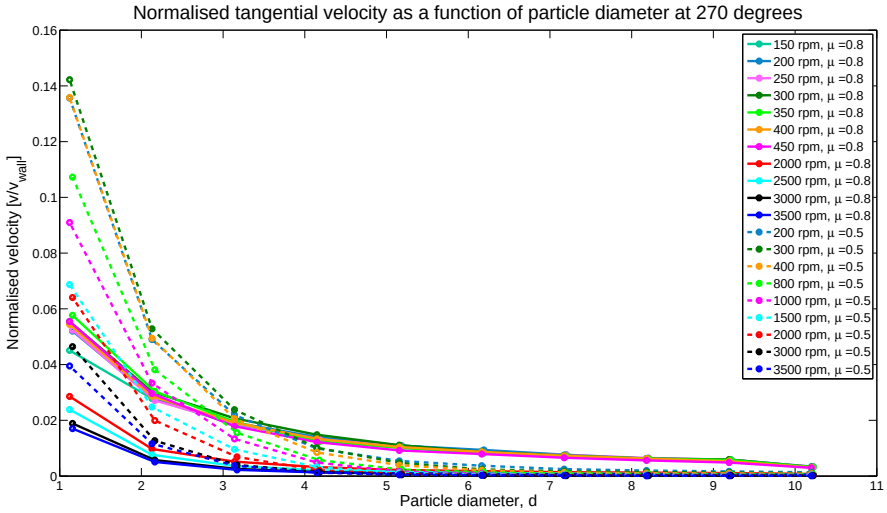

(b) Normalised tangential velocity at 270°.

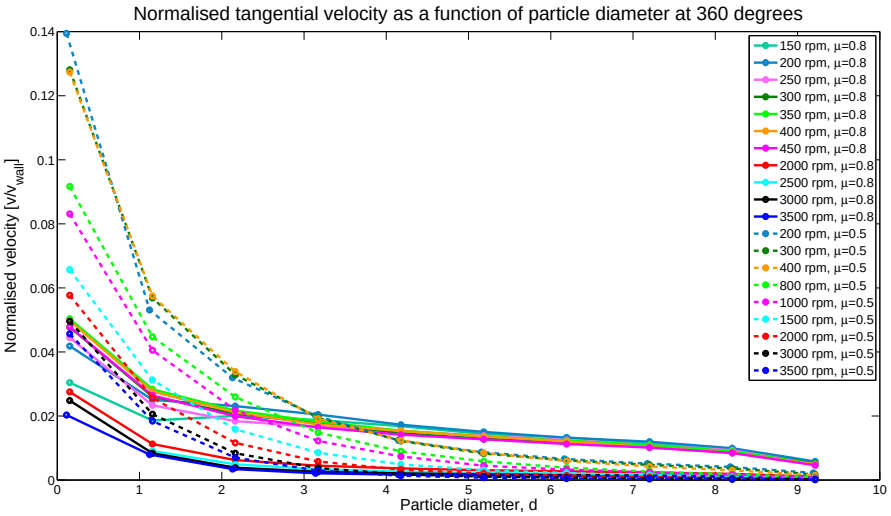

(c) Normalised tangential velocity at 360°.

Figure 5.19.: Normalised tangential velocity as a function of radius, showing both static friction coefficients.

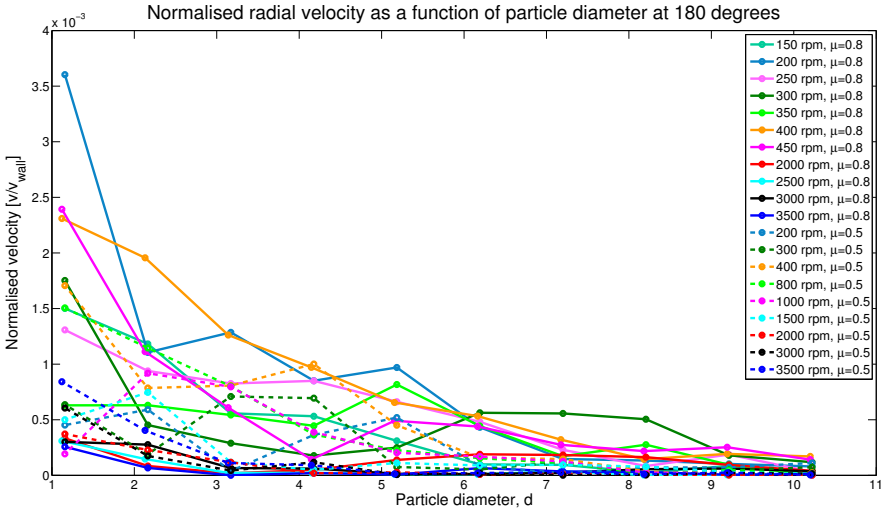

(a) Normalised radial velocity at 180°.

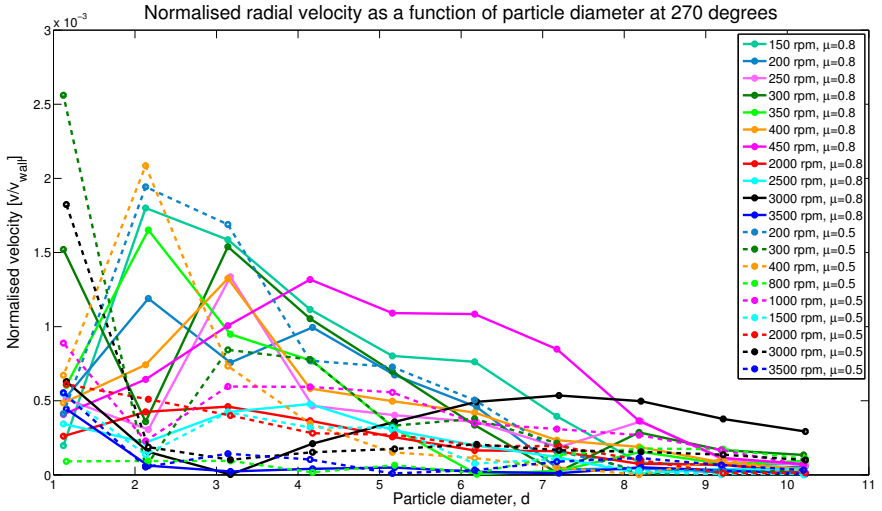

(b) Normalised radial velocity at 270°.

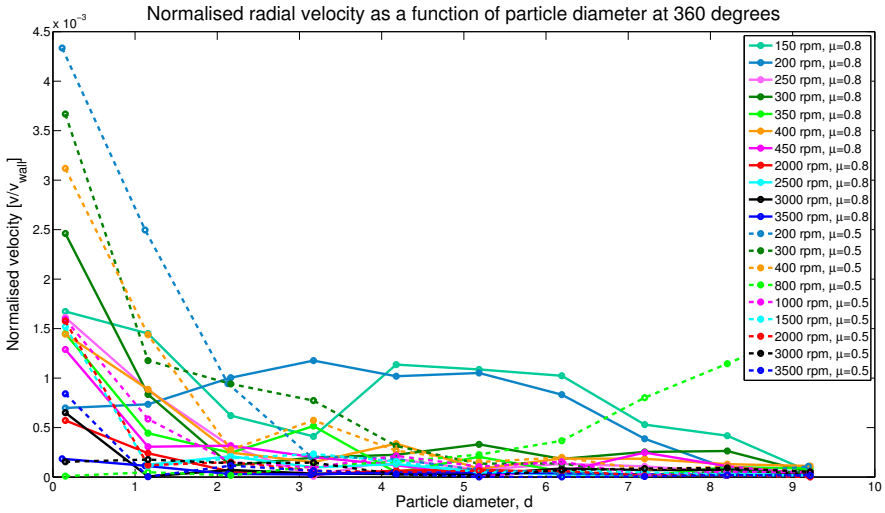

(c) Normalised radial velocity at 360°.

Figure 5.20.: Normalised radial velocity as a function of radius, for all driving wall velocities and both friction coefficients.

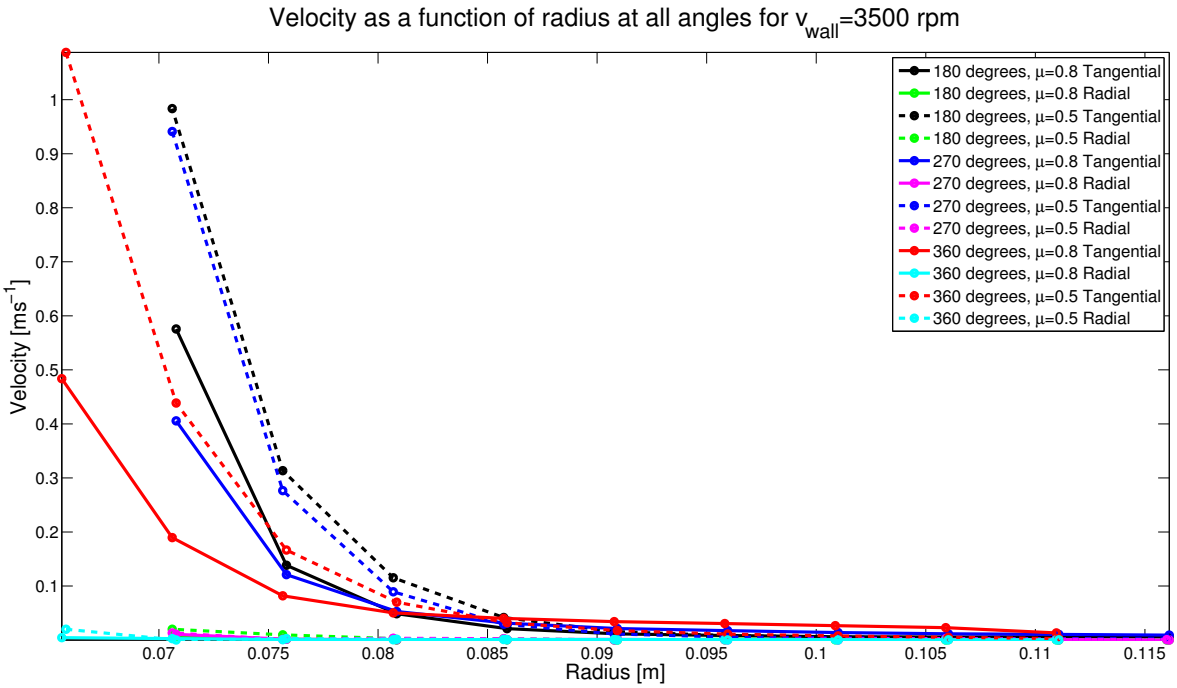

(a) Tangential and radial velocities at $v_{wall} = 3500\,\text{rpm}$.

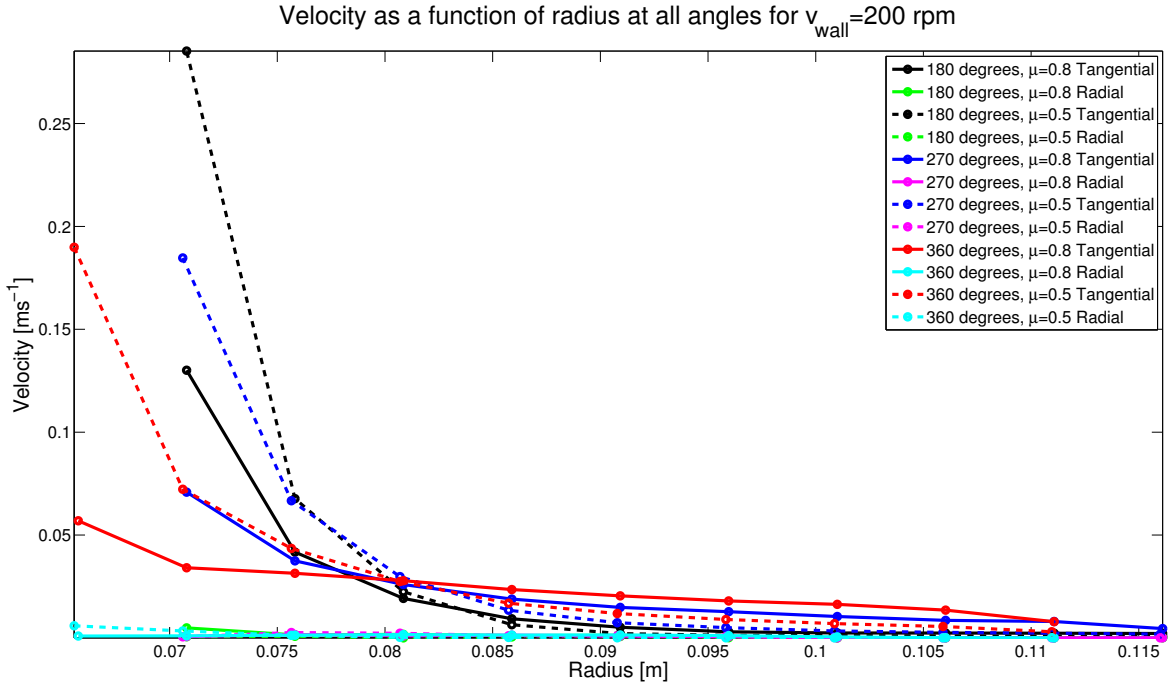

(b) Tangential and radial velocities at $v_{wall} = 200\,\text{rpm}$.

Figure 5.21.: Velocity as a function of radius; comparison at 180°, 270° and 360°.

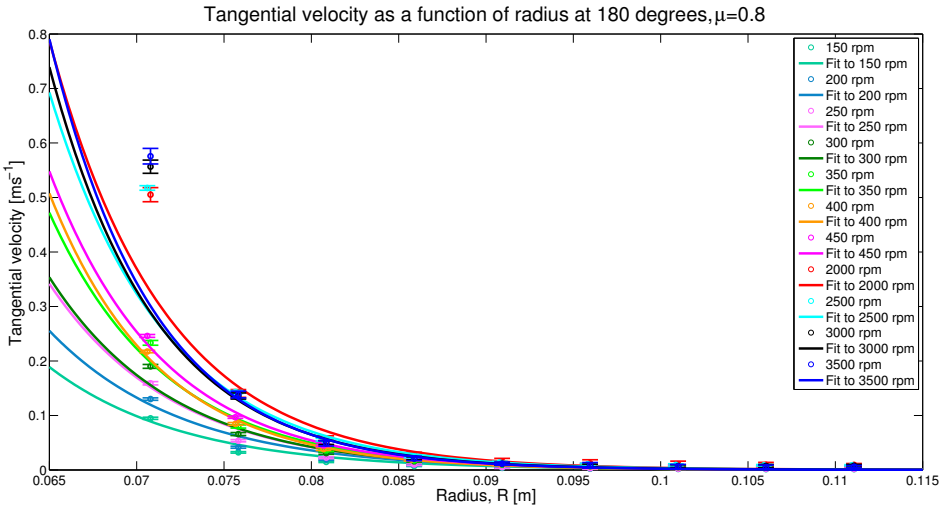

(a) Exponential fit to tangential velocity at 180°.

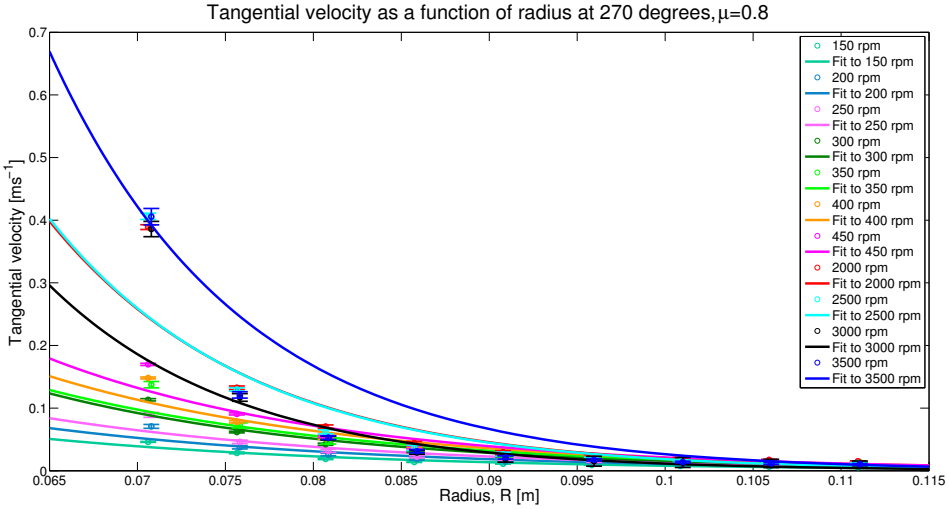

(b) Exponential fit to tangential velocity at 270°.

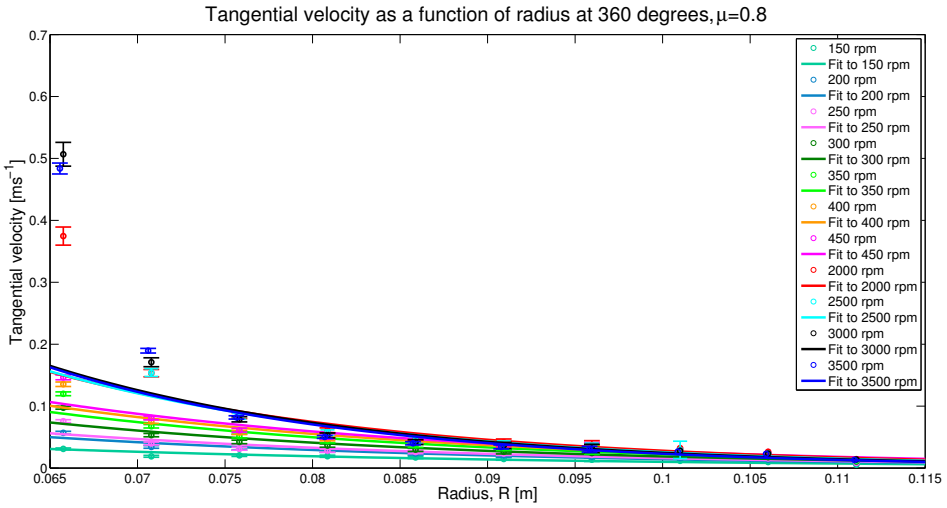

(c) Exponential fit to tangential velocity at 360°.

Figure 5.22.: Tangential velocity as a function of radius with exponential fit at 180°, 270° and 360°, $\mu = 0.8$.

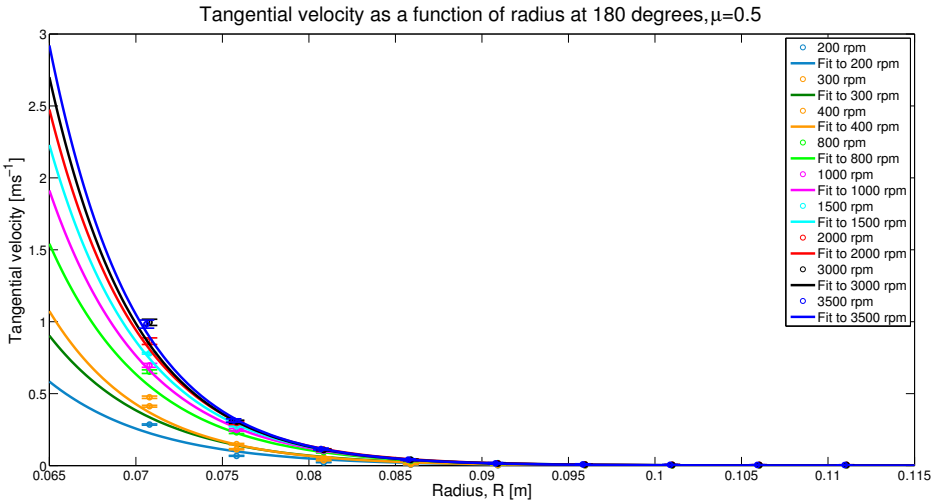

(a) Exponential fit to tangential velocity at 180°.

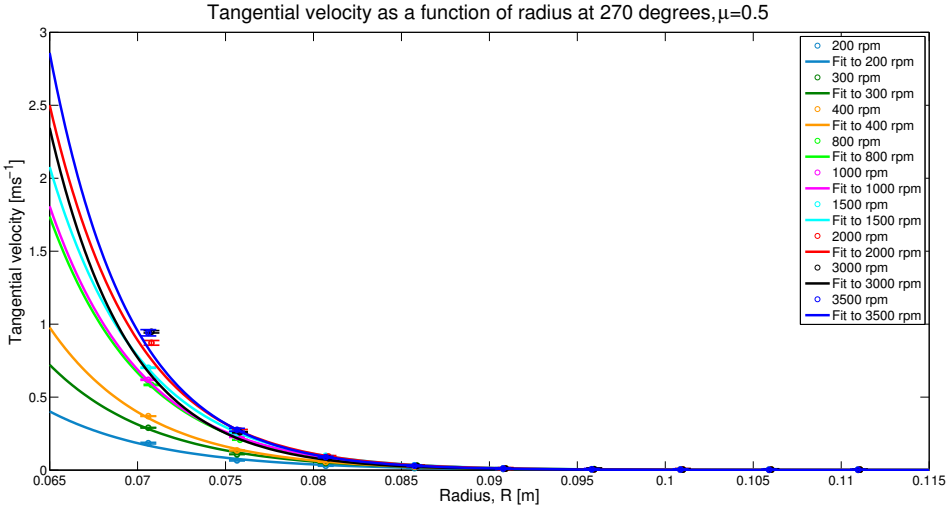

(b) Exponential fit to tangential velocity at 270°.

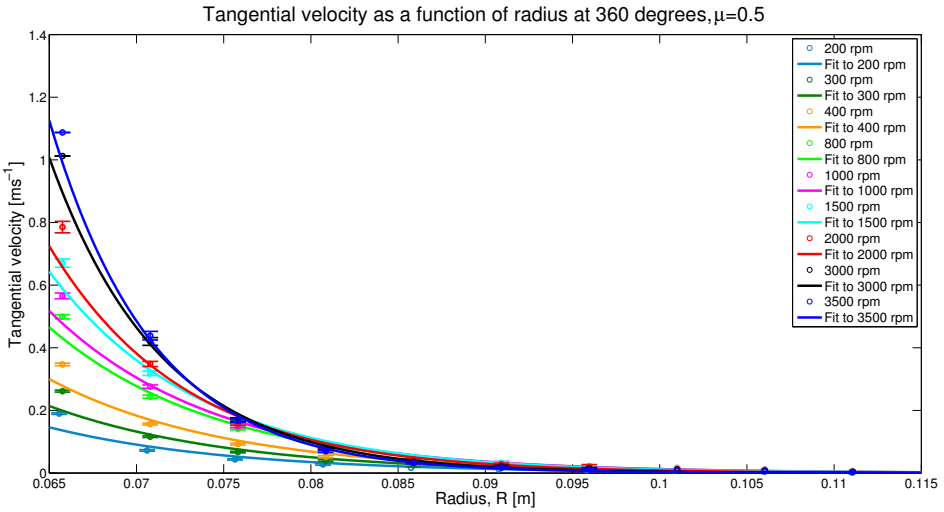

(c) Exponential fit to tangential velocity at 360°.

Figure 5.23.: Tangential velocity as a function of radius with exponential fit at 180°, 270° and 360°, $\mu = 0.5$

for the 180° and 270° angles is the same as the volume fraction data at those angles, 0.07 m to 0.111 m, thus the distribution closer in to the driving wall is an extrapolation beyond the range of the data and should be treated with caution.

The fit coefficients were plotted as a function of velocity, for all angles, in Figure 5.24. The A coefficient is the tangential velocity at the centre of the system, while the B fit coefficient can be considered to be a distance scaling parameter, $1/r_0$, a natural length scale in each configuration. A, shown in Figure 5.24a on a logarithmic scale, increases almost linearly with driving wall velocity. The green dashed line is a reference line, showing the shape of a graph where $x = y$. In the $\mu = 0.8$ configurations, the largest coefficients are at 180°, the middle at 270° and the lowest at 360°, indicating the general trend of maximum material velocity occurring on the downward moving side of the system. The $\mu = 0.5$ configurations have a similar coefficient at 180° and 270°, with 360° also the smallest.

The absolute value of the inverse of B, in Figure 5.24b, shows the change of the natural length scale of the system with velocity, angle and friction. The lower driving wall velocity configurations have a larger length scale than the higher configurations. This length scale gradually decreases as the driving wall velocity increases, except for the 180° angle and the 270° in the $\mu = 0.5$ configurations, which remain mostly constant, close to one particle diameter.

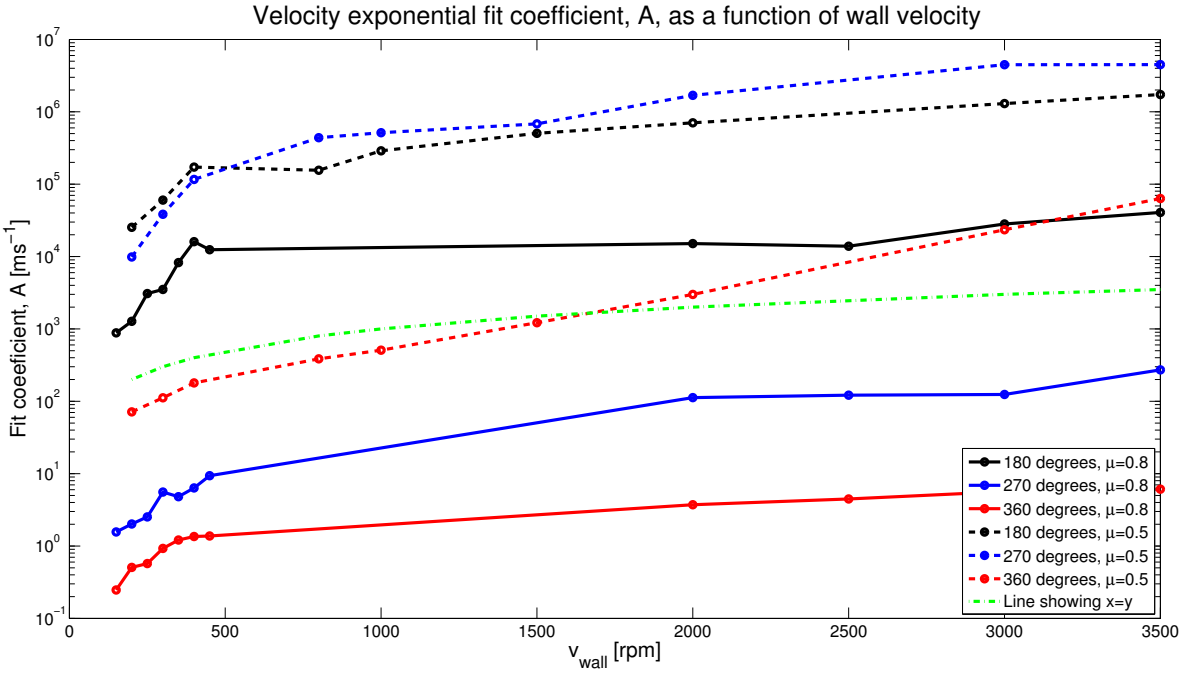

(a) A, a proxy for the velocity at the shearing wall.

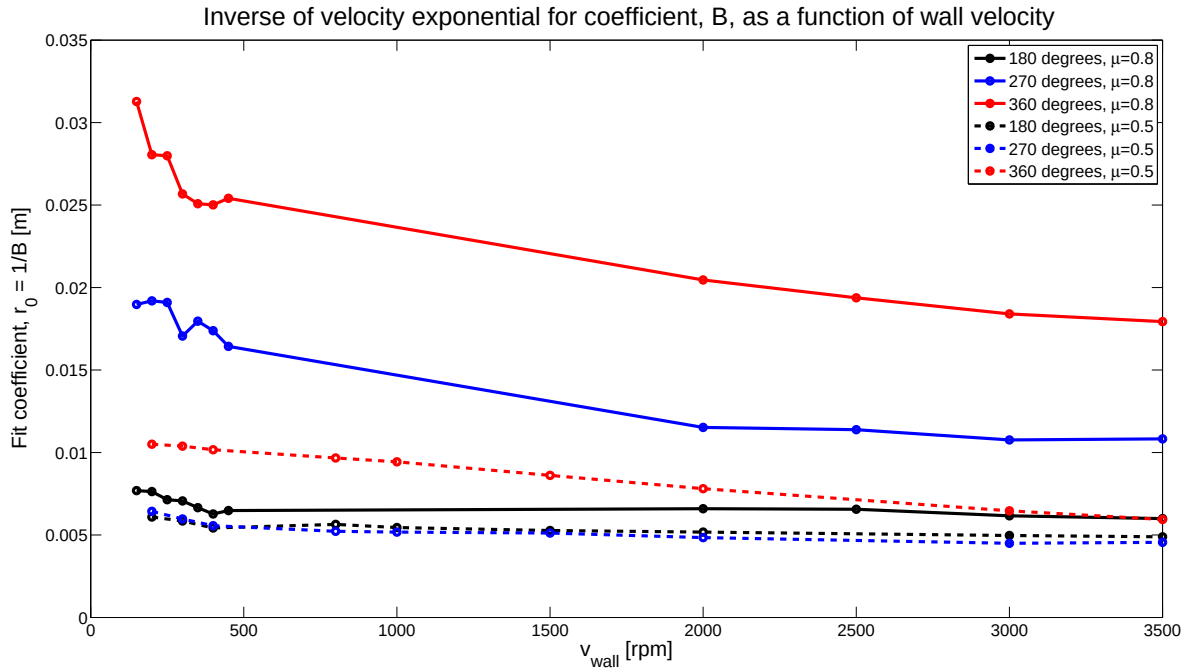

(b) $r_0 = 1/B$, the natural length scale in the shear cell.

Figure 5.24.: Velocity fit coefficients as a function of velocity.

5.3.3. Inertial Number and Shear Rate

The shear rate for each configuration was determined by taking the derivative of the function fit to the tangential velocity distributions. The absolute values of these are shown in Figures 5.25 and 5.26. The data for 180° and 270° range from 0.07 m to 0.115 m, while the distribution at 360° ranges from 0.065 m to 0.110 m. Thus, for all calculations that follow, these ranges were carried through. The reason for the asymmetry in the radial values is due to the binning of a circular system into a square grid and the offset created by the unevenness therein. The binning algorithm also moved all particle centres contained in the bin, to the left. Graphs that go beyond these limits are thus an extrapolation using the form of the functions fit to the data.

The shear rates shown in Figure 5.25 show an increase in maximum value with increasing driving wall velocity, although the shear rate calculated at 2000 rpm in Figure 5.25a (the distribution at 180° with $\mu = 0.8$) is the maximum for most of the radial range, except close to the driving wall. The distributions at 270° and 360° (Figures 5.25b and 5.25c) also show the increase with driving wall velocity. The maximum shear rates achieved in the higher friction configuration is close to $58\,s^{-1}$ for 3500 rpm at 180°, with the values for the 360° distributions are all under $9\,s^{-1}$. The distributions tend to zero towards the outer edge of the shear cell. At 180° the radial value corresponding to the minimum shear rate is between 0.095 m and 0.105 m (between 6 and 8 particle diameters) for all driving wall velocities. The shear rates at 270° converge towards zero at the outer wall, while those at 360° are non-zero at the outer wall of the shear cell. Thus the width of the shear band in the $\mu = 0.8$ configurations does not depend on driving wall velocity, but does differ with the angle under consideration.

The shear rates in the lower friction configurations are shown in Figure 5.26. These distributions also follow the trend of increasing maximum shear rate with increasing driving wall velocity. Once again, the only function that breaks that trend is 2000 rpm, this time at 270°. The maximum values are higher than they are at $\mu = 0.8$, with the maximum being close to $220\,s^{-1}$. The shear rates in the $\mu = 0.5$ configuration also tend towards zero as the distance from the driving wall increases, although the width of the shear band in these configurations is much less. The difference in the shear band width with angle is also less noticeable, with the width being close to 0.03 m or 6 particle diameters for all three angles.

A graph of shear band width as a function of angle and friction is shown in Figure 5.27. As the shear rate approaches but is never 0, the radial point at which the shear rate

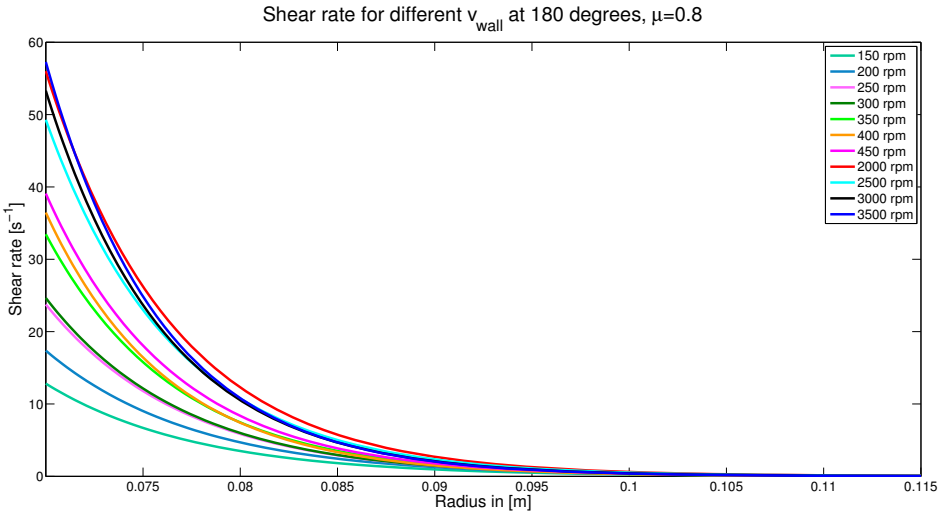

(a) Shear rate at 180°.

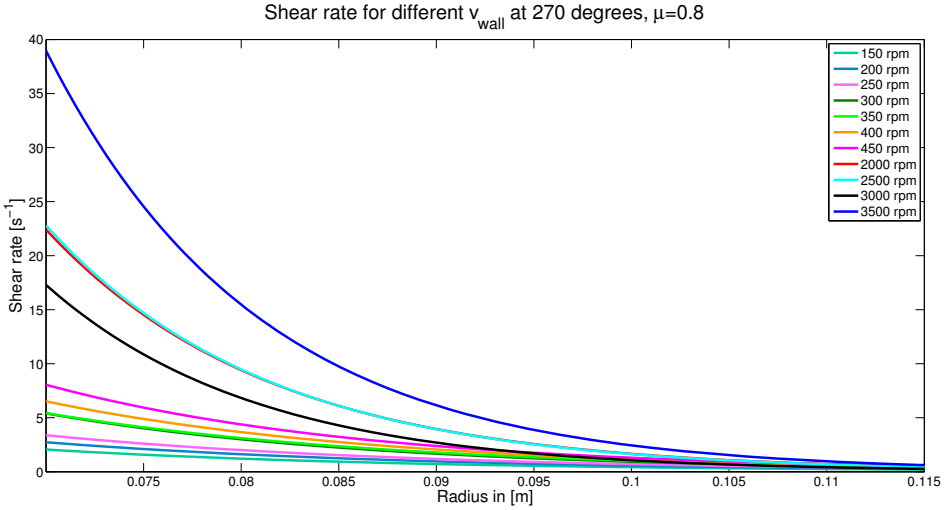

(b) Shear rate at 270°.

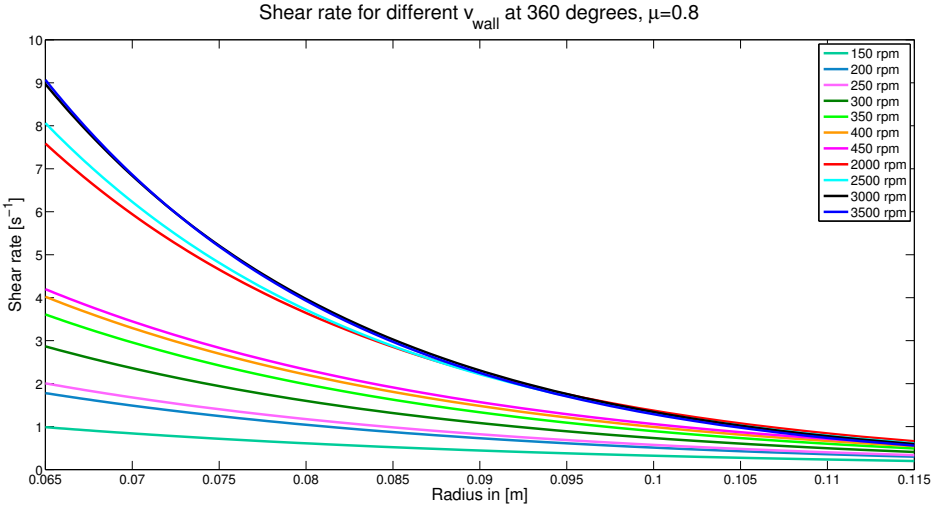

(c) Shear rate at 360°.

Figure 5.25.: Shear rate at 180°, 270° and 360°, $\mu = 0.8$

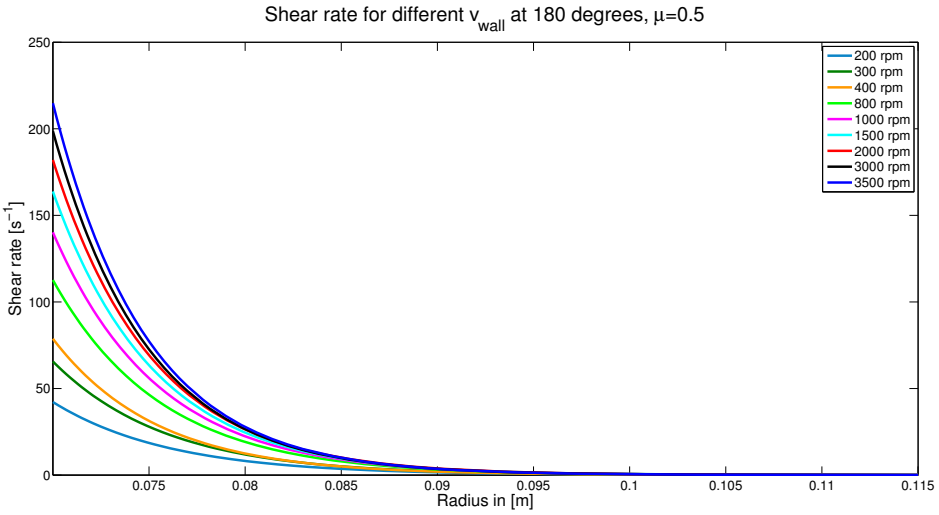

(a) Shear rate at 180°.

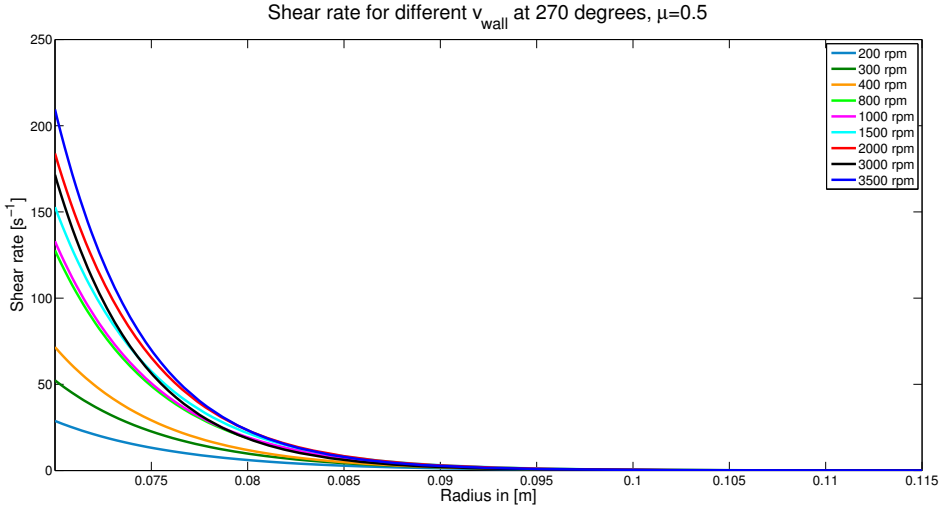

(b) Shear rate at 270°.

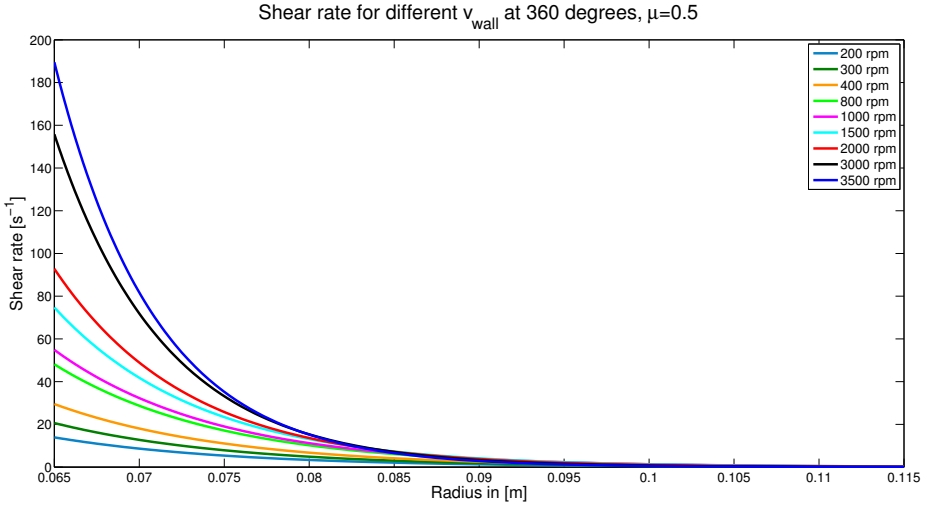

(c) Shear rate at 360°.

Figure 5.26.: Shear rate at 180°, 270° and 360°, $\mu = 0.5$

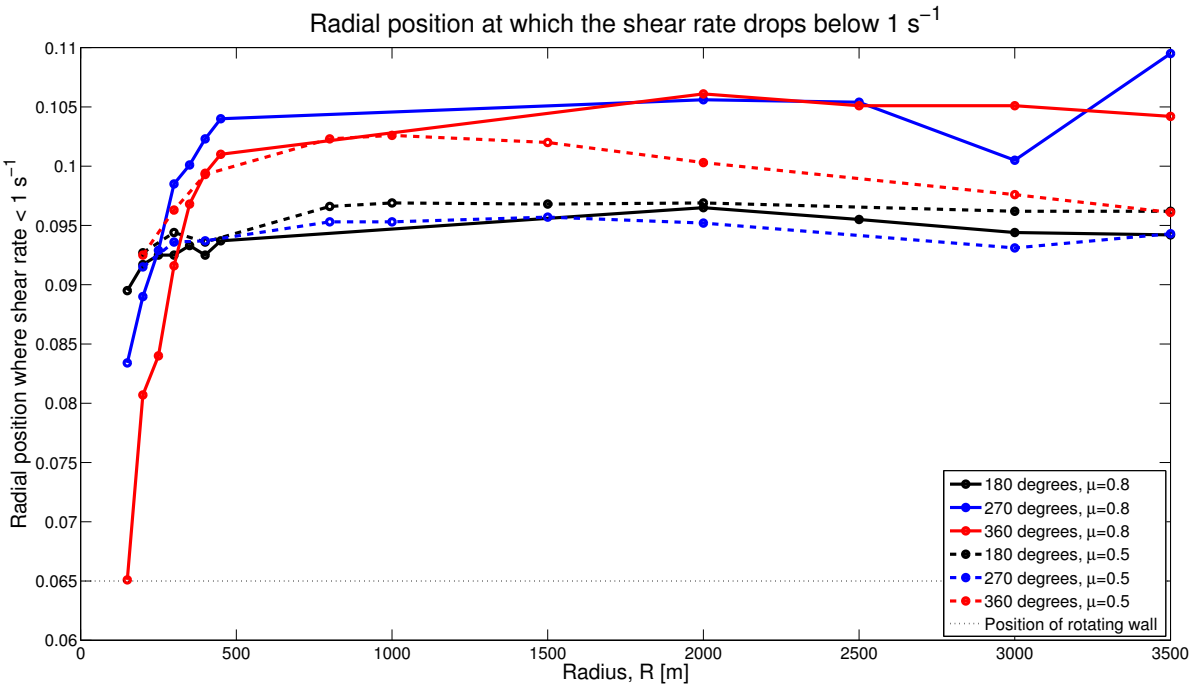

Figure 5.27.: The radial position at which the shear rate drops below $1\,s^{-1}$, an indication of shear band thickness.

drops below $1\,s^{-1}$ is considered. The graph shows the independence of the width of the shear band thickness on the driving wall velocity, once the driving wall velocity has increased beyond a point. There is a much greater change in shear band thickness at lower driving wall velocities in the $\mu = 0.8$ configurations at 270° and 360° (blue and red solid lines). At higher driving wall velocities, the distributions all show an almost constant shear band thickness, except for the $\mu = 0.5$, 360° (red dashed line) distribution, which decreases with increasing velocity. There is also a clear difference between the shear band thickness for different angles and friction coefficients. The position of the driving wall is shown in this figure as the black dashed line for reference.

The inertial number was calculated by rearranging Equation 2.10, with initial values stated in Chapter 2. The inertial number was calculated at discrete points corresponding to the data points of the volume fraction and velocity, using the initial values for b and c. As there is scatter in the data, the equation for I was then fitted to these data points, using b and c as fitting parameters. The resulting fit was then used in the further calculations for pressure, shear stress and power dissipation.

The initial inertial number distributions from the data points are shown in Figures 5.28 and 5.29, with the function fits shown in Figures 5.30 and 5.31. As expected, the inertial number is initially high, close to the driving wall, falling off rapidly as the shear rate drops

off. There is a general increase of inertial number with driving wall velocity, although there are fluctuations between velocities that are close together. The distributions at 180° and $\mu = 0.8$ in Figure 5.28a and at 270° in Figure 5.28b are clumped together in two groups - high and low driving wall velocities, close to the inner wall. All the distributions tend to very small I further away from the driving wall. The distributions shown in Figure 5.28c (360° and $\mu = 0.8$) have much more variation between the velocities, also covering a much smaller range of I.

The inertial numbers for the lower friction configurations also follow the trend of increasing magnitude with increasing velocity, although there are some fluctuations in this too. The maximum values at each angle shown in Figure 5.29 are more spread out than the $\mu = 0.8$ configurations, with the maximum values generally higher. The distribution at 360° (Figure 5.29c) covers a smaller range of I, thus the behaviour as the distributions tend towards zero is more easily seen. The inertial number is never exactly 0, but it does get very small.

The fitted distributions are shown in Figures 5.30 and 5.31. These were created by fitting the rearranged function in Equation 2.10, using b and c as fitting parameters. The distributions are not wholly different from the data point distributions.

A graph of the parameters appears in Figure 5.32. There appears to be no relation between the parameters and velocity or friction coefficient. The b values range between 0.8 and 4.5, with the majority in the range 1.25-2. The fit for the lower driving wall velocities at 270° and $\mu = 0.8$ resulted in b values that were higher than the other configurations. In Figure 5.32b the spread of the c values is similar, with the values in the range between 0.35 and 0.8. A large portion of values are between 0.5 and 0.65, with the 270°, $\mu = 0.8$ low driving wall velocity values once again being higher than the rest.

The range of inertial numbers covered in these distributions indicate that all three granular flow regimes are present in the horizontal annular shear cell. The turbulent regime is close to the shearing wall, and usually only extends to 2 particle diameters from the shearing wall. The dense flow regime width varies with the different configurations, but it also averages approximately 2 particle diameters wide. The quasi-static regime extends for more than half of the annulus width in most of the cases studied.

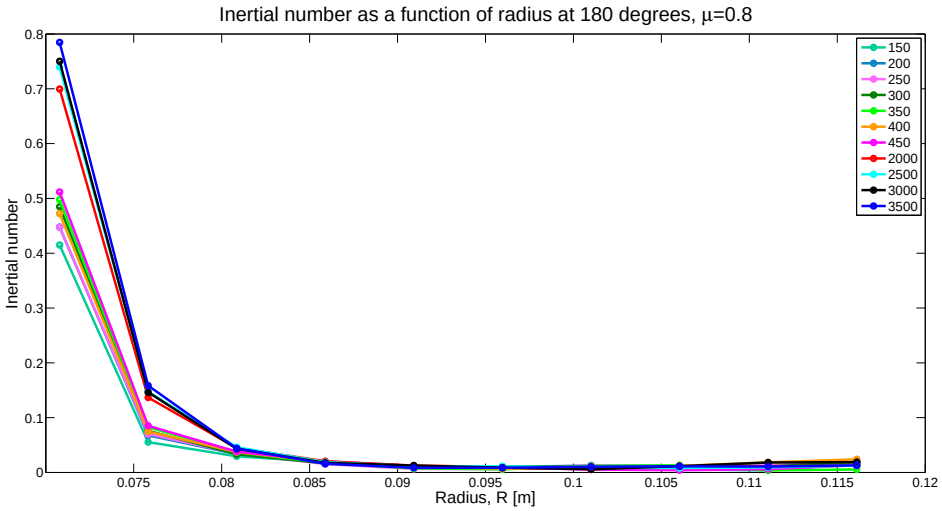

(a) Inertial number at 180°.

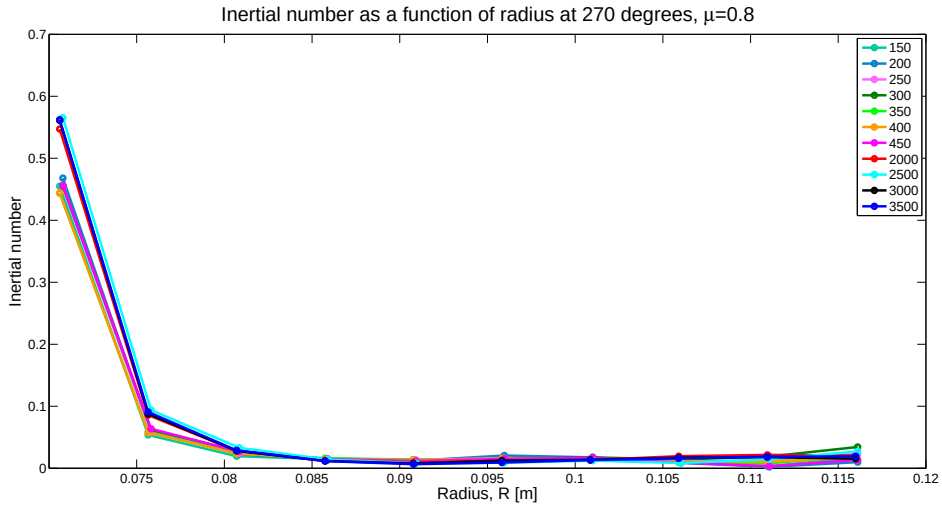

(b) Inertial number at 270°.

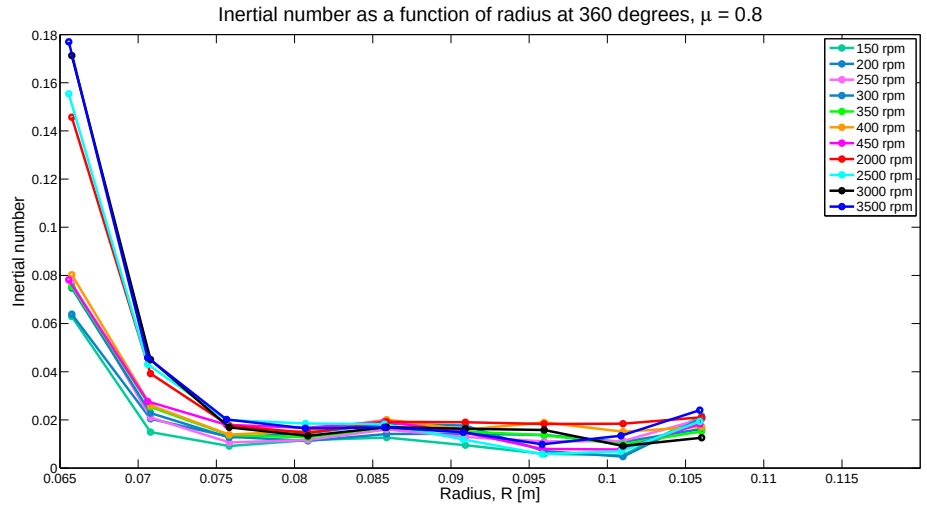

(c) Inertial number at 360°.

Figure 5.28.: Inertial number at 180°, 270° and 360°, $\mu = 0.8$, using the initial values before the fit.

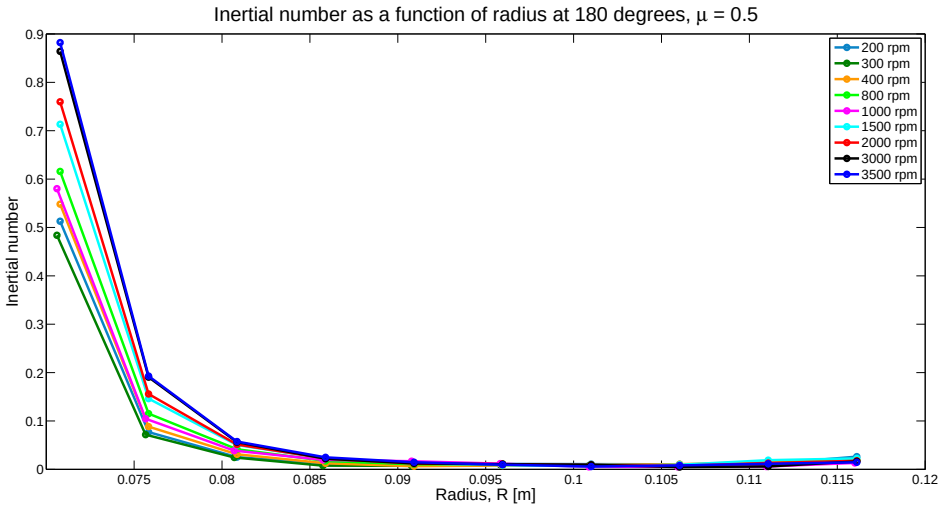

(a) Inertial number at 180°.

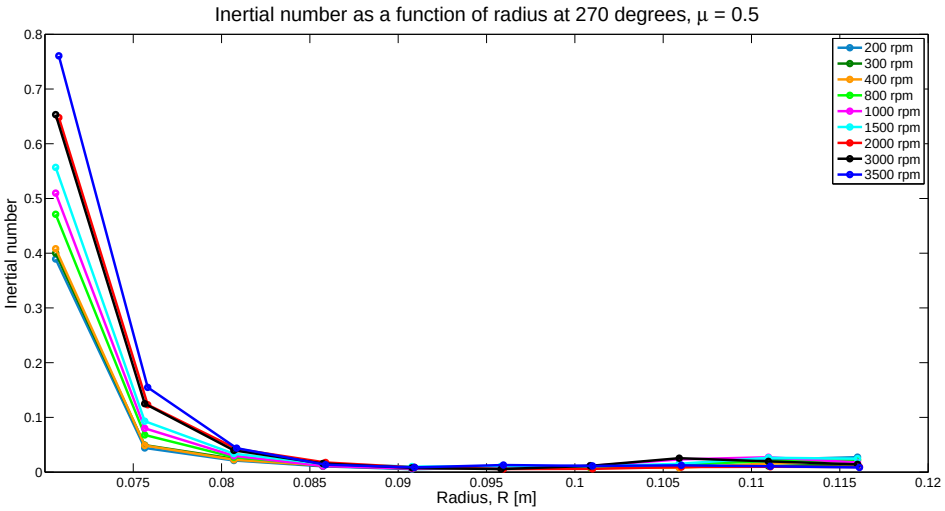

(b) Inertial number at 270°.

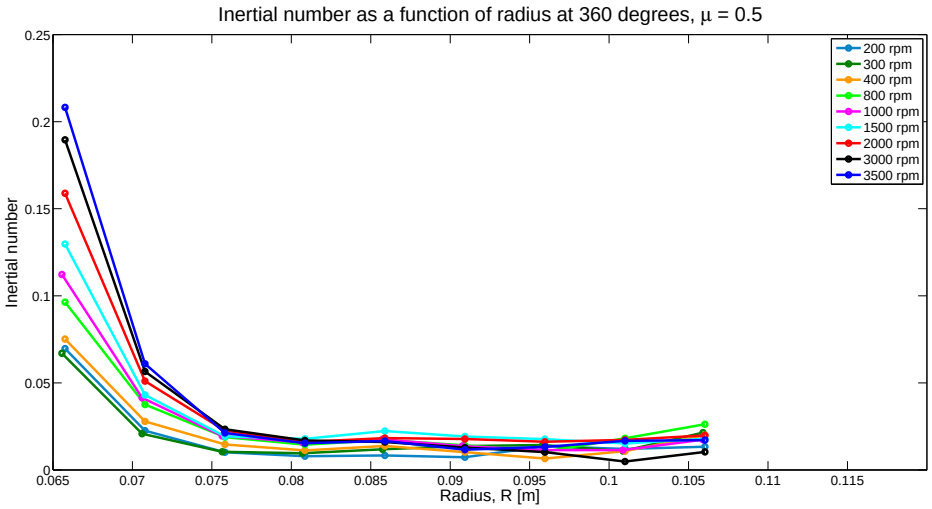

(c) Inertial number at 360°.

Figure 5.29.: Inertial number at 180°, 270° and 360°, $\mu = 0.5$, using the initial values before the fit.

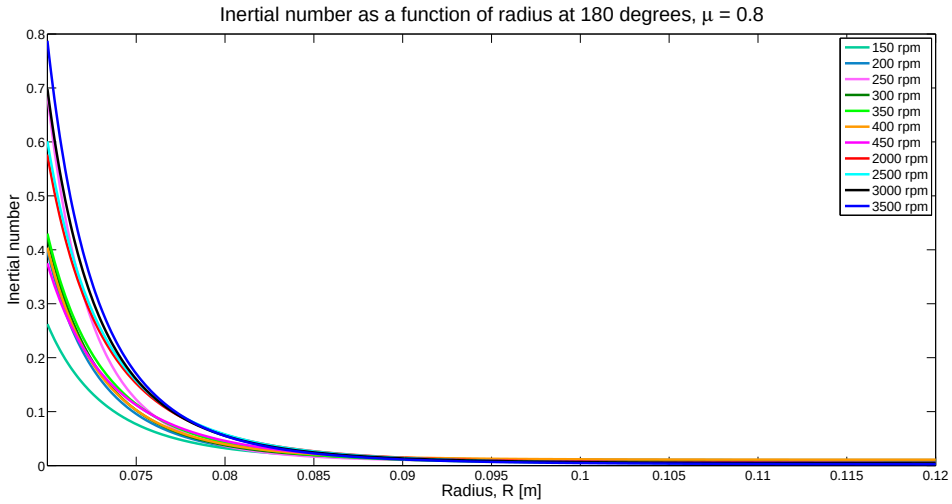

(a) Inertial number at 180°.

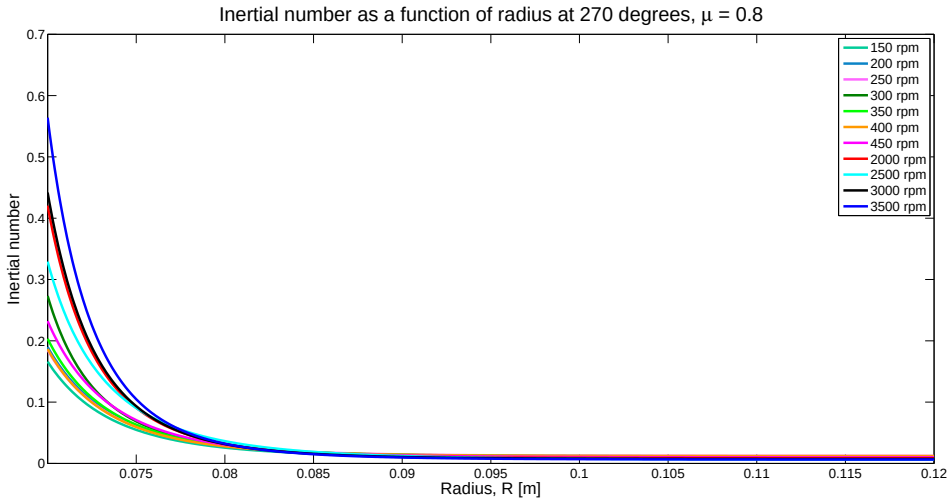

(b) Inertial number at 270°.

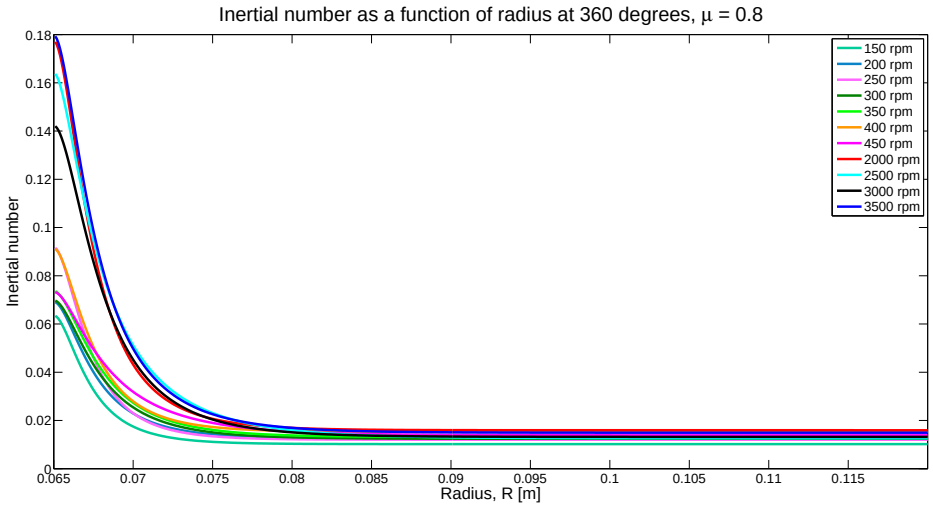

(c) Inertial number at 360°.

Figure 5.30.: Inertial number at 180°, 270° and 360°, $\mu = 0.8$, using the fit.

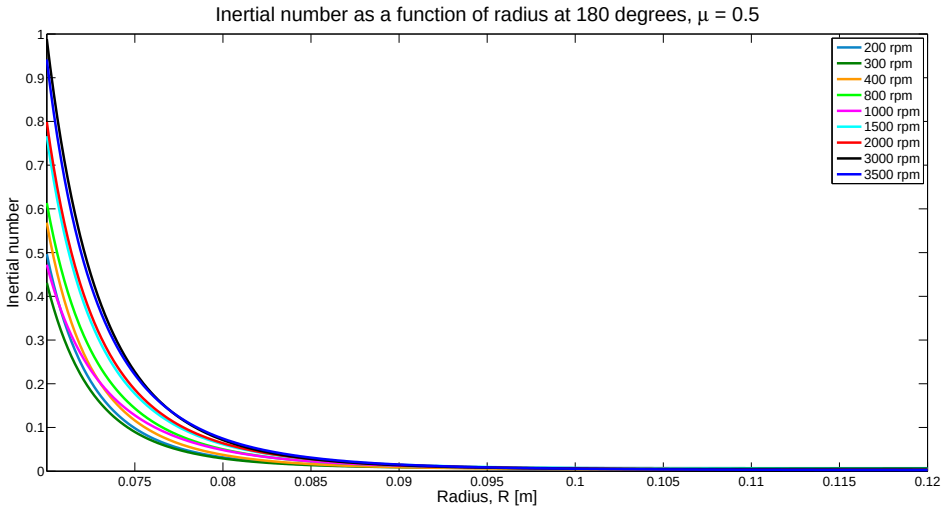

(a) Inertial number at 180°.

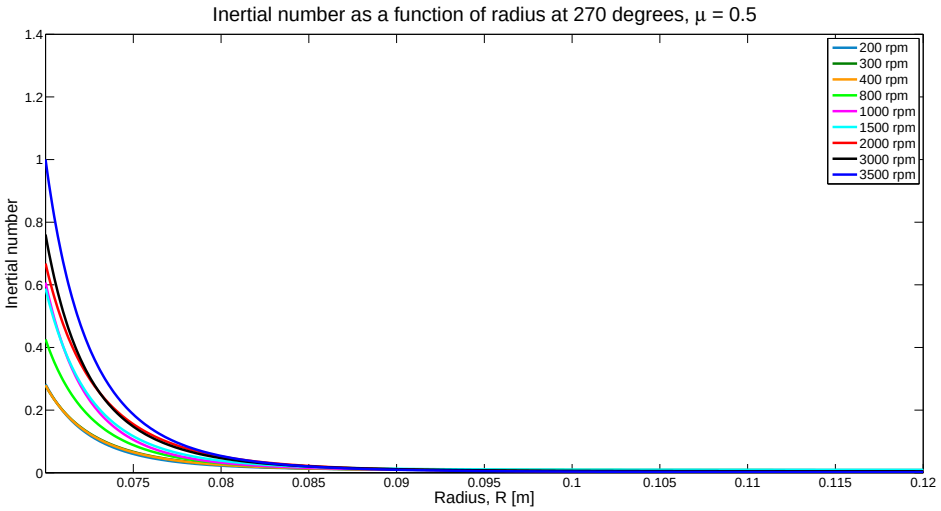

(b) Inertial number at 270°.

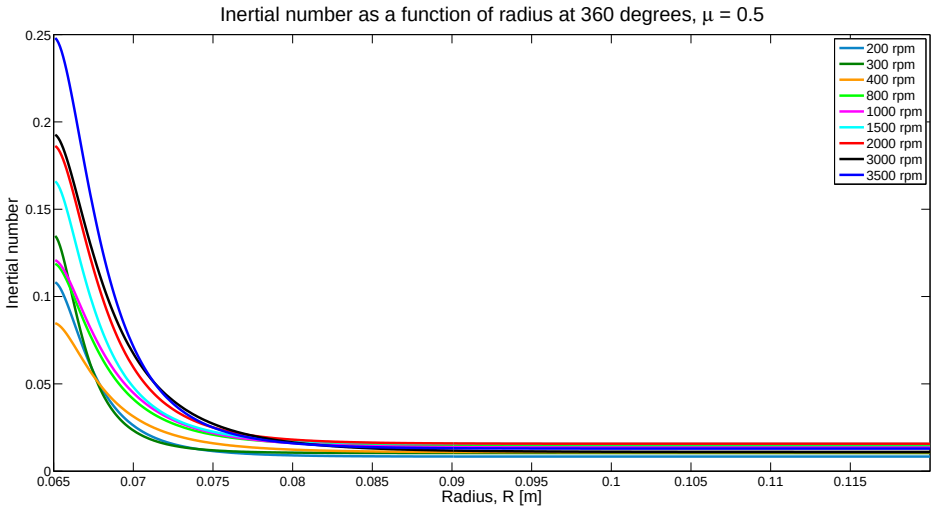

(c) Inertial number at 360°.

Figure 5.31.: Inertial number at 180°, 270° and 360°, $\mu = 0.5$, using the fit.

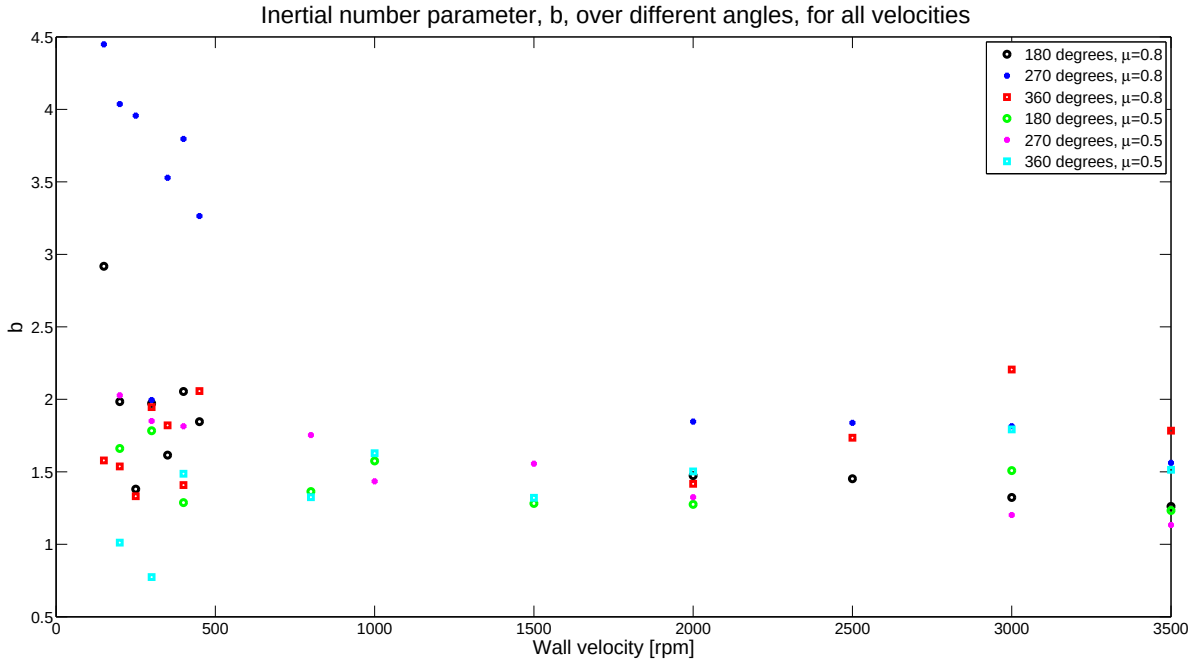

(a) The inertial number parameter, b.

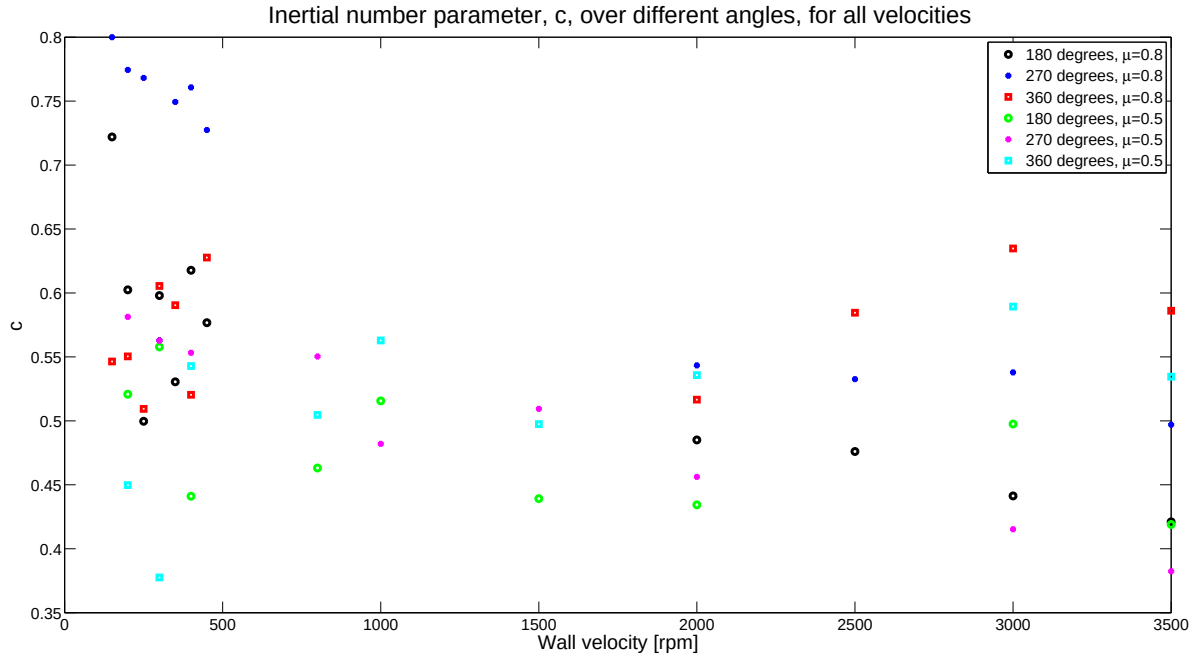

(b) The inertial number parameter, c.

Figure 5.32.: The inertial number parameters b and c from function fits.

5.3.4. Pressure

The total pressure in the system was calculated from the inertial number and volume fraction using Equation 2.11. The pressure for each driving wall velocity and angle is shown in Figures 5.33 and 5.36. For the higher static friction case, there is a general increase in pressure with driving wall velocity, although the relationship is not linear and there are some fluctuations, especially in the distribution at 180°. The distributions cover the radial range 0.065 m to 0.12 m, even though the volume fraction and inertial number at 180° and 270° data only started at 0.07 m. Thus the distributions are an extrapolation in this region. The pressure distributions have a similar symmetrical shape at 180° and 270°, with the maximum values at a similar radial position. This radial position changes with angle. At 180° it is between 0.08 m and 0.09 m (3 to 5 particle diameters away from the driving wall). The maximum at 270° is shifted over by one particle diameter to the range 0.085 m and 0.095 m. The distribution at 360° is skewed towards the driving wall with a maximum occurring in the range 0.075 m to 0.08 m.

The components of the pressure (calculated from the total and the models discussed in Chapter 2) were plotted for each velocity and angle. Figure 5.34a shows the pressure components for 200 rpm, while Figure 5.34b shows the components at 400 rpm and Figure 5.35 at 3500 rpm. In these figures, the black graphs show the pressure components at 180°, the blue graphs show the components at 270° and the red graphs are the components at 360°. At the two lower driving wall velocities shown here, the dominant contribution comes from the quasi-static pressure component at 180°. The other angles of the quasi-static pressure component and the kinetic-collisional pressure contributions are very similar in magnitude, but all have a maximum at different radial positions. The turbulent pressure is very small in comparison to the other components, although at 180° it is comparable to the kinetic-collisional components. It has a maximum value within one particle diameter from the driving wall for all driving wall velocities.

As the driving wall velocity increases, the quasi-static pressure component at 270° increases, until it is the maximum value at 3500 rpm. This value is very much greater than the other components in the distribution. The kinetic-collisional pressure component at 270° is the largest after the quasi-static component.

The quasi-static pressure goes negative in the region 0.065 m to 0.07 m at 180° at the lower velocities, while it is negative in this region for 180° and 270° at 3500 rpm. This is due to the definition of the quasi-static pressure. In this region, the sum of the turbulent and kinetic collisional components exceeds the total pressure calculated

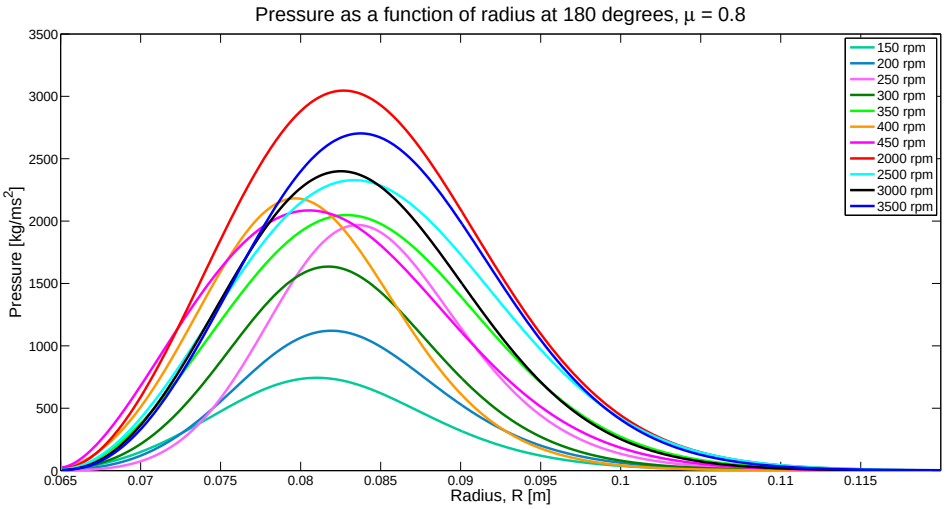

(a) Total pressure at 180°.

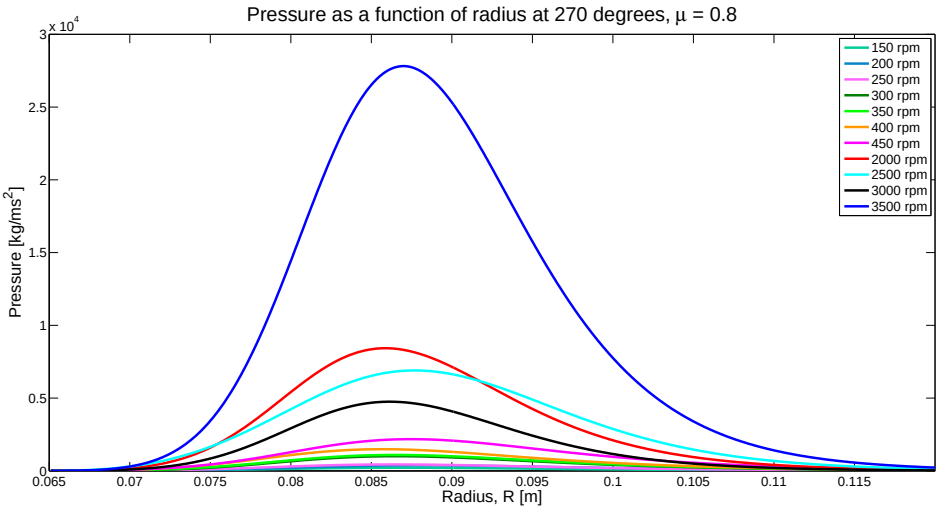

(b) Total pressure at 270°.

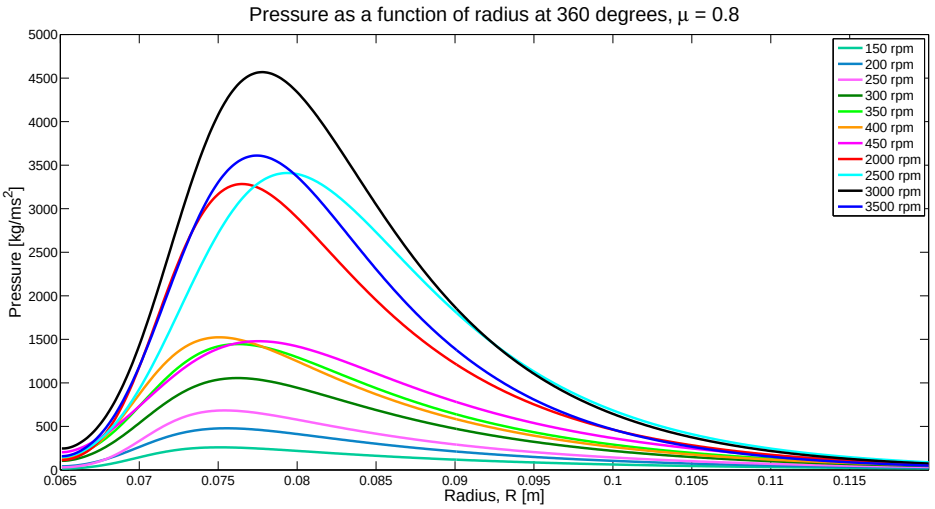

(c) Total pressure at 360°.

Figure 5.33.: Total pressure at 180°, 270° and 360°, $\mu = 0.8$.

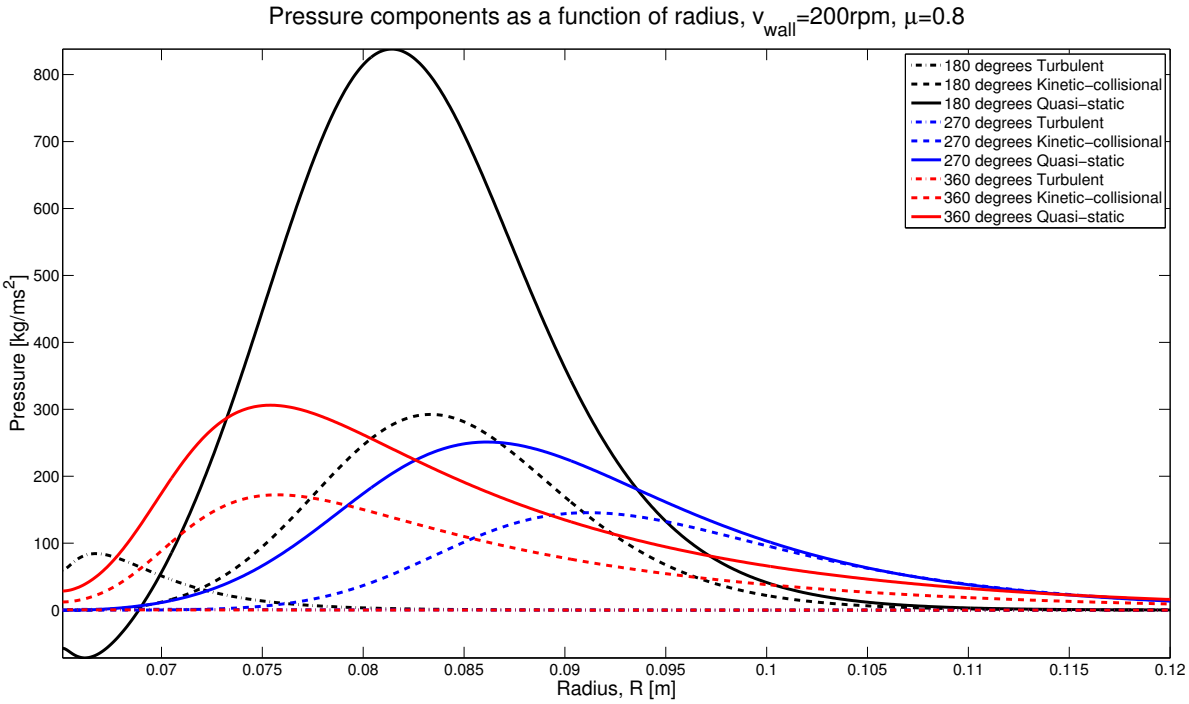

(a) Pressure components at $v_{wall} = 200\,\mathrm{rpm}$.

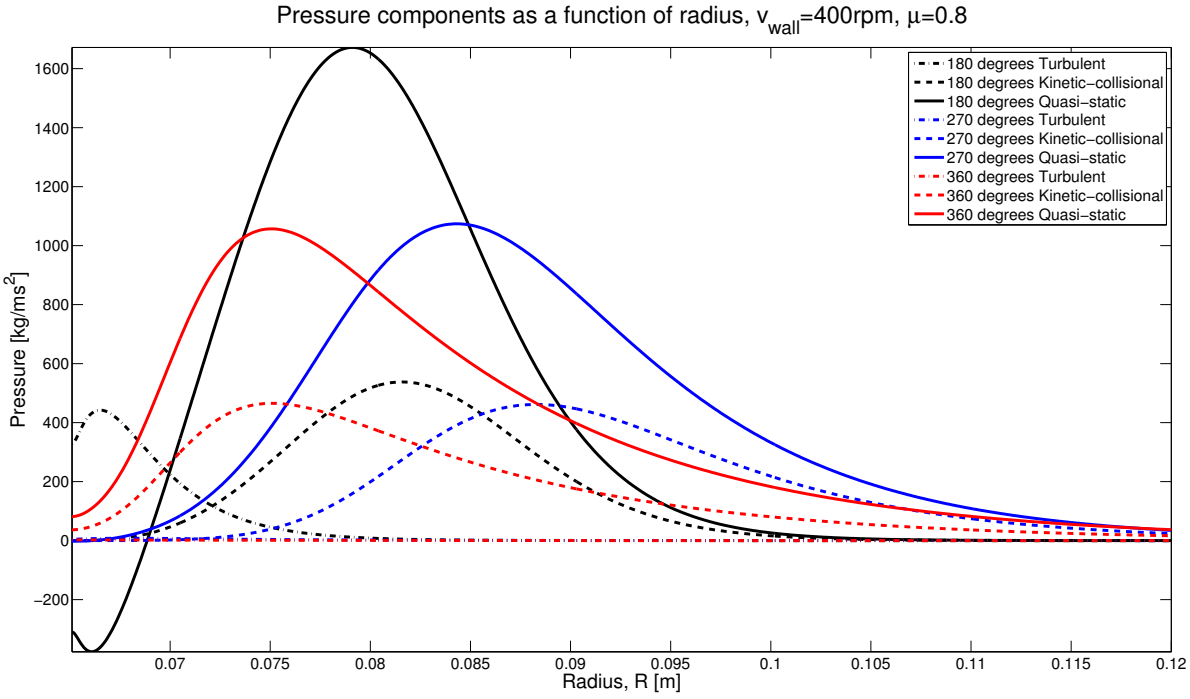

(b) Pressure components at $v_{wall} = 400\,\mathrm{rpm}$.

Figure 5.34.: Pressure components at 200 rpm and 400 rpm, $\mu = 0.8$.

from the inertial number and volume fraction. As the turbulent component is the only

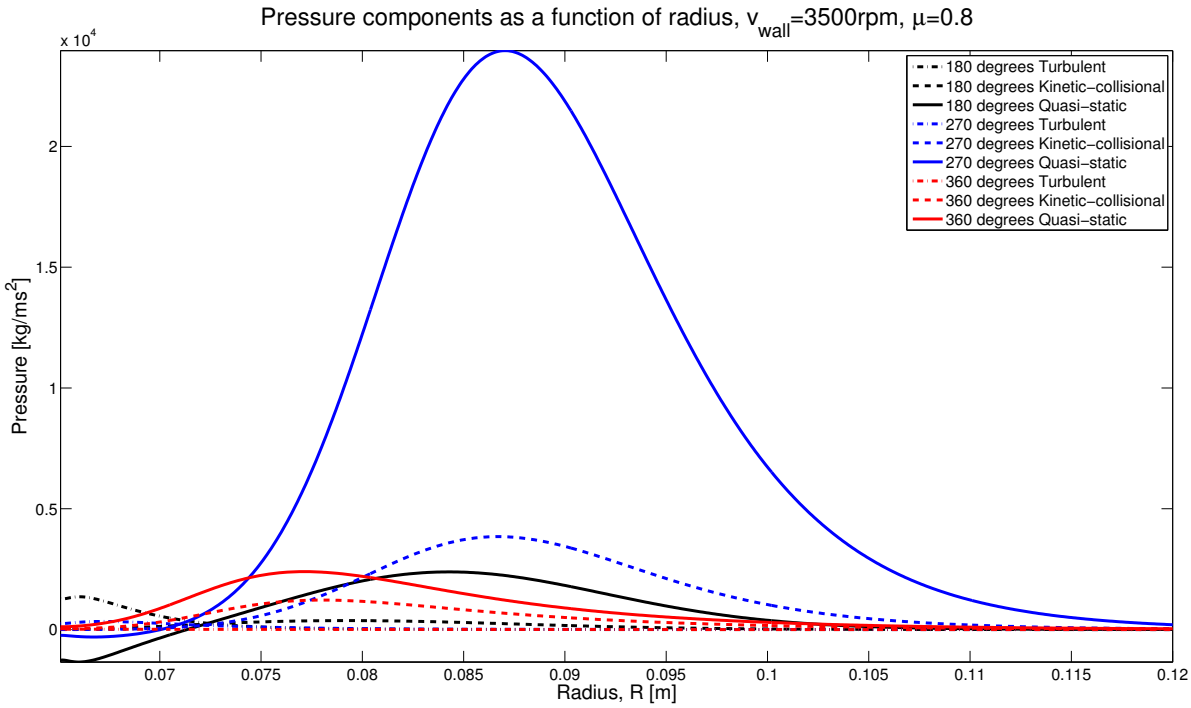

Figure 5.35.: Pressure components at 3500 rpm, $\mu = 0.8$.

considerable contribution to the pressure in this region (and this region is outside the boundaries of the data), it's behaviour could be an extrapolation.

The lower static friction case shows a remarkably different behaviour to the higher friction value simulations. Thus the graphs are presented and analysed separately. Presented in Figure 5.36 are the pressure distributions for all driving wall velocities and angles. The distributions at 180° and 270° are much narrower than they are for $\mu = 0.8$, with the maxima occurring closer in towards the driving wall. They still show a certain amount of symmetry. There is still a general increase of pressure with velocity, however, the simulations at 800 rpm, 1000 rpm and 1500 rpm do not follow this relation. The maximum values reached in these simulations was greater than the values at higher driving wall velocities. The range of radial position of the maxima is also smaller (one particle diameter wide instead of two). The maxima for the distributions at 180° and 270° is around 0.08 m (3 particle diameters) and that for 360° is around 0.075 m.

The components of the pressure at 200 rpm, 800 rpm and 3500 rpm for $\mu = 0.5$ are shown in Figures 5.37 and 5.38. In all three configurations, the quasi-static pressure at 360° (red, solid graph) is the greatest. At 200 rpm the other quasi-static distributions (at 180° and 270°) are similar in magnitude, differing by a small amount and the curve at 180° has a maximum that is shifted towards the outer shell. As the driving wall velocity

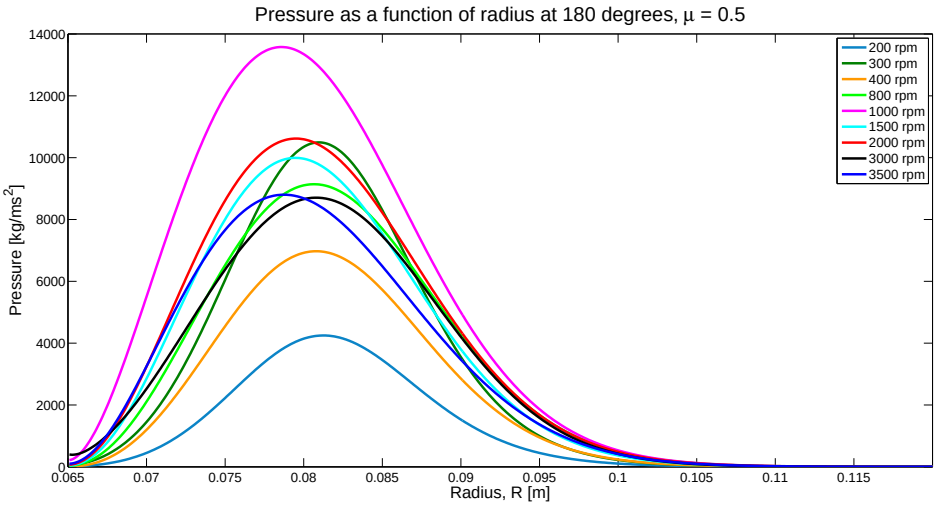

(a) Total pressure at 180°.

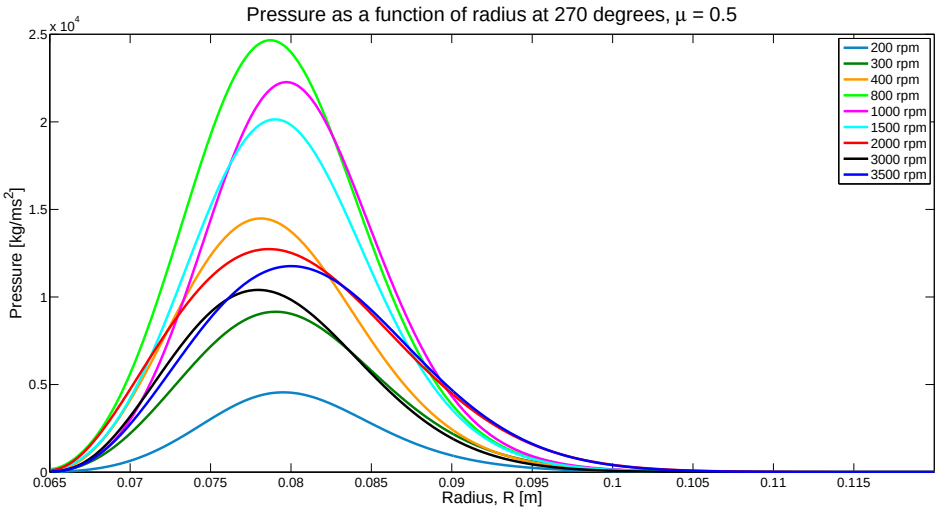

(b) Total pressure at 270°.

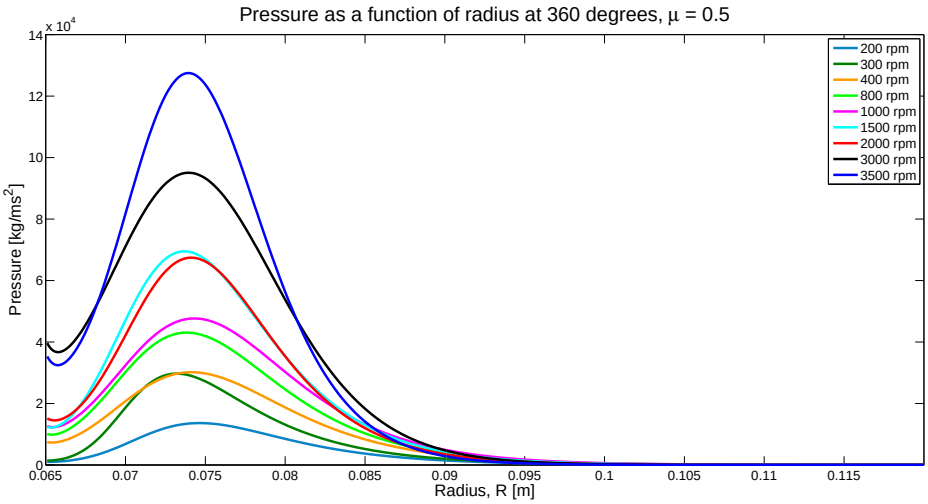

(c) Total pressure at 360°.

Figure 5.36.: Total pressure at 180°, 270° and 360°, $\mu = 0.5$.

increases to 800 rpm, the quasi-static component at 270° increases relative to the other components, where it stays until dropping down again at 3500 rpm.

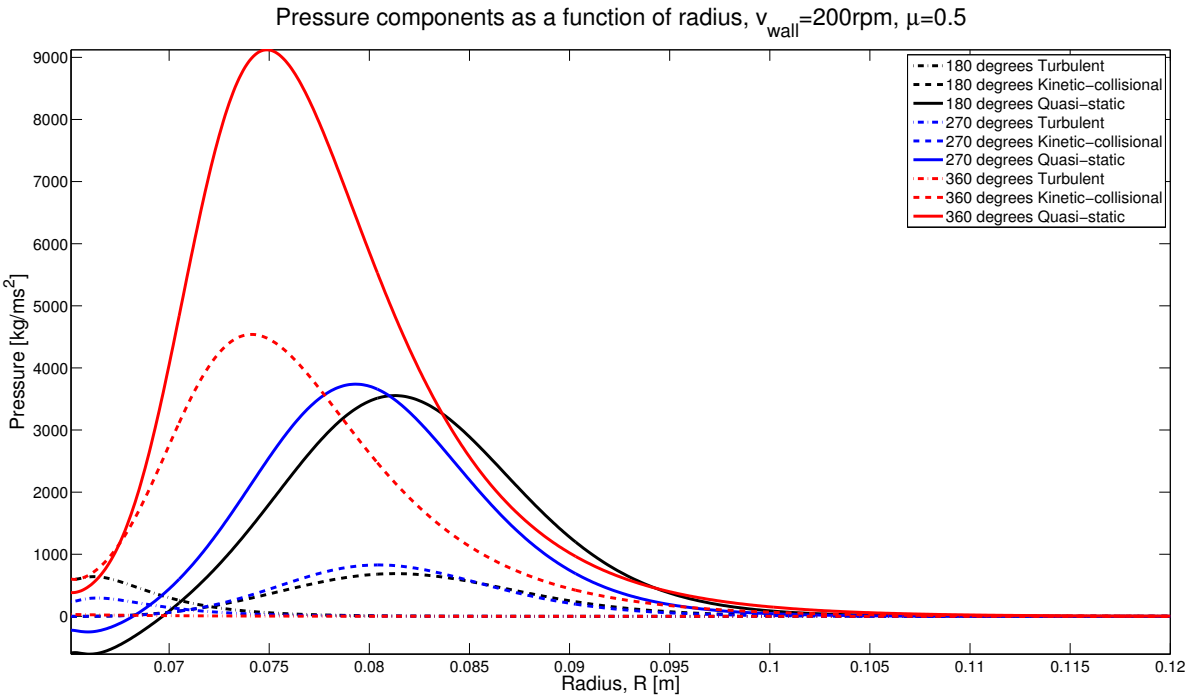

(a) Pressure components at $v_{wall} = 200$ rpm.

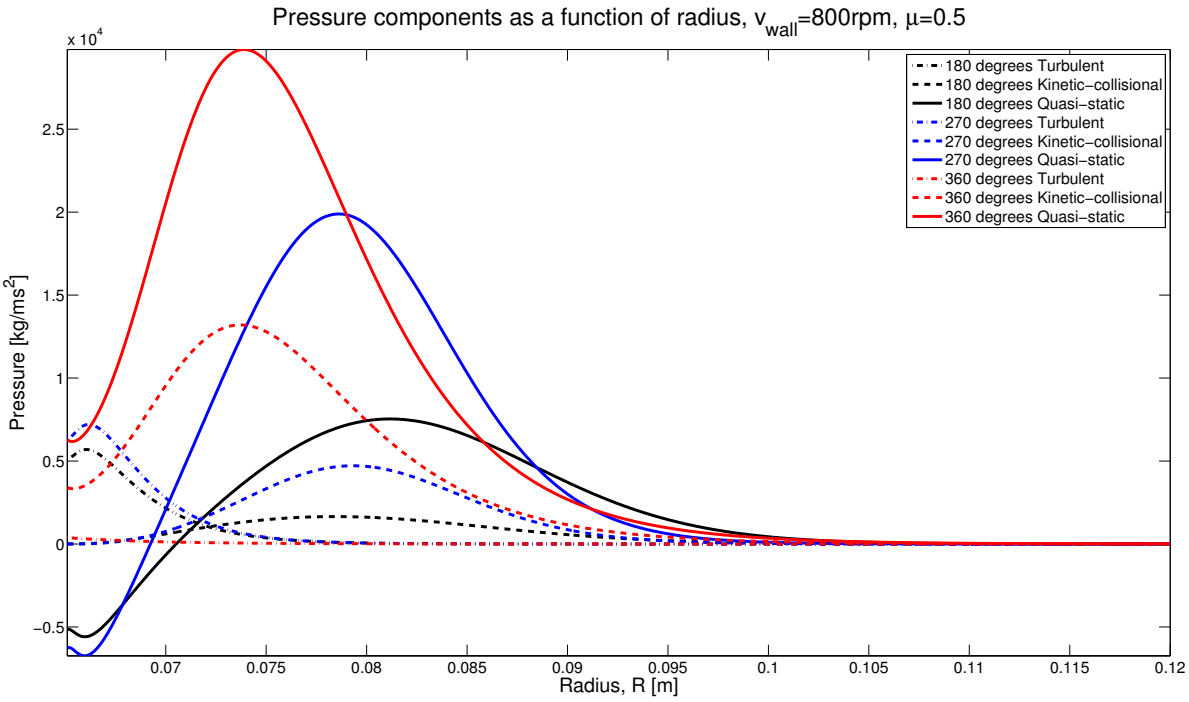

(b) Pressure components at $v_{wall} = 800$ rpm.

Figure 5.37.: Pressure components at 200 rpm and 800 rpm, $\mu = 0.5$.

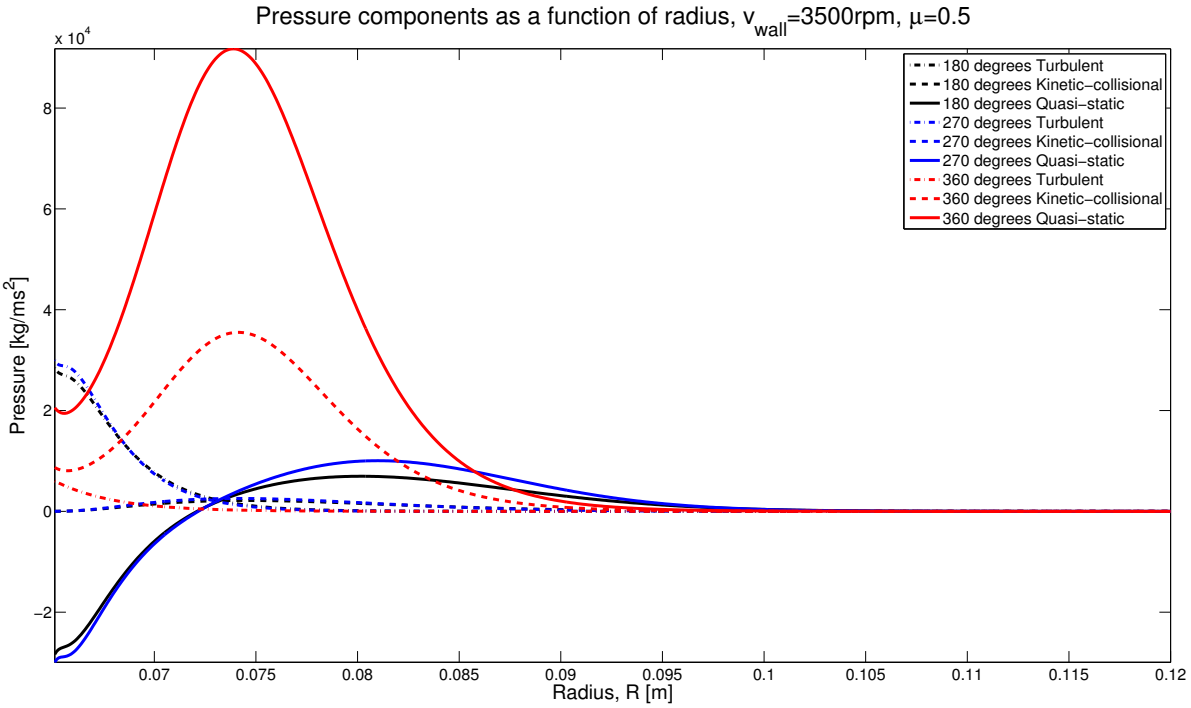

Figure 5.38.: Pressure components at 3500 rpm, $\mu = 0.5$.

The kinetic-collisional components show a similar behaviour with increasing velocity. The component at 360° is the largest, with the other two angles behaving similarly at 200 rpm. The component at 270° then increases relative to the others for 800 rpm and it drops down again when the driving wall velocity is 3500 rpm.

The turbulent component, once again, is only non-zero close to the driving wall, with the components at 180° and 270° consistently larger than the component at 360°. As the total pressure drops close to zero in the region where the turbulent pressure is largest, the quasi-static pressure is calculated as negative in this region. This is a non-physical result, as the absolute pressure in a system cannot be negative.

5.3.5. Shear stress energy distribution

The distributions of the shear stress were calculated from Equations 3.42 to 3.45, using the pressure, inertial number, shear rate and volume fraction distributions shown in the previous sections. The total shear stress energy distributions for each configuration and angle are shown in Figures 5.39 and 5.42. Like the pressure distributions, the shear stress scales with shear rate. This is not a strict rule, however, as there are a few configurations that deviate from this pattern. The shear stress distributions are very similar to the pressure distributions, differing mainly in magnitude. In Figure 5.39a, the shear stress goes negative for radial values less than 0.07 m. This is due to the quasi-static pressure being negative in this region. This is also in the region which extends beyond the limit of the data available as previously mentioned, thus this could be an edge effect.

The largest shear stress energy in the $\mu = 0.8$ configurations is at 270°, with the maximum at that angle occurring for the highest driving wall velocity. This 3500 rpm distribution is much greater than the distributions at lower driving wall velocities. The shear stress distributions at 180° and 270° are symmetrical, while that at 360° is skewed towards the driving wall.

The shear stress at 180° shown in Figure 5.39a appears to show a radial shift outwards in maximum values as the driving wall velocity increases, except for the distribution at 400 rpm. This effect is investigated for all configurations later on in this section.

The components of the shear stress energy distribution for $\mu = 0.8$ in Figures 5.40 and 5.41 show that the quasi-static shear stress at 180° is the only component that goes negative for radial values less than 0.07 m. This is due to the quasi-static pressure component being negative in this region. The maximum contribution comes from the quasi-static component at 180° at the lower velocities, while at 3500 rpm, the maximum is the quasi-static component at 270°. The largest contribution to the shear stress comes from the quasi-static component.

The maximum contribution from the kinetic-collisional components is on par with the maximum from the turbulent component. There is a uniformity of behaviour between the angles maximums for the kinetic-collisional component with lower driving wall velocities. In the 3500 rpm configuration, the kinetic-collisional component is only considerable at 270°. The distribution of the turbulent component is only large at 180°.

The behaviour of the shear stress energy distributions in the $\mu = 0.5$ configurations is shown in Figure 5.42. The general increase of maximum shear stress increasing with driving wall velocity is not followed strictly in these cases, with the mid-range values

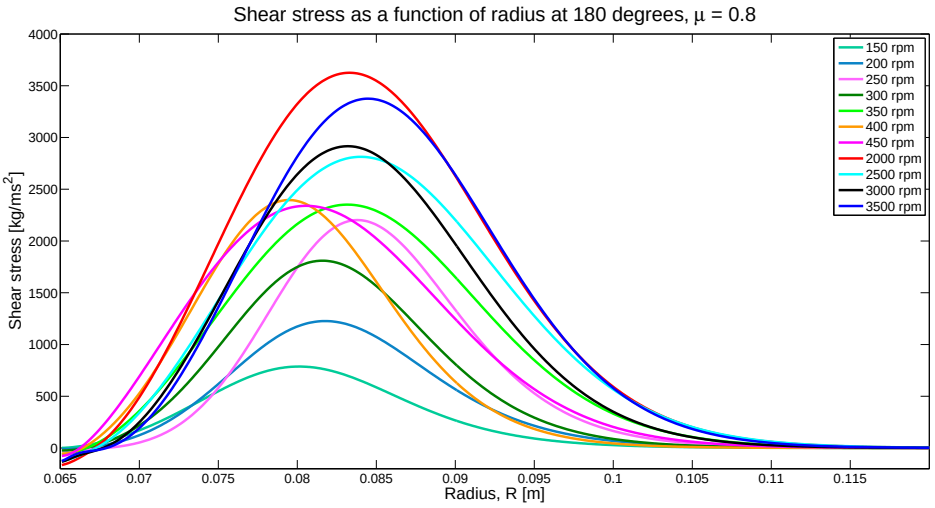

(a) Shear stress at 180°.

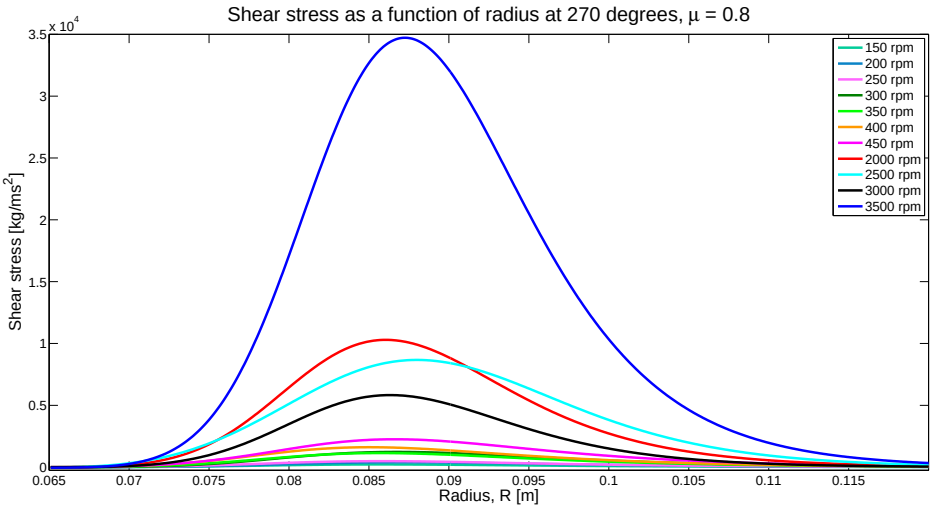

(b) Shear stress at 270°.

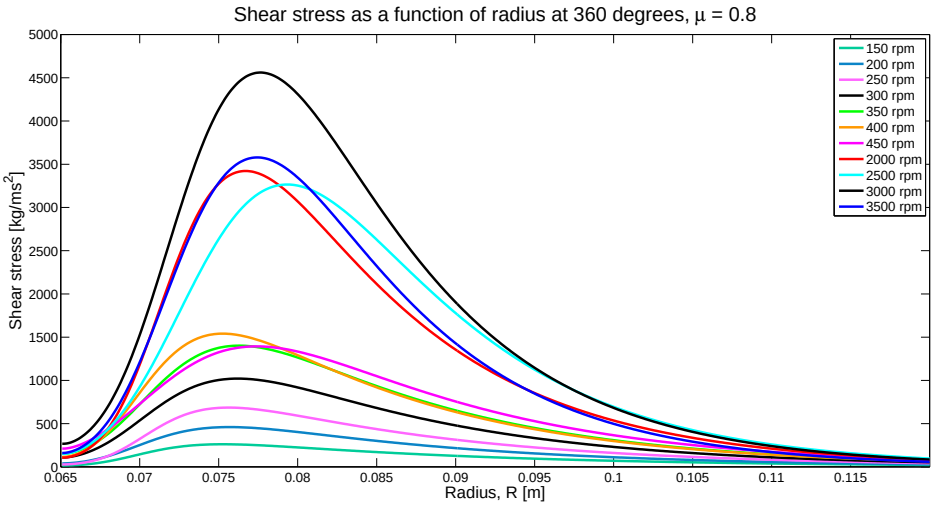

(c) Shear stress at 360°.

Figure 5.39.: Shear stress at 180°, 270° and 360°, $\mu = 0.8$.

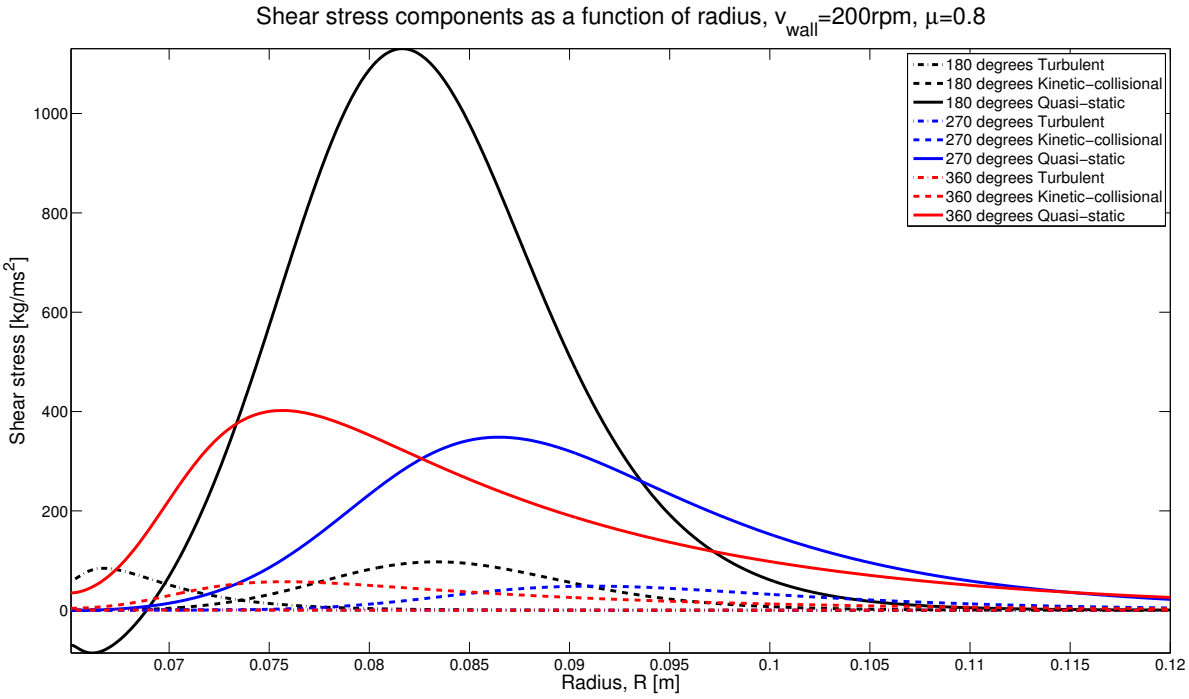

(a) Shear stress components at $v_{wall} = 200\,\text{rpm}$.

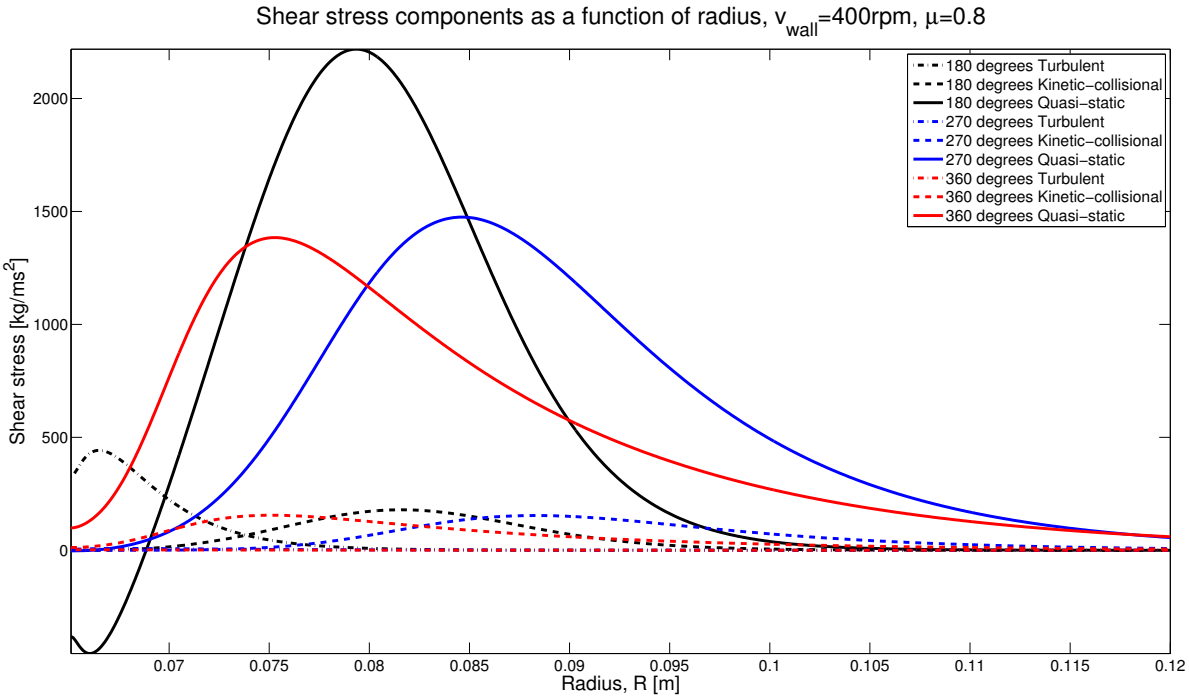

(b) Shear stress components at $v_{wall} = 400\,\text{rpm}$.

Figure 5.40.: Shear stress components at 200 rpm and 400 rpm, $\mu = 0.8$.

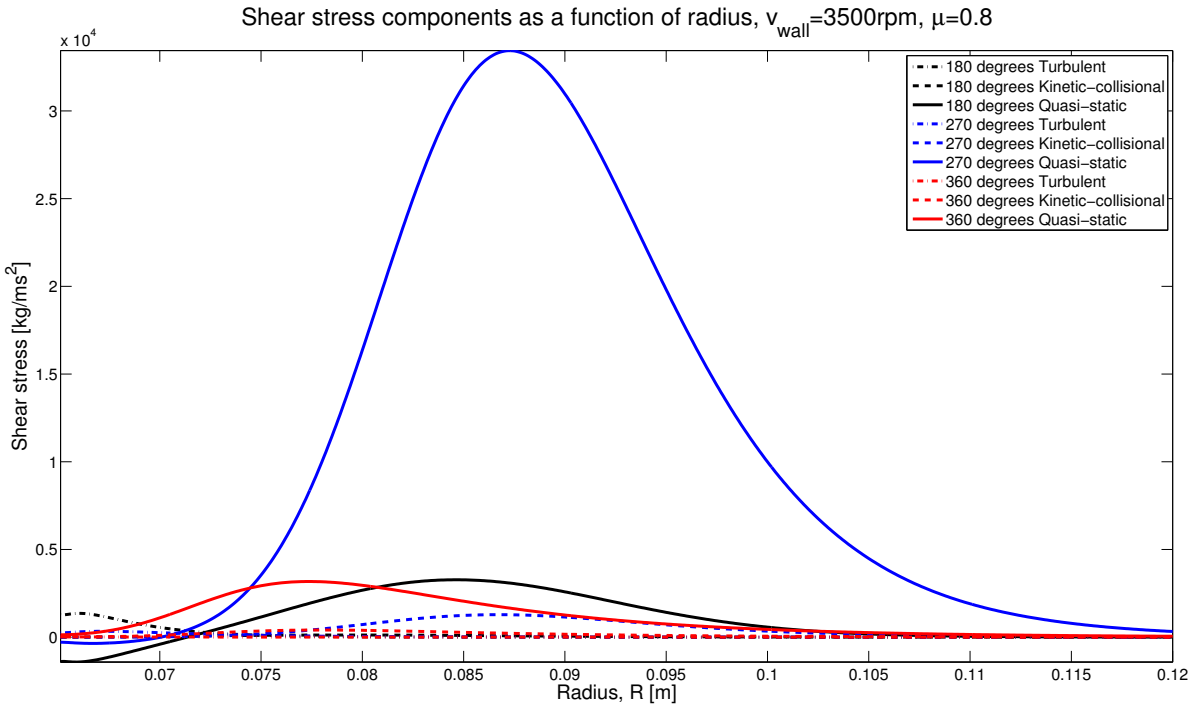

Figure 5.41.: Shear stress components at 3500 rpm, $\mu = 0.8$.

having a higher maximum than the highest driving wall velocities at 180° and 270°. The shear stress for many configurations does not tend to zero close to the rotating wall. The odd behaviour seen on the edge of the system in Figures 5.42a and 5.42b is a numerical effect caused by the extrapolation beyond the range of the data. The distributions at 360° are more symmetrical than their $\mu = 0.8$ counterparts.

The shear stress components are shown for 200 rpm, 800 rpm and 3500 rpm in Figures 5.43 and 5.44. The maximum contribution to the shear stress in the $\mu = 0.5$ configurations comes from the quasi-static component, with the greatest of those being at 360°. As the driving wall velocity increases from 200 rpm to 800 rpm, the quasi-static components at 180° and 270° increase, relative to the other components, with the 270° value increasing more than the 180°. Both of these values decrease in magnitude (relative to the other components) as the driving wall velocity increases further, as is seen in Figure 5.44.

The kinetic-collisional component at 360° remains the largest of these components as the driving wall velocity increases. The components at 180° and 270° have similar behaviour, with the 270° component increasing more at 800 rpm.

The turbulent components are non-zero only within 2 particle diameters of the driving wall. The component at 360° is barely noticeable at 3500 rpm, while those at 180° and 270° are much larger, increasing considerably with driving wall velocity.

The radial position of the maximum shear stress energy for each configuration is shown in Figure 5.45. There appears to be a minor increase in the radial position as the driving wall velocity increases, seen in the $\mu = 0.8$ configurations. The location of the maximum at the smaller driving wall velocity configurations is more scattered than the higher driving wall velocity configurations. The position of the maximum at 360° is much closer to the driving wall than that of the other angles and it appears to remain mostly constant, in the $\mu = 0.5$ case. There is more scatter in the position of the maximum for the 180° and 270° in the $\mu = 0.5$ configurations. For the $\mu = 0.8$ case, the distance of the maximum shear is farthest from the shearing wall for wall velocities. In this direction, the material is mainly moving perpendicular to the direction of gravitational acceleration.

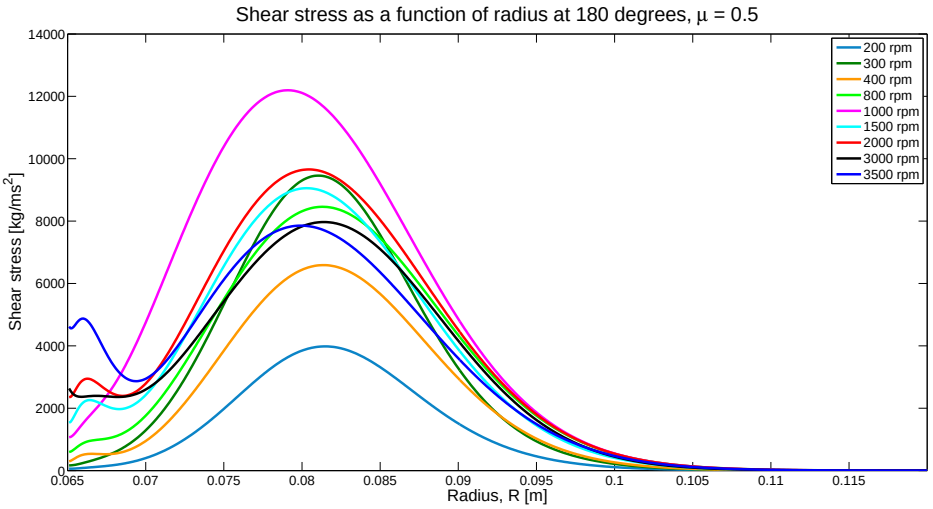

(a) Shear stress at 180°.

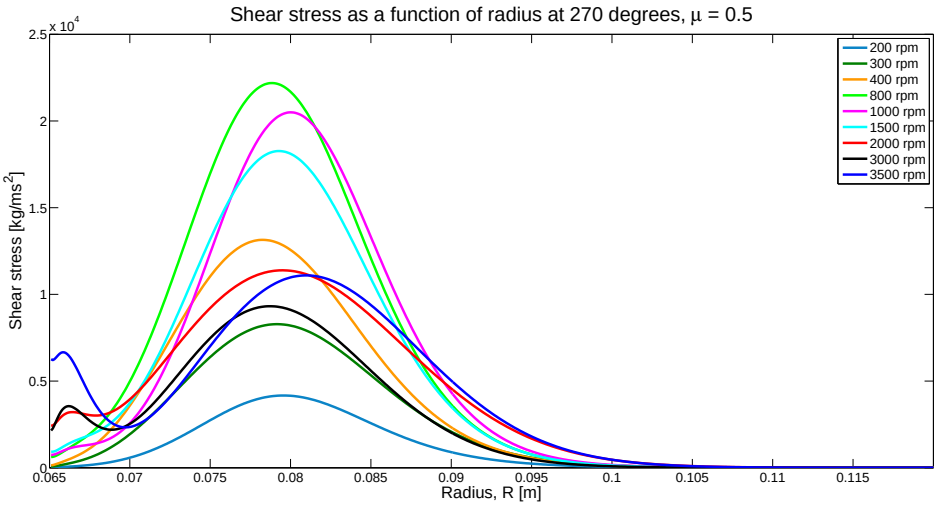

(b) Shear stress at 270°.

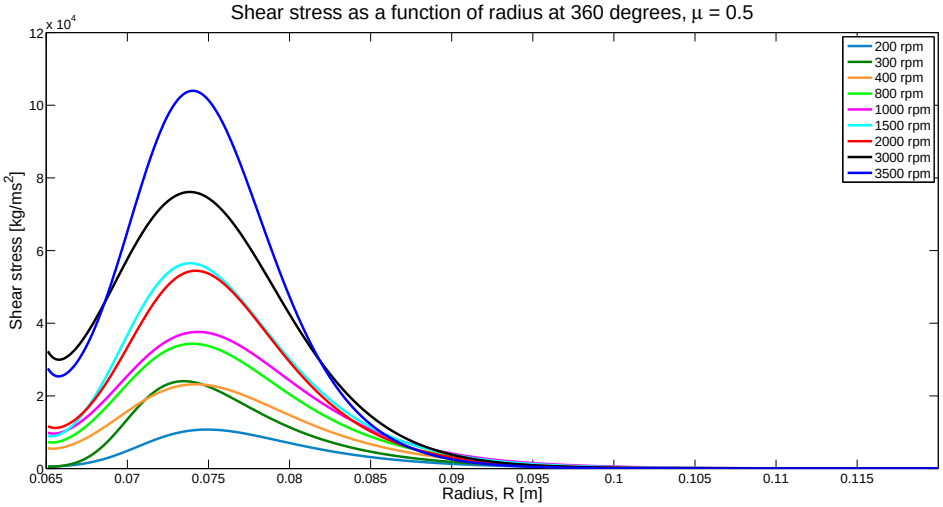

(c) Shear stress at 360°.

Figure 5.42.: Shear stress at 180°, 270° and 360°, $\mu = 0.5$.

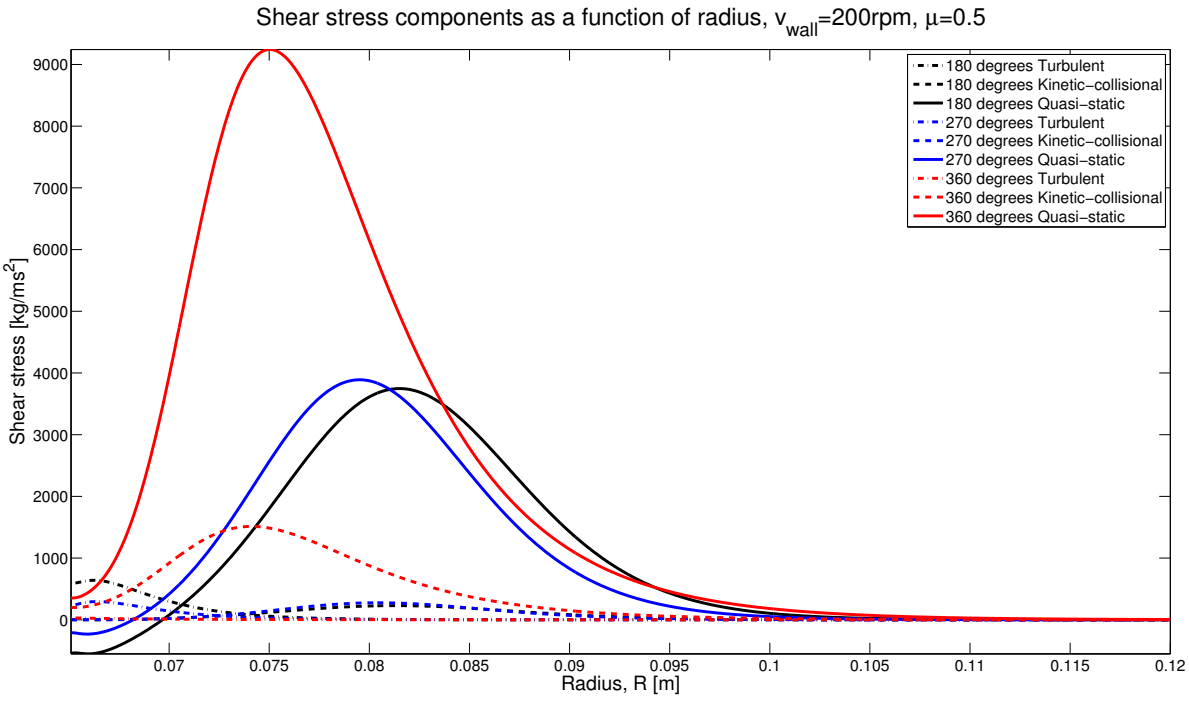

(a) Shear stress components at $v_{wall} = 200\,\text{rpm}$.

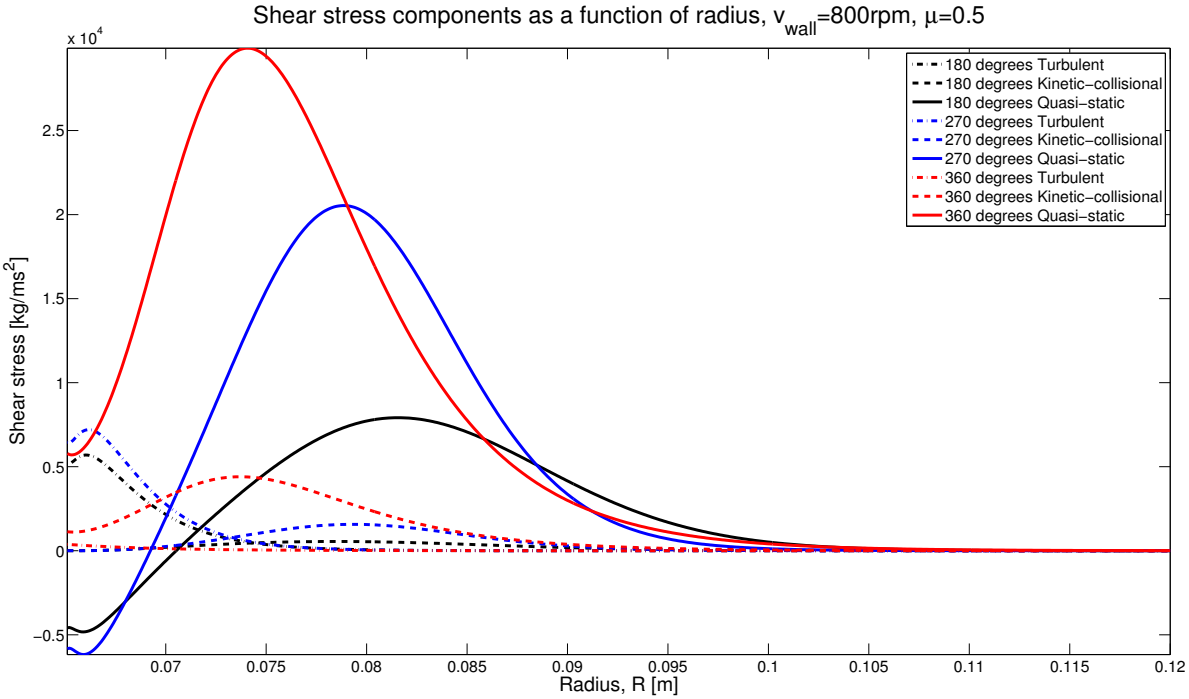

(b) Shear stress components at $v_{wall} = 800\,\text{rpm}$.

Figure 5.43.: Shear stress components at 200 rpm and 800 rpm, $\mu = 0.5$.

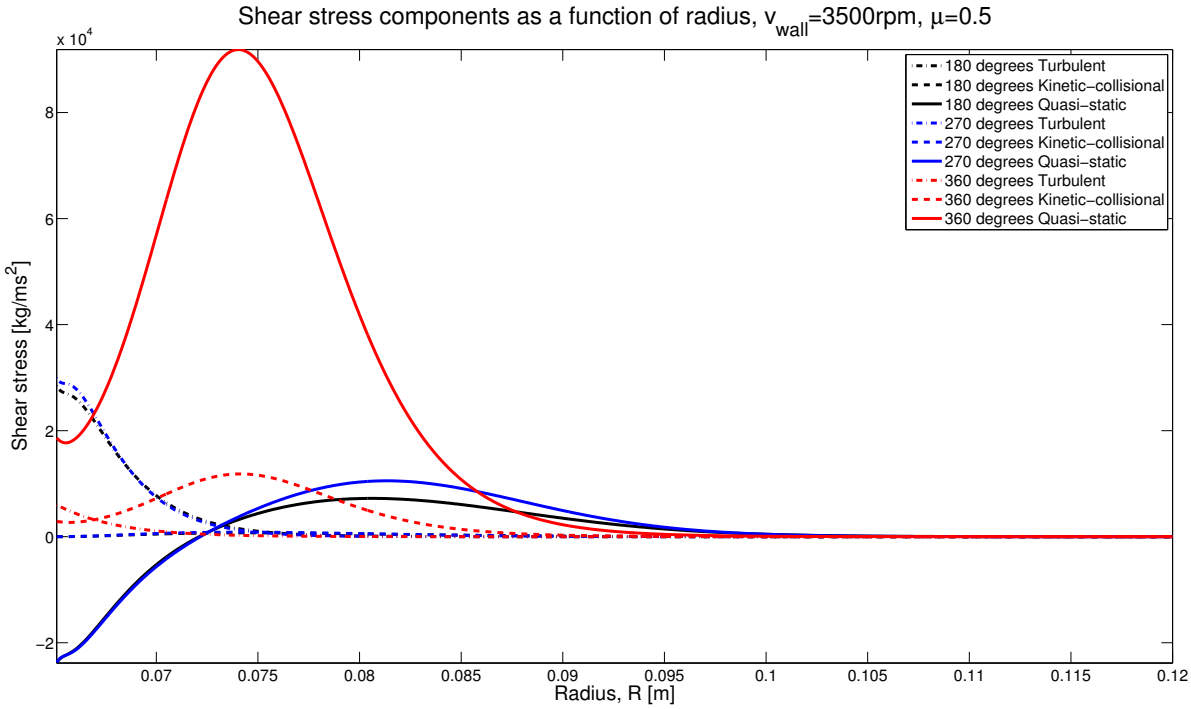

Figure 5.44.: Shear stress components at 3500 rpm, $\mu = 0.5$.

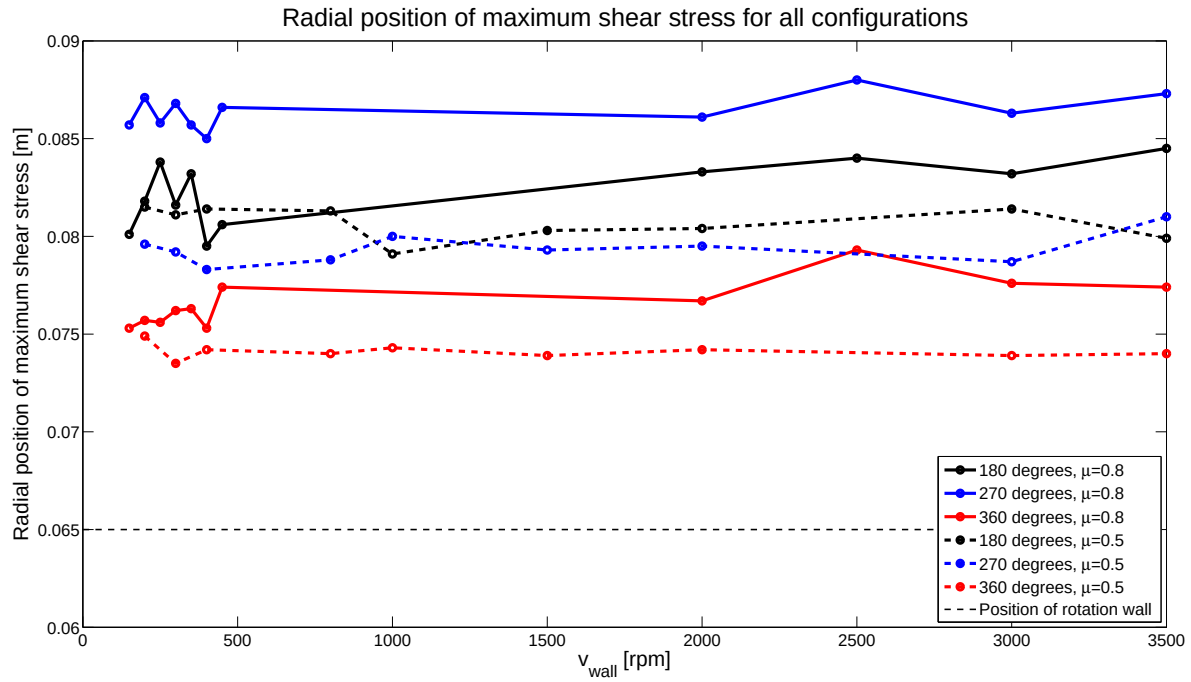

Figure 5.45.: The radial position of the maximum shear stress energy for each configuration.

5.3.6. Effective friction coefficient

The effective friction coefficient was calculated from the pressure and shear stress distributions shown above, using Equation 2.2. These effective friction coefficient distributions are shown in Figures 5.46 and 5.47, as a function of radius in the shear cell annulus.

The effective friction coefficient distributions for the lower friction configurations (Figure 5.46) are confined between $[0.7, 1.3]$. In the region where $|\frac{\tau}{P}| < 1$, the pressure dominates the flow. At 180°, the transition between pressure dominant flow and shear dominant flow occurs between 5 and 7 particle diameters from the shearing wall (0.09 - 0.1 m). In the 270° distributions, this transition is shifted by 1 particle diameter towards the shearing wall, to the range 0.085 - 0.105 m. At this angle, the higher velocity distributions have a larger region of shear dominant flow than the lower velocity distributions. At 360°, the flow is mostly pressure dominated, with the majority of the distributions remaining below the transition threshold ($|\frac{\tau}{P}| = 1$). The higher shearing wall velocity distributions only become shear dominated at the outer edge of the annulus.

The distributions occurring in the shear dominant flow region all show a linear behaviour, increasing with increasing distance from the shearing wall. This region corresponds to the quasi-static flow regime. It appears that a higher effective friction coefficient results from a higher shearing wall velocity, thus implying that a higher shear velocity results in a higher shear stress. This dependence shows variation.

In the region dominated by pressure driven flow (close to the shearing wall), the effective friction coefficient starts high before decreasing to a minimum within a particle diameter of the shearing wall. The distribution then increases towards the outer wall, as the transition to shear dominant flow occurs. This behaviour is clearly apparent in the 180° and 270° distributions, while at 360° the majority of distributions are mostly linear, with only the two lowest shearing wall velocity distributions showing a noticeable minimum.

The higher friction configurations (Figure 5.47) are in the region $0.6 < |\frac{\tau}{P}| < 1.6$. In the 180° cases, the configurations with lower shearing wall velocity are always above the flow transition threshold, meaning that the flow is always dominated by shear stress as opposed to normal stress. For the higher shearing wall velocity distributions, the flow is dominated by pressure very close to the shearing wall (within 2 particle diameters), before transitioning to shear dominated flow. The only exception to this generalisation is the distribution at 150 rpm, which starts out shear dominated and then becomes pressure dominated towards the outer stationary wall.

At 270°, the lower velocity distributions behave similarly to the 150 rpm distribution at 180°. The effective friction coefficient starts out at a value greater than 1 and decreases to a minimum before gradually increasing. Only the configurations with shearing wall velocity below 350 rpm drop to an effective friction coefficient less than 1. Thus, most of these distributions are in a flow regime that is dominated by shear stress over pressure.

The configurations with a higher shearing wall velocity behave similarly to those at 180°. They start at a minimum effective friction coefficient, rapidly increase while still in the shear band and then become linear beyond 5 particle diameters from the shearing wall. These distributions always have $|\frac{\tau}{P}| > 1$, thus are always in a flow regime dominated by shear stress.

The distributions at 360° all have $|\frac{\tau}{P}| > 1$ beyond 7 particle diameters (0.1 m) from the shearing wall. The transition to the shear dominated flow region occurs for some shearing wall velocity configurations at a point 1 particle diameter from the wall (they start in the pressure dominated region and the effective friction coefficient increases). Other distributions have pressure dominated flow close to the shearing wall and transition to shear dominated flow further away from the wall. This behaviour does not seem to be influenced by the shearing wall velocity at this angle.

As with the $\mu = 0.5$ cases, the effective friction coefficient has a linear behaviour in the quasi-static regime, with the linear behaviour occurring beyond the roughly defined edge of the shear band.

The higher shearing wall velocity distributions for the $\mu = 0.8$ case are qualitatively similar to the distributions seen in the $\mu = 0.5$ case.

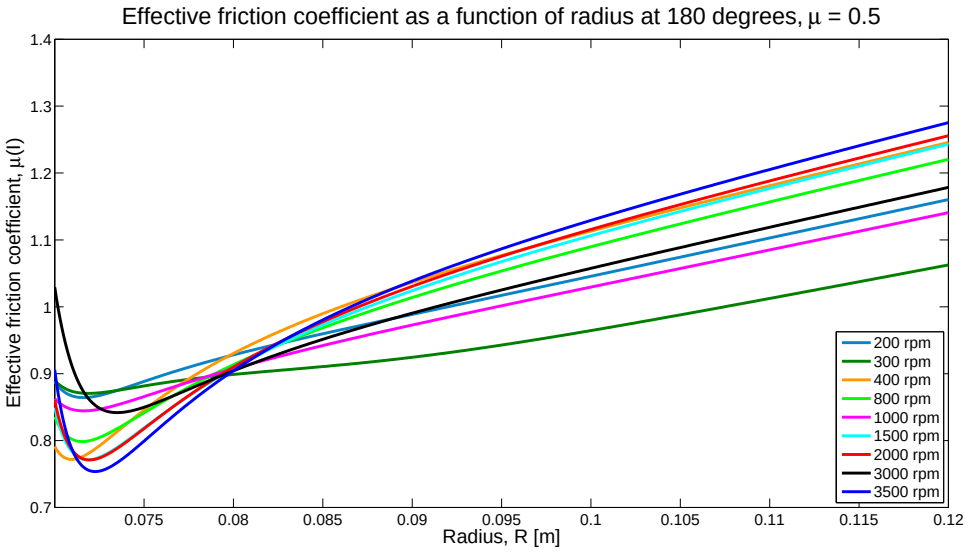

(a) Effective friction coefficient at 180°.

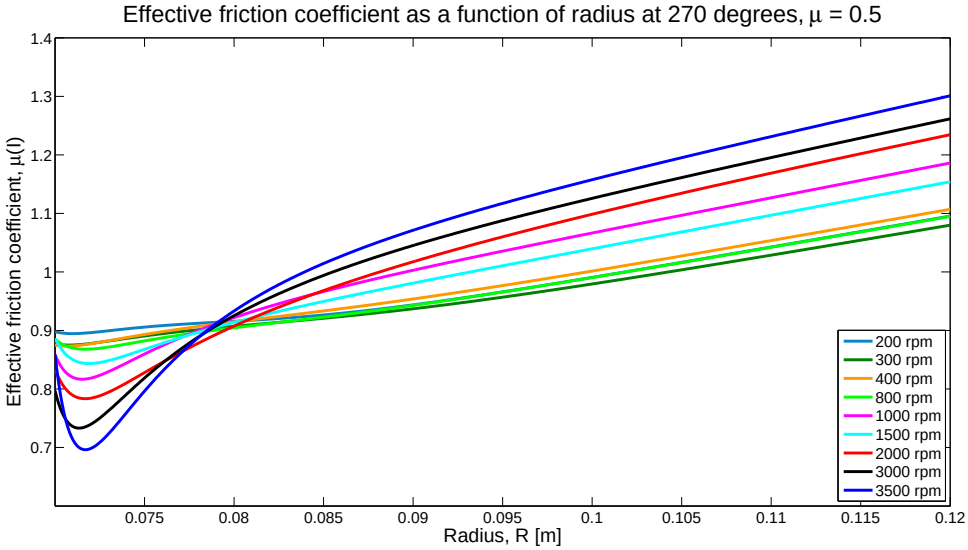

(b) Effective friction coefficient at 270°.

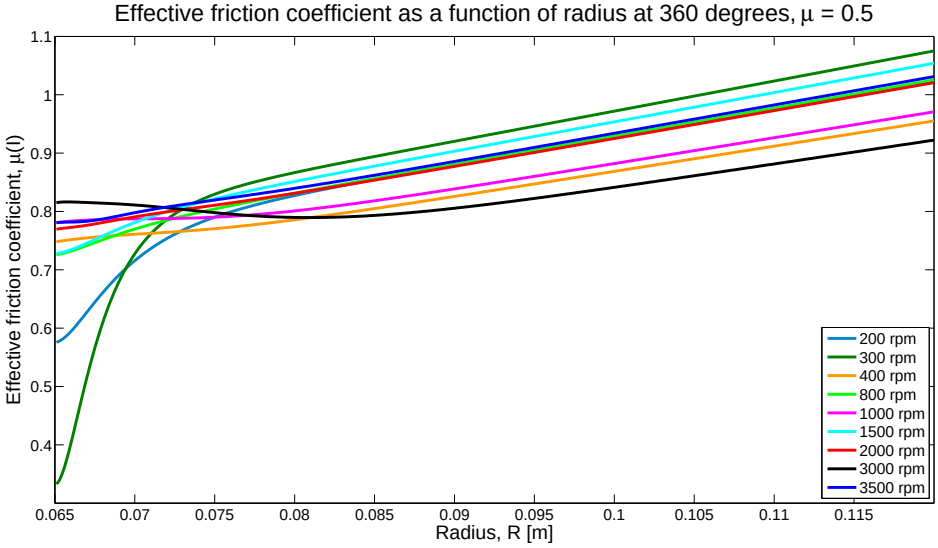

(c) Effective friction coefficient at 360°.

Figure 5.46.: Effective friction coefficient at 180°, 270° and 360°, $\mu = 0.5$.

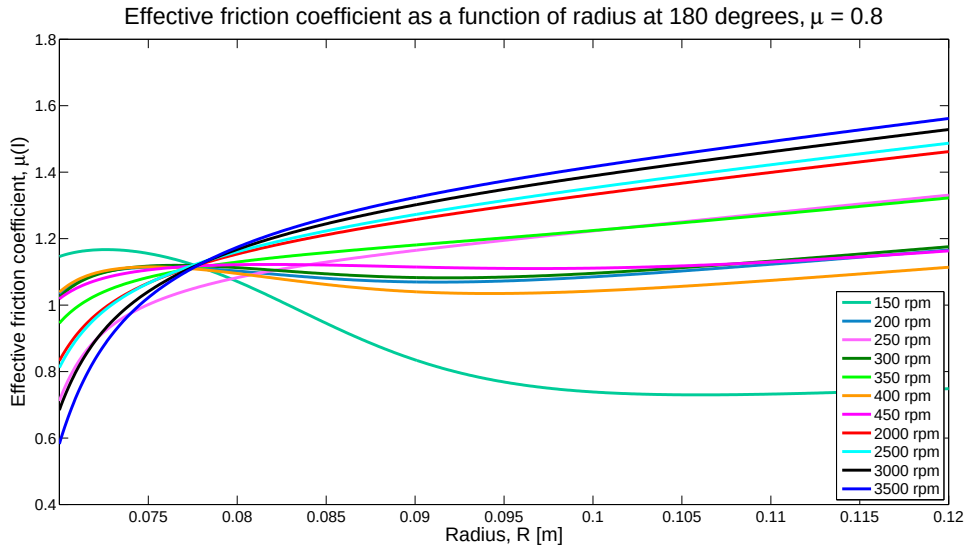

(a) Effective friction coefficient at 180°.

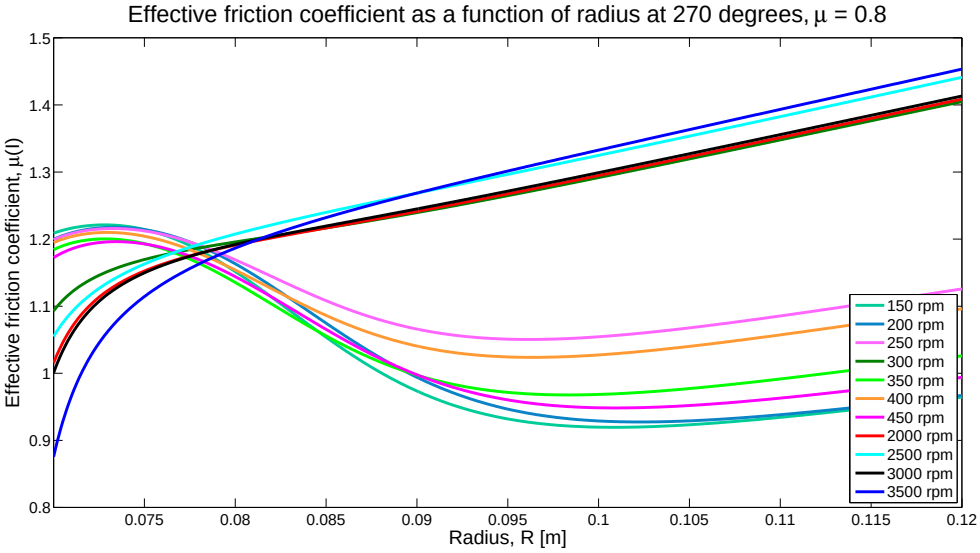

(b) Effective friction coefficient at 270°.

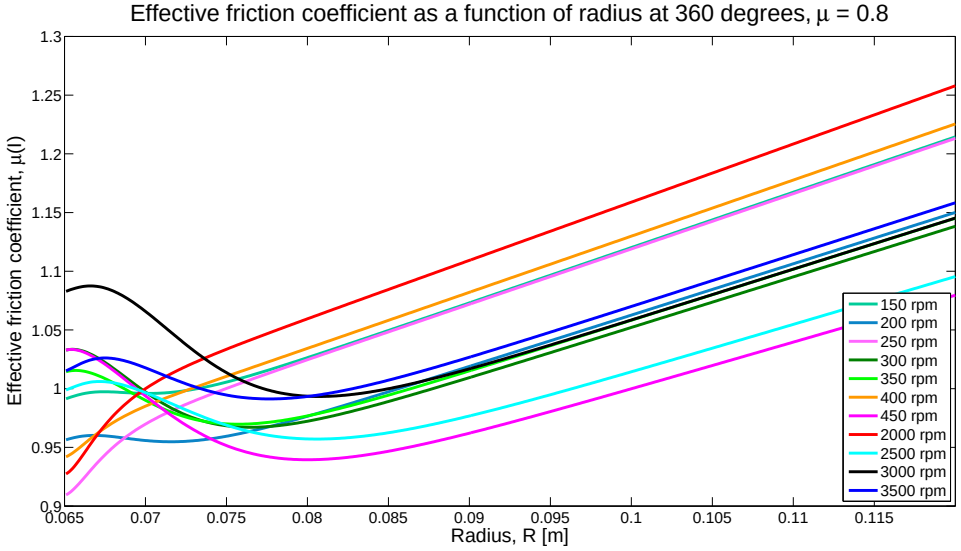

(c) Effective friction coefficient at 360°.

Figure 5.47.: Effective friction coefficient at 180°, 270° and 360°, $\mu = 0.8$.

5.3.7. Power Dissipation distribution

The power dissipation was calculated using Equations 3.50 and 3.51. The derivatives, $\frac{\partial \tau}{\partial r}$ and $\frac{\partial P}{\partial r}$, were calculated from the shear stress and pressure distributions using Mathematica. The total power dissipation distribution for each angle and driving wall velocity is shown in Figures 5.48 and 5.51.

The overall magnitude of the power dissipated increases with driving velocity in the $\mu = 0.8$ configurations. In the 180° case (Figure 5.48a), the highest power dissipation rate is at 2000 rpm, with the configurations with a driving wall velocity higher than that having a lower maximum power dissipation. The distributions at 3000 rpm and 3500 rpm exhibit an unnatural fluctuation close to the driving wall, due to the negative shear stress and quasi-static pressure in this region. The power dissipation rate for the other configurations is almost zero close to the driving wall, increasing rapidly to a maximum value within 4 particle diameters of the inner wall and then falling down to approximately zero as the distance from the driving wall increases.

The distribution's maximums at 180° and 360° are closer to the driving wall than at 270°, which has a less steep increase to the maximum. The higher driving wall velocity distributions at 360° go negative after their peak, before increasing gradually to zero. This same behaviour is seen in the 3500 rpm distribution at 270° (Figure 5.48b).

The panel of plots in Figure 5.49, shows the shear and compressive components of the power dissipation distribution, for all three angles studied, over a range of driving wall velocities. The shear components of the power dissipated are plotted with a solid line, while the compressive components are the dashed lines. The shear component of the power dissipation greatly dominates the graph, hence the compressive components were plotted separately in Figure 5.50.

In Figure 5.49, the change in where the maximum power dissipated in the shear cell is apparent. At lower shear rates, the maximum power dissipated is at 180° (black curve), while at higher shear rates the maximum occurs at 270° (blue curve). As the shear rate increases, the power dissipated at 270° gradually increases, relative to the other angles, until it dominates at 3500 rpm. The power dissipated at 360°, shown by the red curve, starts out greater than 270°, gradually increases at a slower rate, only approaching the value at 180° at 3500 rpm.

The same configurations for the compressive power are shown in Figure 5.50 as for the shear components. The greatest compressive power is dissipated at 360° for the 150 rpm configuration (Figure 5.50a), while the maximum is at 180° in the other lower

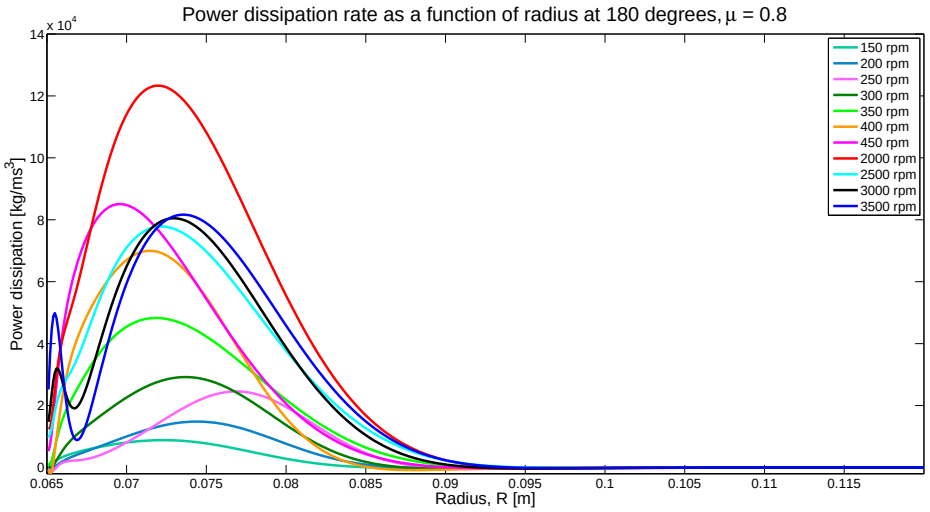

(a) Total power dissipation at 180°.

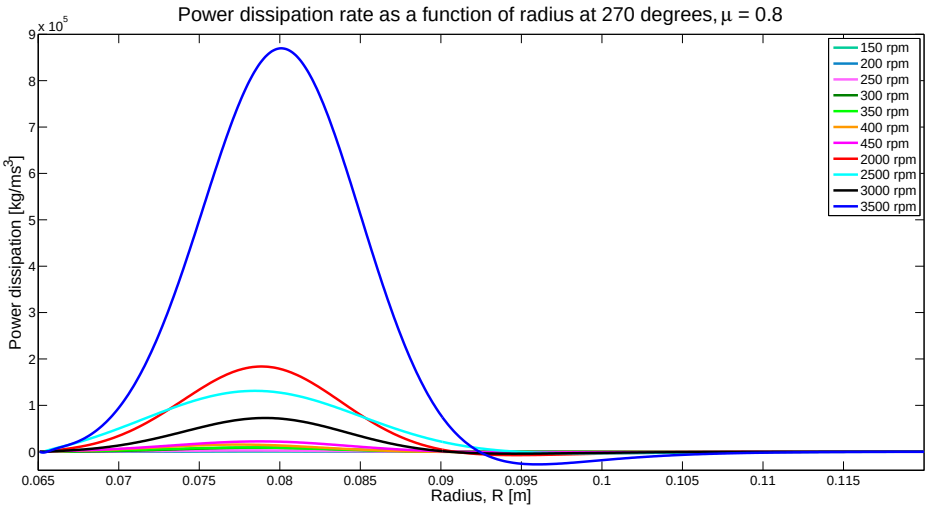

(b) Total power dissipation at 270°.

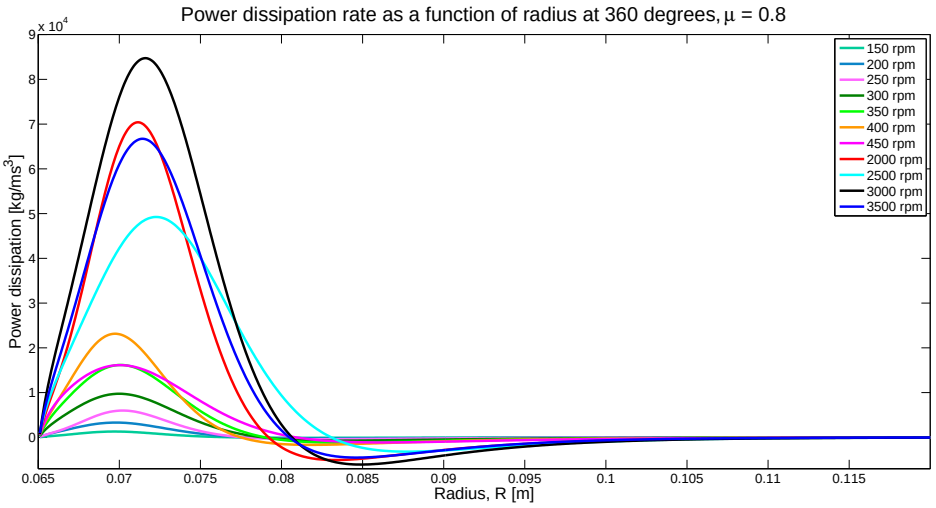

(c) Total power dissipation at 360°.

Figure 5.48.: Total power dissipation at 180°, 270° and 360°, $\mu = 0.8$.

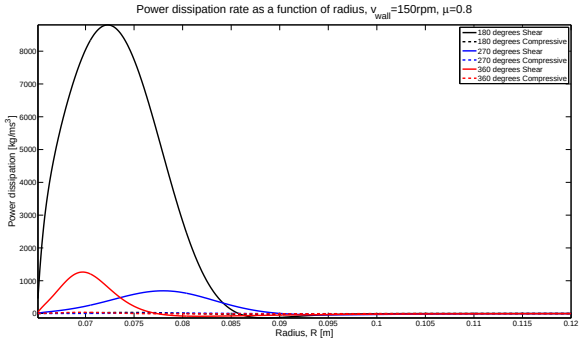

(a) $v_{wall} = 150\,\mathrm{rpm}$

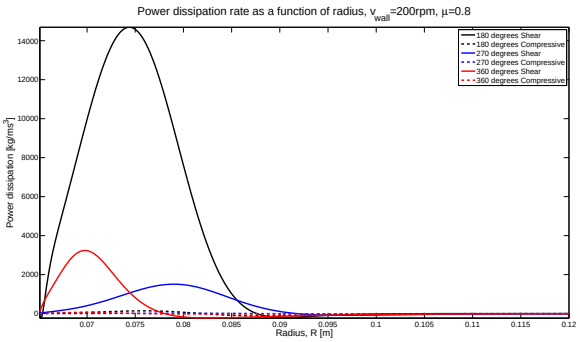

(b) $v_{wall} = 200\,\mathrm{rpm}$

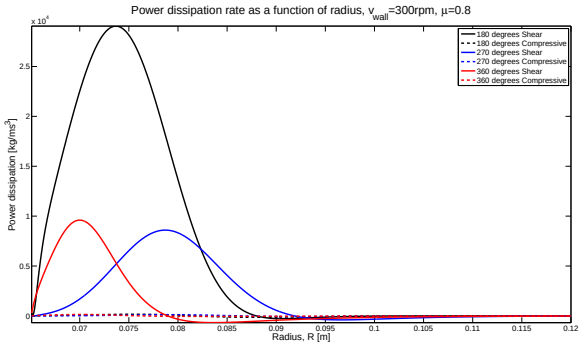

(c) $v_{wall} = 300\,\mathrm{rpm}$

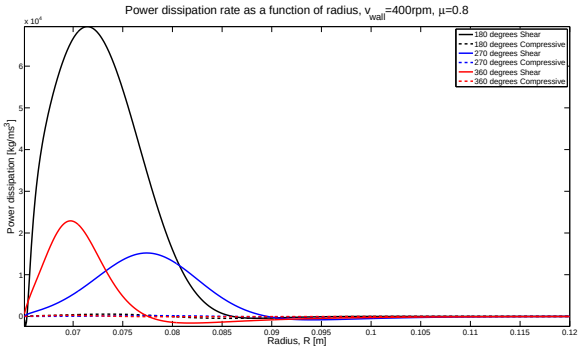

(d) $v_{wall} = 400\,\mathrm{rpm}$

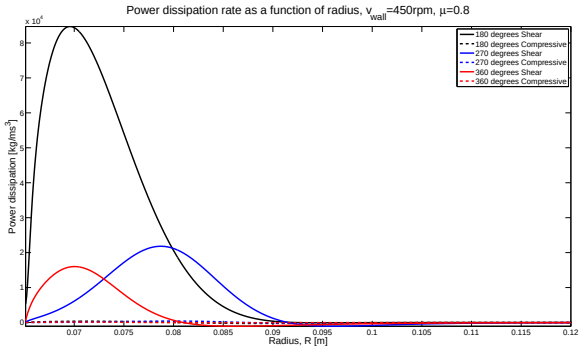

(e) $v_{wall} = 450\,\mathrm{rpm}$

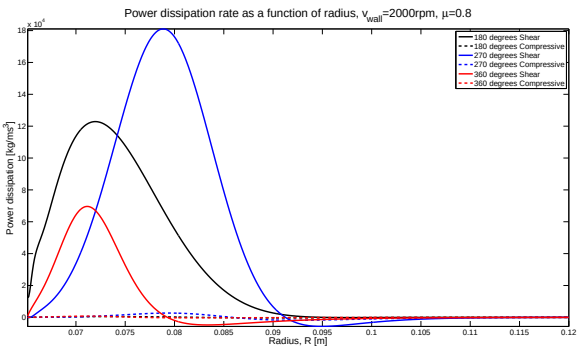

(f) $v_{wall} = 2000\,\mathrm{rpm}$

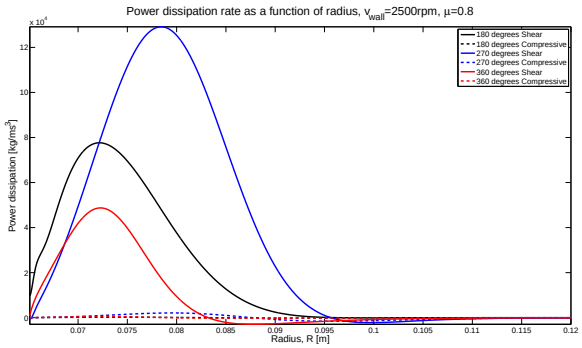

(g) $v_{wall} = 2500\,\mathrm{rpm}$

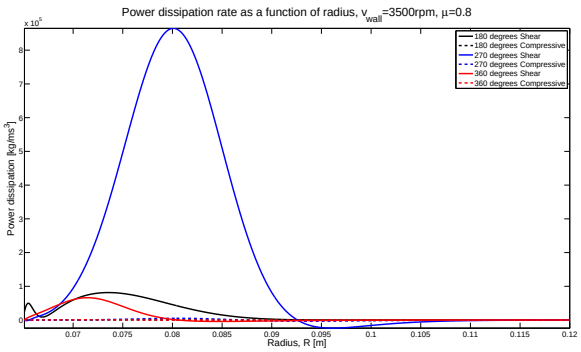

(h) $v_{wall} = 3500\,\mathrm{rpm}$

Figure 5.49.: Power dissipation over the selected angles, for a range of driving wall velocities.

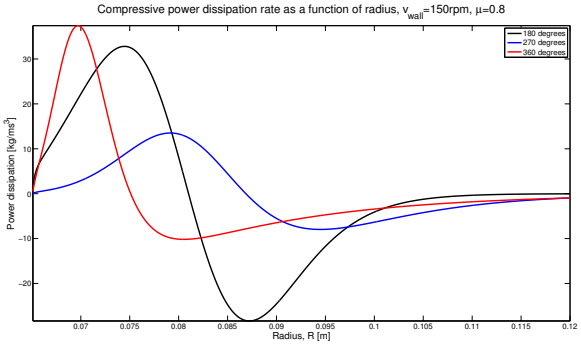

(a) $v_{wall} = 150\,\mathrm{rpm}$

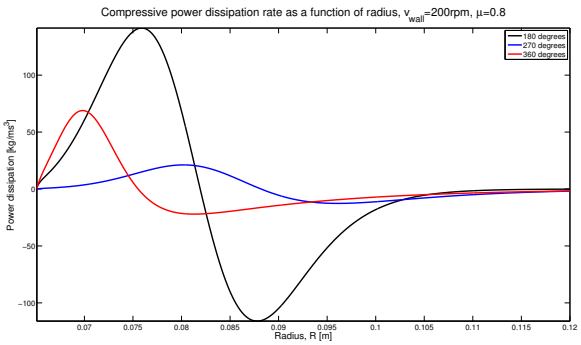

(b) $v_{wall} = 200\,\mathrm{rpm}$

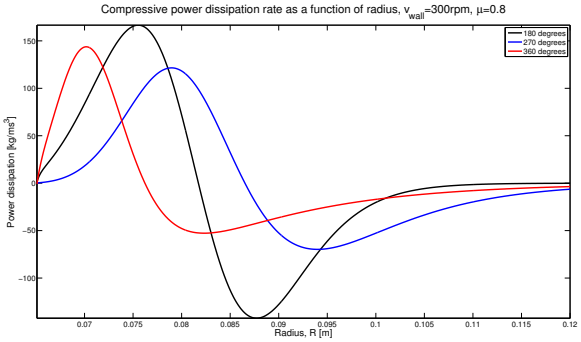

(c) $v_{wall} = 300\,\mathrm{rpm}$

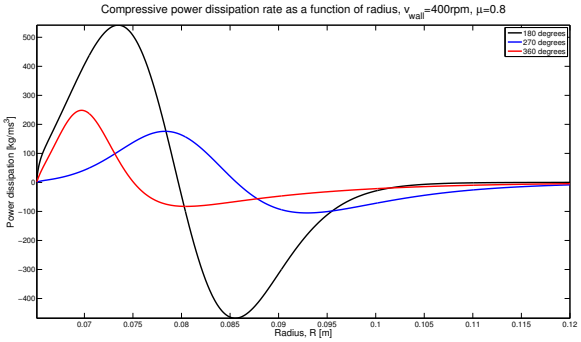

(d) $v_{wall} = 400\,\mathrm{rpm}$

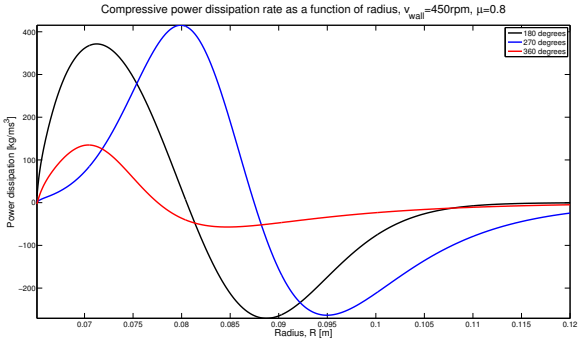

(e) $v_{wall} = 450\,\mathrm{rpm}$

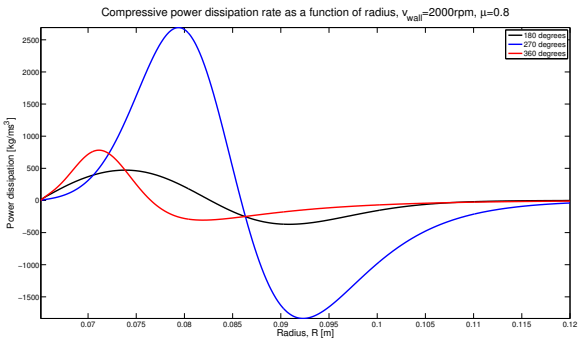

(f) $v_{wall} = 2000\,\mathrm{rpm}$

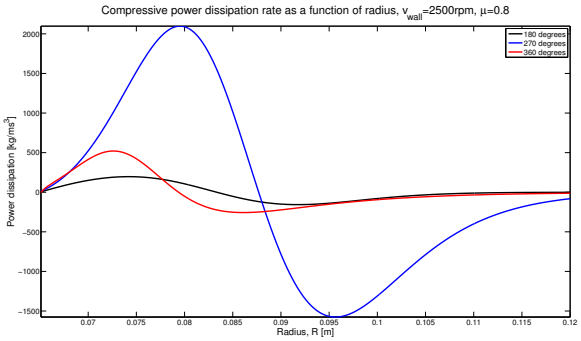

(g) $v_{wall} = 2500\,\mathrm{rpm}$

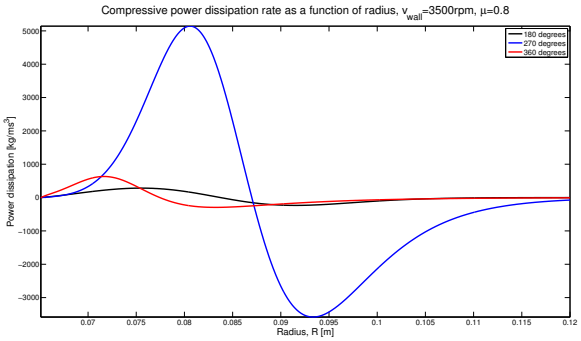

(h) $v_{wall} = 3500\,\mathrm{rpm}$

Figure 5.50.: Compressive power dissipation over the selected angles, for a range of driving wall velocities.

driving wall velocity configurations. As the velocity increases, the power dissipation at 270° becomes the largest. The compressive power dissipation is negative after the peak of the pressure distributions seen in Figure 5.33.

The distribution at a lower friction coefficient has a different behaviour, seen in Figure 5.52. For the lower friction coefficient, the maximum power dissipation is always at 360°. As is seen in the shear stress distributions, the mid-range driving wall velocity configurations have the maximum power dissipation rate, with the highest velocity configurations slightly larger than the lowest velocities. The behaviour of the distributions close to the driving wall is also quite erratic, the edge effects seen in the pressure and shear stress distributions having been amplified by the derivatives. The radial position of the maximum power dissipated in all configurations and angles is closer to the driving wall than in the $\mu = 0.8$ configurations.

The panel of figures in Figure 5.52 shows the components of the power dissipation rate, over the three angles selected for a range of driving wall velocities. As is the case for the $\mu = 0.8$ configurations, these $\mu = 0.5$ configurations show that the shear power dissipation component is by far the largest. Thus, the compressive power dissipation components are shown independently in Figure 5.53.

Figure 5.52 shows clearly that the greatest power is dissipated at 360° for all the configurations. At lower velocities, the power dissipation rate is similar for the 180° and 270° angles. As the driving wall velocity increases, the power dissipation rate at 270° increases, relative to the other angles, reaching it's highest position at 800 rpm. The power dissipation at 180° increases marginally, relative to the other angles, until 1000 rpm where it is greater than 270°. It then decreases again, along with 270°, until a minimum at 3500 rpm.

The compressive power dissipation rate, shown in Figure 5.53, shows similar behaviour to the $\mu = 0.8$ cases. The angular dependence of the maximum power dissipated shows similar behaviour to the shear power dissipation rate, with 360° always being the greatest. The relative behaviour of the power dissipation at 180° and 270° is the same as the shear power dissipation.

The radial position of the maximum power dissipation rate for each configuration is shown in Figure 5.54. The higher friction coefficient configurations at 270° have a maximum which is the farthest away from the driving wall. Apart from the initial oscillations in position of the lower velocity configurations, there is little change in position of the maximum of the higher velocity configurations. The position of the

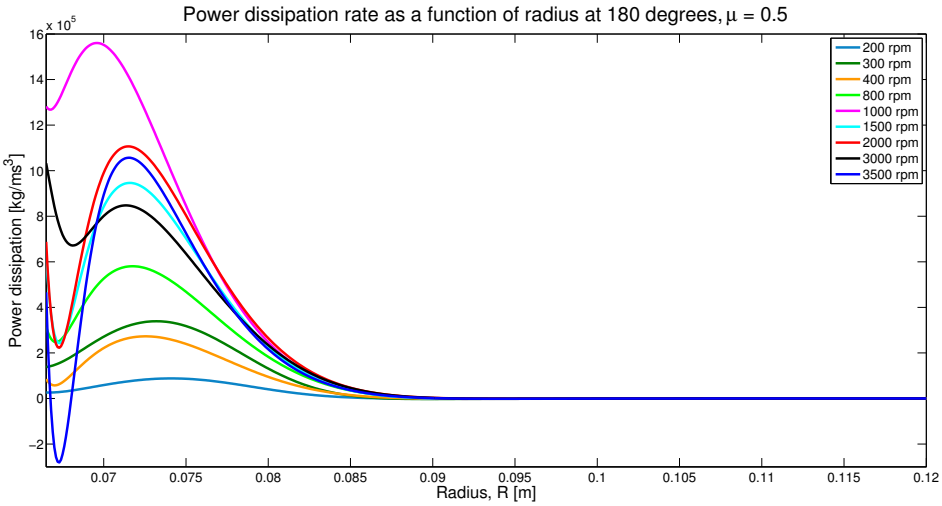

(a) Total power dissipation at 180°.

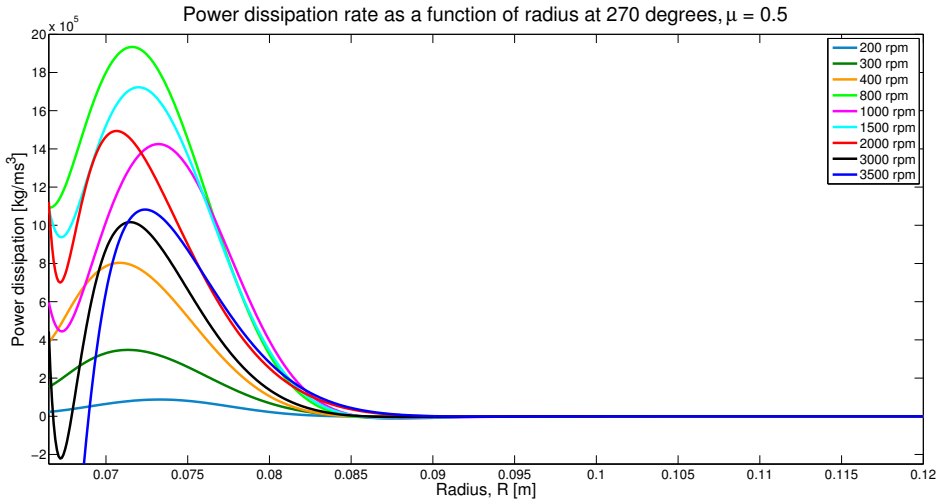

(b) Total power dissipation at 270°.

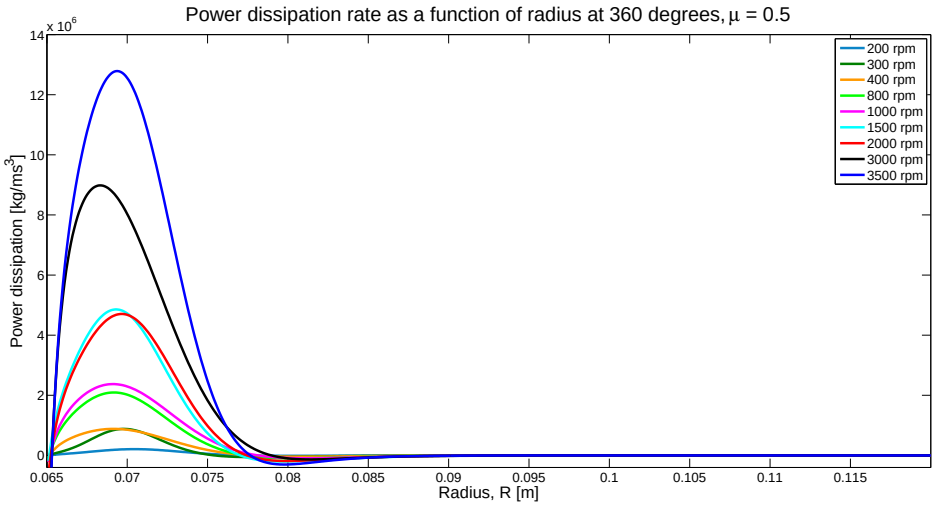

(c) Total power dissipation at 360°.

Figure 5.51.: Total power dissipation at 180°, 270° and 360°, $\mu = 0.5$.

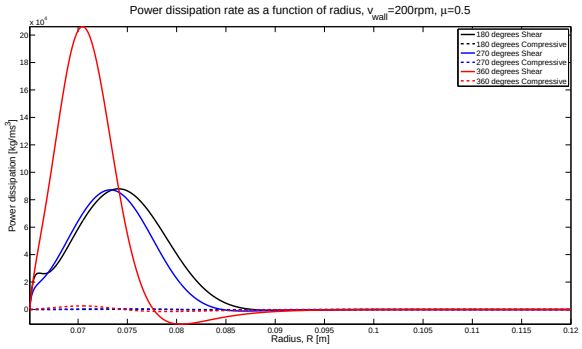

(a) $v_{wall} = 200\,\mathrm{rpm}$

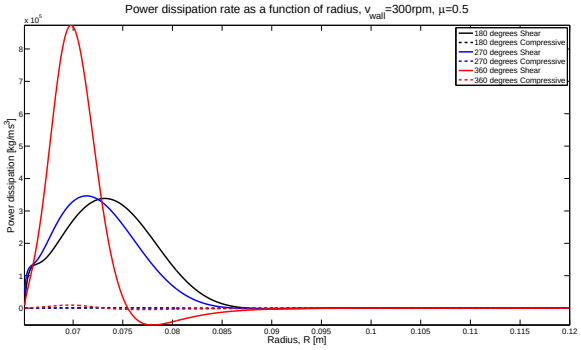

(b) $v_{wall} = 300\,\mathrm{rpm}$

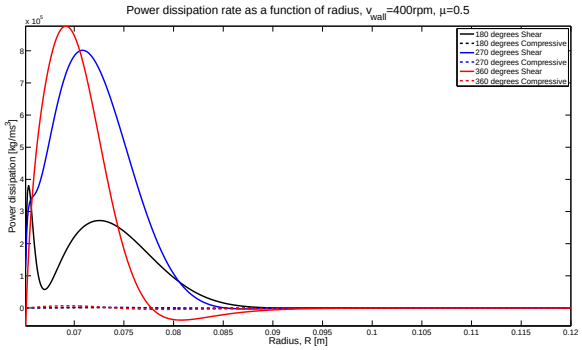

(c) $v_{wall} = 400\,\mathrm{rpm}$

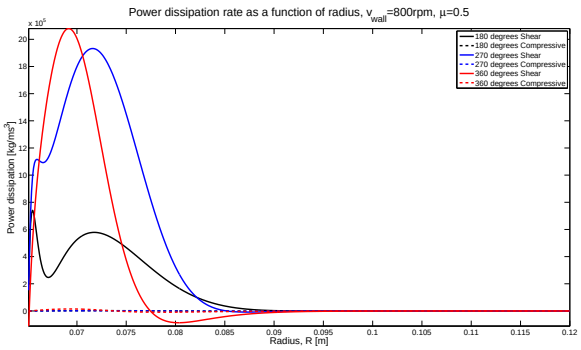

(d) $v_{wall} = 800\,\mathrm{rpm}$

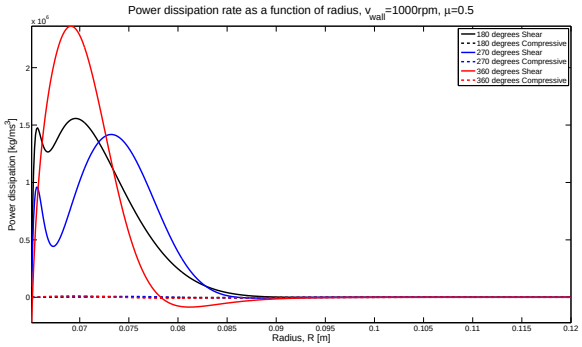

(e) $v_{wall} = 1000\,\mathrm{rpm}$

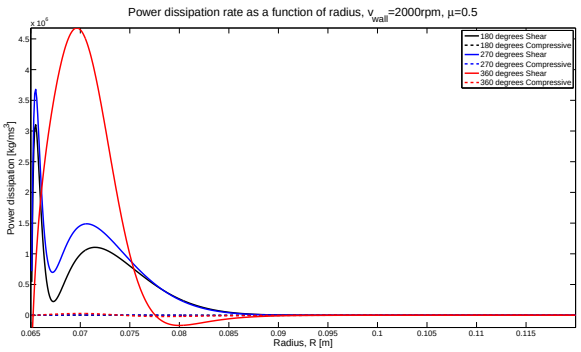

(f) $v_{wall} = 2000\,\mathrm{rpm}$

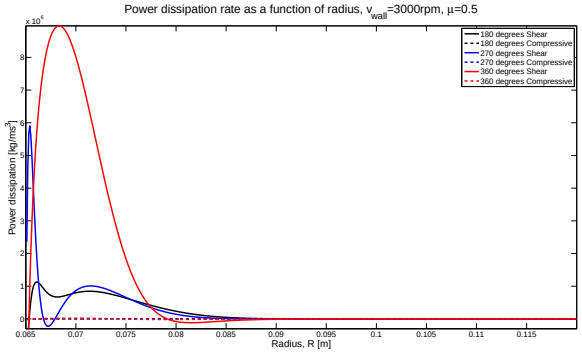

(g) $v_{wall} = 3000\,\mathrm{rpm}$

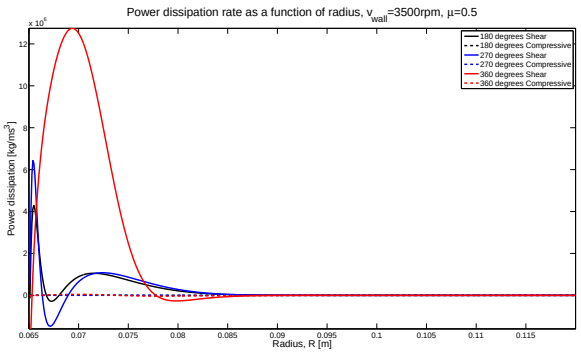

(h) $v_{wall} = 3500\,\mathrm{rpm}$

Figure 5.52.: Power dissipation over the selected angles, for a range of driving wall velocities.

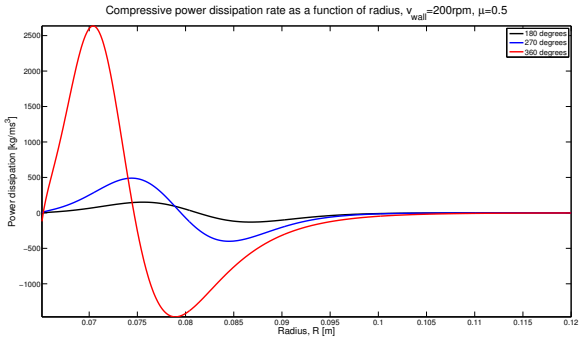

(a) $v_{wall} = 200\,\mathrm{rpm}$

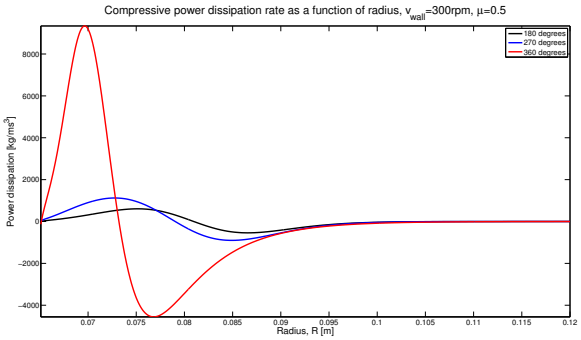

(b) $v_{wall} = 300\,\mathrm{rpm}$

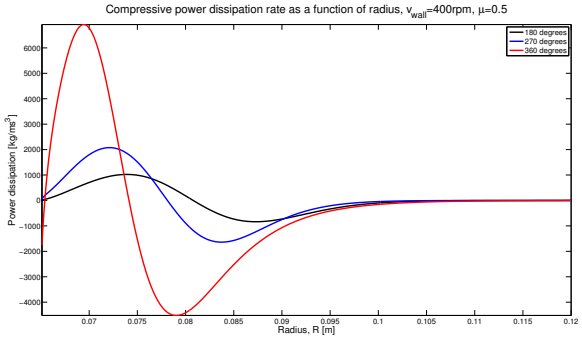

(c) $v_{wall} = 400\,\mathrm{rpm}$

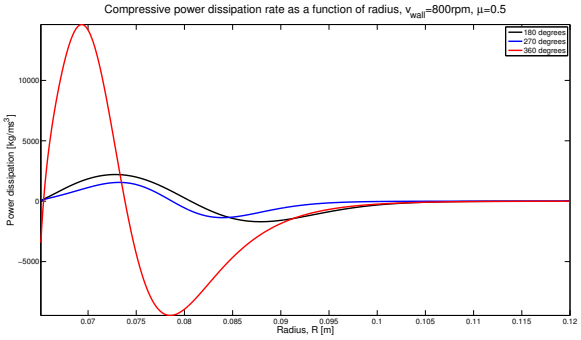

(d) $v_{wall} = 800\,\mathrm{rpm}$

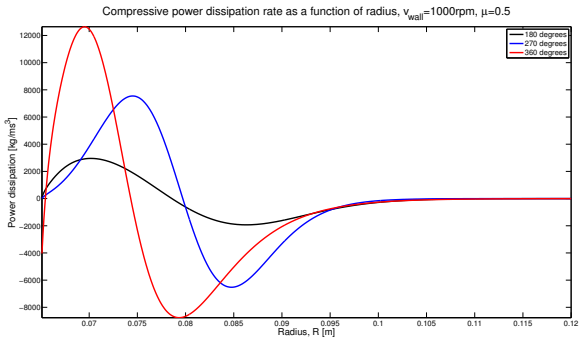

(e) $v_{wall} = 1000\,\mathrm{rpm}$

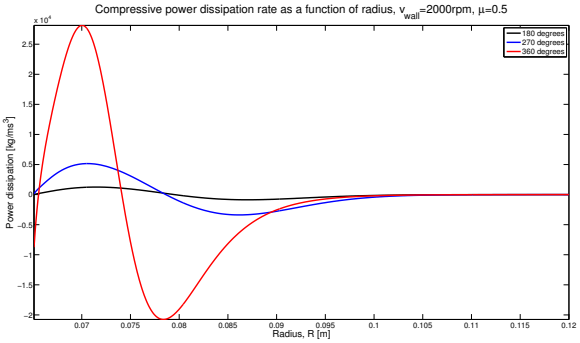

(f) $v_{wall} = 2000\,\mathrm{rpm}$

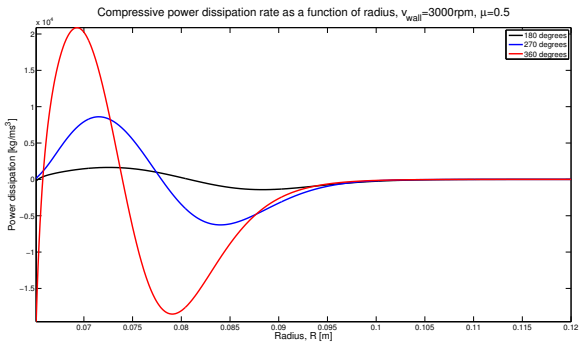

(g) $v_{wall} = 3000\,\mathrm{rpm}$

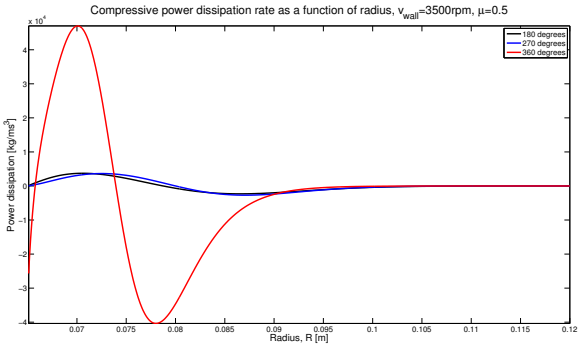

(h) $v_{wall} = 3500\,\mathrm{rpm}$

Figure 5.53.: Compressive power dissipation over the selected angles, for a range of driving wall velocities.

maximum at 180° changes quite considerably at the lower driving wall velocities, with a maximum distance occurring for the 250 rpm configuration. The $\mu = 0.8$ configurations at 360° have a more tightly confined maximum position, with a slight increase in distance away from the driving wall of the maximum as the velocity increases.

The $\mu = 0.5$ configurations do not have a well defined relationship between radial position of the maximum and velocity. The configurations have maximums at 360° that are much closer to the driving wall than the other angles, which behave similarly to each other.

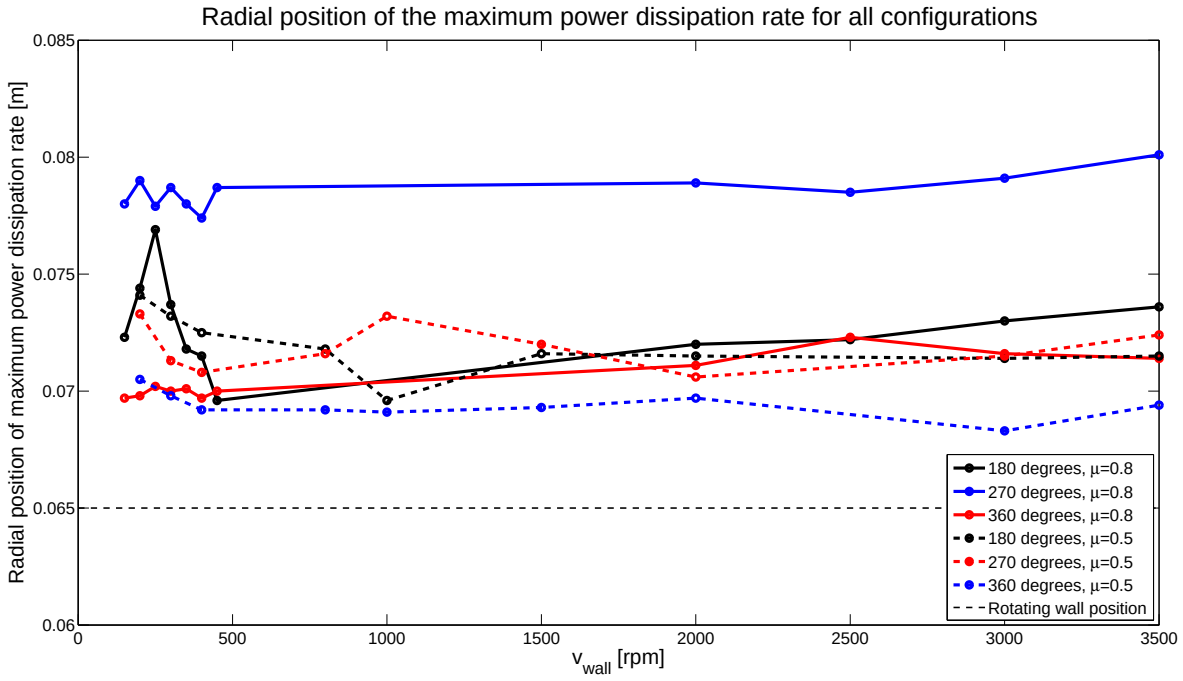

Figure 5.54.: The radial position of the maximum power dissipation rate for each configuration.

5.4. Summary

This chapter covered a thorough investigation of the dynamics of the horizontal annular shear cell. The simulations showed that a steady-state is eventually reached within the system and also confirmed the hypothesis that the tangential velocity component was much greater than the radial velocity component, as was seen in the PEPT experiments.

The volume fraction distributions showed that $0.1 < \phi < 0.7$, with the maximum located on the external wall of the shear cell. Minor differences were noted between the different angular selections of the volume fraction distributions.

DEM derived velocity distributions have a magnitude that is dependent on the angle within the system, while the shape was consistent. The non-dimensional velocity distributions showed that there is greater slip of the material on the shearing boundary at higher shearing velocities than lower ones. The coefficients of the exponential functions fit to the tangential velocity showed that there was a direct correlation between the driving wall velocity and the maximum velocity seen in the simulations. The natural length scale decreased as the shearing velocity increased.

The width of the shear band was found to depend mainly on the angle under consideration, rather than the driving wall velocity.

All three flow regimes were determined to be present within the shear cell, from the range on inertial numbers calculated. It was found that the quasi-static regime was the largest, covering almost half the annulus, while the dense and turbulent regimes were close to the driving wall.

The pressure distributions are no longer the simple hydrostatic pressure gradient along the rotation axis seen in shear cells with their rotation axis upright. The orientation of the shear cell greatly affects this distribution, as well as that of the shear stress distribution. In GDR MiDi [2004], the shear stress in the examined experiments decreased as $1/(y+R_i)^2$ in the xy-plane and the pressure was constant in this plane. In this work, both distributions are described as Gaussian in shape, mostly confined to the rapidly sheared region. There is an angular dependence, as well as a dependence on shear rate and friction coefficient.

The quasi-static components of the pressure and shear stress were the most dominant terms and increased as the driving wall velocity increased. The distributions on the downward side (180°) were symmetric, while the upward side (360°) were skewed towards the driving wall.

The total pressure and shear stress distributions were used to calculate the effective friction coefficient distributions over the annulus of the shear cell. These distributions allowed for the relative importance of the shear stress and pressure within the shear cell annulus to be gauged. It was found that for the majority of cases, the flow was pressure dominated close to the shearing wall, in the same region where the dense and turbulent flow regimes occur. The transition to a flow dominated by the shear stress occurred in the same region as the edge of the shear band. Beyond this transition, the effective friction coefficient distributions showed a linear relationship, in the region of the shear cell believed to be experiencing quasi-static flow.

The power dissipation also showed an angular dependence. It was found that the shear power dissipation component played the largest role in the dissipation and the greatest dissipation occurred within 5 particle diameters of the shearing wall. The compressive power dissipation was largest at the bottom of the shear cell, where the material was moving perpendicular to the direction of gravitational acceleration.

A closer examination of the velocity and volume fraction profiles in relation to the PEPT experiments and experiments discussed in GDR MiDi [2004] follows in Chapter 6.

Part IV.

Validation and Comparison

Chapter 6.

Validation and Comparison

The annular shear cell has been studied extensively in both experiments and simulations. GDR MiDi [2004] used experimental results from Mueth et al. [2000], da Cruz [2004], Da Cruz et al. [2002], Chambon et al. [2003] and Bocquet et al. [2001] to examine the kinematic properties of the flow in the shear cell. These experiments used a range of techniques including Magnetic Resonance Imaging, X-ray Tomography and High Speed Imagining, with particles ranging in size from 0.25 to 2 mm. The distance between the shearing wall and the outer wall ranged between 9 and 100 particle diameters. In both the PEPT experiments and DEM simulations described in this thesis, the diameter of the particles was 5 mm and the gap between the walls was 10 particle diameters wide. In the experiments and simulations examined by GDR MiDi [2004], the motion of the inner cylinder was either controlled by imposing the torque or the rotation rate. The rotation rate is imposed in the experiments and simulations completed here.

Simulations conducted on annular shear cells include the work of Lätzel et al. [2000], Schollmann [1999] and Koval et al. [2009]. These simulations were done in 2D using DEM and Molecular Dynamics (MD). A 2D simulation using a Cellular Automata model was conducted by Jasti and Higgs [2009] with the results being compared with experimental work.

There are considerable differences between these closely examined systems and the system under study in this thesis. First and foremost is the orientation of the rotating axis. This work is performed with the rotational axis horizontal, or perpendicular to the direction of gravity. This change in orientation results in a previously unexamined angular asymmetry in the velocity, volume fraction and other dependent distributions. The next difference comes in at the applied shear. Where most experiments are run below 100 rpm, these experiments and simulations are run at 150 rpm up to 3500 rpm.

The simulations were of a fully 3D system, closely matching the PEPT experiment dimensions.

A comparison of the kinematic properties of the flow derived from the PEPT experiments and DEM simulations with those discussed in GDR MiDi [2004] follows.

6.1. Kinematic flow properties

6.1.1. Velocity profile comparison

In their paper GDR MiDi [2004] use results from three different experiments performed on shear cells to generate an overview of the velocity profile. These results are reproduced in Figure 6.1 to aid with comparison of the DEM and PEPT results presented in this thesis. The same format is used to present the velocity profiles of the DEM simulation results in Figures 6.2, 6.3 and 6.4 and the PEPT data in Figure 6.5. In these figures, the first panel is the tangential velocity as a function of radius, that has been normalised by particle diameter, the middle panel shows the velocity on a logarithmic scale, while the right-hand side panel shows the velocity on a logarithmic scale against the square of the particle diameter.

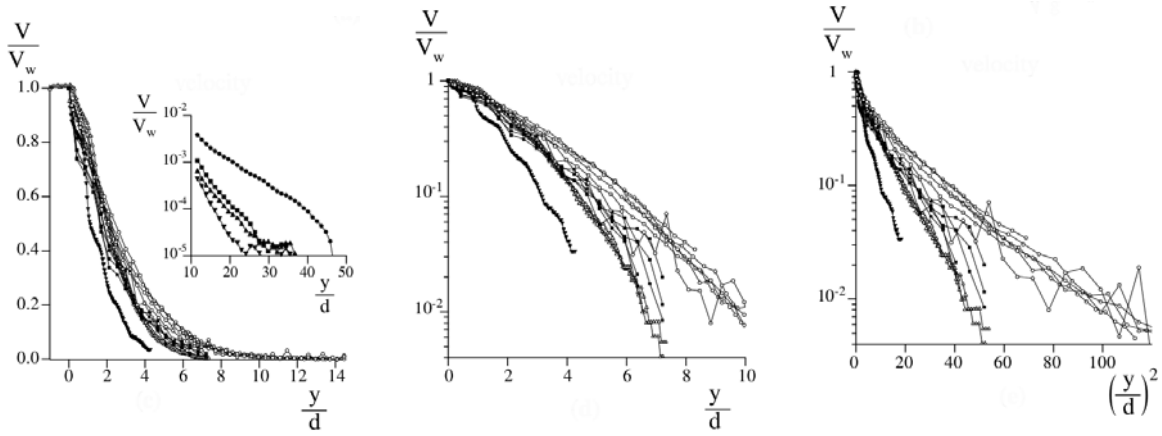

Figure 6.1.: Velocity profiles as presented in GDR MiDi [2004].

In the top row of Figures 6.2, 6.3 and 6.4, the velocity has been normalised by the shearing wall velocity, as is the case in the GDR MiDi [2004] paper. However, considerable slip occurs in the experiments and simulations performed here, so in order

to make the results truly comparable, the velocity normalised by it's maximum value in each experiment has been presented in the bottom row. The results are also split according to the angle at which they were extracted, as the profiles have an angular dependence.

In GDR MiDi [2004], the shear is localised to a few particle diameters from the shearing wall and the profiles are qualitatively similar in all experiments. The shape of the profile does not appear to depend on the shearing rate. Both Gaussian and exponential profiles have been suggested, with the results in GDR MiDi [2004] showing that the experimental profile decays slightly faster than an exponential (Figure 6.1b) and behaves rather like a Gaussian (Figure 6.1c) when not too close to the shearing wall.

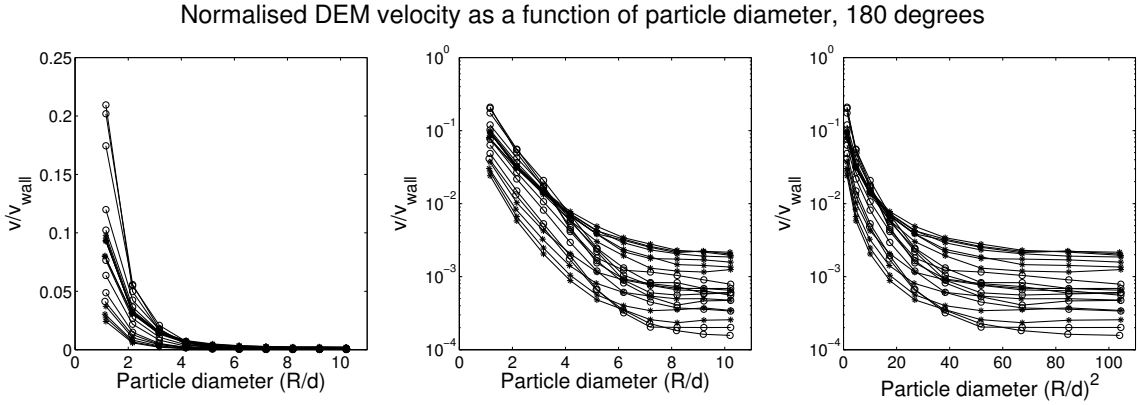

(a) Velocity profiles normalised by the shearing wall velocity.

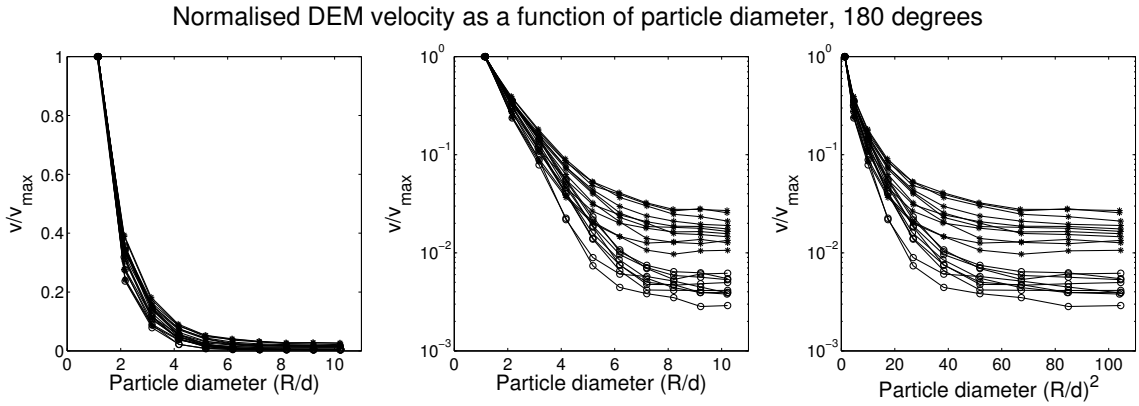

(b) Velocity profiles normalised by the maximum velocity in each experiment.

Figure 6.2.: Velocity profiles at 180°, the open circle data points represent $\mu = 0.5$ and the stars represent $\mu = 0.8$.

The velocity profiles derived from the DEM simulations differ considerably from the profiles shown in GDR MiDi [2004]. The shear is still localised close to the shearing wall and the profile shapes are independent of the shearing velocity. The DEM profiles are exponential in the shear band with a constant tail beyond this. The second panel clearly

shows that in the DEM simulations there is a plug flow region on the outer part of the system. The width of the shear band (and hence plug flow region) has a dependence on shear rate, angle of observation and friction properties of the material. The shape of the profile plotted on a logarithmic axis is similar to that observed in Schollmann [1999], whose MD simulations showed an exponential tangential velocity within the shear zone.

The shear band width is dependent on the angle of the measurement. In the logarithmic plot in Figure 6.3 (270°), the constant tail is much shorter than in the 180° case, while in Figure 6.4 (360°), the tail disappears entirely. In this case, the velocity does not remain exponential in the tail region, becoming almost Gaussian.

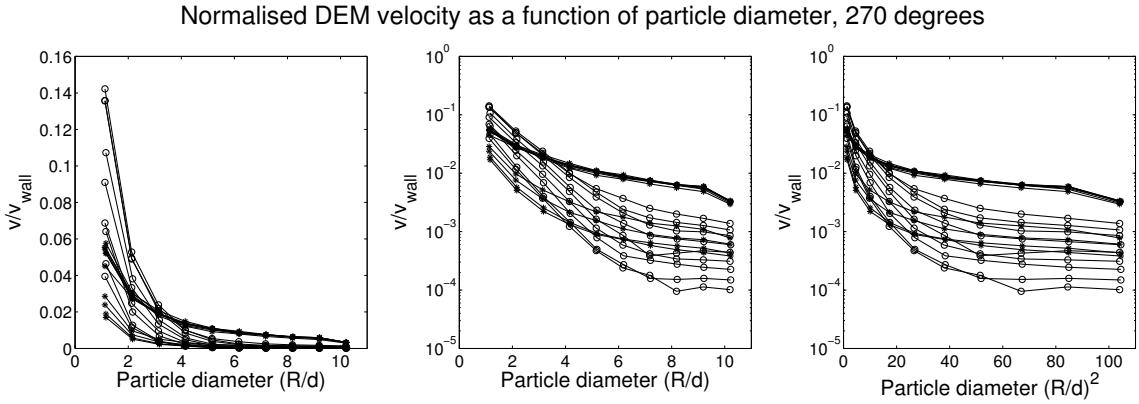

(a) Velocity profiles normalised by the shearing wall velocity.

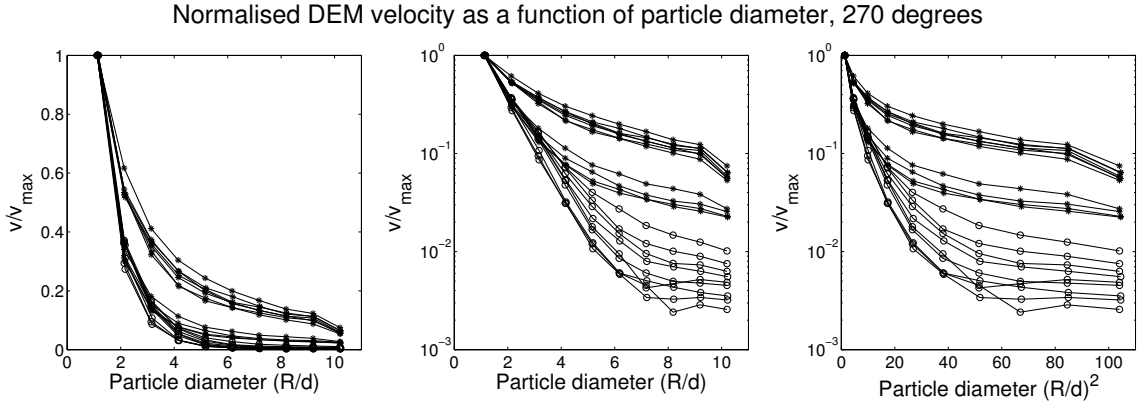

(b) Velocity profiles normalised by the maximum velocity in each experiment.

Figure 6.3.: Velocity profiles at 270°, the open circle data points represent $\mu = 0.5$ and the stars represent $\mu = 0.8$.

In this normalised format, it is apparent that the friction between the particles in the simulations has an effect on the velocity profile. The higher friction coefficient profiles (the star data points) are less steep in the tail region than the lower friction coefficient. This is contrary to the findings of Schollmann [1999], who claimed a comparatively weak influence of the friction coefficient on the velocity profiles.

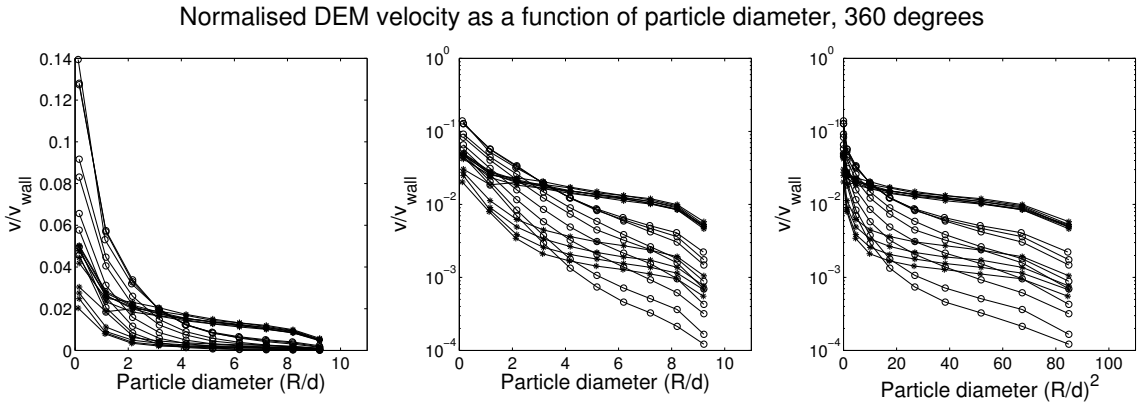

(a) Velocity profiles normalised by the shearing wall velocity.

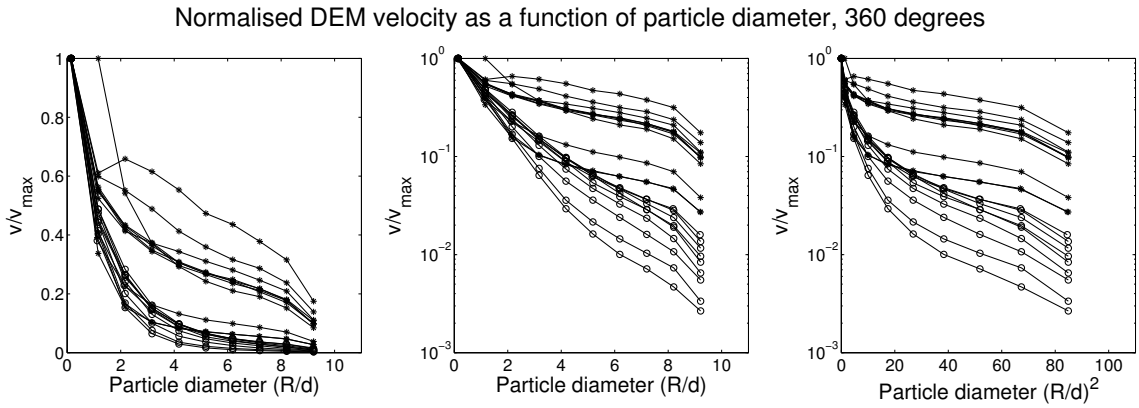

(b) Velocity profiles normalised by the maximum velocity in each experiment.

Figure 6.4.: Velocity profiles at 360°, the open circle data points represent $\mu = 0.5$ and the stars represent $\mu = 0.8$.

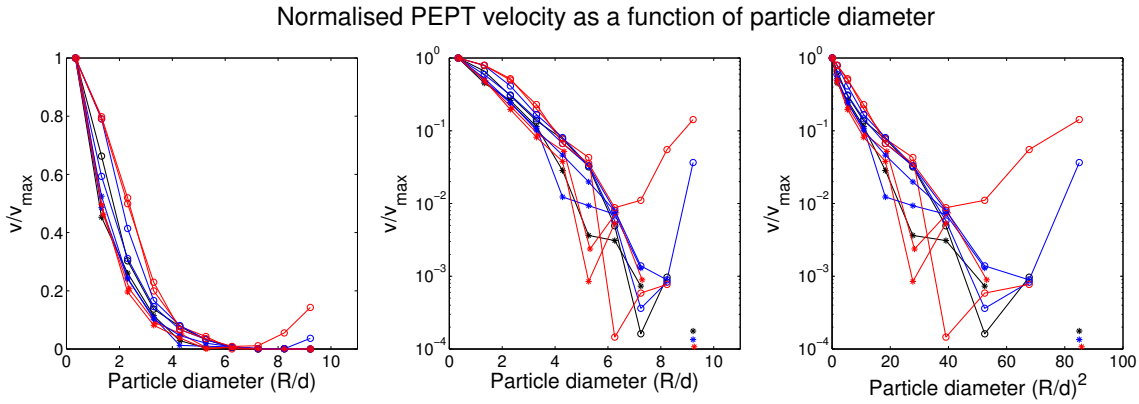

Figure 6.5.: Velocity profiles derived from PEPT data, where the colour represents the angle in the rig (black is at 180°, blue is 270° and red is 360°). The open circle data points correspond to the grooved driving wall, while the stars are the beaded wall data points.

The velocity profiles derived from the PEPT data show better agreement with GDR MiDi [2004]. Close to the shearing wall, a more Gaussian profile is suggested by the

right hand side plot in Figure 6.5. However, the tail behaviour is unclear. The shear is still localised to a few particle diameters of the wall. There is not an obvious change in velocity profile with the change in angle, although the difference due to the different surfaces of the shearing wall is apparent. The open circles represent the grooved cylinder configurations and they appear to have a more Gaussian profile than the profiles from the beaded surface, which are closer to exponential (close to the shearing wall).

6.1.2. Volume fraction comparison

The volume fraction profiles seen in Mueth et al. [2000] show a slight increase of volume fraction with radial distance from the inner wall. These profiles include the seeds that were glued to the inner wall, thus the profile decreases from its highest point at the inner wall, up to $r/d \approx 1$, and then it increases gradually to the outer wall. In this work, layering of the particles is apparent in the profiles and has a larger effect on the spherical particles profile than it does on the non-spherical one.

The DEM derived volume fraction profiles also show an increase with radial distance from the shearing wall. This increase is sharp in the shearing zone and levels off to a maximum value in the outer region of the shear cell. The PEPT profiles show an increase from the inner wall, to a maximum and then a rapid decrease with distance to the outer wall. This outer edge behaviour is due to the lack of coverage in this zone in the experiments.

Jasti and Higgs [2009] have explored the volume fraction profile changes with wall roughness and particle-particle coefficient of restitution. Qualitatively, the profiles evident here are similar to those derived in the DEM simulations. These profiles start from a low point at the shearing wall and increase to their highest point at the stationary wall.

6.1.3. Flow rate and average velocity

The change in the flow regime evident in the logarithmic plots of the tangential velocity was used to define the shear band width for each configuration. This width was selected by calculating the change in the gradient of the velocity. When this change was approximately 0, the radial distance was taken as the edge of the shear band, as beyond this point, the velocity was constant with radius, making this a plug flow region. This is a more rigorous definition of the shear band width than the somewhat arbitrary selection of shear rate dropping below $1\,\mathrm{s}^{-1}$ used previously.

The average velocity (derived from PEPT data and DEM simulation results) as a function of shear band width is shown in Figure 6.6. The shear band values are clumped along specific r/d values because the data is discretely binned at 5 mm intervals.

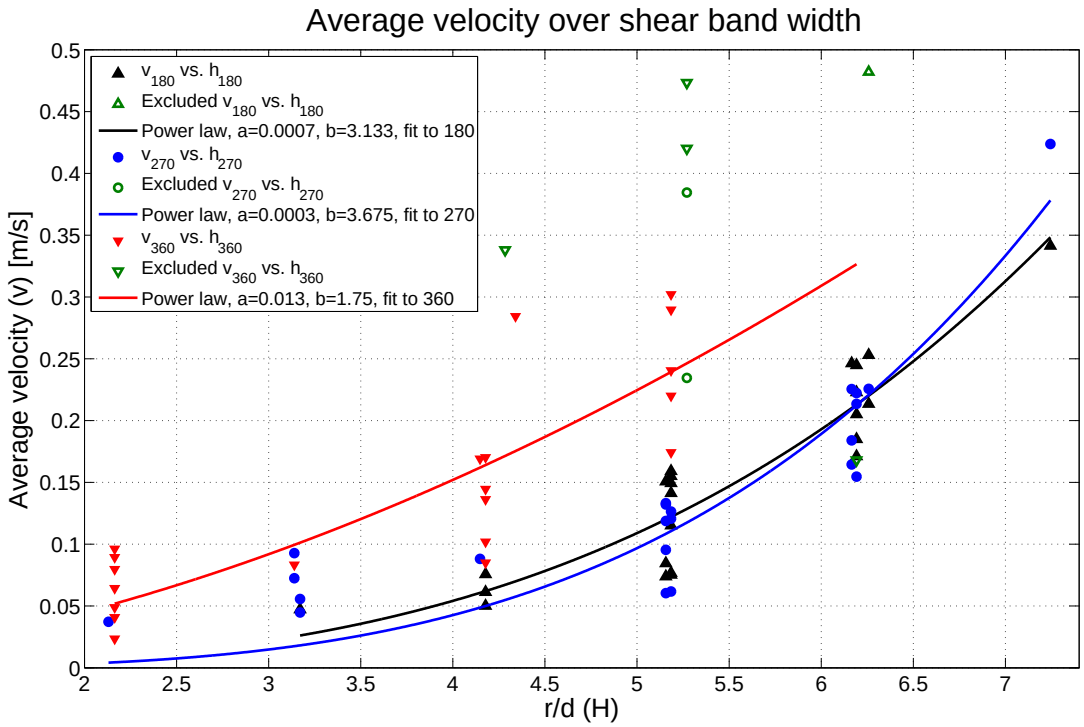

Figure 6.6.: Average tangential velocity calculated over the shear band width for all configurations. Each power law fit is shown in the same colour as the relevant data, with the excluded data points in green.

A power law was fit to these data for each angle examined in the shear cell. The equations for each angles distribution were $v_{180} = 0.0007H^{3.13}$, $v_{270} = 0.0003H^{3.68}$ and $v_{360} = 0.01H^{1.75}$. The goodness of fit calculation for each fit produced r-squared values of 0.86, 0.82 and 0.72 respectively. Data points that were considered outliers were excluded from the calculation of these power law fits (shown in green in Figure 6.6).

The distributions at 180° and 270° are similar, while the distribution from the 360° data is quite different. This trend is seen throughout the analysis of the DEM simulation results.

The flow rate (normalised over the length of the shear cell) was calculated from the above data, given that $Q/L = \langle v_\theta \rangle H$. This is shown in Figure 6.7, where the colours represent the different angles, while the data point shape differentiates the friction conditions (or driving wall condition). The distribution follows the form of the average

velocity, increasing with increasing shear band width. At smaller shear band, the flow rates are closer together, spreading out further as the shear band increases in width.

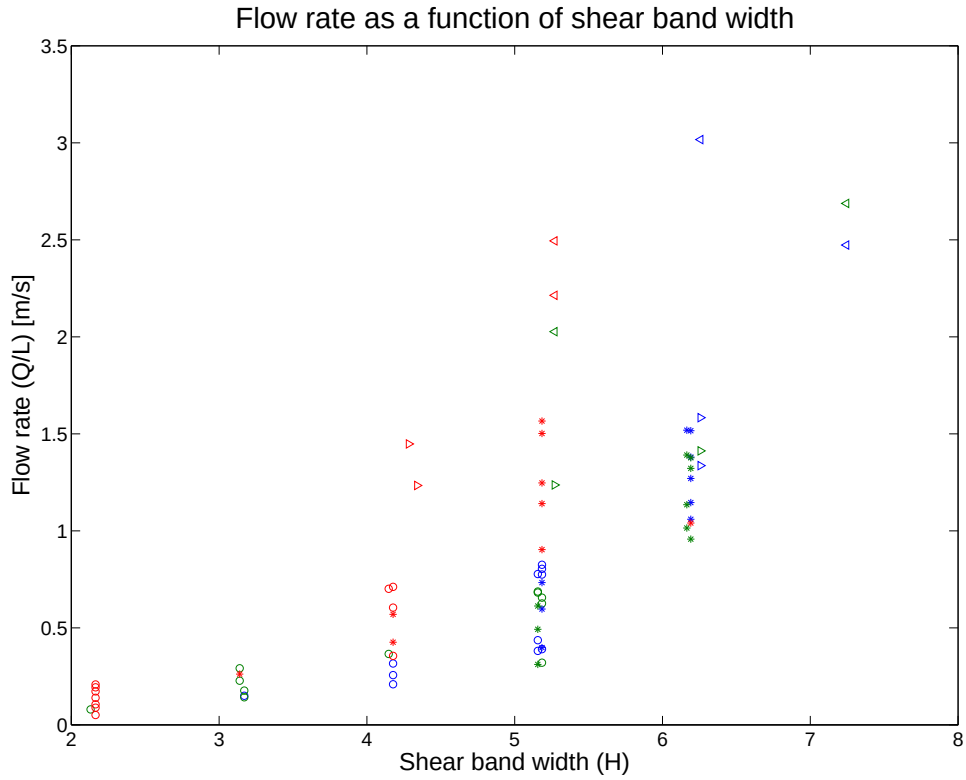

Figure 6.7.: Flow rate calculated over the shear band width for all configurations. The colours represent the angles (blue is 180°, green is 270°, red is 360°), while the plot shape represents the different friction configurations (the open circle is the $\mu = 0.8$, DEM data, the star the $\mu = 0.5$, DEM data, the left triangle is the beaded wall PEPT data and the right triangle is the grooved wall PEPT data).

A power law was fit to this data, excluding the obvious outliers from the fit, with results,

$$Q = 0.0003H^{4.58} + 0.19. \tag{6.1}$$

and an R-squared value of 0.8. This function fit is shown in Figure 6.8.

Power law fits to each angle resulted in better fits for the 180° and 270° distributions. These functions are $Q_{180} = 0.0007H^{4.134} + 0.003$, $Q_{270} = 7.8 \times 10^{-5}H^{5.23} + 0.18$ and $Q_{360} = 0.016H^{2.66} + 0.0013$, with R-squared values for these fits of 0.92, 0.90 and 0.77 respectively.

Attempting to find a single function that effectively describes all the flow rate data requires the non-dimensionalisation of the flow rate. Various attempts were made, with

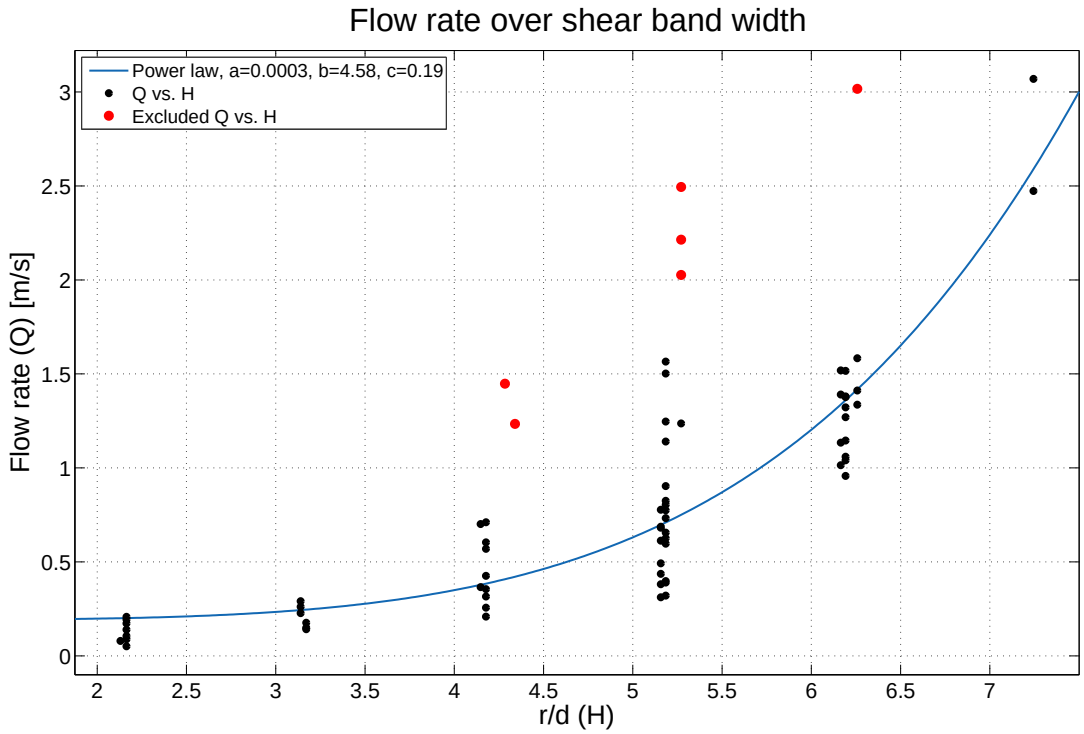

Figure 6.8.: Flow rate calculated over the shear band width for all configurations. The power law fit is shown, along with the excluded outliers.

the most effective shown in Figure 6.9. The material moves in a non-uniform circular motion, thus the effect of the radial and tangential acceleration needs to be accounted for, along with particle size, angle and friction coefficient. The most effective non-dimensionalisation was found to be $\frac{\mu Q}{\sqrt{(\dot{\gamma}^2 r+g)d}}$, although the flow rate is still more spread out at higher shear band values.

6.2. Summary

The data from the PEPT experiments and results from the DEM simulations were compared with the results shown in GDR MiDi [2004], as well as other shear cell literature.

The volume fraction profiles from DEM match qualitatively those from Jasti and Higgs [2009], and differed in the shear region from those of Mueth et al. [2000].

Velocity profiles derived from the DEM simulations were found to have an exponential behaviour in the shear band, with a constant tail. This width of this tail decreased as

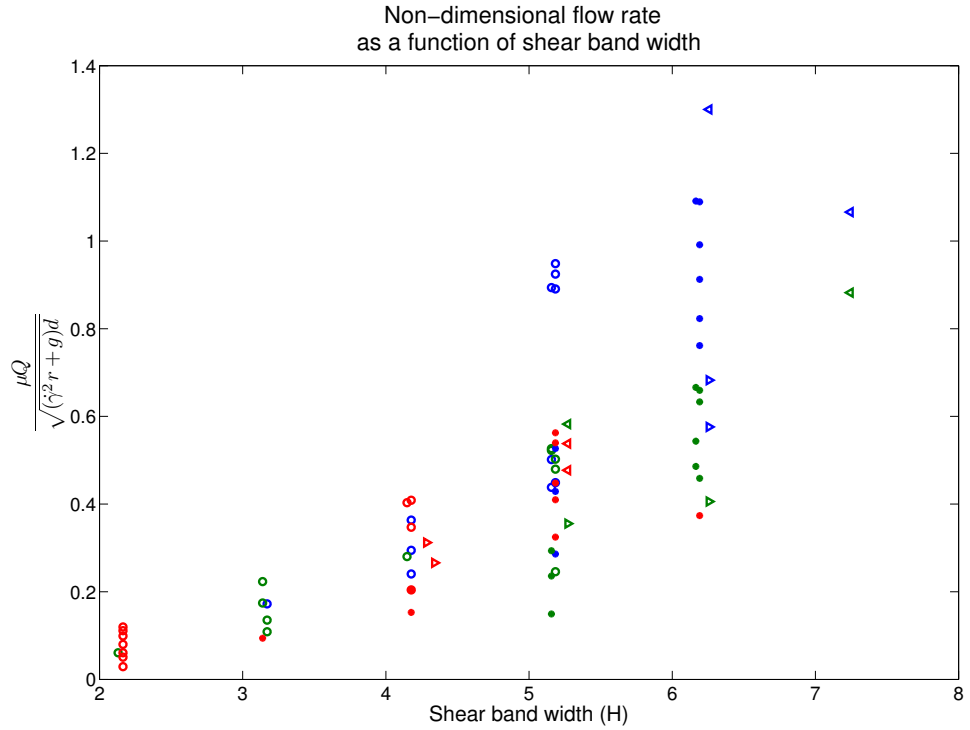

Figure 6.9.: Non-dimensional flow rate calculated over the shear band width for all configurations. The colours represent the angles (blue is 180°, green is 270°, red is 360°), while the plot shape represents the different friction configurations (the open circle is the $\mu = 0.8$, DEM data, the star the $\mu = 0.5$, DEM data, the left triangle is the beaded wall PEPT data and the right triangle is the grooved wall PEPT data).

the angle around the shear cell increased, all but disappearing at 360°. These profiles were qualitatively similar to those seen in Schollmann [1999].

The behaviour of the velocity within the shear band, as derived from the PEPT experiments, more closely followed the behaviour described in GDR MiDi [2004]. These data showed an almost Gaussian profile in the shear band. The tail behaviour could not be derived from the PEPT results.

The logarithmic plots of the velocity were used to form a more rigorous definition of the shear band width. An examination of the average velocity over the shear band width was performed. This showed a power law distribution. As seen elsewhere in the thesis, the behaviour at 180° and 270° was similar, with the 360° distribution differing from them both.

The flow rate of material through each radial line selected was examined. This data also followed a rough power law, although the data points were confined close together at smaller shear bands, becoming more spread out as that width increased. A

non-dimensionalisation of the flow rate was examined, in order to find a suitable scaling. The closest that could be determined was $\frac{\mu Q}{\sqrt{(\dot{\gamma}^2 r+g)d}}$. Even with this non-dimensional scaling, the data are still confined at lower shear bands and spread out at larger shear bands.

Part V.

Conclusion

Chapter 7.

Conclusion

Motivated by the need for a more effective model of particle dynamics leading to the fine grinding taking place in an IsaMill^{TM}, a granular flow model of a horizontally run annular shear cell was developed. As a single encompassing theory for granular flows does not yet exist, a combinatorial stress model was developed. This utilised components of the shear stress tensor developed in literature [Bagnold, 1954b, Takahashi, 2009, Jop et al., 2006, Lee and Huang, 2012] and the constitutive relations of GDR MiDi [2004] and Jop et al. [2005]. The quasi-static shear stress was described by an empirical distribution that depends on both the volume fraction distribution, $\phi(I)$, and inertial number, I. An empirical dilatancy law was developed, $\phi(I) = \phi_{max}e^{-bI^c}$, motivated by the need for the volume fraction distributions to range $0 < \phi < 0.7$ for the range $10^{-4} < I < 1$. The coefficients, b and c were investigated using simulation results. The combinatorial stress was used to derive a description of the effective friction coefficient (Equation 2.24) that captures all flow regimes of granular flow. Figure 2.4 provided the general shape of this effective friction coefficient.

The visco-plastic rheology was incorporated into an athermal energy balance to derive a model for the power dissipation distribution, due to normal and shear stresses (Equations 3.50 and 3.51). Both Positron Emission Particle Tracking (PEPT) experiments and Discrete Element Method (DEM) simulations were used to derive inputs to this model and further study the dynamics within the shear cell. As the hypothesis was made that movement in the z-direction would be limited in relation to the θ-direction, all relevant data was projected onto the r-θ plane, reducing the analysis to a 2-dimensional problem.

The volume fraction distributions derived from the PEPT experiments, seen in Figure 4.7, did not fully cover the annulus. This was due to the existence of a region of

slow moving, dense material (a plug flow region) on the outer part of the annulus. The tracer particle seldom ventured into this region in the experiment runs of 15 min and longer runs were not possible due to heating of the granular media within the shear cell and fear of destroying the tracer particle. For this reason, computer simulations of the system were performed using DEM, which did not have the same susceptibility to the plug flow region, as all the particles in the system are tracked at the same time.

The region of flow explored in the PEPT experiments showed the volume fraction in this region to be $0 < \phi < 0.375$, which corresponds to the dense and collisional regimes ($I > 0.03$). As no functional form of the volume fraction could be extracted, the calculation of the inertial number, shear stress, pressure or power dissipation could not be performed.

PEPT velocity distributions showed that the model hypothesis of a dominant tangential velocity was indeed true. The tangential velocity distributions were initially modelled as exponential functions, shown in Figure 4.15, but it was found in Chapter 6 that they followed a Gaussian distribution more closely in the sheared region. The data were analysed at selected radii in the shear cell, which showed that velocity did have an angular dependence due to the orientation of the rotation axis.

Although the PEPT experimental system indicated a rise in temperature of the material, the meso-scale model developed in this thesis was purpose designed to be insensitive to thermal fluctuations. This is further supported by the fact that the velocities of the large particles used in this work are not discernible at the model scale. Thus, the athermal hypothesis used in the power dissipation model development is considered valid.

Simulations performed on the system using DEM allowed for a thorough examination of the power dissipation model, including the angular dependence created by the horizontal orientation and the dependence on two different friction coefficients of the simulated glass beads.

All three granular flow regimes were determined to be present in the annular shear cell. The volume fraction distributions covered the range $0.1 < \phi < 0.7$, which resulted in the inertial number range $0 < I < 1$.

The volume fraction and velocity components (tangential and radial) were extracted along radial lines, corresponding to the same radial lines examined in the PEPT experiments. Function fits to these data were used to calculate the shear rate, inertial number, pressure, shear stress and effective friction coefficient along these lines. These

distributions all showed a dependence on the driving wall velocity, friction coefficient and the angle under examination.

The volume fraction distributions (Figures 5.12 to 5.15) started low at the shearing wall and increased to a value close to the random close packing limit for spheres. These distributions were similar to those seen in Jasti and Higgs [2009]. The tangential velocity was found to follow an exponential distribution (Figures 5.22 and 5.23), with a constant velocity tail in the plug flow region. The distributions of the inertial number in Figures 5.30 and 5.31 showed that the turbulent and dense flow regimes were limited to the region within 5 particle diameters of the shearing wall, while the quasi-static regime (the plug flow region) covered almost half the annulus, depending on the angle.

On the side of the shear cell that had material moving in the direction of the gravitational acceleration, the pressure and shear stress distributions were symmetric, as seen in Figures 5.33, 5.36, 5.39 and 5.42. This extended to the bottom of the shear cell, where the material was moving perpendicular to the gravitational acceleration. On the upward moving side, the distributions were skewed towards the shearing wall and tended to have a longer tail extending through the quasi-static regime. The quasi-static component was the most dominant contribution to the total pressure and shear stress distributions. In the simulations with a lower friction coefficient, the total pressure and shear stress distributions were narrower than their higher friction coefficient counterparts, with a shorter tail.

The effective friction coefficient distributions, shown in Figures 5.46 and 5.47, over the shear cell annulus allowed for the relative importance of the shear stress and pressure within the shear cell annulus to be determined. It was found that close to the shearing wall, the flow was dominated by pressure ($|\frac{\tau}{P}| < 1$), while the region beyond the shear band was dominated by the shear stress. In this shear dominated region, quasi-static flow occurs, and the effective friction coefficient had a linear relationship with the radial distance from the shearing wall.

The power dissipation distributions were calculated along the selected radial lines. Here it was discovered that the shear power dissipation component was the greatest contribution to the total power dissipation (apparent in Figures 5.49 and 5.52), which was largest in the region less than 5 particle diameters from the shearing wall. In general, the magnitude of the power dissipation increased as the driving wall velocity increased. As with the shear stress and pressure distributions, the lower friction coefficient had a narrower power dissipation band, the width of which was largely independent of the shearing wall velocity (in both high and low friction cases). The angle of observation

affected the magnitude of the distribution (the maximum value reached) and the symmetry of the distribution, seen clearly in the total power dissipation distributions of Figures 5.48 and 5.51. Here, the material moving perpendicular to the direction of the gravitational acceleration had a symmetric power dissipation distribution, while the other angles had maximums skewed towards the shearing wall.

Data from DEM and PEPT were used in Chapter 6 to calculate the average velocity (Figure 6.6) and flow rate (Figure 6.8) over the width of the shear band, for each configuration studied. A power law relation was fit to this data, so $\langle v \rangle \propto H^n$, where n was found to vary with angle. For the 180° and 270° cases, $n = 3.13$ and 3.68 and for 360° $n = 1.75$. The flow rate also showed a power law dependency on the shear band width. However, the data were closer together for narrower shear bands, spreading out further as shear band width increased. Attempts to non-dimensionalise the flow rate resulted in $\frac{\mu Q}{\sqrt{(\dot{\gamma}^2 r+g)d}}$ being the closest to collapsing the data onto a single curve.

Overall, the orientation of the shear cell under consideration added immense complexity to the even the simple relations usually used to describe vertical shear cells, although the constitutive description of the flow field performed reasonably well. Future work should aim to achieve greater coverage of the annulus in PEPT experiments by developing a method to cool the granular media during longer experiment runs. This will mean that the PEPT data can be used to further validate the power dissipation model developed, as well as providing a better handle of the description of the volume fraction distribution, $\phi(I)$. A comparison of DEM simulations with a full tensorial formulation of the constitutive stress model should be undertaken. The validity of the constitutive relations used in this work should be examined by comparing them to the full tensorial descriptions. The connection between the inertial number, I, and the distributions of the effective friction coefficient over radial depth should be determined in order to compare results with the full stress tensor description of Cortet et al. [2009].

Bibliography

B. Andreotti, Y. Forterre, and O. Pouliquen. *Granular Media*. Cambridge University Press, 2013.

K. Ashida, S. Egashira, H. Kamiya, and H. Sasaki. The friction law and moving velocity of a soil block on slopes. *Annals of the Disaster Prevention Research Institute, Kyoto University*, 28(B-2):297–307, 1985. (in Japanese with English summary).

R. A. Bagnold. Experiments on a gravity-free dispersion of large solid spheres in a newtonian fluid under shear. *Proceedings of the Royal Society of London. Series A, Mathematical and Physical Sciences*, 225(1160):49–63, 1954a.

R. A. Bagnold. Experiments on a gravity-free dispersion of large solid spheres in a Newtonian fluid under shear. *Proceedings of the Royal Society of London. Series A, Mathematical and Physical Sciences*, 225(1160):49–63, Aug. 1954b. ISSN 1364-5021. doi: 10.1098/rspa.1954.0186. URL http://rspa.royalsocietypublishing.org/cgi/doi/10.1098/rspa.1954.0186.

O. Baran, D. Ertaş, T. C. Halsey, G. S. Grest, and J. B. Lechman. Velocity correlations in dense gravity-driven granular chute flow. *Phys. Rev. E*, 74:051302, Nov 2006. doi: 10.1103/PhysRevE.74.051302. URL http://link.aps.org/doi/10.1103/PhysRevE.74.051302.

R. Barley, J. Conway-Baker, R. Pascoe, J. Kostuch, B. McLoughlin, and D. Parker. Measurement of the motion of grinding media in a vertically stirred mill using positron emission particle tracking (PEPT) Part II. *Minerals Engineering*, 17(11-12):1179–1187, Nov. 2004. ISSN 08926875. doi: 10.1016/j.mineng.2004.06.034. URL http://linkinghub.elsevier.com/retrieve/pii/S0892687504001840.

G. K. Batchelor. *An introduction to fluid dynamics*. Cambridge University Press, 1967.

G. W. Baxter, R. P. Behringer, T. Fagert, and G. A. Johnson. Pattern formation in flowing sand. *Physical Review Letters*, 62(24):2825–2829, 1989.

L. Bbosa, I. Govender, A. Mainza, and M. Powell. Power draw estimations in experimental tumbling mills using PEPT. *Minerals Engineering*, 24(3-4):319–324, Feb. 2011. ISSN 08926875. doi: 10.1016/j.mineng.2010.10.005. URL http://linkinghub.elsevier.com/retrieve/pii/S0892687510002839.

R. B. Bird, W. E. Stewart, and E. N. Lightfoot. *Transport Phenomena*. John Wiley and Sons, Inc, second edition, 2002.

L. Bocquet, W. Losert, D. Schalk, T. Lubensky, and J. Gollub. Granular shear flow dynamics and forces: Experiment and continuum theory. *Physical Review E*, 65 (1):011307, Dec. 2001. ISSN 1063-651X. doi: 10.1103/PhysRevE.65.011307. URL http://link.aps.org/doi/10.1103/PhysRevE.65.011307.

A. Buffler, I. Govender, J. Cilliers, D. Parker, J. Franzidis, A. Mainza, R. Newman, M. Powell, and A. Van der Westhuizen. PEPT Cape Town: a new positron emission particle tracking facility at iThemba LABS. In *Proceedings of International Topical Meeting on Nuclear Research Applications and Utilization of Accelerators*, pages 4–8, 2009.

C. S. Campbell. Granular shear flows at the elastic limit. *Journal of Fluid Mechanics*, 465:261–291, 2002.

C. S. Campbell and C. E. Brennen. Computer simulation of granular shear flows. *Journal of Fluid Mechanics*, 151:167–188, 1985.

G. Chambon, J. Schmittbuhl, A. Corfdir, J. P. Vilotte, and S. Roux. Shear with comminution of a granular material: microscopic deformations outside the shear band. *Phys. Rev. E*, 68:011304, Jul 2003. doi: 10.1103/PhysRevE.68.011304. URL http://link.aps.org/doi/10.1103/PhysRevE.68.011304.

S. Chapman and T. G. Cowling. *The mathematical theory of non-uniform gases : an account of the kinetic theory of viscosity, thermal conduction, and diffusion in gases.* Cambridge University Press, 1953.

X. Cheng, J. Lechman, A. Fernandez-Barbero, G. Grest, H. Jaeger, G. Karczmar, M. Möbius, and S. Nagel. Three-Dimensional Shear in Granular Flow. *Physical Review Letters*, 96(3):038001, Jan. 2006. ISSN 0031-9007. doi: 10.1103/PhysRevLett.96.038001. URL http://link.aps.org/doi/10.1103/PhysRevLett.96.038001.

T. Chung. *General continuum mechanics*. Cambridge University Press, 2007.

S. L. Conway, T. Shinbrot, and B. J. Glasser. A Taylor vortex analogy in granular flows. *Nature*, 431(7007):433–7, Sept. 2004. ISSN 1476-4687. doi: 10.1038/nature02901. URL http://www.ncbi.nlm.nih.gov/pubmed/15386007.

J. Conway-Baker, R. Barley, R. Williams, X. Jia, J. Kostuch, B. McLoughlin, and D. Parker. Measurement of the motion of grinding media in a vertically stirred mill using positron emission particle tracking (PEPT). *Minerals Engineering*, 15 (1-2):53–59, Jan. 2002. ISSN 08926875. doi: 10.1016/S0892-6875(01)00199-6. URL http://linkinghub.elsevier.com/retrieve/pii/S0892687501001996.

P.-P. Cortet, D. Bonamy, F. Daviaud, O. Dauchot, B. Dubrulle, and M. Renouf. Relevance of visco-plastic theory in a multi-directional inhomogeneous granular flow. *EPL (Europhysics Letters)*, 88(1):14001, 2009.

P. A. Cundall and O. D. Strack. A discrete numerical model for granular assemblies. *Geotechnique*, 29(1):47–65, 1979.

F. da Cruz. *Friction and jamming in dry granular flows*. Theses, Ecole des Ponts ParisTech, Feb. 2004. URL https://pastel.archives-ouvertes.fr/pastel-00000946.

F. Da Cruz, F. Chevoir, D. Bonn, and P. Coussot. Viscosity bifurcation in granular materials, foams, and emulsions. *Phys. Rev. E*, 66:051305, Nov 2002. doi: 10.1103/PhysRevE.66.051305. URL http://link.aps.org/doi/10.1103/PhysRevE.66.051305.

F. da Cruz, S. Emam, M. Prochnow, J.-N. Roux, and F. Chevoir. Rheophysics of dense granular materials: Discrete simulation of plane shear flows. *Phys. Rev. E*, 72:021309, Aug 2005. doi: 10.1103/PhysRevE.72.021309. URL http://link.aps.org/doi/10.1103/PhysRevE.72.021309.

R. C. Daniel, A. P. Poloski, and A. E. Saez. Vane rheology of cohesionless glass beads. *Powder Technology*, 181(3):237–248, 2008.

DEM Solutions. *EDEM Technical Overview*. DEM Solutions, 2012.

A. Di Renzo and F. P. Di Maio. Comparison of contact-force models for the simulation of collisions in DEM-based granular flow codes. *Chemical Engineering Science*, 59 (3):525–541, Feb. 2004. ISSN 00092509. doi: 10.1016/j.ces.2003.09.037. URL http://linkinghub.elsevier.com/retrieve/pii/S0009250903005414.

J. Ding and D. Gidaspow. A bubbling fluidization model using kinetic theory of granular flow. *AIChE Journal*, 36(4):523–538, 1990. URL http://onlinelibrary.wiley.com/doi/10.1002/aic.690360404/abstract.

P. G. Fairhurst, M. Barigou, P. J. Fryer, J.-P. Pain, and D. J. Parker. Using positron emission particle tracking (PEPT) to study nearly neutrally buoyant particles in high solid fraction pipe flow. *International Journal of Multiphase Flow*, 27:1881–1901, 2001.

Y. Forterre and O. Pouliquen. Flows of Dense Granular Media. *Annual Review of Fluid Mechanics*, 40(1):1–24, Jan. 2008. ISSN 0066-4189. doi: 10.1146/annurev.fluid.40.111406.102142. URL http://www.annualreviews.org/doi/abs/10.1146/annurev.fluid.40.111406.102142.

Y. C. Fung. *A first course in continuum mechanics*. Englewood Cliffs, N.J. : Prentice-Hall, 1969.

GDR MiDi. On dense granular flows. *The European physical journal. E, Soft matter*, 14(4):341–65, Aug. 2004. ISSN 1292-8941. doi: 10.1140/epje/i2003-10153-0. URL http://www.ncbi.nlm.nih.gov/pubmed/15340859.

J. Geng, G. Reydellet, E. Clément, and R. Behringer. Greens function measurements of force transmission in 2D granular materials. *Physica D: Nonlinear Phenomena*, 182(34):274 – 303, 2003. ISSN 0167-2789. doi: http://dx.doi.org/10.1016/S0167-2789(03)00137-4. URL http://www.sciencedirect.com/science/article/pii/S0167278903001374.

D. Gidaspow. *Multiphase flow and fluidization: continuum and kinetic theory descriptions*. Academic press, 2012.

I. Goldhirsch. Rapid Granular Flows. *Annual Review of Fluid Mechanics*, 35(1):267–293, Jan. 2003. ISSN 0066-4189. doi: 10.1146/annurev.fluid.35.101101.161114. URL http://www.annualreviews.org/doi/abs/10.1146/annurev.fluid.35.101101.161114.

I. Govender, N. Mangesana, A. Mainza, and J.-P. Franzidis. Measurement of shear rates in a laboratory tumbling mill. *Minerals Engineering*, 24(3-4):225–229, Feb. 2011. ISSN 08926875. doi: 10.1016/j.mineng.2010.08.009. URL http://linkinghub.elsevier.com/retrieve/pii/S0892687510002086.

I. Govender, P. Cleary, and A. Mainza. Comparisons of PEPT derived charge features in wet milling environments with a friction-adjusted DEM model. *Chemical Engineering Science*, 97:162–175, June 2013. ISSN 00092509. doi: 10.1016/j.ces.2013.04.023. URL http://linkinghub.elsevier.com/retrieve/pii/S0009250913002820.

I. Govender, T. Pathmathas, and D. De Klerk. Power dissipation modelling in tumbling mills using positron emission particle tracking. In *XXVII IMPC*, number 705, 2014.

T. Hatano. Power-law friction in closely packed granular materials. *Physical Review E*, 75(6):060301, 2007.

M. R. Hawkesworth, D. J. Parker, P. Fowles, J. F. Crilly, N. L. Jefferies, and G. Jonkers. Nonmedical applications of a positron camera. *Nuclear Instruments and Methods in Physics Research A*, 310:423–434, Dec. 1991. doi: 10.1016/0168-9002(91)91073-5.

N. Hotta. Basal interstitial water pressure in laboratory debris flows over a rigid bed in an open channel. *Natural Hazards & Earth System Sciences*, 12(8), 2012.

D. Howell, R. P. Behringer, and C. Veje. Stress Fluctuations in a 2D Granular Couette Experiment : A Continuous Transition. *Physical Review Letters*, 82(26):5241–5244, 1999.

S.-S. Hsiau and H.-W. Jang. Measurements of velocity fluctuations of granular materials in a shear cell. *Experimental Thermal and Fluid Science*, 17:202–209, 1998.

A. Ingram, M. Hausard, X. Fan, D. J. Parker, J. Seville, N. Finn, and M. Evans. Portable Positron Emission Particle Tracking (PEPT) for Industrial Use. In *The 12th International Conference on Fluidization - New Horizons in Fluidization Engineering*, 2007.

H. M. Jaeger, S. R. Nagel, and R. P. Behringer. Granular solids, liquids, and gases. *Reviews of Modern Physics*, 68(4):1259, 1996.

V. Jasti and C. Higgs. Experimental study of granular flows in a rough annular shear cell. *Physical Review E*, 78(4):041306, Oct. 2008. ISSN 1539-3755. doi: 10.1103/PhysRevE.78.041306. URL http://link.aps.org/doi/10.1103/PhysRevE.78.041306.

V. K. Jasti and C. F. Higgs. A fast first order model of a rough annular shear cell using cellular automata. *Granular Matter*, 12(1):97–106, Dec. 2009. ISSN 1434-5021. doi: 10.1007/s10035-009-0159-x. URL http://link.springer.com/10.1007/s10035-009-0159-x.

J. T. Jenkins and S. B. Savage. A theory for the rapid flow of identical, smooth, nearly elastic, spherical particles. *Journal of Fluid Mechanics*, 130:187–202, 1983.

J. T. Jenkins and C. Zhang. Kinetic theory for identical, frictional, nearly elastic spheres. *Physics of Fluids (1994-present)*, 14(3):1228–1235, 2002.

S. Ji and H. H. Shen. Effect of contact force models on granular flow dynamics. *Journal of engineering mechanics*, 132(11):1252–1259, 2006.

S. Ji, D. M. Hanes, and H. H. Shen. Comparisons of physical experiment and discrete element simulations of sheared granular materials in an annular shear cell. *Mechanics of materials*, 41(6):764–776, 2009.

P. C. Johnson, P. Nott, and R. Jackson. Frictional–collisional equations of motion for participate flows and their application to chutes. *Journal of fluid mechanics*, 210: 501–535, 1990.

P. Jop, Y. Forterre, and O. Pouliquen. Crucial role of sidewalls in granular surface flows: consequences for the rheology. *Journal of Fluid Mechanics*, 541:167–192, Oct. 2005. ISSN 0022-1120. doi: 10.1017/S0022112005005987. URL http://www.journals.cambridge.org/abstract_S0022112005005987.

P. Jop, Y. Forterre, and O. Pouliquen. A constitutive law for dense granular flows. *Nature*, 441(7094):727–730, 2006.

C. Josserand, P.-Y. Lagrée, and D. Lhuillier. Granular pressure and the thickness of a layer jamming on a rough incline. *EPL (Europhysics Letters)*, 73:363–369, Feb. 2006. doi: 10.1209/epl/i2005-10398-1.

D. V. Khakhar, J. J. McCarthy, T. Shinbrot, and J. M. Ottino. Transverse flow and mixing of granular materials in a rotating cylinder. *Physics of Fluids*, 9:31–43, 1997.

D. V. Khakhar, A. V. Orpe, P. Andresen, and J. M. Ottino. Surface flow of granular materials: model and experiments in heap formation. *Journal of Fluid Mechanics*, 441: 255–264, 2001.

G. Koval, J.-N. Roux, A. Corfdir, and F. Chevoir. Annular shear of cohesionless granular materials: from inertial to quasistatic regime. *Physical Review E*, 79(2), 2009.

M. Lätzel, S. Luding, and H. J. Herrmann. Macroscopic material properties from quasi-static, microscopic simulations of a two-dimensional shear-cell. *Granular Matter*, 2(3): 123, 2000. ISSN 14345021. doi: 10.1007/s100350050004. URL http://link.springer.de/link/service/journals/10035/bibs/0002003/00020123.htm.

C.-H. Lee and C.-J. Huang. Kinetic-theory-based model of dense granular flows down inclined planes. *Physics of Fluids (1994-present)*, 24(7):073303, 2012.

P.-A. Lemieux and D. Durian. From avalanches to fluid flow: A continuous picture of grain dynamics down a heap. *Physical Review Letters*, 85(20):4273, 2000.

S.-Y. Lim, J. Davidson, R. Forster, D. Parker, D. Scott, and J. Seville. Avalanching of granular material in a horizontal slowly rotating cylinder: PEPT studies. *Powder*

Technology, 138(1):25–30, Nov. 2003. ISSN 00325910. doi: 10.1016/j.powtec.2003.08.038. URL http://linkinghub.elsevier.com/retrieve/pii/S0032591003002274.

W. Losert, L. Bocquet, T. C. Lubensky, and J. P. Gollub. Particle Dynamics in Sheared Granular Matter. *Physical Review Letters*, 85(7):1428–1431, 2000.

C. K. K. Lun. Kinetic theory for granular flow of dense , slightly inelastic , slightly rough spheres. *Journal of Fluid Mechanics*, 233:539–559, 1991.

C. K. K. Lun, S. B. Savage, D. J. Jeffrey, and N. Chepurniy. Kinetic theories for granular flow: inelastic particles in Couette flow and slightly inelastic particles in a general flowfield. *Journal of Fluid Mechanics*, 140:223–256, 1984.

B. Miller, C. O'Hern, and R. P. Behringer. Stress fluctuations in continuously sheared dense granular materials. *Physical Review Letters*, 77(15):3110–3113, Dec. 1996. ISSN 1063-651X. URL http://www.ncbi.nlm.nih.gov/pubmed/11970656.

R. D. Mindlin and H. Deresiewicz. Elastic spheres in contact under varying oblique forces. *Transactions of ASME, Series E. Journal of Applied Mechanics*, 20:327–344, 1953.

B. Mishra. A review of computer simulation of tumbling mills by the discrete element method: Part I – contact mechanics. *International Journal of Mineral Processing*, 71 (1-4):73–93, Sept. 2003. ISSN 03017516. doi: 10.1016/S0301-7516(03)00032-2. URL http://linkinghub.elsevier.com/retrieve/pii/S0301751603000322.

A. J. Morrison. Using PEPT to investigate the motion of granular material in a tumbling mill. Master's thesis, University of Cape Town, 2012.

D. Mueth. Measurements of particle dynamics in slow, dense granular Couette flow. *Physical Review E*, 67(1):011304, Jan. 2003. ISSN 1063-651X. doi: 10.1103/PhysRevE.67.011304. URL http://link.aps.org/doi/10.1103/PhysRevE.67.011304.

D. M. Mueth, G. F. Debregeas, G. S. Karczmar, P. J. Eng, S. R. Nagel, and H. M. Jaeger. Signatures of granular microstructure in dense shear flows. *Nature*, 406 (6794):385–389, July 2000. ISSN 1476-4687. doi: 10.1038/35019032. URL http://www.ncbi.nlm.nih.gov/pubmed/10935630.

R. M. Nedderman. *Statics and kinematics of granular materials*. Cambr. Univ. Press, Cambridge, 1992.

S. Ogawa, A. Umemura, and N. Oshima. On the equations of fully fluidized granular materials. *Zeitschrift für angewandte Mathematik und Physik ZAMP*, 31(4):483–493, 1980.

A. V. Orpe and D. V. Khakhar. Rheology of surface granular flows. *Journal of Fluid Mechanics*, 571:1–32, 1 2007. ISSN 1469-7645. doi: 10.1017/S002211200600320X. URL http://journals.cambridge.org/article_S002211200600320X.

D. Parker, C. Broadbent, P. Fowles, M. Hawkesworth, and P. McNeil. Positron emission particle tracking – a technique for studying flow within engineering equipment. *Nuclear Instruments and Methods in Physics Research Section A: Accelerators, Spectrometers, Detectors and Associated Equipment*, 326(3):592–607, 1993.

D. Parker, M. Hawkesworth, C. Broadbent, P. Fowles, T. Fryer, and P. McNeil. Industrial positron-based imaging: principles and applications. *Nuclear Instruments and Methods in Physics Research Section A: Accelerators, Spectrometers, Detectors and Associated Equipment*, 348(2):583–592, 1994.

D. Parker, A. Dijkstra, T. Martin, and J. Seville. Positron emission particle tracking studies of spherical particle motion in rotating drums. *Chemical Engineering Science*, 52(13):2011–2022, 1997a. ISSN 00092509. doi: 10.1016/S0009-2509(97)00030-4. URL http://linkinghub.elsevier.com/retrieve/pii/S0009250997000304.

D. J. Parker, D. A. Allen, D. M. Benton, P. Fowles, P. A. McNeil, M. Tan, and T. D. Beynon. Developments in particle tracking using the Birmingham Positron Camera. *Nuclear Instruments and Methods in Physics Research Section A: Accelerators, Spectrometers, Detectors and Associated Equipment*, 392(97):421–426, 1997b.

T. Pathmathas. *Granular Flow modelling of Rotating Drum Flows using Positron Emission Particle Tracking*. Theses, University of Cape Town, February 2015.

O. Pouliquen. Scaling laws in granular flows down rough inclined planes. *Physics of Fluids*, 11(3):542–548, 1999.

O. Pouliquen and F. Chevoir. Dense flows of dry granular material. *Comptes Rendus Physique*, 3(2):163–175, Jan. 2002. ISSN 16310705. doi: 10.1016/S1631-0705(02)01309-9. URL http://linkinghub.elsevier.com/retrieve/pii/S1631070502013099.

O. Pouliquen and Y. Forterre. Friction law for dense granular flows: application to the motion of a mass down a rough inclined plane. *Journal of Fluid Mechanics*, 453:133–151, Mar. 2002. ISSN 0022-1120. doi: 10.1017/S0022112001006796. URL http://www.journals.cambridge.org/abstract_S0022112001006796.

O. Pouliquen, C. Cassar, Y. Forterre, P. Jop, and M. Nicolas. How do grains flow: towards a simple rheology for dense granular flows. *Powders and Grains*, pages 859–865, 2005.

O. Pouliquen, C. Cassar, P. Jop, Y. Forterre, and M. Nicolas. Flow of dense granular material: towards simple constitutive laws. *Journal of Statistical Mechanics: Theory and Experiment*, 2006(07):P07020, 2006.

J. Rajchenbach. Flow in powders: From discrete avalanches to continuous regime. *Physical Review Letters*, 65(18):2221–2225, 1990.

J. Rajchenbach. Stress transmission through textured granular packings. *Phys. Rev. E*, 63:041301, Mar 2001. doi: 10.1103/PhysRevE.63.041301. URL http://link.aps.org/doi/10.1103/PhysRevE.63.041301.

K. K. Rao and P. R. Nott. *An Introduction to Granular Flow*. Cambridge University Press, 2008. ISBN 9780511611513. URL http://dx.doi.org/10.1017/CBO9780511611513. Cambridge Books Online.

P. G. Rognon, J.-N. Roux, M. Naaim, and F. Chevoir. Dense flows of cohesive granular materials. *Journal of Fluid Mechanics*, 596:21–47, 2008.

R. Roufail, B. Klein, and P. Radziszewski. Morphological features and discrete element method (DEM) forces produced in high speed stirred mill. In *XXVI International Mineral Processing Congress 2012 Proceedings*, number 707, pages 4526–4536, New Delhi, 2012.

C. H. Rycroft, K. Kamrin, and M. Z. Bazant. Assessing continuum postulates in simulations of granular flow. *Journal of the Mechanics and Physics of Solids*, 57 (5):828–839, May 2009. ISSN 00225096. doi: 10.1016/j.jmps.2009.01.009. URL http://linkinghub.elsevier.com/retrieve/pii/S002250960900009X.

S. B. Savage. Streaming motions in a bed of vibrationally fluidized dry granular material. *Journal of Fluid Mechanics*, 194:457–478, 1988.

S. B. Savage. Analyses of slow high-concentration flows of granular materials. *Journal of Fluid Mechanics*, 377:1–26, Dec. 1998. ISSN 00221120. doi: 10.1017/S0022112098002936. URL http://www.journals.cambridge.org/abstract_S0022112098002936.

S. B. Savage. Free-surface granular flows down heaps. *Journal of Engineering Mathematics*, 60(2):221–240, Mar. 2007. ISSN 0022-0833. doi: 10.1007/s10665-007-9141-y. URL http://link.springer.com/10.1007/s10665-007-9141-y.

S. B. Savage and K. Hutter. The motion of a finite mass of granular material down a rough incline. *Journal of fluid mechanics*, 199:177–215, 1989.

S. B. Savage and D. J. Jeffrey. The stress tensor in a granular flow at high shear rates. *Journal of Fluid Mechanics*, 110:255–272, 1981.

S. Schollmann. Simulation of a two-dimensional shear cell. *Physical Review E*, 59(1): 889–899, 1999.

O. J. Schwarz, Y. Horie, and M. Shearer. Discrete element investigation of stress fluctuation in granular flow at high strain rates. *Physical Review E*, 57(2):2053–2061, 1998.

T. Suzuki, N. Hotta, and K. Miyamoto. Influence of riverbed roughness on debris flows. *Japan Society of Erosion Control Engineerng Journal*, 56(2):5–13, 2003.

N. Taberlet, P. Richard, A. Valance, W. Losert, J. Pasini, J. Jenkins, and R. Delannay. Superstable granular heap in a thin channel. *Physical Review Letters*, 91(26):264301, Dec. 2003. ISSN 0031-9007. doi: 10.1103/PhysRevLett.91.264301. URL http://link.aps.org/doi/10.1103/PhysRevLett.91.264301.

N. Taberlet, P. Richard, and E. J. Hinch. S shape of a granular pile in a rotating drum. *Physical Review E*, 73(5):050301, 2006.

T. Takahashi. A review of Japanese debris flow research. *International Journal of Erosion Control Engineering*, 2(1):1–14, 2009.

G. I. Tardos. A fluid mechanistic approach to slow, frictional flow of powders. *Powder Technology*, 92(1):61 – 74, 1997. ISSN 0032-5910. doi: http://dx.doi.org/10.1016/S0032-5910(97)03218-X. URL http://www.sciencedirect.com/science/article/pii/S003259109703218X.

G. I. Tardos, M. I. Khan, and D. G. Schaeffer. Forces on a slowly rotating, rough cylinder in a Couette device containing a dry, frictional powder. *Physics of Fluids*, 10(2): 335–341, 1998.

C. A. Truesdell and R. G. Muncaster. *Fundamentals of Maxwell's kinetic theory of a simple monatomic gas: Treated as a branch of rational mechanics*, volume 83. Academic Press, 1980.

G. Tupper, I. Govender, A. Mainza, and N. Plint. A mechanistic model for slurry transport in tumbling mills. *Minerals Engineering*, 43-44(October):102–104, Apr. 2013. ISSN 08926875. doi: 10.1016/j.mineng.2012.09.015. URL http://linkinghub.elsevier.com/retrieve/pii/S0892687512003238.

A. van der Westhuizen, I. Govender, A. Mainza, and J. Rubenstein. Tracking the motion of media particles inside an IsaMill using PEPT. *Minerals Engineering*, 24 (3-4):195–204, Feb. 2011. ISSN 08926875. doi: 10.1016/j.mineng.2010.07.018. URL http://linkinghub.elsevier.com/retrieve/pii/S0892687510001998.

C. Veje, D. Howell, and R. Behringer. Kinematics of a two-dimensional granular Couette experiment at the transition to shearing. *Physical Review E*, 59(1):739–745, Jan. 1999. ISSN 1063-651X. doi: 10.1103/PhysRevE.59.739. URL http://link.aps.org/doi/10.1103/PhysRevE.59.739.

T. Volkwyn, A. Buffler, I. Govender, J.-P. Franzidis, A. Morrison, A. Odo, N. van der Meulen, and C. Vermeulen. Studies of the effect of tracer activity on time-averaged positron emission particle tracking measurements on tumbling mills at PEPT Cape Town. *Minerals Engineering*, 24(3-4):261–266, Feb. 2011. ISSN 08926875. doi: 10.1016/j.mineng.2010.08.020. URL http://linkinghub.elsevier.com/retrieve/pii/S0892687510002190.

R. Wildman and D. Parker. Coexistence of two granular temperatures in binary vibrofluidized beds. *Physical Review Letters*, 88(6):064301, Jan. 2002. ISSN 0031-9007. doi: 10.1103/PhysRevLett.88.064301. URL http://link.aps.org/doi/10.1103/PhysRevLett.88.064301.

R. D. Wildman, T. W. Martin, J. M. Huntley, J. T. Jenkins, H. Viswanathan, X. Fen, and D. J. Parker. Experimental investigation and kinetic-theory-based model of a rapid granular shear flow. *Journal of Fluid Mechanics*, 602:63–79, Apr. 2008. ISSN 0022-1120. doi: 10.1017/S0022112008000700. URL http://www.journals.cambridge.org/abstract_S0022112008000700.